Electrically-Assisted Evaporation of Charged Fluids: Fundamental Modeling and Studies on Ionic Liquids

by

Chase Coffman

B.S., University of Florida, 2009
S.M., Massachusetts Institute of Technology, 2012
Submitted to the Department of Aeronautics and Astronautics
in partial fulfillment of the requirements for the degree of
Doctor of Philosophy
at the
MASSACHUSETTS INSTITUTE OF TECHNOLOGY
February 2016

Author . . . .
Department of Aeronautics and Astronautics
January 28, 2016

Certified by . . . .
Paulo C. Lozano
Associate Professor of Aeronautics and Astronautics
Thesis Supervisor

Certified by . . . .
Manuel Martinez-Sanchez
Professor Emeritus of Aeronautics and Astronautics
Thesis Committee Member

Certified by . . . .
Qiqi Wang
Associate Professor of Aeronautics and Astronautics
Thesis Committee Member

Accepted by . . . .
Paulo C. Lozano
Associate Professor of Aeronautics and Astronautics
Chairman, Graduate Program Committee

Electrically-Assisted Evaporation of Charged Fluids: Fundamental Modeling and Studies on Ionic Liquids

by

Chase Coffman

Submitted to the Department of Aeronautics and Astronautics
on January 28, 2016, in partial fulfillment of the
requirements for the degree of
Doctor of Philosophy

Abstract

Electrosprays of the pure-ion variety embody a unique collection of attributes that have compelled interest in derivative technologies across a spectrum of applications ranging from Focused Ion Beams (FIB) to microrocketry. Unlike conventional colloid sources (i.e., so-called cone-jets or others sources from which droplets typically emanate), pure ion sprays are commonly characterized by narrow distributions of high specific charge and nominal energy deficits as a result of their evaporative mechanisms. Among other properties of the spray, these are known to enable well-behaved optics (e.g. for nanometric patterning with FIB) and low power overhead (e.g. for efficient electrical-to-kinetic energy transduction in microrocketry) while also providing for innate simplicity and spatial compactness.

In spite of their potential for paradigm-shifting impact, the practicality of contemporary pure-ion sources has been tempered by issues relating to reliability and predictability. In contrast to droplet emission, for example, empirical studies strongly suggest that pure-ion modes are only permissible under special sets of circumstances and that important beam qualities (namely the stability but also the current) are sensitive functions of the meniscus configuration. The difficulty in controlling these modes is somewhat abated through the use of fluids like ionic liquids (IL), particularly in connection with several heuristics that have emerged, but the process remains substantially fickle. This is believed to owe most directly to an undeveloped physical understanding.

While the physics that govern conventional colloid sources are at least functionally understood at this point, an analogous grasp of their ion relatives has proven elusive. The purpose of this thesis is to begin addressing this issue by way of rigorous theoretical investigations, with the ultimate aim of offering deeper fundamental insight and additional recourse to future design initiatives beyond the existing set of over-simplified heuristics.

In this thesis we first conduct a survey of potential contributors to the very multi-physical phenomenon of charge evaporation and identify key influences through basic order-of-magnitude analyses. These are used to inform the formulation of a detailed mathematical framework that is subsequently leveraged in the exploration of evaporation behaviors for a prototypical ionic liquid meniscus across a range of field, media, and hydraulic conditions. The results uncover a previously uncharted family of highly-stressed but ostensibly stable solutions for the problem of a volumetrically-unconstrained source. These appear to be confined to a particular subregion of the global parameter space that emphasizes thoughtful sizing of the meniscus and architecting of the feeding system. The impedance aspect of the latter, in particular, is believed to play a critical role in steady emission when large scale disparities, which are common in practical settings, exist across the parent meniscus. Additional influences that are often neglected in the literature, such as that of the liquid permittivity, are also elucidated and shown to play meaningful roles in evaporation. We conclude by outlining a reasonably comprehensive set of conditions that should be met for steady emission and substantiate these with tangible evidence from our studies.

Thesis Supervisor: Paulo C. Lozano
Title: Associate Professor of Aeronautics and Astronautics

Acknowledgments

Of the many people to which I am indebted, I would like to pay special thanks to Professor Paulo Lozano, for offering me an opportunity in his group and providing keen tutelage over the years; to Professor Manuel Martinez-Sanchez, for his enduring scientific enthusiasm and remarkable lucidity; to Professor Qiqi Wang, for his kind help in directing my novice efforts at computation; to Professor F. J. Higuera, for his patient and deeply insightful correspondence and laudable passion for difficult problems; and to my family, perhaps most importantly, for simply being.

I would also like to thank the Air Force Office of Scientific Research and NASA Space Technology Research Fellowships program for invaluable financial assistance.

Contents

Chapter 1

Introduction

1.1 Motivation

The family of electrospray ion sources embodies an intriguing collection of candidate technologies that have begun to find utility across a broad spectrum of disciplines in recent years. This is particularly true of a special subset of monodisperse and low-solvation sources, i.e., “purely ionic” sources, that are sometimes enabled through the use of ionic liquid (IL) fluids, a class of molten salt that is stable near room temperature and largely involatile. Among the group of potentially high-impact applications are focused ion beams (FIB) and microrocketry, where unique “purely ionic” physics promise to affect paradigm-shifting advances. Owing to localized emanation of monoergetic species and the amazing wealth of potential IL chemistries, which could facilitate tailorable reaction properties, such sources could very well allow for extreme nanometric processing capabilities across a spectrum of novel materials in FIB. Similarly, their unification of fuel and power economies with unprecedented architectural simplicity is enacting a new age of ultra-scalable propulsion elements for microrocketry.

In spite of substantial incentive, the subset of purely ionic IL sources have still to approach the operational maturity of some of their relatives from the broader electrospray family, e.g. sources based upon cone-jet (droplet) emission. This is perhaps most directly attributable to the nascent understanding of fundamental ion emission processes and the attendant lack of systematic design tools. While several heuristics have emerged, *ad-hoc* methods continue to typify an unfortunate majority of developmental efforts.

Before purely ionic systems can realize their potential, basic emission processes will need to be explored in the course of (1) outlining subregions of the global operational space that ensure steady ion operation; (2) elucidating the relative influences of various design factors; and (3) identifying specific points within the feasible envelope that confer favorable operational traits, e.g. high current or stability. In a broad sense, these will be the focus of the thesis presented herein.

1.2 Background & Fundamental Physics

Electrospray ionization is a field emission phenomenon that produces focused streams of high velocity particles through the breakdown of an electrically stressed meniscus. In the presence of a sufficiently strong electric field, the interface of a conducting fluid and an adjoining dielectric (often vacuum but sometimes air or even another liquid) destabilizes before resettling in a pseudoconic state. The attendant geometry is dynamically stable over a range of field conditions and enables the binding forces of surface tension to locally balance the prevailing electrical traction. While qualitative observations of this process were made as early as 1914 (see Zeleny [1, 2]), a satisfactory mathematical framework remained elusive until 1964 when G. I. Taylor came to the very remarkable conclusion that all such cones must obey a universal half-angle (49.29 °), regardless of the working fluid or far-field perturbations [3]. In recognition of this insight and the profound impact it has had in the intervening years, the term "Taylor cone" is now conventionally used to reference these structures in electrospray parlance.

A rich spectrum of conducting fluids -- these include, but are not limited to, liquid metals (LM), solvents with ionic dopants, and a class of room-temperature molten salt known as an ionic liquid (IL) -- are known to support Taylor cone formation in spite of what are sometimes large disparities in the intrinsic properties. Liquid metals, for example, are often characterized by electrical conductivities that are $\gg 1$ S/m while those of doped solvents are many orders of magnitude smaller. Interestingly, this leads to a similarly impressive range of feasible operating modes. The so-called cone-jet mode typifies low conductivity fluids and involves a thin cylindrical protuberance that extends from the Taylor cone tip before breaking into an ensemble of charged droplets shortly downstream. When certain hydraulic conditions are met, i.e. when the flow rate is sufficiently small, the same cone-jet may produce a concurrent stream of individual ions that are distinguished from their droplet counterparts by drastically elevated specific charges (C/kg); this is the ion-droplet mixed mode. For higher conductivity fluids like liquid metals and many ionic liquids, still smaller flow rates may sometimes enact pathways to a purely ionic mode in which the cone-jet is fully extinguished and the emission of low-solvation ions is permitted to prevail exclusively.

Among the potential modes, cone-jet emission has been studied most extensively as a result of its widespread utility in several fields (it is perhaps best known in the application of soft ionization for bio-molecules in mass spectrometry, for which John Fenn won the 2002 Nobel Prize in Chemistry). In certain respects, however, the purely ionic mode is singularly attractive: for example, high specific charges enable superior propellant economy in microrocketry while minimal flow rates sometimes afford passive hydraulic management schemes that simplify the system-level engine architecture.

As a foundation for the detailed analyses that will emerge throughout this thesis, in the following sections we introduce fundamental electrospray mechanics and emphasize important elements of pure ion emission. Topics include Taylor cone formation, field emission processes, and "emitter" utilization concepts. We conclude the introduction by offering a specific and detailed example of pure ion utility in

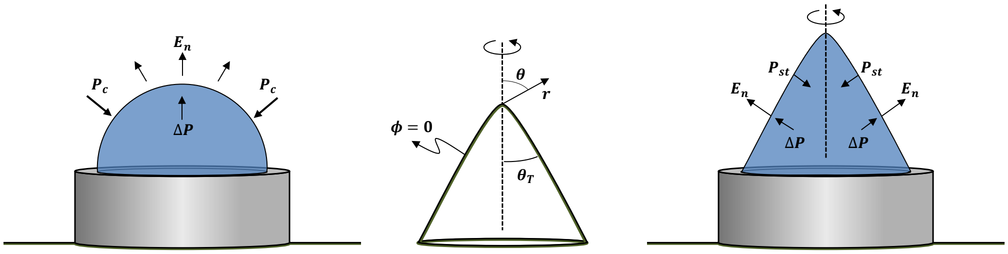

Figure 1-1: Diagram of Taylor cone formation and spherical coordinate convention. **Left:** Smooth, quasi-hemispherical meniscus preceding transition to Taylor geometry. **Center:** Spherical coordinate convention used to identify equipotential half-angle. **Right:** Stabilized Taylor structure highlighting local balance between electrical traction, hydrostatic pressure, and surface tension. The latter force, P_{ST}, intensifies with the electric field as the governing length scales shrink in the direction of the apex.

microrocketry.

1.2.1 Taylor cone formation

Critical aspects of Taylor cone formation, including geometric phenomena, follow from a pressure balance governing the fluid-dielectric interface. When electrical stressing is present, this balance reads

$$\frac{1}{2}\epsilon_0 \left(\nabla\Phi\right)^2 + \Delta P = \gamma \boldsymbol{\nabla} \cdot \vec{n} \tag{1.1}$$

where the first term on the left-hand side is the familiar electric pressure and the second is a hydrostatic pressure jump across the interface. γ is the intrinsic surface energy of the fluid (J/m^2) that combines with the divergence of the surface normal, $\boldsymbol{\nabla} \cdot \vec{n}$, to describe the pressure that is supported by surface tension. It is, in general, equivalent to $\gamma\left(r_1^{-1} + r_2^{-1}\right)$, where r_1 and r_2 are the principal radii of curvature at a given point along the interface.

In practical situations the working fluid is often anchored in place by some form of feeding mechanism. This can be, for example, the end of a capillary tube or a sharp needle. In either case, sub-critical stressing of the meniscus will result in the growth of a smooth, continuous interface (to first approximation) until the LHS of Eq. 1.1 reaches some threshold value. For capillary tubes this is typically approximated by the so-called capillary pressure, $P_c = 2\gamma/r_c$, which is determined in part by the radius of the tube head, r_c. Conventional wisdom suggests that stressing beyond this point results in rapid deformation of the interface and ultimately its reconstitution as a stable pseudocone (see Fig. 1-1). While certain metastable geometries may exist between the cone itself and the spheroidal cap that is believed to precede it [4], we often take license to view the transition as an instantaneous snap-over process.

Topographical characteristics of the resulting structure can be identified by finding a boundary geometry that satisfies equipotentiality. Although the nature of charge emission, which we have yet to discuss, must naturally perturb the equipotential condition, it is very often a feasible approximation. After placing a spherical coordinate system at the apex of the interface we can invoke a Laplacian "product" solution of the form

$$\Phi\left(r,\theta\right)=\sum_{n}\left[a_{n}r^{n}+b_{n}r^{-(n+1)}\right]P_{n}\left(\cos\theta\right) \tag{1.2}$$

for the dielectric region outside of the cone so long as azimuthal symmetry is appropriate. This incorporates the Legendre function of the first kind, P_n, but ignores the counterpart Q_n due to its singular behavior near θ=0 (in the dielectric region of interest). If we further neglect the hydrostatic pressure term ΔP as in the classical Taylor analysis, we can use Eq. 1.1 to show that the balance governing the pseudocone structure must only involve electric pressure and surface tension. When this is the case, the boundary very nearly approaches a perfect conical geometry for which the normal component of the interfacial field is known to scale like (see, for example, [5])

$$E_{n}=\sqrt{\frac{2\gamma\cot\theta_{T}}{\epsilon_{0}r}} \tag{1.3}$$

where the Taylor angle, θ_T, is the half-angle of the conic body. This must be the same field described by the Laplacian solution. Taking the derivative of Eq. 1.2 at the equipotential interface gives

$$E_{n}=E_{\theta}=-\frac{1}{r}\frac{\partial\Phi}{\partial\theta}=-\sum_{n}\left[a_{n}r^{n-1}+b_{n}r^{-(n+2)}\right]\frac{\partial}{\partial\theta}P_{n}\left(\cos\theta\right) \tag{1.4}$$

which can only agree with Eq. 1.3 when $b_n \to 0$ and $n \to 1/2$. The corresponding Legendre function, $P_{1/2}\left(\cos\theta\right)$, has a zero at $\theta = 130.71°$ and provides for the Taylor angle θ_T = 180 - 130.71 = 49.29°. This result has two very remarkable features:

- First, the cone solution is independent of any property of the working fluid and suggests a universal geometry. In formulating the solution we ignored the presence of a hydrostatic pressure jump, ΔP, which is not always vanishing when the cone is in communication with a feeding system (e.g. a pressurized reservoir of fluid) or when charge emission is present. Although these factors are known to perturb the cone geometry [6] to some degree, the nominal θ_T is typically a reasonable first approximation for the half-angle.

- Second, the Laplacian solution is local to the cone and ignores perturbations in the far-field. To low order, this suggests that the fields very near to the interface are somewhat insensitive to external ones once the Taylor cone has been established.

1.2.2 Charge emission

From Eq. 1.3, the field at the apex of a perfectly conical Taylor structure is unbounded. This cannot be strictly physical, of course, and nature addresses the apparent absurdity through the dynamics of charged particle emission. In most cases, strong apex fields disrupt the cone topography and force an open meniscus that is characterized by a thin jet extending in the axial direction. This jet carries a current [6]

$$I_d = g\left(\epsilon\right)\sqrt{\gamma K Q} \tag{1.5}$$

where K and Q are the conductivity (Si/m) and flow rate (m^3/s) of the fluid, respectively, and $g\left(\epsilon\right)$ is some empirical factor depending upon the dielectric constant. The characteristic length scale of the protuberance, namely its diameter, approaches

$$d_j = G\left(\epsilon\right)\left(\frac{\epsilon\epsilon_0 Q}{K}\right)^{1/3} \tag{1.6}$$

where $G\left(\epsilon\right)$ is a related empirical factor, before it breaks into a stream of charged droplets briefly downstream. These carry a specific charge

$$\left(\frac{q}{m}\right)_d = \frac{g\left(\epsilon\right)}{\rho}\sqrt{\frac{\gamma K}{Q}} \tag{1.7}$$

that depends on the intrinsic density of the fluid, ρ ($\mathrm{kg/m}^3$), and the ratio I/Q. Values of the droplet specific charge vary across different fluids and flow conditions but typically fall within the range from 10^2 - 10^4 C/kg. From Eqs. 1.5, 1.6, and 1.7 we see that a decreasing flow rate results in a shrinking jet that produces droplets of stronger specific charge, albeit at the expense of the overall current. When the flow rate becomes sufficiently small, such that the jet approaches the 10^{-8} m regime, a process known as "field evaporation" begins to compensate the waning current by releasing a concurrent population of low-solvation ions from the neck. These particles are characterized by specific charges in the range from 10^5 - 10^6 C/kg. Interestingly, further reduction in the flow may sometimes give way to complete extinction of the jet and evaporation of a stream of pure ions from a closed meniscus (see Fig. 1-2), though this is not the general case. With organic electrolytes, for example, there exists a minimum stable flow rate

$$Q_{min} \approx \frac{\epsilon\epsilon_0\gamma}{\rho K} \tag{1.8}$$

that is very often larger than that which would otherwise be required for recovery of a closed configuration.

The mechanics of the closed meniscus problem are still only tenuously understood but in practice it is known that high conductivity fluids like liquid metals and certain ionic liquids possess special circumstances that do sometimes facilitate this configuration. When it does prevail, it is known that the emission obeys the phenomenological Arrhenius rate [7]

$$j = \sigma\frac{k_B T}{h}e^{-E_a/k_B T} \tag{1.9}$$

where j is the density of evaporated current ($\mathrm{A/m}^2$), σ is the density of charge

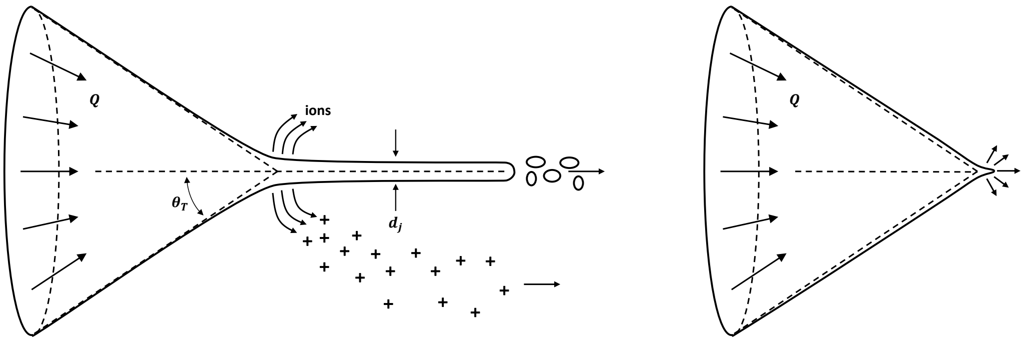

Figure 1-2: Diagrams of cone-jet emission (left) and pure ion emission from a closed meniscus (right). The jet net shrink for small flow rates and sometimes produces ion currents upstream of the droplet breakup. For special circumstances that are not yet fully understood, very small flows give way to total extinction of the jet and pure ion desorption from a sharp but closed meniscus structure.

at the liquid-dielectric interface (C/m^2), k_B is Boltzmann's constant, T is the liquid temperature, h is Planck's constant, and E_a is some characteristic activation energy. At 1-2 eV, the nominal activation energy for many ionic liquids (this is sometimes referred to as the solvation energy, ΔG [8]) is extremely large with respect to the thermal product k_BT and precludes significant evaporation near room temperature. This kinetic barrier is, however, artificially defrayed by the presence of strong fields near the tip of a sharp meniscus. In very polar media ($\epsilon \gg 1$), for example, the barrier reduction scales like

$$E_a = \Delta G - G\left(E_n\right), \text{ where} \tag{1.10}$$

$$G\left(E_n\right) = \sqrt{\frac{e^3 E_n}{4\pi\epsilon_0}} \tag{1.11}$$

with e the fundamental charge and E_n the normal component of the electric field acting at the interface. Eq. 1.11 applies to singly charged particles and garners validity insofar as an image charge approximation holds [9]. Copious ion emission occurs for

$$E_n \gtrsim \frac{4\pi\epsilon_0 \Delta G^2}{e^3} \tag{1.12}$$

when the potential energy supplied by the external field meets or exceeds the nominal solvation barrier. This suggests that fields on the order of 10^9 V/m (ionic liquids) to 10^{10} V/m (liquid metals) are required for meaningful currents. These are extremely strong, and by invoking Eq. 1.3 it can be seen that they can only be permitted to exist in the vicinity of a very small region ($\sim$ 10 nm radius) encircling the apex of a Taylor source or similarly sharp meniscus.

1.2.3 Emitter Architectures

From a theory perspective it is sometimes convenient to view the enabling electrospray fields in an abstract way, as simply "externally supplied", but real devices require some feasible means for producing them. More often than not, the requisite fields are realized by forcing a relative bias across two neighboring electrodes, one of which is wetted with the working fluid. The wetted electrode, or “emitter”, is generally deformed to a sharp point that amplifies the ambient field at its apex and localizes cone formation to the same area. This serves the twofold purpose of enabling emission at tractable potentials and restricting charge production to specific sites that are locationally known *a priori*. The latter affords alignment to perforations in the opposing electrode and unimpeded pathways for interstitial charge flows. Several common emitter architectures are diagrammatically sketched in Figure 1-3 and briefly expounded upon in what follows.

Open-flow emitters

Open-flow architectures operate by transporting fluid along the external surface of a solid emitter body. The result is a simple electrospray structure with a large interfacial area that is in some ways advantageous but comes at the expense of propellant selection. Owing to full exposure, liquids of non-negligible vapor pressure (e.g. organic electrolytes) are generally precluded in low pressure operating environments.

From a geometric perspective, open-flow emitters -- sometimes referred to as externally-wetted emitters -- may safely adopt one of a number of different shapes. Previous studies, for example, have used "volcano" geometries, which naturally follow from the isotropy of electrochemical etches on wires or planar surfaces; "pencil" geometries, which follow from specially-masked plasma etches and are akin to the former, albeit with greater anisotropy in the sidewalls; and "plateau" geometries, which are characterized by anisotropic sidewalls and flat tops designed to augment the active

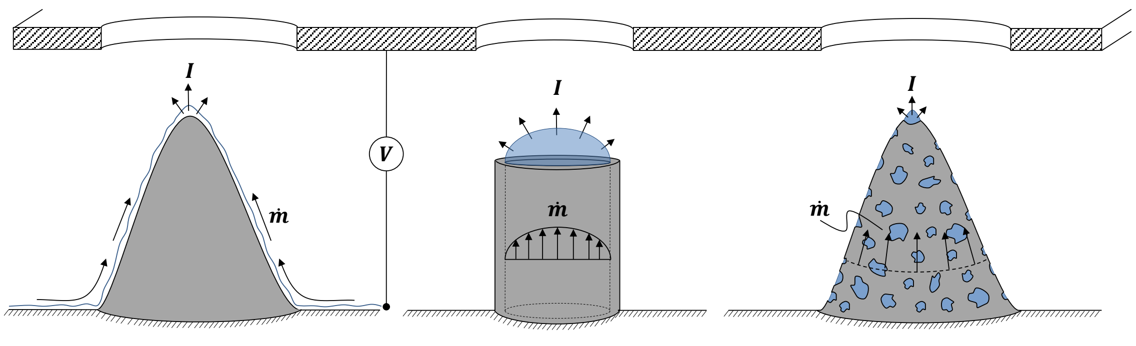

Figure 1-3: Common emitter architectures. Common emitter architectures are depicted along with the typical counter-electrode biasing scheme. **Left:** Open-flow emitter transporting liquid along its body. **Center:** Closed-flow emitter transporting liquid through an internal channel. **Right:** Hybrid emitter passing liquid through a porous bulk.

emission area. Other permutations are possible, of course, but limited insofar as the related manufacturing methods. Additional caveats include tenuous fluid transport, which is related to the difficulties of external wicking, and the near-impossibility of a feeding pressure.

Closed-flow emitters

Closed-flow architectures are the antithesis of their open-flow counterparts in that they transport fluid via sealed internal channels, which mitigates losses attendant to normal evaporation in low-pressure environments and restricts Taylor cone formation to the exposed head of the liquid column. Liquid metals, ionic liquids, and organic electrolytes are all feasible fluids.

The closed-flow emitter geometry is almost always that of a traditional capillary, though slit-style variations which are similar but elongated in one direction are known to exist. In this way, they benefit from a degree of simplicity that lends them to both conventional and MEMS manufacturing. Only the latter, however, is well-suited to multiplexing. Owing to their closed infrastructure, they are adept at transporting strong flows such as those provided through external pumping, and this has made them useful as cone-jet sources in a number of different applications ranging from spectrometry to thin-film deposition to propulsion. They are, however, susceptible to clogging and overflow for the same reasons.

Hybrid (porous) emitters

Porous architectures transport fluid via networks of internal channels. They combine the high capacity hydraulics of closed-flow designs with a robustness to clogging and overflow that is characteristic of their open-flow counterparts. They are hybrids in this sense, and offer compatibility with liquid metals, ionic liquids, and organic electrolytes to varying extents.

Functional geometries for porous emitters generally coincide with those of the open-flow variety although creative configurations are theoretically possible. Bulk porous substrates are only commonly available in metallic and ceramic forms, both of which are plasma-chemically inert and sputter-hard, and this has traditionally restricted manufacturing to electrochemical techniques. As a result, the literature is largely limited to "pencil" and "volcano" style features.

Geometric limitations notwithstanding, porous emitters are generally capable of operating with or without back pressure and of exhibiting modal versatility in their emission, i.e. the ability to support either cone-jet or ionic sprays. In conjunction with a proclivity for large ionic throughputs, this has helped them to garner a great deal of interest in recent years.

1.3 Example of pure ion utility: micropropulsion

As an example of pure ion utility we offer here a brief analysis of the performance of an electrospray microrocket. Among other metrics, we show that fuel economy is a strong function of beam composition and leverage the results in motivating further studies on the ion mode.

The function of any emitter structure is to amplify the local electric field and stress the fluid at its surface. For a specific starting voltage, V_s, the field at the tip will reach a threshold level and begin driving an electrospray current, I. The attendant mass flow

$$\dot{m} = \sum_n I_n \left(\frac{m}{q}\right)_n \tag{1.13}$$

may, in general, contain both ionic and droplet contributions (subscripts i and d hereafter). The n^{th} constituent in this charge stream will experience an electrostatic free-fall through the beam voltage V_B and reach a terminal velocity

$$c_n = \sqrt{2\left(\frac{q}{m}\right)_n V_B} \tag{1.14}$$

as dictated by the conservation of total energy (which is only between kinetic and electrostatic potential energy factors in this case), before exhausting into free space at an angle θ_n with respect to the axial direction. The momentum flux embodied by the aggregate flow has an axial projection $\sum\left(\dot{m}c\cdot\cos\theta\right)_n$ that imparts a thrust force F on the parent needle. Assuming two particle families of monodisperse specific charge (one family of ions and another of droplets, neglecting both "cold" neutrals arising from thermal evaporation from the meniscus and their "hot" counterparts that may arise from molecular fragmentation events in the accelerating part of the beam [10, 11]), this thrust can be cast as

$$F = \eta_{tr}\eta_\theta\sqrt{\eta_E\eta_p}I_T\sqrt{2\left(\frac{m}{q}\right)_m V} \tag{1.15}$$

where I_T is the total current, $I_i + I_d$, and $(q/m)_m$ is the average specific charge of the mixed mass flows

$$\left(\frac{q}{m}\right)_m = \left(\frac{q}{m}\right)_i\left[\beta + (1-\beta)\,\psi\right]^{-1} = \left(\frac{q}{m}\right)_d\left[\frac{\psi}{\beta + (1-\beta)\,\psi}\right] \tag{1.16}$$

In Eq. 1.16, β is taken to be the ratio of transmitted ion current to total transmitted current ($1-\beta$, therefore, is the corresponding droplet fraction), and ψ is the ratio of specific charges, $(q/m)_i\,/\,(q/m)_d$. The efficiency factors are defined as

$$\eta_{tr} = \frac{I_{tr}}{I_T} \tag{1.17}$$

$$\eta_\theta = \frac{\beta \cos\langle\theta_i\rangle + (1-\beta)\cos\langle\theta_d\rangle\sqrt{\psi}}{\beta + (1-\beta)\sqrt{\psi}} \tag{1.18}$$

$$\eta_E = \frac{V_B}{V} \tag{1.19}$$

$$\eta_p = \frac{\left[\beta + (1-\beta)\sqrt{\psi}\right]^2}{\beta + (1-\beta)\,\psi} \tag{1.20}$$

The transmission efficiency, η_{tr}, is the ratio of transmitted current to total current and accounts for imperfect extractor transparency. The angular efficiency, η_θ, takes care of angular losses in the part that of the beam that successfully propagates. The characteristic angles $\langle\theta_i\rangle$ and $\langle\theta_d\rangle$ are averaged over the beam and account for potentially dissimilar distributions of the particle families

$$\cos\langle\theta_n\rangle = \int_B \cos\theta_n \cdot \left(\frac{d\dot{m}_n}{\dot{m}_n}\right), \text{ for both } n \tag{1.21}$$

The energetic effiency, η_E, is the ratio of the actual beam voltage to the emitter one and describes the characteristic "ion cost". This is often just a few volts in ion modes. The polydispersity efficiency, η_p, is very important in mixed-mode operation and accounts for losses related to concurrent acceleration of dissimilar specific charges.

Currents on the order of 10^{-7} - 10^{-6} A are typical when a pure ion stream is achieved. For $(q/m)_i \sim 10^5$ - 10^6 C/kg and $V \sim 10^3$ Volts, these lead to thrust values (Eq. 1.15) that are on the order of 10^{-9} - 10^{-7} N and generally small in comparison to in-space needs. Multiplexing of individual needles is a common solution for this issue and can provide for engines of substantial thrust density when arrays are sufficiently populated. Figure 1-4 briefly introduces this idea.

Beyond the thrust, the total efficiency of the electrical to kinetic energy transduction process and the effective specific impulse are important engine parameters. These are cast as

$$c = \eta_i \eta_{tr} \eta_\theta \sqrt{\eta_E \eta_p} \cdot \sqrt{2\left(\frac{q}{m}\right)_m V} \tag{1.22}$$

$$\eta_T = \eta_u \eta_i \eta_E \eta_p \left(\eta_{tr}\eta_\theta\right)^2 \tag{1.23}$$

where η_i is an ionization efficiency accounting for any flow of neutral mass, $\eta_i = (\dot{m}_i + \dot{m}_d)/\dot{m}$, and η_u is a factor accounting for upstream losses in the power management system (e.g. the PPU) [12]. The specific impulse in particular, which is sometimes referenced in units of seconds after dividing by the gravitational acceleration constant, is a critical metric in system-level design as it dictates aspects of vehicle sizing and mass/volume budgeting.

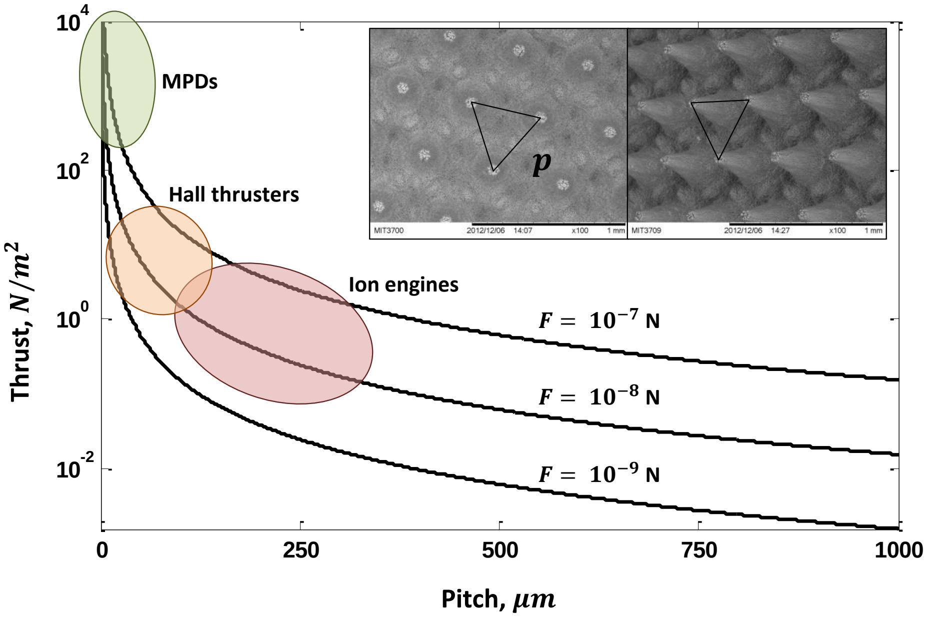

Figure 1-4: Notional scaling of thrust density with emitter population. Estimated thrust densities for several values of F (the thrust per emitter) are shown alongside nominal F/A ranges for select engine technologies. The inset delineates the emitter pitch, p, that governs the feature density in an actual array.

Consider the equation for an ideal rocket traveling in a vacuum devoid of external forces, $dm/m = -dv/c$, which can be integrated to identify the propellant fraction that is required to achieve a given Δv [13, 14, 15, 16]. This is

$$\frac{m_p}{m_0} = 1 - e^{-\Delta v/c} \tag{1.24}$$

where m_p/m_0 is the ratio of propellant mass to the initial wet mass of the vehicle, Δv is a mission-specific velocity increment, and c is the characteristic specific impulse of the engine (assumed constant). Many missions require substantial velocity increments and therefore high values of c in order to mitigate the attendant propellant need. The latter is often facilitated by a pure ion beam, rather than a mixed or pure droplet one, and Figure 1-5 illustrates this point. On the left, the polydispersity efficiency is observed to suffer for mixed beams, especially for large ψ. Losses are wholly mitigated for either a pure ion beam or a pure droplet beam, but from Fig. 1-5 (center) we see that only the former confers good specific impulse performance. The vehicular ramifications of this are delineated in Fig. 1-5 (right), which shows propellant budgeting for three cases of velocity increment: 100 m/s, which is on the order of simple orbit raising requirements [17]; 1000 m/s, which is on the order of long-term drag cancellation or stationkeeping requirements [18]; and 10,000 m/s, which is on the order of high-altitude and interplanetary requirements (e.g. Lunar missions) [19]. The budgets for pure droplet and mixed stream engines are substantially larger than those of their pure ion counterparts. While this clearly underscores

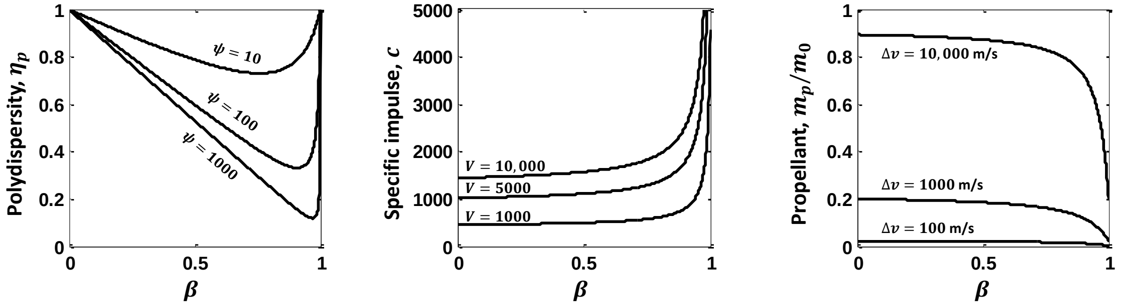

Figure 1-5: Various metrics for a general (mixed ion-droplet) electrospray engine. **Left:** Polydispersity efficiency for various ratios of specific charge. **Center:** Effective specific impulse (seconds) for three select voltages and the case [ψ = 100, $(q/m)_i$ = 10^6 C/kg]. **Right:** Propellant fraction for various Δv requirements and the case [ψ = 100, $(q/m)_i$ = 10^6 C/kg, V = 1000V].

the need to reliably design for and operate within a purely ionic envelope, the present collection of *a posteriori* insights have proven rather prohibitive. With that in mind, the fundamental studies to be undertaken hereafter are intended as a first remedial step.

Chapter 2

Literature review

The literature review is divided along two lines. The first section covers theoretical and experimental aspects of purely ionic IL evaporation while the second presents a representative snapshot of previous microrocket development programs. The attention of the latter is restricted to purely ionic IL engines of the porous type. It is intended to introduce the current state-of-the-art as a way of highlighting several deficiencies that are common amongst the broader family of purely ionic technologies. In the brief chapter that immediately follows, the collection of existing art is used to motivate a series of high-level objectives for the thesis.

2.1 Fundamental research

2.1.1 Experimentation

In the cone-jet literature it is well-known that the emitted current begins to favor ionic pathways in lieu of droplet ones at very low flow rates, which often leads to speculation that a pure ion mode is within reach when a sufficiently small value can be prescribed for the latter. In many cases, however, this belies possibility as there exists a limiting flow rate for conventional fluids (e.g. doped organic electrolytes) that demarcates a stability threshold and precludes transition to the pure ion regime. Still, the fact that ion emission has been observed in liquid metals since at least the 1960's [26, 27] has given hope that it is permitted for certain fluids under special circumstances.

Notwithstanding a 1969 study by Perel [28], in which the spray properties of concentrated sulfuric acid were explored, the pure ion mode has remained largely elusive until only recently. In 2003, Romero-Sanz [29] first reported on a fluid for which droplet extinction could be navigated in a stable way. Using a 20 μm ID capillary line (30 cm long) biased to 1375V, the ionic liquid EMI-BF4 (1-ethyl-3-methyl imidazolium tetrafluoroborate) was sprayed at various flow rates by modulating an upstream reservoir pressure. While a mixed ion/droplet current prevailed in most of the cases investigated, as expected, the droplet component appeared to completely extinguish (as evidenced by time-of-flight spectrometry) when the reservoir pressure and flow rates were throttled to their low values of 28 Torr and $0.56{\cdot}10^{-12}$ kg/s, respectively. Very remarkably, an ion current in the neighborhood of $\sim$ 200 nA remained. Though a firm rationalization for the enabling facets of EMI-BF4 could not be offered at the time, it is now somewhat apparent that this is possibly owing to a unique combination of high electrical conductivity ($\gtrsim$ 1 Si/m) and surface tension ($\gtrsim$ 50 dyn/cm) [30]. Note that liquid metals, for which ion emission is pervasive, share this combination of attributes albeit to a much greater extent.

Around the same time, Lozano [31] explored the emission properties of the same ionic liquid from electrochemically sharpened tungsten wires at MIT. Starting voltages of $\sim$ 1.6 kV were observed for emitter tip radii of $\sim$ 20 μm and corresponded to incipient currents of 100 nA near room temperature. These nearly tripled to 300 nA for biases of 2 kV though time-of-flight (TOF) measurements suggested purely ionic emission for all cases. Energy tests and angularity-resolved beam measurements also showed low voltage losses (not more than a few percent of the needle voltage) and minimal spray divergence not exceeding $\sim$ 18°. Interestingly, the author also explored the thermal dependence of the emission properties and demonstrated enhanced currents at elevated temperatures. While holding the fluid at 65°, for example, measured currents were $\sim$ 400 nA and $\sim$ 600 nA for needle voltages of 1.6 kV and 2 kV, respectively. While this led to some speculation on a limiting hydraulic mechanism `--` the temperature increase must have reduced the effective fluid viscosity and improved convective transport thereby `--` similar conduction effects could not be ruled out. Lastly, in all cases Lozano observed detrimental electrochemistry that degraded both the needle and the fluid quality during extended operation in a single polarity. This was attributed to capacitive charging of the liquid-metal double layer beyond the so-called electrochemical window and ultimately rectified with a voltage alternation strategy in which excessive overpotentials were discouraged through periodic polarity reversal [32]. This is the same technique that is now widely employed in the maintenance of source integrity for long-life, IL-based sprays.

Lozano followed up on this work by characterizing a source based on the ionic liquid EMI-Im and concluded that it displayed similarly advantageous energetic properties whilst achieving pure ion emission [33]. A 5-10 μm tungsten tip was used to facilitate the spray, as before, but now operated in the voltage band from ±900V to ±1200V. Rather than the energy results, the most striking facet of this study was the fact that it achieved ion emission with a fluid that typically produces droplets when fed from a capillary. This is an important phenomenon of externally-wetted electrosprays that was later corroborated through exploration of more exotic ionic liquid permutations [34, 35] and suggests that upstream hydraulic properties play a major role in determining the nature and quality of the source.

Further indication of this notion was evidenced by Castro [36] in a study on the tip curvature dependency of the emission characteristics. The author presented the level of evaporated current for a panoply of fluids and observed sizable excursions that varied monotonically with the sharpness of the emitting electrode. While just tens of nA were produced with the smallest tip in the study (2.5 μm radius), greater than 1 μA was seen for the largest (60 μm radius). Additional information was given for a 50 μm tip case, where the authors plotted biases covering the full range of stability

(2225V - 2425V) and corresponding currents ($\sim$ 500 nA to $\sim$ 700 nA). Mention was also made of an 80 μm tip that could not support an ion emission mode; rather, the production of droplets led the authors to point specifically to the influence of the upstream hydraulic impedance on the emitted current. For small tips, they argued, a high impedance must somehow ensure ion emission while simultaneously restricting the allowable flow rate. The governing impedance is relaxed for larger tips, permitting elevated currents, but appears to reach a threshold for excessively blunt surfaces where it gives way to other emission modes. Though still qualitative, this argument was compelling in its seeming ability to reconcile the difference between externally-wetted and capillary sources. Beyond that, however, no treatment or discussion was offered for the nature of the Taylor cones that produced the immense currents observed in the blunt-tip cases, which were anomalously large in relation to typical findings ($\geq$ 1 μA compared to hundreds of nA). Interestingly, more recent research has hinted that bifurcations [37, 38], in which a single Taylor cone splits into two coupled sources, or other "multi-cone" mechanisms [39] could have been factors, though the degree to which these phenomena are connected to the noted hydraulic ones is still relatively unclear.

Velasquez-Garcia [40, 41] and Gassend [39, 42] attempted to leverage the phenomenon described in Ref. [36] by exploring externally-wetted tips with large emission areas. Unfortunately, they showed that the high current regime (more than several hundred nA) is unstable in many cases and likely the result of poor fluid transport properties upstream of the evaporation zone. Owing to the depletion of fluid pools near the tip, which were not being steadily fed by the needle, intermittent spray extinction was reported for several experiments. In view of this, an ad-hoc “black silicon” surface treatment was explored as a way of improving the wetting characteristics (see Garza [43, 44] for details); however, engine sputtering could not be cleanly eliminated.

As a byproduct of these difficulties, the most recent purely ionic IL sources have tended toward capillary and porous emitters where similar fates are not necessarily met. Krpoun, for example, has presented a modified capillary system in which the emitter tubes were packed with silanized silica microbeads [45]. The capillaries themselves were 70 μm tall and 24 μm in (inner) diameter while the beads were 5 μm wide. The stated purpose of the bead packing was to augment the impedance of the hydraulic line as a way of ensuring uniform performance across a multiplexed array during pressure fed operation, which is known to occur when the viscous drop dominates the driving electrodynamic pull [46, 47]. This could presumably serve the ancillary benefit of enabling pure ion emission from fluids that would otherwise require externally-wetted sources; however, any benefit derived therein was perhaps marginalized due to the low currents that Krpoun reported. For voltages between $\pm$1000V and $\pm$1200V, little more than $\sim$ 20 nA was observed. A later study that spanned the much larger voltage range from $\pm$ 700V to $\pm$ 1400V came to the same findings [48]. To further compound matters, the latest work in this area has shown that pure ion emission from these capillaries is still a relatively precarious proposition owing to the uncertainty of the bead process. While it has proven effective in ideal cases, consistent and controllable packing is a challenge which often precludes the array-level uniformity that was originally sought [49], i.e. emitters sometimes run in a mixed ion/droplet mode despite the presence of the beads. A new effort is underway to fully reconcile this issue through the use of ultra-high aspect ratio tubes, though early reports have yet to indicate pure ion emission [50, 51].

In the area of porous emitters, initial forays were reported by Legge and involved the use of bulk porous metal sheets [52, 53, 54]. The primary substrate metal, tungsten, was chosen for its heritage in earlier externally-wetted studies, most notably those of Lozano. Legge described a simple photolithographic process for etching a 2.14 mm long, 1.196 mm wide (at the base) triangular tip from a 600 μm thick sheet [54]. The resulting tip had principal curvature radii of 8.25 and 9.77 μm, yielding a 4.47 μm effective tip radius that was large enough to maintain macroscopic smoothness despite a nominal pore size of 0.5 μm. Time-of-flight measurements indicated purely ionic emission from four ionic liquids (EMI-BF4, EMI-IM, EMI-Beti, and MPI), though several are predisposed to droplets in capillary instances. Noting that Legge did not use a feed pressure, this is qualitatively similar to the same phenomenon in externally-wetted configurations and possibly owing to similar hydraulic mechanisms. Legge also reported current measurements for biases ranging from a starting voltage of $\sim \pm$ 1500V to $\sim \pm$ 2900V. Current/voltage traces appeared quasi-linear and reached between $\sim$ 200 nA (for MPI, the most resistive fluid) and $\sim$ 1 μA (for EMI-BF4, the most conductive fluid) near the high-voltage end. The author noted that these magnitudes are substantial in comparison to what externally-wetted sources of similar size produce in the steady-state and attributed the discrepancy to superior hydraulics.

Courtney extended this work to bulk porous nickel ($\sim$ 1 - 5 μm nominal pore size) and presented detailed emission characteristics for $\sim$ 150 μm tall tips with 15 - 25 μm apex curvature radii [55, 25, 56, 57]. In the absense of a feed pressure, as before, pure ion emission was demonstrated through a time-of-flight technique before presenting several current measurements. For the ILs EMI-BF4 and EMI-IM, these were provided for biases between the starting voltage of $\sim \pm$ 800V and roughly $\pm$ 1150V (for EMI-BF4) and $\pm$ 1600V (for EMI-IM). These levels allowed the latter to reach $\sim$ 1 μA near the high-voltage end and the former to approach 400 nA. Encouragingly, the explanation provided for these high currents was somewhat more concrete and well-founded than those offered previously. Rather than simply craft a qualitative hydraulic argument, Courtney used a witness plate to create a visible impaction pattern that ostensibly reflected the concurrent activation of several Taylor cones at the tip. In interesting fashion, this was used to suggest that not one but multiple cones must have been at least partially responsible for enabling such high throughputs.

Based on the Legge and Courtney studies it would be tempting, though premature, to conclude that porous emitters are invariably robust in their ability to support pure ion emission. If the insights from Castro [36] are any lesson, it is likely that conditions exist for which they similarly engage a droplet regime. Indeed, Coffman appeared to demonstrate this explicitly while investigating the properties of a porous glass emitter [58]. Using tips that were geometrically similar to those of Courtney, the author presented both time-of-flight and current measurements for the ionic liquid EMI-BF4, which has often been noted for its partiality to the ionic mode even when fed from a capillary (recall Romero-Sanz [29]). Despite quantitative agreement between those current measurements and others reported elsewhere for purely ionic evaporation, the time-of-flight results suggested a small but non-zero droplet population in the beam. Whether this curious finding is the result of larger and somewhat irregularly shaped pores (5 - 10 μm nominal diameter with noticeable non-circularity) conferring a smaller hydraulic impedance than that which is apparently necessary for pure ion emission [36], a wetting issue, or perhaps a difference between metal and dielectric substrates remains unclear. Regardless, as with Castro [36] the finding squarely underscores the important roles that upstream conditions and surface properties play in governing the spray.

2.1.2 Modeling

A strong fundamental understanding for the governing facets of purely ionic evaporation from ionic liquids remains elusive despite experimental heuristics, e.g. that high hydraulic impedance promotes pure ions. Accordingly, the literature on the side of fundamental theory is thin and somewhat undeveloped.

Similar to cone-jet emission studies, the Taylor-Melcher "leaky dielectric" model is a powerful tool for investigating purely ionic evaporation from fluids of modest but finite conductivity (see Saville [59] for a review of the salient elements first introduced by Taylor [60] and then Taylor and Melcher [61]). Using the basic framework described therein, Higuera [62] has constructed one of the few models for an IL meniscus by examining the behavior of a hypothetical drop that is subject to a strong external field while resting on a flat, perfectly conducting plate (to simplify the treatment). The problem was organized with three distinct regions, each of which possessed its own governing equations: there was a fluid-dynamic region inside the liquid globule, a Laplacian space outside of it, and an interfacial region separating the two. Charge conservation in the fluid region, $\nabla \cdot j = 0$, ensured that the interior field was wholly solenoidal. Owing to small Reynolds numbers, basic Stokes flow was also invoked while neglecting possible body forces (i.e. $\nabla P \sim \mu \nabla^2 u$), which seems to be justified in view of the fact that the non-neutral region permitted to exist near the interface is very nearly vanishing [63]. The Laplacian region outside the globule ignored space charge, by definition, and the interface served as the forum for electromechanical coupling: there, surface tension and hydraulic pressure balanced the normal electric traction and the tangential shear described by Maxwell's tensor.

Higuera has offered a measure of perspective on the conventional Taylor analysis and added generality by virtue of the fact that neither conical nor ellipsoidal geometries were assumed *a priori*. Rather, the interface of the rounded globule was permitted to propagate in time until a steady solution was found for the aforementioned equations. This was accomplished via a basic boundary element method for the spatial equations and a second order Runge-Kutta algorithm for the temporal marching. Two distinct cases of ionic emission were considered with this technique, one in which the volume of the meniscus was held constant and another in which a feed pressure was used to pump fluid from an upstream reservoir. In the latter case, the effects of a non-zero hydraulic impedance between the reservoir and meniscus were briefly considered. For all numerical examples the relative dielectric constant $\epsilon_r = 50$ was used along with a dimensionless β parameter of 10. The former is typical of ionic liquids solutions in propylene carbonate [8] and several times larger than those of pure ILs [64, 65]. The latter, which is related to the electrostatic energy term from Eq. 1.11, appears to correspond to menisci with anchoring radii (similar to the radius of a supporting capillary or pore) in the vicinity of 2.5 μm and not far from those that are often observed for commonly investigated porous materials. In an effort to make the numerical problem tractable, the author also artificially modified the value of the related liquid solvation energy so that emission could occur at reduced fields. While this might raise questions about direct numerical applicability of the results, certain qualitative attributes still warrant discussion.

In the constant volume example, Higuera has plotted the menisci shapes, surface field distributions, and surface charge densities as functions of the external field with the dimensionless volume as a parameter. The evaporated current was also shown as a function of the same field and used to qualitatively corroborate the notion of a starting voltage, which is often observed in practice. The current traces contained therein began to appreciably grow for stresses much lower than the critical one often thought of in the context of Taylor ($\sim E_c/4$, where $E_c = \sqrt{2P_c/\epsilon_0}$) and terminate shortly thereafter ($\sim E_c/2$) with the onset of an instability. They were also markedly linear, which contrasts with the Iribarne & Thomson expression (Eq. 1.9), as a result of conduction limitations within the “leaky dielectric” fluid.

Unfortunately, treatment of the feeding case was somewhat less complete than for the constant volume counterpart. There, Higuera formulated the hydrodynamic pressure drop that arises as a result of a feeding impedance and subtracted it from a positive reservoir pressure. The force that the drop exerts on the plate was also accounted for even though it does not likely have meaning in real situations where the fluid rests atop an hydraulic line. Subsequently, several current-field traces were presented for notional combinations of reservoir pressure and impedance. They displayed stability behavior similar to that of the preceding case but adopted dissimilar slopes and achieved maximum currents that varied wildly as functions of the upstream conditions. For example, the trace corresponding to small feed pressure and negligible impedance ($p_0 = 2, \hat{\alpha} = 0$, both dimensionless) reached an exceptionally large current (I $\sim 10^3$, also dimensionless) while the trace corresponding to ($p_0 = 5, \hat{\alpha} = 1$) merely achieved I ~ 1. Though no quantitative pathway was offered for reaching the high current branch, nor any heuristics, the author hinted that careful selection of an appropriate p_o-$\hat{\alpha}$ combination is paramount.

The noted deficiencies of the model notwithstanding, qualitative aspects of the results are intriguing for several reasons. First, the notion of a maximum external field suggests that purely ionic emission might only be permissible within a narrow band of stability. Second, broad excursions in the current traces for the feeding example underscore the importance of upstream conditions in determining emission behavior. These seem to agree with the body of experimental work. Higuera also shows depleted surface charge equilibria during emission in the constant volume case. For regions of strong evaporation in particular, the prevailing charge density is but a small fraction of the fully relaxed value and the author argues that this is a byproduct of limited conduction in the fluid bulk, which scales in proportion to the vacuum field. This is a profound observation that could perhaps explain to some degree the linearity seen in many ILIS current/voltage characteristics. It is, however, not immune to scrutiny in view of the difficulties inherent to the interpretation of surface charge layers for ionic liquid solutions, particularly those that are nearly pure. If a fluid has only two components (a pure mixture of molecular cations and anions), how is the surface charge structured when the length of the associated layer is only of sub-molecular scale? What happens when it is “depleted”? In spite of its historical utility for dilute electrolytic solutions, the conventional “leaky dielectric” model is perhaps not strictly equipped to handle pure IL fluids or answer such fundamental questions.

Beyond Higuera, a fair amount of literature exists on the geometry and stability of electrified droplets suspended in free space. Taylor [3], for example, famously treated the problem of a perfectly conducting droplet subjected to a uniform external field. By assuming a purely ellipsoidal elongation of the major axis in the direction of the applied field and fixing the drop volume, that author constructed a two-point method in which the relevant pressures (electric, interfacial tension, and hydrostatic) were concurrently balanced at both the pole and equatorial locations. This led to stable elongations (as measured by the ratio of major to minor axis, a/b) that grew monotonically until a turning point was reached in the vicinity of $a/b \sim 2$ and scaled field $\sqrt{4\pi\epsilon_0 r_0/\gamma} \cdot E_0$, where r_0 and E_0 were the quiescent droplet radius and the field far from the drop, respectively. No stable solution for a closed ellipsoidal meniscus was found for higher fields, though it was noted that a second but unstable branch of equilibrium solutions existed at exaggerated elongations, i.e. the equilibrium a/b curve was multi-valued for sub-critical E_0.

The same fixed-volume drop problem is examined several more times throughout the literature using progressively more sophisticated techniques to relax the geometric constraints implied by Taylor’s analysis (see, for example, Refs. [66, 67, 68, 69, 70, 71]). It is also extended to the case of pure dielectric drops (i.e. no “leakiness” attendant to free charge [68, 69, 70, 71]) where an interesting phenomenon is observed. For fluids with a relative dielectric constant above a certain threshold ($\epsilon_c \gtrsim 20$) the stability behavior is qualitatively similar to that of the perfect conductor case in that a turning point is met at a specific external field, beyond which no stable solutions for closed menisci are found. For dielectric constants below the threshold, however, elongation is apparently indefinitely stable due to the abbreviated traction of the field. This is an extremely interesting result that reflects to some degree on the Higuera model. Higuera[62] showed depleted surface charge for emitting regions of the IL meniscus, suggesting that initially conductor-like behavior (the fluid fully shields itself with surface charge when it is not emitting) gave way to dielectric behavior when emission was achieved in advance of the stability limit. In the cases examined, emission was indeed observed but the stability limit was still met because, ostensibly, the fluid had a high intrinsic dielectric constant ($\epsilon_r = 50$) that was well beyond ϵ_c. It is interesting, however, to speculate on what may have happened had the fluid possessed a value below this demarcation. Could instability have been postponed?

In addition to the free drop problem, Basaran [70] and Wohlhuter [71] considered cases in which a fixed-volume droplet was attached to a flat plate with either a constant contact distance (i.e. a fixed base radius) or constant contact angle, the so-called sessile and pendant drop cases. The former of these constraints was shown to confer more stability. In situations where the drop had a non-wetting quiescent configuration (contact angle greater than 90°), both anchoring cases went unstable for low fields but permitted substantial elongations of the meniscus. The opposite was true of wetting configurations. By examining the magnetohydrostatic problem of a ferrofluid drop attached to a plate in a uniform field, which is mathematically similar to the electric field problem in question, Boudouvis [72] appeared to show that wetting does indeed lend itself to augmented stability, at least in the sense that higher fields can be sustained.

2.2 Porous microrocket programs

The first porous IL engines were developed from the porous tungsten emitters described by Legge. The same author examined the propulsion significance of the four liquids from the previously noted emission study [54] by using the current and TOF measurements to infer the average charge-to-mass ratio (q/m), thrust, specific impulse, and propulsion efficiency of each fluid as a way of comparing relative performance. These were used to show that, at a given emitter voltage, the lower q/m of the heavier fluids (e.g. MPI) was not significant enough to offset the higher current of the lighter fluids (e.g. EMI-BF4) on a thrust basis. Accordingly, EMI-BF4 alone was selected for further study in a multiplexed system.

Legge proceeded to construct linear arrays of individual porous tips and explore the effects of emitter spacing for three different densities (1, 1.33, and 2 tips per mm). New current measurements were obtained as the metric for this purpose. Interestingly, the current per emitter was shown to vary little with this parameter over the voltage band from $\sim \pm$ 1000V to $\sim \pm$ 2000V in spite of additional disparities in the emitter heights. In the 1 tip/mm case, for example, the emitters were 1168 μm tall while in the 2 tip/mm case they were 458 μm. On the strength of this finding, a two-dimensional array was assembled by integrating several linear strips in a macroscopic package. A third collection of current measurements indicated that per-emitter performance was once again conserved in the 2D configuration, which was likely owing to the relative sparseness of the array (0.5 mm^2 for 49 total tips). Direct thrust measurements were also presented, showing up to 6 μN in a highly stressed state ($\sim$ +2400V). In view of these encouraging results, the author espoused further miniaturization as a pathway for this system to realize compatibility with small spacecraft.

In an effort to simplify the packaging and generate higher thrust densities, Courtney [56, 57] iterated on the Legge efforts by exploring planar arrays of porous nickel tips. This material was selected for its low cost, availability, and geometric similarity to the tungsten. Courtney [57] developed a novel electrochemical cell to machine quasi-isotropic features directly into the surface. These were approximately 150 μm tall and spaced at a pitch of 450 μm. Unlike previous studies in which the liquid selection alone was used to modify thrust (e.g. Legge [54]), Courtney aptly recognized that the emitter topography represented an additional parameter through which certain performance objectives could be affected. Consequently, tip apices across the array were post-processed to hemispherical geometries of radii between 10 and 25 μm in order to reduce the starting potential and augment the attendant thrust-to-power (i.e. increase the thrust output at a given power level). As an ancillary benefit, this also discouraged off-axis emission, although beam angles as large as 30° to 40° were estimated for the highest operational powers (compare this to the $\sim$ 18° half-angle observed by Lozano [31]). The author speculated that this effect was likely the byproduct of concurrent Taylor cone formations in the high-current regime [55].

Courtney [25] also reported on the development of a fully-integrated MEMS engine head for these arrays. A small silicon frame measuring roughly 1.2cm x 1.2cm x 0.3cm was used to house a thin plate of bulk porous nickel containing 480 electrochemically micromachined emitter features. While operating with the ionic liquid EMI-BF4 and an integrated silicon extractor, Courtney reported array-level currents as high as 500 μA in the vicinity of 1500V. Along with grid transparencies approaching unity ($\sim$ 97-98% were typical of many tests), these were used to indirectly estimate the production of $\sim$ 25 μN of thrust at specific impulses from $\sim$ 2500-3000s. Very remarkably, Courtney emphasizes that these performance levels were achieved with a passive, capillarity-driven propellant transport scheme that obviated the need for an active pump and limited complete engine head mass to just 0.75 grams. Total power consumption was $\sim$ 0.6W.

Despite the conceptual successes of the Courtney work, Coffman [58] noted issues with the yield and scalability of the electrochemical manufacturing approach that would need to be addressed prior to technology transfer (commercialization) or densification studies. Among others (see Xie [73]), the same author has been looking for alternative porous materials and more flexible fabrication techniques very recently. As in the case of laser-machined glass tips [58], however, it is becoming abundantly apparent that pure ion emission is not always guaranteed with certain materials and emitter configurations. The reasons for this are not currently clear.

Chapter 3

Thesis objectives

Evidence from the literature indicates that pure ion emission from ionic liquids is only permissible under specific conditions, and that large disparities in spray quality (e.g. the evaporated current [36]) can exist even when it is achieved. While empirical observations have motivated a collection of emission heuristics, in some cases these have led to paradoxical design questions that have been difficult to fully resolve.

In the interest of greater recourse, this thesis will seek a more fundamental understanding for the problem of electrically-assisted evaporation. To high level, specific objectives are

- to identify the various physics which might affect purely ionic electrospray emission in a material way;
- to formulate a fundamental model for electrified menisci;
- to utilize the model for investigating fundamental properties of purely ionic electrospray emission over a range of field and fluid conditions;
- to purpose the results in outlining specific types or sets of conditions that could confer useful emission properties (e.g. high current); and
- to offer a measure of corresponding physical rationalization.

Owing to our heritage with ionic liquids and their burgeoning interest we will attempt to emphasize these fluids throughout the thesis, including borrowing representative numerical values where necessary. It is our firm belief, however, that the basic principles and findings to be set forth will, as a matter of generality, be extensible to many other liquids.

Chapter 4

Orders of magnitude for ion evaporation

4.1 Emission field and tip size

Evaporation of charged species from the tip of a fluid meniscus is governed through the phenomenological kinetic law given by Eq. 1.9, i.e.

$$j = \sigma \frac{k_B T}{h} \exp\left(-\frac{1}{k_B T} \left\{ \Delta G - \sqrt{\frac{q^3 E_n^v}{4\pi\epsilon_0}} \right\} \right) \tag{4.1}$$

where σ is the prevailing density of surface charge (C/m^2), ΔG is the characteristic solvation energy of the evaporating species (J), and E_n^v is the normal component of the vacuum electric field (V/m). The strong nonlinearity of this relationship implies an activated process for which little to no emission is seen until

$$E_n^v \sim \frac{4\pi\epsilon_0 \left(\Delta G\right)^2}{q^3} = E^* \tag{4.2}$$

which we can interpret as a critical condition for strong evaporation. Unlike hard-body or solid field emitters (e.g. hot cathodes), steady emission from electrified menisci is only permissible when the fluid interface is able to achieve a mechanical balance between the governing stresses. Of these, the electrical traction and surface tension are typically salient. It is generally a good approximation then to take $\boldsymbol{\tau_e} \sim 2\gamma/r^*$ near the tip, where $\boldsymbol{\tau_e}$ is the electric stress and r^* is the characteristic scale. After invoking the Maxwell tensor this can be expanded to give

$$\frac{1}{2}\epsilon_0 \left[\left(E^*\right)^2 - \epsilon_r \left(E_n^l\right)^2 \right] \sim \frac{2\gamma}{r^*} \tag{4.3}$$

where ϵ_r is the relative permittivity of the fluid and where the tangential component of $\boldsymbol{\tau_e}$ has been omitted in view of the fact that the associated field, E_t, must vanish near the apex of the meniscus by symmetry. The remaining fields exist on either side of the interface but are both orthogonal (E^* on the vacuum side and E_n^l on the liquid side) and obey the conventional jump condition for idealized surface

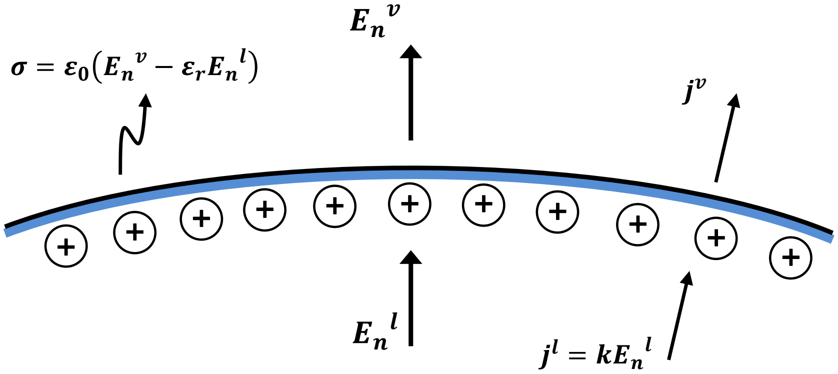

Figure 4-1: Electrical mechanics at a liquid-vacuum interface. In the vacuum there is a field with a component normal to the interface. Its counterpart in the liquid, E_n^l, may or may not vanish depending on evaporation conditions. When the conductivity of the fluid is nonzero there exists a layer of charge at the interface that ideally occupies a region of infinitessimal thickness. If the vacuum field is strong enough, some of this charge is permitted to evaporate while conduction in the fluid attempts to replenish it.

charge, $\sigma = \epsilon_0(E_n^v - \epsilon_r E_n^l)$, as in Fig. 4-1.

Insofar as conduction is the dominant charge transport mechanism (more on this in a subsequent section) and Ohm's law is valid we can further invoke $j = kE_n^l$ along with Eq. 4.1 and the jump condition to recast the stress balance in terms of the vacuum field alone. This has merit in that it will allow us to more clearly visualize the relationship between the outside field and the topography of the tip. Performing a current balance at the interface

$$j = kE_n^l = \epsilon_0 \left(E_n^v - \epsilon_r E_n^l\right) \frac{k_B T}{h} \exp\left(-\frac{1}{k_B T}\left\{\Delta G - \sqrt{\frac{q^3 E_n^v}{4\pi\epsilon_0}}\right\}\right) \tag{4.4}$$

where k is the bulk conductivity of the fluid (S/m), we solve for the liquid field

$$E_n^l = \frac{E_n^v/\epsilon_r}{1 + \frac{hk}{\epsilon_0\epsilon_r k_B T}\exp\left(\frac{1}{k_B T}\left\{\Delta G - \sqrt{\frac{q^3 E_n^v}{4\pi\epsilon_0}}\right\}\right)} \tag{4.5}$$

The denominator of this expression contains the dimensionless group $kh/(\epsilon_0\epsilon_r k_B T)$ which is the ratio of the characteristic charge emission time to the characteristic charge relaxation time, τ_e (not to be confused with the stress $\boldsymbol{\tau_e}$). In terms of values that are typical of pure ionic liquids near room temperature ($k \sim 10^0$ S/m, $\epsilon_r \sim 10^1$-10^2) it evaluates to $\sim 10^{-3}$ and is always much smaller than unity. When the vacuum field is small ($E_n^v \to 0$) the exponential for which this group is a prefactor is still large enough to dominate and drive $E_n^l \to 0$. On the other hand, only the prefactor is left when $E_n^v \to E^*$ because the exponent vanishes. Owing to its magnitude we see that $E_n^l \sim E_n^v/\epsilon_r$ in this limit. In other words, when the vacuum field approaches the critical value for emission the interface becomes depleted because of conduction limitations in the fluid. As a result, the region of the meniscus local to the emission site begins to mimic the behavior of a pure dielectric.

For the sake of the stress balance we can evaluate Eq. 4.5 as $E_n^v \to E^*$ and substitute this in Eq. 4.3

$$\frac{1}{2}\epsilon_0 \left(E^*\right)^2 \left[\frac{\epsilon_r - 1}{\epsilon_r}\right] \sim \frac{2\gamma}{r^*} \tag{4.6}$$

The factor $(\epsilon_r - 1)/\epsilon_r$ on the left-hand side should be very close to unity typical permittivity strengths. When that is true, solving for the characteristic tip scale gives

$$r^* \sim \frac{4\gamma}{\epsilon_0 \left(E^*\right)^2} = \frac{q^6\gamma}{4\pi^2\epsilon_0^3 \left(\Delta G\right)^4} \tag{4.7}$$

Using common ionic liquid values ($\gamma \sim 10^{-2}$ - 10^{-1} N/m, $\Delta G \sim 1$ eV) it is possible to show that $E^* \sim 10^9$ V/m and $r^* \sim 10^{-8}$ - 10^{-10} m, both of which are noteworthy for their extremity (the field is very high while the tip is very small). Furthermore, we would be remiss if we were not to note that the latter scale in particular is very sensitive to the value of ΔG and that this parameter is difficult to quantify precisely. If, for example, the solvation energy were closer to 2 eV than to just 1 eV, we would have that $E^* \sim 10^{10}$ V/m and $r^* \sim 10^{-9}$ m, a decided and even more extreme change!

4.2 Emission strength and basic scaling

From the previous section we have that

$$\begin{aligned} E_n^l \sim & \frac{4\pi\epsilon_0 \left(\Delta G\right)^2}{\epsilon_r q^3} = \frac{E^*}{\epsilon_r} \\ r^* \sim & \frac{q^6\gamma}{4\pi^2\epsilon_0^3 \left(\Delta G\right)^4} = \frac{4\gamma}{\epsilon_0 \left(E^*\right)^2} \end{aligned}$$

when the vacuum field approaches the characteristic value for strong emission ($E_n^v \to E^*$). We anticipate that the associated current should scale like $I \sim jA$ where $j \sim kE_n^l$ from Ohm's law and $A \sim \pi \left(r^*\right)^2$ is the characteristic area for evaporation. When this is expanded in terms of the intrinsic fluid properties

$$I^* \sim \frac{k\gamma^2 q^9}{4\pi^2\epsilon_0^5\epsilon_r \left(\Delta G\right)^6} \tag{4.8}$$

which is again very sensitive to the solvation energy. If we now take $k \sim 1$ S/m, $\gamma \sim 0.05$ N/m, $\epsilon_r \sim 10$, and allow ΔG to vary between 1 eV and 1.5 eV this relationship evaluates in the range from 50 to 500 nA. These would, at the very least, seem to bracket the spectrum of experimentally-observed values and support the present approach to scaling.

Interestingly, we might also investigate the change in the evaporated current as a function of the vacuum field, albeit in a very crude way. Assuming that the scale for the tip must always obey the mechanical balance dictated by the electrical stress, $\epsilon_0(E_n^v)^2/2 \sim 2\gamma/r$, the approximate area available for emission at an arbitrary field is

$$A\left(E_n^v\right) \sim \frac{16\pi\gamma^2}{\epsilon_0^2\left(E_n^v\right)^4} \tag{4.9}$$

The corresponding liquid field, Eq. 4.5, also varies in a nonlinear way with the vacuum field. If we take

$$\chi = \frac{hk}{\epsilon_0\epsilon_r k_B T} \tag{4.10}$$

$$\psi = \frac{\Delta G}{k_B T} \tag{4.11}$$

we can nondimensionalize and solve for the scaled current

$$\frac{I}{I^*} \sim \frac{1}{\left(\frac{E_n^v}{E^*}\right)^3\left[1+\chi\exp\left(\psi\left\{1-\sqrt{\frac{E_n^v}{E^*}}\right\}\right)\right]} \tag{4.12}$$

This relationship is plotted in Fig. 4-2, with $\chi = 10^{-3}$ and $\psi = 40$, and seems to capture empirical trends in at least a qualitative way. Notwithstanding the slight discrepancy observed for high fields, the behavior near incipience mimics laboratory generated I-V curves very closely. If we can safely assume a linear relationship between the applied field (the external one that we enforce far downstream of the meniscus) and the one acting at the meniscus tip, an argument can be made that this result further validates the scaling here.

4.3 Space charge

Space charge will be generated in the vicinity of the meniscus during the course of evaporation and for certain conditions it is conceivable that that this could disrupt the Laplacian potential field. To identify these conditions we might consider the Poisson equation in vacuum

$$\nabla \cdot \vec{E} = \frac{\rho_{sc}}{\epsilon_0} \tag{4.13}$$

from which we can easily extract the homogeneous (Laplacian) part

$$\nabla \cdot \vec{E_{sc}} = \frac{\rho_{sc}}{\epsilon_0} \tag{4.14}$$

The space charge in Eq. 4.14 (which, as an equation, is identical in form to Eq. 4.13 but involves different boundary conditions) is related to both the current density and particle velocity though the prevailing number density of charges local to the

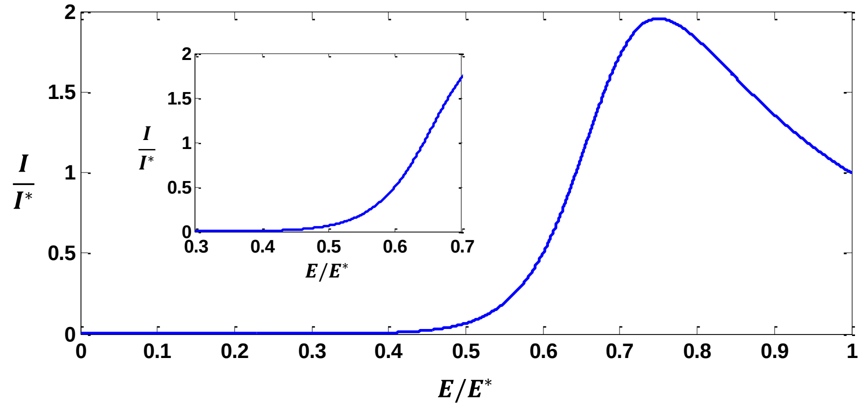

Figure 4-2: Scaled evaporation I/I^* as a function of the vacuum field E/E^* with $\chi =$ 10^{-3} and $\psi = 40$. Although the estimated emission area begins to shrink more quickly than the current density is able to grow at fields approaching E^*, the behavior near the onset of evaporation (sometimes referred to as the startup voltage in practice) is very similar to what we observe experimentally. The inset highlights this region of growth where a small exponential transition is followed by an approximately linear tail.

emitting tip, $\rho_{sc} \sim qn_{sc} \sim j/v$. The velocity here follows from a basic kinetic energy balance $mv^2/2 \sim q\Phi$ and allows us to write

$$\nabla \cdot \vec{E_{sc}} \sim \frac{j}{\epsilon_0\sqrt{2\frac{q}{m}\Phi}} \tag{4.15}$$

Assuming that E^* and r^* are the important field and length scales, respectively, we can take $j \sim kE^*/\epsilon_r$ and $\Phi \sim E^*r^*$ to find

$$\frac{E_{sc}}{E^*} \sim \frac{k}{\epsilon_0\epsilon_r}\sqrt{\frac{r^*}{2\frac{q}{m}E^*}} \sim \sqrt{\frac{1}{8\pi}\frac{I^*}{\gamma\,(q/m)}\frac{k}{\epsilon_0\epsilon_r}} \tag{4.16}$$

which is the ratio of the characteristic residence time for a particle in electrostatic free-fall around the tip (residence time $\sim r^*/\sqrt{2(q/m)\Phi} \sim r^*/\sqrt{2(q/m)E^*r^*}$) to the charge relaxation time, $\epsilon_0\epsilon_r/k$. Under typical ionic liquid emission conditions we can expect that $I^* \sim 10^{-7}$ - 10^{-6} A at most and $\epsilon_0\epsilon_r/k \sim 10^{-10}$ s. If we now also take $\gamma \sim$ 10^{-1} N/m and $q/m \sim 10^6$ C/kg we see that E_{sc}/E^* might vary anywhere from 10^{-2} to 10^{-1}. While this suggests that space charge effects are certainly not pronounced for ionic liquid sources it also reminds us that they are not vanishingly small either, something that we often take for granted.

In an effort to highlight one of the more marked differences between ionic liquid ion sources and those of liquid metals (which will not be directly investigated in this thesis but do relate in some way to the problem of pure ion evaporation), it is at this point useful to perform a brief but similar analysis on the latter fluids. Owing to very high conductivities, liquid metals are known to produce significantly elevated currents and so it stands to reason that their space charge properties could be somewhat different. If we consider them as perfect conductors, which is sufficient for a first approximation, Eq. 4.1 suggests that the current density at the tip of an evaporating liquid metal meniscus should be

$$j \sim \epsilon_0 E^* k_B T / h \tag{4.17}$$

when the normal component of the vacuum field $E_n^v \to E^*$ (recall that $E^* \sim 10^{10}$ V/m for many liquid metals). After substituting this into Eq. 4.15 and performing several algebraic manipulations we find that

$$\frac{E_{sc}}{E^*} \sim \frac{k_B T}{h} \sqrt{\frac{2\gamma}{\epsilon_0 \left(E^*\right)^3 q/m}} \tag{4.18}$$

is a measure of the space charge influence. For many liquid metals it can be expected that $E^* \sim 10^{10}$ V/m, $\gamma \sim 1$ N/m [100], and $q/m \sim 10^6$ C/kg which suggests $E_{sc}/E^* \sim 10^0$. In other words, the space charge could perhaps completely dominate the nature of the field surrounding the activated tip. Given the earlier result for the more modestly conductive ionic liquids, it is clear that this represents a substantial line of demarcation between the two fluids and something that should be kept in mind as we assess the strengths and limitations of our emission model later on.

4.4 Charge transport

In addition to conduction it is possible for charge within the meniscus to be convected through the action of a passing flow. For emission regimes characterized by very strong/high flow rates this phenomenon can play an important role in governing the observable properties of the meniscus. In the case of the cone-jet, for example, the characteristic dimension of the neck is correlated with the location at which the magnitude of the convected charge begins to approach that of its conducted counterpart.

The process of convective charge transport is strictly a surface phenomenon and in that sense it is easily distinguished from conduction. Owing to quasineutrality of the fluid in the meniscus bulk, flows are unable to carry net charge. At the interface, however, tangential fluid motion allows for entrainment of the surface charge population. One might imagine, for example, an active meniscus in which a flow is moving from an electrically relaxed upstream region to an evaporation region where a supply of fresh charge is needed to maintain steady operation. On its way, an element of initially neutral fluid traveling along the surface might capture an element of surface charge from the relaxed region and transport it to the depleted emission zone. It is this small amount of rearranged surface charge that we refer to when we discuss the convected current for electrified flows of fluids like ionic liquids. To visualize it, consider a surface charge distribution determined primarily through the conducted current so that we can manipulate Eq. 4.5 to write

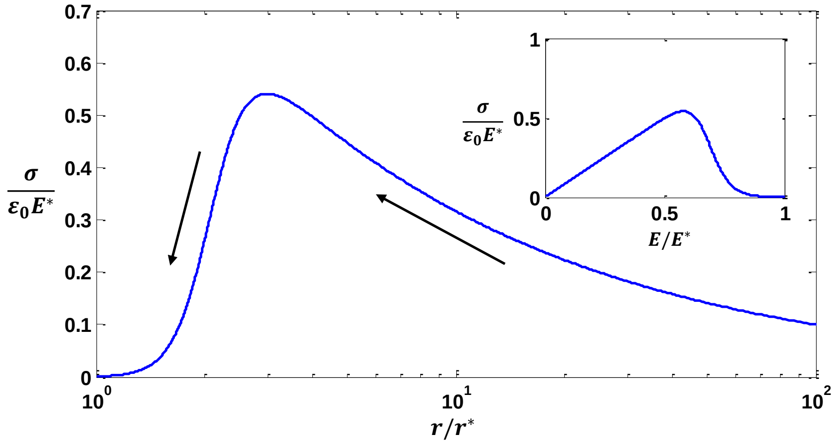

Figure 4-3: Approximate interfacial charge plotted as a function of the vacuum field E_n^v/E^* and the approximate radial distance from the meniscus tip r/r^* when the stress balance $\epsilon_0 E^2/2 \sim 2\gamma/r$ is satisfied. At the interface, fluid elements pass through regions of changing σ and might therefore rearrange the charge to some degree. Near the tip ($E_n^v/E^* \to 1$ and $r/r^* \to 1$) the surface charge becomes depleted due to transport limitations in the fluid. The black arrows indicate the direction of the flow toward this location and suggest that fluid from an upstream area of high σ might offer it a strong convection current.

$$\sigma \sim \frac{\epsilon_0 E_n^v}{1+\frac{\epsilon_0\epsilon_r k_B T}{hk}\exp\left(-\frac{1}{k_B T}\left\{\Delta G-\sqrt{\frac{q^3 E_n^v}{4\pi\epsilon_0}}\right\}\right)} \Rightarrow \frac{\sigma}{\epsilon_0 E^*} \sim \frac{(E_n^v/E^*)}{1+\frac{1}{\chi}\exp\left(\psi\left\{\sqrt{\frac{E_n^v}{E^*}}-1\right\}\right)} \tag{4.19}$$

where χ and ψ are the same quantities defined by Eqs. 4.10 and 4.11. This relationship is plotted in Fig. 4-3 as a function of E_n^v/E^* and r/r^* after imposing the stress balance $\epsilon_0 E^2/2 \sim 2\gamma/r$. Notice that the surface flow, the direction for which is delineated by the arrows, passes through regions of varying surface charge. The hump represents the transition between the relaxed upstream region and the depleted emission zone. After passing the hump, fluid propagating toward the center of the tip moves from an area of comparatively high surface charge to an area of comparatively little surface charge while working to even out this distribution through the process of charge convection.

An understanding for the relative magnitudes of the conduction and convection transport mechanisms is an important prerequisite for anticipating emission behavior. A comparison of these is facilitated by first recalling that $j_{cond} \sim kE_n^l$ as we have already used several times for the conducted current density. The convected current density, by contrast, ends up depending upon the gradient of the product of the surface charge and the interfacial velocity (see chapter on model formulation for a detailed derivation of the transport expressions) and might be approximated by

$$j_{conv} \sim \frac{\sigma\left(\vec{u}\cdot\vec{t}\right)}{r} \tag{4.20}$$

where $\vec{u}$ is the velocity vector for the fluid, $\vec{t}$ is the tangent vector at the liquid-vacuum interface, and $\vec{u}\cdot\vec{t}$ is the component of the surface flow in its direction. By symmetry, the latter must vanish at the apex of an axisymmetric tip where the local surface charge could also be at least partially depleted due to transport limitations during emission (assuming $E_n^v \sim E^*$). The $1/r$ factor is there to account for the fact that fluid moving toward the tip is carrying a fixed amount of charge into a gradually decreasing area (a shrinking area for a fixed charge results in a growing spatial density of that charge). As a consequence we might expect the maximum magnitude of the convected current to be colocated with tip, in spite of the tangential velocity and partially depleted surface charge there. In order to resolve the local singularity, observe that

$$\lim_{r\to 0} j_{conv} = \frac{\frac{\partial}{\partial r}\left(\sigma\vec{u}\cdot\vec{t}\right)}{1} = \sigma\frac{\partial\left(\vec{u}\cdot\vec{t}\right)}{\partial r} + \underbrace{\left(\vec{u}\cdot\vec{t}\right)\frac{\partial\sigma}{\partial r}}_{\vec{u}\cdot\vec{t}\big|_{r=0}=0} = \sigma\frac{\partial\left(\vec{u}\cdot\vec{t}\right)}{\partial r} \tag{4.21}$$

after invoking L'Hôpital. At the edge of the emission region we can use a simple mass balance, $\dot{m} \sim \rho u \pi (r^*)^2$ where $u \sim \vec{u}\cdot\vec{t}$, to calculate the velocity of the incoming flow and its first spatial derivative. For the sake of estimating the *maximum* current density we might also take $\sigma \sim \epsilon_0 E^*$ even though the surface charge is probably somewhat depleted. Together these yield

$$j_{conv} \sim \frac{\epsilon_0 E^*}{r^*}\frac{\dot{m}}{\pi\rho\left(r^*\right)^2} \tag{4.22}$$

The mass flow rate is related to the aggregate current density through $\dot{m} \sim j_e \pi\left(r^*\right)^2(m/q)$ where $j_e = j_{cond} + j_{conv}$ by continuity. Substituting this

$$\frac{j_{conv}}{j_{cond}} \sim \frac{\frac{\epsilon_0 E^*}{\rho(q/m)r^*}}{\left[1 - \frac{\epsilon_0 E^*}{\rho(q/m)r^*}\right]} \tag{4.23}$$

Under typical emission conditions with ionic liquids (say $E^* \sim 10^9$ V/m; $\rho \sim 10^3$ kg/m^3; $q/m \sim 10^6$ C/kg; $r^* \sim 10^{-8}$ m) the group in the numerator and denominator of this equation is small, $\epsilon_0 E^*/[\rho(q/m)r^*] \sim 10^{-3}$. This admits the simplification

$$\frac{j_{conv}}{j_{cond}} \sim \frac{\epsilon_0 E^*}{\rho\left(q/m\right)r^*} \tag{4.24}$$

which says that convection is likely very inconsequential for pure ion evaporation with ionic liquids. For a physical interpretation of why, we could recast Eq. 4.24 by multiplying the numerator and denominator by $\epsilon_r k$ to get

$$\frac{j_{conv}}{j_{cond}} \sim \frac{\epsilon_0\epsilon_r}{k}\frac{kE^*}{\epsilon_r\rho\left(q/m\right)r^*} \tag{4.25}$$

where we now recognize $\epsilon_0\epsilon_r/k$ to be the familiar charge relaxation time. The quantity kE^*/ϵ_r is the conduction current density (essentially the full current density under present conditions) and $j_{cond}/[\rho(q/m)]$ is the associated flow velocity. Since r^*/u is the time required for a fluid element to propagate through the tip we can interpret the transport ratio j_{conv}/j_{cond} as the ratio of the electrical relaxation time to the flow residence time. This is the same result that is obtained with other magnitude analyses. Apparently, convection is not very important if the charges have good mobility and if the rate of mass evaporation is modest, such as the case is with liquids of high specific charge. This would also seem to shed some light on the cone-jet mode where conventional liquids (e.g. doped organic electrolytes) do not always possess good conductivity and where upstream feeding enforces high flow rates.

4.5 Hydrodynamic stresses

In addition to the electrical traction and surface tension there will generally exist a distribution of hydrodynamic stresses in the fluid that could influence the mechanical balance at the interface. An analysis of these stresses might start by considering the classical Navier-Stokes equation for fluid momentum

$$\rho\frac{\partial\vec{u}}{\partial t} + \rho\left(\vec{u}\cdot\nabla\right)\vec{u} = \nabla\cdot\left[-p\boldsymbol{I} + \boldsymbol{\tau}\right] + \vec{F} \tag{4.26}$$

where $\vec{u}$ is the velocity vector for the fluid, p is its hydrostatic pressure, $\boldsymbol{\tau}$ is the viscous (or deviatoric) stress tensor, and $\vec{F}$ is a vector describing the net body force acting on the fluid, if any. When the flow is steady, incompressible, and devoid of body forces the momentum balance reduces to

$$\rho\left(\vec{u}\cdot\nabla\right)\vec{u} = \nabla\cdot\left[-p\boldsymbol{I} + \boldsymbol{\tau}\right] \tag{4.27}$$

It is common to nondimensionalize this equation by identifying for the flow a characteristic velocity and a characteristic length scale (say u_0 and r_0, respectively). The dimensionless variables in this case are

$$\begin{aligned}\hat{u} &\to \frac{u}{u_0}\\ \hat{\nabla} &\to \nabla r_0\\ \hat{p} &\to \frac{p}{\mu\left(\frac{u_0}{r_0}\right)}\\ \hat{\boldsymbol{\tau}} &\to \frac{\boldsymbol{\tau}}{\mu\left(\frac{u_0}{r_0}\right)}\end{aligned}$$

where μ is the fluid viscosity (Pa·s) and where we have dropped the vector arrows for notational simplicity. After substituting these, the momentum equation becomes

$$\underbrace{\frac{\rho u_0 r_0}{\mu}}_{Re}\left[\left(\hat{u}\cdot\hat{\nabla}\right)\hat{u}\right]=\hat{\nabla}\cdot\left[-\hat{p}\boldsymbol{I}+\hat{\boldsymbol{\tau}}\right] \tag{4.28}$$

We recognize the prefactor for the inertial term on the left-hand side of this equation to be the Reynolds number. For ionic liquid menisci operating in a purely ionic mode we might expect the characteristic length scale to be in the neighborhood of r^*. From the previous section, the flow velocity in this vicinity is $u \sim I/[\pi\rho(q/m)(r^*)^2]$. This leads to

$$Re \sim \frac{I}{\pi\mu\left(q/m\right)r^*} \tag{4.29}$$

which, at the very most ($I \sim 10^{-6}$ A; $\mu \sim 10^{-2}$ Pa·s; $q/m \sim 10^6$ C/kg; $r^* \sim 10^{-8}$ m), is still no greater than $Re \sim 10^{-2}$. It is likely safe to conclude then that the flow is of the creeping variety and governed by $\nabla\cdot[-p\boldsymbol{I}+\boldsymbol{\tau}]=0$. The viscous component of this equation, $\nabla\cdot\boldsymbol{\tau}=\nabla\cdot[\mu(\nabla\vec{u}+(\nabla\vec{u})^T)]$, reduces it to the Stokes relationship when the viscosity is constant

$$\nabla p=\mu\nabla^2 u \tag{4.30}$$

We will work from this equation and attempt to estimate the hydrodynamic forces affecting the interface. Owing to the fact that the flow is concentrated in the emission region of the tip, it stands to reason that the interface in the same area is also the forum for the largest fluid stresses. If we take

$$\frac{\Delta p}{r^*}\sim\mu\frac{u}{\left(r^*\right)^2} \tag{4.31}$$

and use the same characteristic velocity as above we find

$$\Delta p\sim\frac{\mu I}{\pi\rho\left(q/m\right)\left(r^*\right)^3} \tag{4.32}$$

For comparison, the ratio of this stress with the local surface tension is

$$\frac{\Delta p}{\left(\frac{2\gamma}{r^*}\right)}\sim\frac{\mu I}{2\pi\rho\gamma\left(q/m\right)\left(r^*\right)^2} \tag{4.33}$$

When the emission and viscosity are both very strong (say $I \sim 10^{-6}$ A; $\mu \sim 10^{-1}$ Pa·s; $r^* \sim 10^{-8}$ m) this flow stress could well be comparable to what would otherwise be the dominate pressures (electrical and surface tension). On the other hand, for more modest conditions that might better typify pure ion evaporation from ionic liquids ($I \sim 10^{-7}$ A; $\mu \sim 10^{-2}$ Pa·s) the stress appears to be small. Also, it is worth noting here that the stress ratio $\Delta p/(2\gamma/r^*)$ can be interpreted as (1) the ratio of the viscous capillary time $\mu r^*/\gamma$ to the flow residence time r^*/u, or (2) the so-called Capillary number, $C_a = u\mu/\gamma$.

4.5.1 Shearing flow

For the flow that is directly induced by the evaporation dynamics we have estimated the characteristic velocity

$$u^* \sim \frac{kE^*}{\epsilon_r \rho \left(q/m\right)} \tag{4.34}$$

and shown that the corresponding hydraulic stresses should be relatively modest in comparison to the important electrical and surface tension effects, as evidenced by the prevailing Capillary number. In addition to this basic flow, situations of strong evaporation will afford the electric field a non-trivial component tangential to the liquid-vacuum interface that will necessarily create a supplementary motion of the liquid. This is a direct byproduct of the fact that in a steady balance of tangential stresses

$$\sigma E_t = \mu \frac{\partial u}{\partial t} \tag{4.35}$$

where t denotes the tangential direction, only viscous shearing is available to counteract any electrical traction, however tenuous (compare this to, for example, the balance of normal stresses, where surface tension and hydraulic stresses are permitted to act in concert to counter any electrical pull). To determine whether this shearing flow could be important we can start by estimating the magnitude of the tangential electric field, which at most could be of the order $E_t \sim E^*/\epsilon_r$. This field will, in part, affect regions of the interface where the charge is somewhat depleted but still possibly in the neighborhood of the relaxed value $\sigma \sim \epsilon_0 E^*$. Insofar as the local length scale is roughly r^*, we can now formulate

$$\frac{\epsilon_0 \left(E^*\right)^2}{\epsilon_r} \sim \mu \frac{u_s}{r^*} \tag{4.36}$$

where u_s is a measure of the velocity induced by electrical shear. After recalling the approximate mechanical balance at the tip of the meniscus $\epsilon_0 (E^*)^2 \sim \gamma / r^*$, we can rearrange Eq. 4.36 to find that $u_s \sim \gamma / \mu \epsilon_r$, which suggests that the shearing flow is smaller than the so-called viscous-capillary speed by a factor $1/\epsilon_r$. Similarly, in comparison to the primary flow u^* we find that

$$\frac{u_s}{u^*} \sim \frac{\gamma \rho \left(q/m\right)}{\mu k E^*} \tag{4.37}$$

For a fluid with $\gamma/\mu \sim 1$ m/s, $\rho \sim 10^3$ kg/m^3, $q/m \sim 10^6$ C/kg, $k \sim 1$ S/m, and $E^* \sim 10^9$ V/m this ratio reduces to approximately $u_s/u^* \sim 10^0$. The conclusion, therefore, must be that the shearing flow should not significantly affect the relative role of hydraulic stresses in the meniscus. In certain situations it could, however, engender a measure of fluid recirculation that would be at least of academic interest. Indeed, in a later chapter we point out that such a phenomenon has an analog in the cone-jet world and show that it is likely to occur for evaporating ionic liquids.

4.6 Heating effects

Through the process of ion evaporation it is possible that Ohmic dissipation in the fluid might modify the nominal temperature near the tip. In the event that the heating is not insignificant, this could affect the evaporation behavior in two ways: (1) from Eq. 4.1 it is clear that augmented interfacial temperatures would increase the local current density in possibly an exponential way, and (2) augmented bulk temperatures would similarly increase the local electrical conductivity of the fluid and presumably enhance its ability to transport charge to the interface. Therefore, it is not unreasonable to imagine scenarios in which heated menisci generate considerably more current than that which would otherwise be expected, something that could also influence the balance of mechanical stresses and stability of the interface.

Before estimating the order of the expected temperature increment we might attempt to isolate the effect that an arbitrary temperature has on the evaporated current density and interfacial stress. From Eq. 4.5 we can write the equilibrium current density for a conduction-controlled interface

$$j = \frac{k\left(E_n^v/\epsilon_r\right)}{1 + \frac{hk}{\epsilon_0 \epsilon_r k_B T} \exp\left(\frac{\Delta G}{k_B T}\left\{1 - \sqrt{\frac{E_n^v}{E^*}}\right\}\right)} \tag{4.38}$$

The electrical conductivity in this relationship will in general be a function of the local temperature. In the case of ionic liquids, for example, we might adopt the linear approximation $k = k_0 + k'(T - T_0)$ where k_0 is the nominal conductivity (S/m) at the reference temperature T_0 (K) and k' is a characteristic thermal sensitivity (S/m-K). After introducing this approximation with Eq. 4.38 we nondimensionalize using the scales

$$\begin{aligned}\hat{E} &\rightarrow \frac{E_n^v}{E^*}\\ \hat{T} &\rightarrow \frac{T}{T_0}\\ \hat{j} &\rightarrow \frac{j}{k_0\left(E^*/\epsilon_r\right)}\end{aligned}$$

The vacuum fields are scaled by the characteristic evaporation strength, temperatures are scaled by a reference (ambient) value, and the current density is scaled by the product of the nominal conductivity and E^*/ϵ_r. When we do this we find

$$\hat{j} = \frac{\hat{E}\left[1 + \Lambda \cdot \Delta\hat{T}\right]}{1 + \chi \frac{1 + \Lambda \cdot \Delta\hat{T}}{1 + \Delta\hat{T}} \exp\left(\frac{\psi}{1 + \Delta\hat{T}}\left\{1 - \sqrt{\hat{E}}\right\}\right)} \tag{4.39}$$

where we have defined the dimensionless groupings

$$\chi = \frac{hk_0}{\epsilon_0 \epsilon_r k_B T_0} \tag{4.40}$$

$$\psi = \frac{\Delta G}{k_B T_0} \tag{4.41}$$

$$\Lambda = \frac{k' T_0}{k_0} \tag{4.42}$$

$$\Delta \hat{T} = \frac{T}{T_0} - 1 \tag{4.43}$$

The first two of these, for χ and ψ, are analogous the definitions from Eqs. 4.10 and 4.11 while the third is a new grouping that describes the thermal sensitivity of the working fluid. Note that when there is no heating the current density reduces to

$$\hat{j}\left(\Delta \hat{T} = 0\right) = \frac{\hat{E}}{1 + \chi \exp\left(\psi \left\{1 - \sqrt{\hat{E}}\right\}\right)} \tag{4.44}$$

Similarly, the electrical stress acting on the interface

$$P_e = \frac{1}{2}\epsilon_0 \left[\left(E_n^v\right)^2 - \epsilon_r \left(E_n^l\right)^2\right] \tag{4.45}$$

can be nondimensionalized after noting that the normal component of the liquid field is related to the current density, i.e. $E_n^l = j/k$, for the conduction-controlled meniscus. After some manipulation

$$\frac{P_e}{\frac{1}{2}\epsilon_0 \left(E^*\right)^2} = \hat{P}_e = \hat{E}^2 - \frac{1}{\epsilon_r}\left(\frac{\hat{j}}{1 + \Lambda \cdot \Delta \hat{T}}\right)^2 \tag{4.46}$$

which, when the heating vanishes, must reduce to

$$\hat{P}_e\left(\Delta \hat{T} = 0\right) = \hat{E}^2 - \frac{\hat{j}^2}{\epsilon_r} \tag{4.47}$$

In Fig. 4-4 we plot the current density produced by a heated interface for several different values of dimensionless temperature ΔT with $\chi = 10^{-3}$, $\psi = 40$, and $\Lambda = 10$ (all loosely representative of pure ionic liquids such as the popular EMI-BF4). The increments $\Delta \hat{T} = 10^{-2}$, $\Delta \hat{T} = 10^{-1}$, and $\Delta \hat{T} = 10^{0}$ roughly correspond to thermal excursions of $\sim 10^0$ K, $\sim 10^1$ K, and $\sim 10^2$ K, respectively, when the nominal temperature T_0 is near room levels (say $\sim$ 300K). Based on this we observe that when the interface is heated by more than just a few degrees it may begin to exhibit radically different emission behavior. On the other hand, for the electrical traction we can see by inspection that elevated temperatures should not modify the prevailing stress so long as ϵ_r is sufficiently high (perhaps about $\epsilon_r \sim 10$ or greater). Physically, even though the heating may shift the field strength for which the interface starts to become depleted of charge and behave locally like a dielectric, the permittivity of

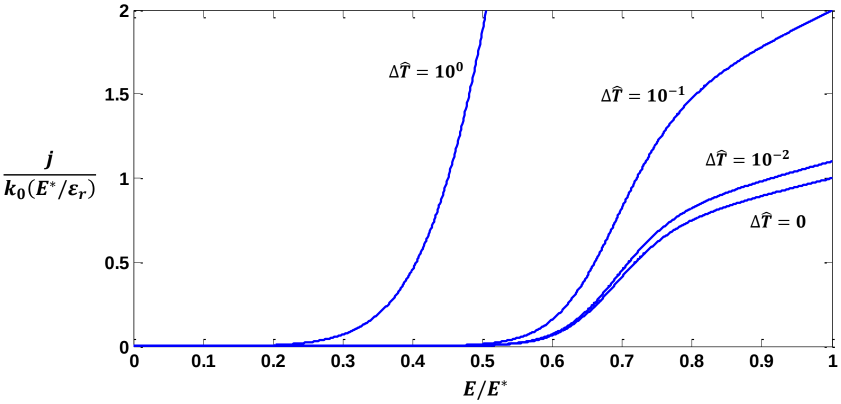

Figure 4-4: Current density produced by a heated interface for $\chi = 10^{-3}$, $\psi = 40$, and $\Lambda = 10$. The dimensionless temperature increments approximately represent thermal excursions ranging up to several hundred Kelvin. When the heating is more than just a few Kelvin it is clear that evaporation levels may climb quickly.

the fluid will always preclude large fields in the liquid that could offset the vacuum component of the stress.

To this point we have treated the heating as an independent variable but in reality it is coupled to the emission properties. To garner a sense for the magnitude of the temperature increment in an ionic liquid meniscus we can consider the steady-state thermal transport equation

$$\rho c_p \left(\vec{u} \cdot \nabla T\right) = k_T \nabla^2 T + \dot{q} \tag{4.48}$$

which is general for heat transfer in a moving fluid with heat capacity c_p (J/kg-K) and thermal conductivity k_T (W/m-K). The generation term, $\dot{q}$, is equivalent to the Joule heating value j^2/k if we restrict our attention to Ohmic dissipation. It is possible to glean the relative magnitudes of the terms in this equation by nondimensionalizing. For this exercise we elect the scales

$$\hat{T} \rightarrow \frac{T}{T_0} \tag{4.49}$$

$$\hat{u} \rightarrow \frac{u}{u^*}, \text{ where } u^* = \frac{k\left(E^*/\epsilon_r\right)}{\rho\left(q/m\right)} \tag{4.50}$$

$$\hat{j} \rightarrow \frac{j}{j^*}, \text{ where } j^* = k\left(\frac{E^*}{\epsilon_r}\right) \tag{4.51}$$

$$\hat{\nabla} \rightarrow \nabla r^* \tag{4.52}$$

These yield, after substitution

$$\underbrace{\left[\frac{\rho c_p T_0}{\left(\frac{(j^*)^2}{k}\right)}\frac{u^*}{r^*}\right]}_{\tau_d/\tau_{res}}\left(\hat{u}\cdot\hat{\nabla}\hat{T}\right) = \underbrace{\left[\frac{\rho c_p T_0}{\left(\frac{(j^*)^2}{k}\right)}\frac{k_T}{\rho c_p \left(r^*\right)^2}\right]}_{\tau_d/\tau_{cond}}\left(\hat{\nabla}^2\hat{T}\right)+\hat{j}^2 \tag{4.53}$$

The first dimensionless grouping on the left-hand side is the ratio of the characteristic ohmic dissipation time $\tau_d \sim \rho c_p T_0/[(j^*)^2/k]$ to the fluid residence time in the tip $\tau_{res} \sim r^*/u^*$. The heat capacity for pure ionic liquids should be in the vicinity of $c_p \sim 10^3$ J/kg-K and so for the former we find that $\tau_d \sim 10^{-8}$ s when $j \sim kE^*/\epsilon \sim 10^8$ A/m^2 with $k \sim 1$ S/m. Similarly, for the latter we get $\tau_{res} \sim 10^{-7}$ s. The ratio of these two time scales is then $\sim 10^{-1}$. By contrast, the dimensionless group on the right-hand side is the ratio of the dissipation time to the characteristic conduction time

$$\frac{\partial T}{\partial t} \sim \frac{k_T}{\rho c_p}\frac{\partial T}{\partial x^2} \Rightarrow \tau_{cond} \sim \frac{\rho c_p \left(r^*\right)^2}{k_T} \tag{4.54}$$

The thermal conductivity of pure ionic liquids is $k_T \sim 10^{-1}$ W/m-K and so $\tau_{cond} \sim 10^{-9}$ s. The time scale ratio for conduction is then $\tau_d/\tau_{cond} \sim 10$.

Based on this analysis it is clear that conduction, rather than convection, is the dominant heat transfer mechanism for ionic liquid menisci operating in a pure ion evaporation mode. To reasonable order, it follows that

$$k_T \nabla^2 T \sim \frac{j^2}{k} \Rightarrow \frac{\Delta T}{T_0} \sim \frac{j^2 \left(r^*\right)^2}{k \cdot k_T T_0} \sim \frac{\tau_{cond}}{\tau_d} \tag{4.55}$$

which means that the temperature increment could be on the order of tens of Kelvin if the prevailing current density is in the vicinity of the characteristic value $j^* = k(E^*\epsilon_r)$. We might, however, choose to look at it in terms of the current and write

$$\frac{\Delta T}{T_0} \sim \frac{I^2}{k \left(r^*\right)^2 k_T T_0} \tag{4.56}$$

Assuming the current is toward the low end of the usual spectrum (say $I \sim 10^{-8}$ A) then $\Delta T/T_0 \sim 10^{-2}$ and an excursion of just a few Kelvin could be expected, although it deserves to be noted that this is still on the border of what might elicit a very real change in the emission behavior (recall Fig. 4-4).

4.7 Momentum exchange

During the process of field-assisted emission, evaporated species will accelerate away from the source and commonly attain very high momenta before escaping the influence of the prevailing fields. In exchange for this acceleration it is incumbent upon the meniscus from which evaporating species originate to bear some related distribution of stresses. In fact, this is the exact stress through which the source garners its own

Figure 4-5: Stress considerations for a thermo-chemical rocket. The static pressure in the chamber of the rocket, P_c, is high and typically owes to exothermic reactions between an oxidizer and a fuel. High pressure gas from this chamber is convectively accelerated through a nozzle where it exits with a pressure P_e that may differ from the ambient P_a. The integral of the pressures acting on the solid surfaces of the rocket plus the momentum exchange embodied by the exhaust gas defines the total thrust powering the vehicle.

useful momentum; for example, when it is purposed as a means for propulsion.

To look at the momentum exchange another way, it is useful to draw an analogy to the more familiar situation of a thermo-chemical rocket (Fig. 4-5). The rocket utilizes chemical reactions to generate a reservoir of thermally-excited gas that also exists at a high pressure. In the upstream reaction chamber we might call this P_c. Gas from the reservoir is forced downstream where it undergoes convective acceleration in a nozzle before exiting the back of the rocket. The pressure along the exhaust plane is now P_e, which in general may differ from the ambient level P_a.

In order to discern the forces that are acting on the rocket we can start by considering the pressure P pushing on all of the interior surfaces. If propagation is in the x-direction, we can draw a control volume that hugs the inner contour of the rocket and write

$$\sum F_x = \int P \times dA_x - \int P_e \times dA_{ex} - \int u_x \underbrace{(\rho \vec{u}_e \cdot \vec{n}) \times dA_{ex}}_{d\dot{m}} \tag{4.57}$$

where dA_x is the differential part of the interior surface with a unit normal in the x-direction, dA_{ex} is the x-directed part of the exhaust surface, and u_x is the x-component of the gas velocity in the same vicinity. From this expression we can now subtract an external force due to the ambient pressure. The result is

$$\underbrace{\sum F_x - P_a A_{ex}}_{thrust=T} = \int P \times dA_x - \int (P_e - P_a) \times dA_{ex} - \int u_x (\rho \vec{u}_e \cdot \vec{n}) \times dA_{ex} \tag{4.58}$$

from which we recognize $\sum F_x - P_a A_{ex}$ to be the total thrust T acting on the rocket system. It is at this point conventional to define several spatially-averaged quantities. These are

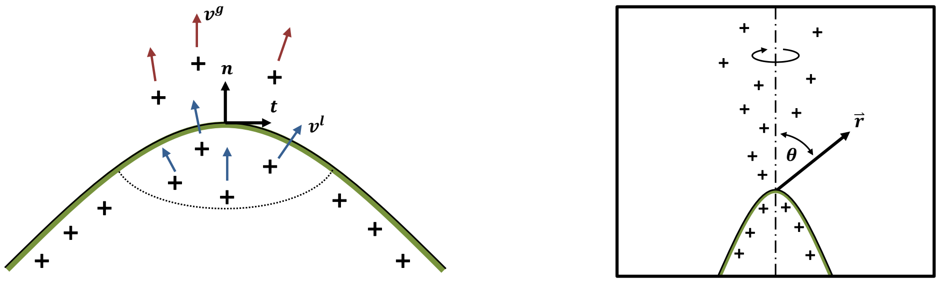

Figure 4-6: Momentum exchange scenarios for evaporation of an electrified fluid. **Left:** Charged particles approach the active part of an evaporating meniscus with velocity v^l and depart with a related velocity v^g after changing phase but before accelerating in the surrounding fields. The momentum carried by the flux of particles leaving at speed v^g creates a stress on the local fluid surface. **Right:** After changing phase, free species begin to accelerate in the prevailing electrostatic fields. The momentum that they accumulate during this process is communicated back to the liquid where it creates an additional stress.

$$\bar{u}_e = \frac{\int u_x \left(\rho \vec{u} \cdot \vec{n}\right) dA_{ex}}{\int \rho \vec{u} \cdot \vec{n} dA_{ex}} \tag{4.59}$$

and also

$$\bar{P}_e = \frac{1}{A_{ex}} \int P_e dA_{ex} \tag{4.60}$$

which handle the possibilities of non-uniform exit pressures and velocities. After substituting these in Eq. 4.58 we see that

$$T = \dot{m}\bar{u}_e + \left(P_e - P_a\right) A_{ex} \tag{4.61}$$

For the rocket, the total stress is the aggregate of a net pressure force pushing on the exit plane and a force related to the momentum that is transferred to accelerating species. The fact that both of these contribute is an important observation because of the direct analogy that can be drawn to the situation of an evaporating meniscus. In that case, the electrical traction pushing on the interface, nominally $\epsilon_0 E^2/2$, is analogous to the net pressure $P_e - P_a$ while the influence of the electrostatically accelerated particles is analogous to $\dot{m}\bar{u}_e$.

Although we have already touched on electrical traction and its relative importance at the interface, we have yet to address the transfer of momentum to evaporating particles and what that could mean in terms of stresses. An attempt will be made to do so in the brief sections that follow. These will examine the two types of transfer phenomena (see Fig. 4-6) that could presumably be in play: (1) transfer of momentum to particles undergoing phase change directly at the interface, and (2) electrostatic repulsion away from the surface thereafter.

4.7.1 Momentum transferred directly at the interface

In order for steady evaporation to prevail it is true that constituents of the liquid must approach the interface with a non-zero velocity component normal to the interface, at least in the region of the tip where the vacuum fields are of sufficient strength. We have already shown that this velocity is roughly

$$u^l = \frac{j_e}{\rho\,(q/m)} \sim \frac{kE^*}{\epsilon_r \rho\,(q/m)} \tag{4.62}$$

Once the liquid constituents evaporate they possess an outward (gas-phase) velocity u^g but still reside very near the meniscus since they have yet to propagate through the electrostatic fields. Assuming that $u^g \sim u^l$, i.e. there is no change in velocity during the change in phase, we can investigate a momentum transfer stress equal to $\dot{m}u^l$ that must be acting on the interface. We find

$$\boldsymbol{\tau}^{me} \sim \frac{\dot{m}}{A}u^l \sim \frac{1}{\rho}\left(\frac{j^*}{(q/m)}\right)^2 \tag{4.63}$$

where the characteristic current density at the tip is $j^* \sim kE^*/\epsilon_r$. The ratio of this stress to the local electric stress is

$$\frac{\boldsymbol{\tau}^{me}}{\boldsymbol{\tau}^{e}} \sim \frac{k^2}{\rho\epsilon_0\epsilon_r^2\,(q/m)^2} \tag{4.64}$$

For an ionic liquid typified by $k \sim 1$ S/m, $\rho \sim 10^3$ kg/m^3, $\epsilon_r \sim 10$, and $q/m \sim 10^6$ C/kg this evaluates to approximately 10^{-6}. In other words, the momentum exchange is extremely insignificant, which should comes as no surprise in view of the fact that Eq. 4.64 is essentially tantamount to the ratio of inertial forces to electrical forces at the tip, $\rho(u^*)^2/\epsilon_0(E^*)^2$. Since we have already identified the characteristic Reynolds number of the evaporation process (the ratio of inertial forces to viscous forces) as well as the ratio of viscous forces to surface tension forces (the latter of which should be more or less equivalent to electrical forces), it is worth pointing out that this result could also have been arrived at by multiplying those two quantities. Given that each is very small in its own right, it stands to reason that the momentum carried by the evaporating liquid should be largely inconsequential.

Another possibility is that particles are impulsively accelerated as they change phase and begin flying away with a velocity much greater than u^l even before electrostatic free-fall. In this instance it is tempting to consider the so-called "ion cost" (a penalty of several volts of energy that is consumed during evaporation) as a vehicle for this acceleration; however, the nature of the cost would seem to preclude this categorically. If indeed the species were impulsively gifted with several volts per particle in the midst of their phase change we would observe this energy in experiments, and conclude that there is actually no cost at all! Instead we see a deficit, and so impulsive acceleration appears unlikely.

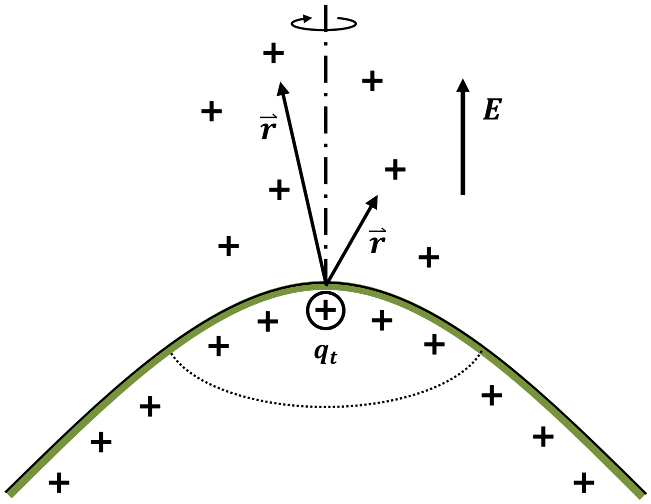

Figure 4-7: Scenario for the interaction of a test charge at the tip of an electrified meniscus with accelerating gas-phase charges. The test charge q_t is co-located with the origin of a spherical coordinate system so that the appropriate Coulombic interaction distance is simply $|\vec{r}|$. While moving through the background field $\vec{E}$, the free charges will collectively push on the test charge with some as-of-yet determined force.

4.7.2 Electrostatic acceleration of gas-phase species

In the immediate aftermath of evaporation, gas-phase species near the surface of the meniscus will experience mutual Coulombic repulsion with charges in the liquid. This is the electrostatic process by which they are accelerated downstream and away from the source, often at high speeds. An unavoidable consequence of the attendant momentum exchange is a stress on the liquid; however, the corresponding magnitude is as of yet unclear.

To discern the prevailing forces we can start by invoking Coulomb's law, which states that the force of electrical attraction/repulsion between two charged bodies is proportional to the product of their charge numbers and falls off as the square of the intervening distance, i.e.

$$\vec{F} = \frac{1}{4\pi\epsilon_0}\frac{q_1 q_2}{|\vec{r}_{21}|^2}\left(\frac{\vec{r}_{21}}{|\vec{r}_{21}|}\right) \tag{4.65}$$

where $\vec{r}_{21}$ is the vector separating the two charged bodies. Now consider the situation of electrically-induced evaporation in which a charged meniscus is stressed by gas-phase particles that are being accelerated downstream. Since the gaseous particle velocities are not of relativistic magnitude, we can take a snapshot in time of their positions and attempt to determine how hard they are pushing on the upstream fluid. By placing a test charge q_t at the exact tip of the meniscus and co-locating it with a spherical coordinate system (Fig. 4-7) we can write

$$\sum \vec{F} = \frac{1}{4\pi\epsilon_0}\sum_j \frac{q_t q_j}{|\vec{r}_j|^2}\left(\frac{\vec{r}_j}{|\vec{r}_j|}\right) \tag{4.66}$$

which represents the aggregated effect of all charges $j = 1, 2, ..., N$ in the gas-phase. Since the summed forces on the test charge are equivalent to $q_t\vec{E}_t$, dividing through by q_t gives

$$\vec{E}_t = \frac{1}{4\pi\epsilon_0}\sum_j \frac{q_j}{|\vec{r}_j|^2}\left(\frac{\vec{r}_j}{|\vec{r}_j|}\right) \tag{4.67}$$

Note here that $\vec{E}_t$ is not in general the only field acting on the test charge. Owing to the presence of companion charges along the boundaries (for example, at the liquid interface and on the surfaces of the electrodes forming the electrical architecture of the global emitter system), there will also exist a Laplacian field $\vec{E}_L$. The total field is then $\vec{E} = \vec{E}_L + \vec{E}_t$.

If we choose now to work in a continuum it is helpful to take $\rho = \rho(\vec{\boldsymbol{x}})$ (C/m^3) as the distribution of charges j. This affords a conversion of the summation in Eq. 4.67 to the more convenient integral form

$$\vec{E}_t = \frac{1}{4\pi\epsilon_0}\int_V \frac{\rho}{|\vec{r}|^2}\left(\frac{\vec{r}}{|\vec{r}|}\right) dV \tag{4.68}$$

where $\rho \times dV$ embodies the former charges q_j at a given location. From Poisson we know that the volumetric charge density is tantamount to the divergence of the local displacement field, $\rho = \nabla \cdot (\epsilon_0 \vec{E}_p)$, where $\vec{E}_p$ is the so-called Poisson field that is the particular solution to Poisson's differential equation. We can substitute this to find

$$\vec{E}_t = \frac{1}{4\pi}\int_V \frac{\nabla \cdot \vec{E}_p}{|\vec{r}|^2}\left(\frac{\vec{r}}{|\vec{r}|}\right) dV \tag{4.69}$$

In many practical instances it suffices to model the tip of the meniscus as a spherical diode, at least locally. When this is true, $\vec{E}_p \to \vec{E}_p(\vec{r})$ and $dV \to 4\pi r^2 dr$, making it easy to show that Eq. 4.69 reduces to

$$\vec{E}_t = \int \nabla \cdot \vec{E}_p \left(\frac{\vec{r}}{|\vec{r}|}\right) \times dr \tag{4.70}$$

For the spherical diode we must have that

$$\vec{E}_p = E_p\left(\frac{\vec{r}}{|\vec{r}|}\right) \tag{4.71}$$

$$\nabla \to \frac{d}{dr}\left(\frac{\vec{r}}{|\vec{r}|}\right) \tag{4.72}$$

Taking these into account, Eq. 4.70 evaluates to

$$\vec{E}_t = \left(\int \frac{dE_p}{dr} \times dr \right) \frac{\vec{r}}{|\vec{r}|} = E_p \left(\frac{\vec{r}}{|\vec{r}|} \right) = \vec{E}_p \tag{4.73}$$

From this result we clearly see that the field responsible for momentum exchange between the liquid and the accelerating gas-phase species is identical to that of Poisson. The conclusion is extensible to arbitrary domains, i.e. configurations other than just spherical diodes, and should come as no surprise since the forces are communicated electrostatically.

To phrase the result in another way, the Poisson field is the one that is responsible for exchanging momentum between the fixed electrodes, including the liquid, and the free particles. As we have already seen, the tendency of this field is to reduce the influence of the corresponding Laplacian field. Since the latter works to pull the liquid out, a physical interpretation for the former is that it mitigates the effective electrical stress, just as we might expect. In terms of importance, however, we have shown that the Poisson field is relatively insignificant under present conditions. Coupled with the extremely small inertia of the evaporating species, it stands to reason that momentum exchanges should not impact the mechanics of the meniscus in any meaningful way.

4.8 Time scales

In what follows we briefly review several time scales that are germane to the process of ion evaporation from electrified ionic liquid menisci, including those referenced in the preceding sections.

4.8.1 Electric relaxation time

Consider an electrified fluid-vacuum interface in which the liquid has a nonzero electrical conductivity. A vacuum field is instantaneously imposed at an arbitrary moment in time and held at a constant value orthogonal to the interface. The initial surface charge $\sigma(t = t_0) = \sigma_0$ is not necessarily equivalent to the vacuum displacement field, i.e. $\sigma_0 \neq \epsilon_0 E_n^v$, which permits a field to permeate the fluid. In turn, this field works to conduct charge to the interface as it asymptotically approaches a state of full charge relaxation. Mathematically, this situation is described by the transport relationship

$$\frac{\partial \sigma}{\partial t} = k E_n^l \tag{4.74}$$

where k is the conductivity of the fluid (S/m) and E_n^l is the component of the liquid field orthogonal to the interface. The latter obeys the interfacial jump condition

$$\sigma = \underbrace{\epsilon_0 E_n^v}_{D_n^v} - \underbrace{\epsilon_0 \epsilon_r E_n^l}_{D_n^l} \Rightarrow E_n^l = \frac{E_n^v}{\epsilon_r} - \frac{\sigma}{\epsilon_0 \epsilon_r} \tag{4.75}$$

at all times. Using this allows us to recast Eq. 4.74 as

$$\frac{\partial \sigma}{\partial t} + \sigma \underbrace{\left(\frac{k}{\epsilon_0 \epsilon_r}\right)}_{1/\tau_e} - k\frac{E_n^v}{\epsilon_r} = 0 \tag{4.76}$$

from which we can glean the characteristic time scale for charge relaxation at the interface. This turns out to be $\tau_e \sim \epsilon_0 \epsilon_r / k$, a value which can be very small for fluids that are relatively conductive ($k \sim 1$ S/m, or greater) and apolar ($\epsilon_r \sim 10^2$, or less). For example, an ionic liquid with $k \sim 1$ S/m and $\epsilon_r \sim 10$ has an electrical relaxation time of just $\tau_e \sim 10^{-10}$ s, or about 100 picoseconds.

4.8.2 Viscous capillary time

When viscous flow forces dominate their inertial counterparts, i.e. the flow is characterized by a low Reynolds number, the more general Navier-Stokes equation reduces to that of Stokes

$$\nabla p = \mu \nabla^2 \vec{u} \tag{4.77}$$

which describes the so-called creeping flow regime. After identifying a specific length scale that typifies the creeping flow (e.g. r_0) we can make use of dimensional analysis to elucidate important velocity and temporal properties. Assuming that the driving force for the flow is a surface tension effect, it makes sense to take $p \sim \gamma / r_0$ where γ is the characteristic interfacial energy of the fluid (J/m^2 or, equivalently, N/m). Substituting this gives

$$\frac{1}{r_0}\frac{\gamma}{r_0} \sim \mu \frac{u_0}{r_0^2} \Rightarrow u_0 \sim \frac{\gamma}{\mu} \tag{4.78}$$

The characteristic velocity u_0, commonly referred to as the viscous-capillary speed, is the ratio of the interfacial tension to the dynamic fluid viscosity (Pa-s). As for a corresponding time scale, we can make use of u_0 and r_0 to formulate

$$\tau_{vis} \sim \frac{r_0}{u_0} \sim \frac{\mu r_0}{\gamma} \tag{4.79}$$

From a physical perspective this is the characteristic residence time for fluid elements within a flow driven strictly by surface tension forces. In practice, it is simply referred to as the viscous-capillary time. To garner a sense for its magnitude, consider an ionic liquid in which $\gamma \sim 10^{-2}$ N/m and $\mu \sim 10^{-2}$ Pa-s so that $u_0 \sim 1$ m/s. When the ionic liquid is supporting field evaporation from a tip that is $r^* \sim 10^{-8}$ - 10^{-7} m we find that $\tau_{vis} \sim 10^{-8}$ - 10^{-7} s also. In comparison to the electrical relaxation time, for example, it is clearly very long.

4.8.3 Inertial time

To consider the inertia of a viscous fluid driven by capillary forces we might again identify an important length scale r_0 and then invoke Newton's second law, $F = m \cdot a$, to find

$$\underbrace{\gamma r_0}_{F} \sim \underbrace{\rho r_0^3}_{m} \underbrace{\frac{r_0}{\tau_{in}^2}}_{a} \tag{4.80}$$

The representative capillary force is $F \sim \gamma r_0$. This acts on a mass of fluid $m \sim \rho r_0^3$ and accelerates it at a rate of $a \sim r_0/(\tau_{in})^2$ where τ_{in} is the characteristic inertial time scale. Rearranging Eq. 4.80

$$\tau_{in} \sim \sqrt{\frac{\rho r_0^3}{\gamma}} \tag{4.81}$$

For a numerical example, consider a fluid with $\rho \sim 10^3$ kg/m^3 and $\gamma \sim 10^{-1}$ N/m that is supporting ion evaporation from an emission region that has the size $r^* \sim 10^{-8}$ m. Using these values $\tau_{in} \sim 10^{-10}$ s, at least near the tip, which is small in comparison to the viscous time and possibly on the order of τ_e.

4.8.4 Feeding flow time

In practice it is common for feed systems to deliver fluid to the area near the interface. These could be the emitters that were briefly discussed in the introductory chapter (e.g. externally wetted tips, porous tips, or capillary tubes) or other configurations capable of transporting fluid from an upstream reservoir. Just like viscous-capillary and inertial effects, consideration for the delivery mechanism is important because it could potentially influence the dynamics of the meniscus. For example, if the time scale for equilibration of the feeding flow in response to downstream perturbations at the interface is very long, the delivery system could very well be the bottleneck that governs the meniscus motion. This is a point that seems to be overlooked very often in the discussion of electrosprays.

Consider a feeding system that can be idealized as a capillary tube of radius r_0. When it carries a steady flow of viscous liquid the momentum equation is that of Stokes, $\nabla p = \mu \nabla^2 \vec{u}$. If we choose to resolve the tube in cylindrical coordinates then $\nabla p = dp/dz \cdot \vec{i}_z$ only and $\vec{u} = u(r) \cdot \vec{i}_z$. The momentum equation reads

$$-P = \mu \left(\frac{d^2 u}{dr^2} + \frac{1}{r}\frac{du}{dr} \right) \tag{4.82}$$

where $P = ||dp/dz||$. The general solution to this differential equation is

$$u\left(r\right) = C_1 \ln\left(r\right) + C_2 - \frac{Pr^2}{4\mu} \tag{4.83}$$

For the viscous flow we have the boundary conditions

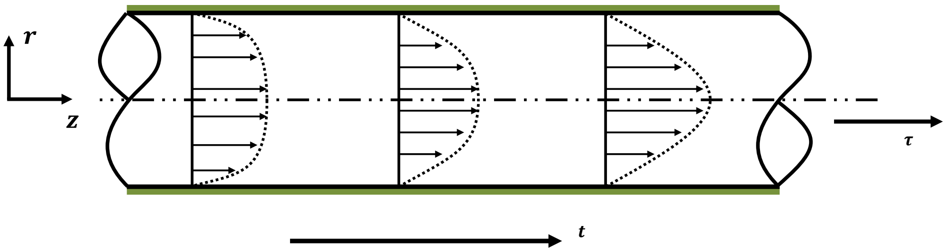

Figure 4-8: Schematic of transient feeding flow evolution. A stress $\boldsymbol{\tau}$ (also P) is instantaneously applied and held through external means to enforce a given hydraulic gradient dP/dz in an axisymmetric tube. The initial velocity distribution in the tube (left) will evolve in time, t, until full development is reached (right).

$$u\left(r=r_0\right)=0$$
$$\left.\frac{du}{dr}\right|_{r=0}=0$$

which ensure axial symmetry and a no-slip condition along the wall. The velocity distribution that satisfies these is

$$u\left(r\right)=\frac{P}{4\mu}\left(r_0^2-r^2\right) \tag{4.84}$$

which is essentially the well-known Poiseuille solution for tube flow. Now consider the same feeding system (tube) with fluid that is initially at rest before being set in motion by an instantaneously imposed pressure gradient maintained by external measures (Fig. 4-8). For this situation the momentum equation reads

$$\frac{\partial u}{\partial t}=\frac{P}{\rho}+\frac{\mu}{\rho}\left(\frac{\partial^2 u}{\partial r^2}+\frac{1}{r}\frac{\partial u}{\partial r}\right) \tag{4.85}$$

and the corresponding boundary and initial conditions are

$$u\left(r=r_0,t\right)=0 \text{ for all } t,$$
$$\left.\frac{\partial u}{\partial r}\right|_{r=0,t}=0 \text{ for all } t,$$
$$u\left(r,t=0\right)=0 \text{ for } 0\leq r\leq r_0$$

As Batchelor shows [81], Eq. 4.85 can be converted to a homogeneous form through the change of variable $w(r,t)=u_s(r)-u(r,t)$ where $u_s(r,t)$ is the steady flow solution from Eq. 4.84. The unsteady momentum equation is now

$$\frac{\partial w}{\partial t}=\frac{\mu}{\rho}\left(\frac{\partial^2 w}{\partial r^2}+\frac{1}{r}\frac{\partial w}{\partial r}\right) \tag{4.86}$$

subject to

$$\begin{aligned} w\left(r=r_0,t\right)=&0\\ w\left(r,t=0\right)=&\frac{P}{4\mu}\left(r_0^2-r^2\right)\end{aligned}$$

As a particular solution to this equation, Batchelor [81] offers

$$J_0\left(\lambda_n\frac{r}{r_0}\right)\cdot\exp\left(-\lambda_n^2\frac{\mu t}{\rho r_0^2}\right)$$

in which λ_n is the n$^{\text{th}}$ positive root of the Bessel function of the first kind, J_0. This satisfies the boundary condition at $r=r_0$. The additional condition at $t=0$ can be satisfied by summing over all possible λ_n so that

$$w\left(r,t\right)=\frac{P}{4\mu}\sum_{n=1}^{\infty}A_nJ_0\left(\lambda_n\frac{r}{r_0}\right)\cdot\exp\left(-\lambda_n^2\frac{\mu t}{\rho r_0^2}\right) \tag{4.87}$$

Without needing to go further, we can already see that the time scale for the feeding flow must be

$$\tau_f\sim\frac{\rho r_0^2}{\mu} \tag{4.88}$$

This is to be compared against the viscous-capillary and inertial time scales of the full meniscus, i.e. the scales that are calculated using the contact line or anchoring radius of the meniscus rather than r^*. As an example, for a liquid with $\rho\sim10^3$ kg/m^3 and $\mu\sim10^{-2}$ Pa-s that has a contact radius $r_0\sim10^{-6}$ m we find that $\tau_f\sim10^{-7}$ s. At the same scale, the viscous-capillary and inertial times might be $\tau_{vis}\sim10^{-6}$ s and $\tau_{in}\sim10^{-13/2}$ s, respectively. The feeding time is the fastest while the viscous-capillary time is still limiting.

4.8.5 Evaporative residence times: liquid and gaseous states

The residence times associated with evaporation are the characteristic time scales describing the propagation of charges in and around the emission zone. The liquid residence is the time required for a fluid element to move through the electrically stressed meniscus tip while the gas residence is the time required for evaporated species to be accelerated away from the same area.

Either residence time can be formulated as the ratio r/u where r is the characteristic propagation distance and u is the characteristic propagation speed. In both cases the former should evaluate to $r\sim r^*$. The velocities, however, are likely to be very different as a result of the change of states: one is for a viscous fluid flow and the other is for particles in electrostatic free-fall. As we have already seen, the characteristic liquid velocity is roughly

$$u_{liq} \sim \frac{j}{\rho\left(q/m\right)} \sim \frac{kE^*}{\epsilon_r \rho\left(q/m\right)} \tag{4.89}$$

by continuity. On the other hand, for the particle motion it is usually most appropriate to invoke a basic kinetic energy balance $mu^2/2 \sim q\Phi$ before finding

$$u_{gas} \sim \sqrt{2\left(\frac{q}{m}\right)\Phi} \tag{4.90}$$

The characteristic potential drop in the vicinity of the emission zone must be $\Phi \sim E^* r^*$ and so

$$u_{gas} \sim \sqrt{2\left(\frac{q}{m}\right)E^* r^*} \tag{4.91}$$

Notice that the ratio of these two velocities

$$\frac{u_{gas}}{u_{liq}} \sim \frac{\sqrt{\left(\frac{q}{m}\right)E^* r^*}}{\left[\frac{kE^*}{\epsilon_r \rho\left(\frac{q}{m}\right)}\right]} \rightarrow \frac{\epsilon_r \rho}{k}\left(\frac{q}{m}\right)^{3/2}\sqrt{\frac{r^*}{E^*}} \tag{4.92}$$

could be very large if the specific charge is sufficiently high. For a liquid with $q/m \sim 10^6$ C/kg, for example, it could be that $u_{gas}/u_{liq} \gg 10^3$ or 10^4 even if r^* is small and E^* is large. From these results we can formulate the time scales

$$\tau^l_{res} \sim \frac{\epsilon_r \rho\left(q/m\right) r^*}{kE^*} \tag{4.93}$$

$$\tau^g_{res} \sim \sqrt{\frac{r^*}{\left(q/m\right)E^*}} \tag{4.94}$$

For the same liquid with $q/m \sim 10^6$ C/kg and also $E^* \sim 10^9$ V/m, $r^* \sim 10^{-8}$ m, $\epsilon_r \sim 10$, $k \sim 10^0$ S/m, and $\rho \sim 10^3$ kg/m^3 these evaluate to $\tau^l_{res} \sim 10^{-7}$ s and $\tau^g_{res} \sim 10^{-11}$ - 10^{-12} s. The particle residence is obviously very short and this is at least part of the reason why ionic liquid menisci elude the limitations of space charge.

4.8.6 Thermal generation, conduction, and convection times

During ion evaporation the process of Ohmic dissipation (and possibly viscous dissipation, but to a much lesser extent in view of the weak flow) will deposit thermal energy within the fluid near the tip. Given that thermal excursions could appreciably modify the behavior of the source it is important to understand the mechanisms that handle the transport of heat as well as their characteristic time scales. These include thermal conduction (analogous to electrical conduction) and also convection when the fluid is in motion.

In a quiescent state the liquid will hold an amount of specific thermal energy equivalent to $\rho c_p T_0$ where ρ is the density of the fluid (kg/m^3), c_p is its specific heat at constant pressure (J/kg-K), and T_0 is the ambient temperature (K). A time scale for thermal energy generation is then very easily defined as

$$\tau_{gen}^{T} \sim \frac{\rho c_p T_0}{\dot{q}} \tag{4.95}$$

where $\dot{q}$ is now the generation rate (W/m^3). Physically, this is the approximate time required for the generate process to deposit an amount of energy tantamount to what is stored at the nominal temperature. In the case of electrical evaporation the mechanism of generation is Ohmic

$$\dot{q} \sim \vec{j} \cdot \vec{E}^{l} \sim \frac{k\left(E^{*}\right)^{2}}{\epsilon_r^2} \tag{4.96}$$

which in turn gives

$$\tau_{gen}^{T} \sim \frac{\rho c_p T_0 \epsilon_r^2}{k\left(E^{*}\right)^{2}} \tag{4.97}$$

Conduction is one channel through which thermal energy can be carried away from the generation site and roughly analogous to the process of electrical conduction for charge transport. Using a basic transient heat balance

$$\rho c_p \frac{\partial T}{\partial t} \sim k_T \frac{\partial^2 T}{\partial x^2} \Rightarrow \tau_{cond}^{T} \sim \frac{\rho c_p \left(r^{*}\right)^{2}}{k_T} \tag{4.98}$$

where k_T is the thermal conductivity (W/m-K) and x is the coordinate in simplified one-dimensional space. For ion evaporation, the characteristic distance should be $x \sim r^*$ near the tip.

Convection of heated fluid is a second channel through which thermal energy can be transported; unlike its conduction counterpart, however, it is not directly analogous to electrical convection in the sense that it is a bulk fluid phenomenon (electrical convection is primarily predicated upon the motion of surface charges). Because it involves the flow of bulk fluid we can surmise that the associated time scale should essentially be that of fluid residence, i.e. $\tau_{conv}^{T} \sim \tau_{res}^{l} \sim r^*/u_{liq}$. For a fluid with $c_p \sim 10^3$ J/kg-K, $k_T \sim 10^{-1}$ W/m-K, $T_0 \sim 10^2$ K, $\epsilon_r \sim 10$, $k \sim 10^0$ S/m, $E^* \sim 10^9$ V/m, and $r^* \sim 10^{-8}$ m we find the time scales $\tau_{gen}^{T} \sim 10^{-8}$ s, $\tau_{cond}^{T} \sim 10^{-9}$ s, and $\tau_{conv}^{T} \sim 10^{-7}$ s. It is clear that conduction is the primary mechanism for the transport of thermal energy because $\tau_{cond}^{T} \ll \tau_{conv}^{T}$ and also that a meniscus supporting ion evaporation could experience a reasonable temperature excursion, but perhaps not as great as $\Delta T \sim T_0$ since $\tau_{cond}^{T} < \tau_{gen}^{T}$.

4.9 Summary

The kinetic law from Eq. 4.1 suggests that charge evaporation from electrified fluids should happen in the vicinity of

$$E^* = \frac{4\pi\epsilon_0 \left(\Delta G\right)^2}{q^3} \tag{4.99}$$

The solvation energy of many ionic liquids is somewhere in the range from 1-2 eV and this necessitates strong fields on the order of $E^* \sim 10^8$ - 10^9 V/m. Stable maintenance of ion evaporation requires that the associated electrical stress $\boldsymbol{\tau_e} \sim \epsilon_0 \left(E^*\right)^2/2$ be balanced by a sharply curved meniscus of characteristic size

$$r^* \sim \frac{4\gamma}{\epsilon_0 \left(E^*\right)^2} = \frac{\gamma q^6}{4\pi^2\epsilon_0^3 \left(\Delta G\right)^4} \tag{4.100}$$

that is typically 10^{-8} - 10^{-7} m. This defines an evaporation area $A^* \sim \pi \left(r^*\right)^2$ over which 10^{-8} - 10^{-6} A could be reasonably emitted, depending upon conditions such as the actual field strength. When the latter is very strong, for example, the current density reaches its conduction-limited maximum of $j \sim kE^*/\epsilon_r$ and a similarly large I would be expected.

The fluid flows that develop during evaporation are relatively tenuous as a result of the high specific charges, among other things, that typify pure ion emission regimes. As a direct consequence, all convective processes are apparently subordinate to their conduction counterparts. This is true for the transport of both heat and electrical charge. Similarly, the weak flow results in a low Capillary number which indicates that viscous stresses are somewhat unimportant in comparison to surface tension effects.

Finally, heating may occur during the evaporation process as a result of Ohmic dissipation in the fluid. While the timescale for thermal conduction is believed to be small in comparison to the one for thermal generation, the behavior of the source could be radically different for even minor temperature excursions. A basic schematic of these fundamental processes is provided in Fig. 4-9.

In the tables that follow we distill salient results from this chapter. Several important emission properties are formulated in terms of the intrinsic fluid properties, the evaporated current, and the governing time scales while numerical examples are given for a small selection of solvation energies within the range from 0.5 - 2 eV. Given that this parameter is only loosely quantified within this range, we would expect the stated numbers to bracket the set of physical possibilities. In all cases the sample fluid is one with $\epsilon_r = 10$; $k = 1$ S/m; $q/m = 10^6$ C/kg; $\gamma = 10^{-1}$ N/m; $\mu = 10^{-1}$ Pa-s; $\rho = 10^3$ kg/m^3; $c_p = 10^3$ J/kg-K; $k_T = 10^{-1}$ W/m-K; and $T_0 = 300$ K unless otherwise stated.

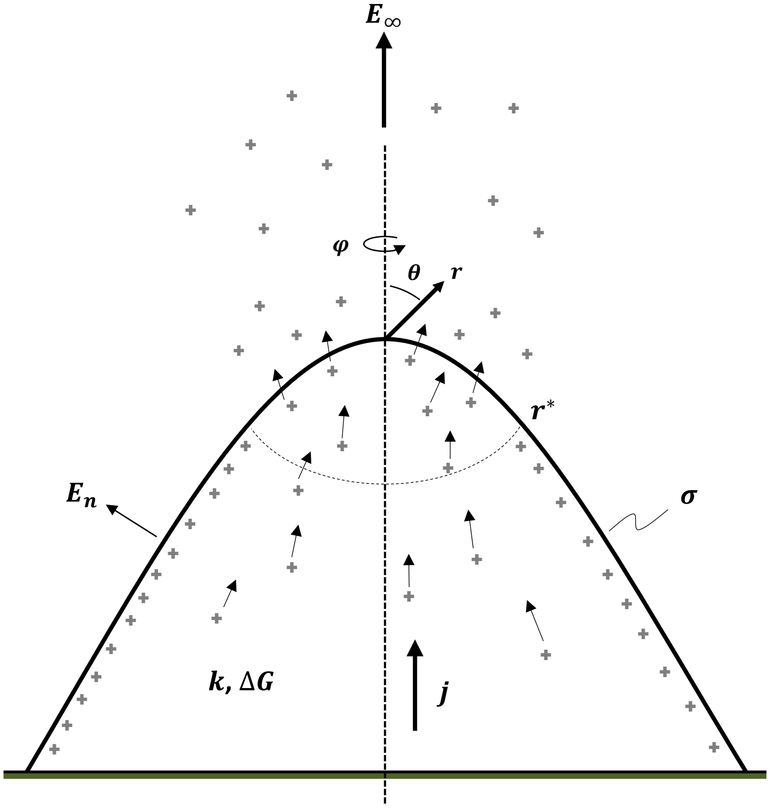

Figure 4-9: Schematic illustration of several fundamental processes for evaporation of ionic liquids. The curved meniscus satisfies a mechanical balance that nominally includes electrical traction and surface tension. Surface charge accumulates in its relaxed state over most of the meniscus. Near the tip with characteristic scale r^* the vacuum field $E_n^v \sim E^*$ is strong enough to extract ions and locally deplete the surface of net charge. Flows of replenishing fluid within the meniscus are relatively tenuous, such that the attendant Capillary number is small (i.e., viscous stresses can be ignored to first approximation), but might still lead to non-trivial heating by way of Ohmic dissipation.

Table 4.1: Evaporation parameters formulated in terms of (1) the intrinsic fluid properties, (2) the evaporated current, and (3) the governing time scales

Parameter	Formulation		
	Intrinsic properties	Current	Time scales
Evaporation field, E^*	$\frac{4\pi\epsilon_0(\Delta G)^2}{q^3}$	–	–
Tip size, r^*	$\frac{\gamma q^6}{4\pi^2\epsilon_0^3(\Delta G)^4}$	–	–
Evaporation current, I^*	$\frac{k\gamma^2 q^9}{4\pi^2\epsilon_0^5\epsilon_r(\Delta G)^6}$	–	–
Surface charge, $\sigma/\epsilon_0 E^*$	$\frac{hk}{\epsilon_0\epsilon_r k_B T}$	–	$\frac{\tau_{emis}}{\tau_e}$
Space charge, E_{sc}/E^*	$\frac{k}{8\epsilon_r}\left[\frac{2\gamma q^9}{\pi^3\epsilon_0^6(q/m)(\Delta G)^6}\right]^{1/2}$	$\left[\frac{kI^*}{8\pi\epsilon_0\epsilon_r\gamma(q/m)}\right]^{1/2}$	$\frac{\tau_{res}^g}{\tau_e}$
Charge convection, j_{conv}/j_{cond}	$\frac{16\pi^3\epsilon_0^5(\Delta G)^6}{\rho\gamma(q/m)q^9}$	$\frac{\epsilon_0\epsilon_r I^*}{\pi k\rho(q/m)(r^*)^3}$	$\frac{\tau_e}{\tau_{res}^l}$
Viscous stress, $\Delta p/P_{st}$	$\frac{2\pi\mu\epsilon_0 k(\Delta G)^2}{\epsilon_r\rho\gamma(q/m)q^3}$	$\frac{\mu I^*}{2\pi\rho\gamma(q/m)(r^*)^2}$	$\frac{\tau_{vis}}{\tau_{res}^l}$
Meniscus heating, $\Delta T/T_0$	$\frac{k\gamma^2 q^6}{\pi^2\epsilon_r^2\epsilon_0^4(\Delta G)^4 k_T T_0}$	$\frac{(I^*)^2}{k(r^*)^2 k_T T_0}$	$\frac{\tau_{cond}^T}{\tau_{gen}^T}$

Table 4.2: Numerical examples near the tip of a fluid with $E \to E^*$

Parameter	Approx. value near tip			
	$\Delta G = 0.5$ eV	1.0 eV	1.5 eV	2.0 eV
Evaporation field, E^* (V/nm)	$2 \cdot 10^{-1}$	$7 \cdot 10^{-1}$	2	3
Tip size, r^* (nm)	$2 \cdot 10^{3}$	93	19	6
Evaporation current, I^* (nA)	10^{5}	$2 \cdot 10^{3}$	$2 \cdot 10^{2}$	30
Surface charge, $\sigma/\epsilon_0 E^*$	$2 \cdot 10^{-3}$	$2 \cdot 10^{-3}$	$2 \cdot 10^{-3}$	$2 \cdot 10^{-3}$
Space charge, E_{sc}/E^*	$7 \cdot 10^{-1}$	$9 \cdot 10-2$	$3 \cdot 10^{-2}$	10^{-2}
Charge convection, j_{conv}/j_{cond}	10^{-6}	10^{-4}	$8 \cdot 10^{-4}$	$4 \cdot 10^{-3}$
Viscous stress, $\Delta p/P_{st}$	$9 \cdot 10^{-3}$	$3 \cdot 10^{-2}$	$8 \cdot 10^{-2}$	10^{-1}
Meniscus heating, $\Delta T/T_0$	20	10^{0}	$3 \cdot 10^{-1}$	$9 \cdot 10^{-2}$

Table 4.3: Formulations for the governing time scales and approximate numerical values near the tip of a fluid with $E \to E^*$ and $\Delta G = 1$ eV

Time scale	Formulation	Approx. value (s)
Emission, τ_{emis}	$\frac{h}{k_B T}$	$2 \cdot 10^{-13}$
Electric relaxation, τ_e	$\frac{\epsilon_0 \epsilon_r}{k}$	$9 \cdot 10^{-11}$
Viscous capillary, τ_{vis}	$\frac{\mu r}{\gamma}$	$9 \cdot 10^{-8}$
Inertial, τ_{iner}	$\sqrt{\frac{\rho r^3}{\gamma}}$	$3 \cdot 10^{-9}$
Feeding flow, τ_f	$\frac{\rho r^2}{\mu}$	–
Liquid residence, τ^l_{res}	$\frac{\pi \rho (q/m) r^3}{I}$	$1 \cdot 10^{-6}$
Gas residence, τ^g_{res}	$\sqrt{\frac{\pi k r^3}{\epsilon_r (q/m) I}}$	$1 \cdot 10^{-11}$
Thermal generation, τ^T_{gen}	$\frac{\rho c_p T_0 k \left(\pi r^2\right)^2}{I^2}$	$6 \cdot 10^{-8}$
Thermal conduction, τ^T_{cond}	$\frac{\rho c_p r^2}{k_T}$	$9 \cdot 10^{-8}$
Thermal convection, τ^T_{conv}	$\frac{\pi \rho (q/m) r^3}{I}$	$1 \cdot 10^{-6}$

Chapter 5

Equilibria, stability, and evaporation of spheroidal menisci

If the order-of-magnitude analyses from the previous chapter are to be believed then it is likely that electrified ionic liquid menisci are conduction-controlled and not limited by the vacuum effects of the space charge that they generate. Owing to the small capillary number, the topographical properties of their interfaces should be determined primarily through the balance of electrical and surface tension stresses. When thermal effects can also be ignored, this set of conditions lends itself to a simplified description of the fluid that might be described through analytical means. In this chapter we explore this possibility as a means of discerning basic emission phenomena and highlighting several weaknesses attendant to non-numerical approaches.

5.1 Fixed-volume problem

Fixed-volume droplets that protrude from a conducting plate while being subjected to a uniform downstream field E_0 (or simply rest in a uniform background field, which is mathematically equivalent) have significant heritage in the literature where they have been studied with a variety of different methods [66, 67, 68, 69, 70, 71]. These include numerical investigations but also analytical treatments [3] predicated upon the fact that their stressed morphologies closely resemble a family of prolate spheroids (see Fig. 5-1). Very conveniently, this facilitates closed-form solutions for the stresses that govern the problem (especially when systems of special coordinates are used, as we show) and for this reason we begin by considering the fixed-volume droplet.

We can start to formulate the mathematical framework for the fixed-volume problem by considering the stress balance at the liquid-vacuum interface. This should read $P_e + P_l = P_{st}$ where P_e is the local electric pressure, P_l is the hydrostatic pressure of the liquid, and P_{st} is the surface tension. Using the Maxwell tensor this can be expanded to find [77, 78, 79]

$$\frac{1}{2}\epsilon_0 \left[\left(E_n^v\right)^2 - \epsilon_r \left(E_n^l\right)^2 + \left(\epsilon_r - 1\right) E_t^2 \right] + P_l = P_{st} \tag{5.1}$$

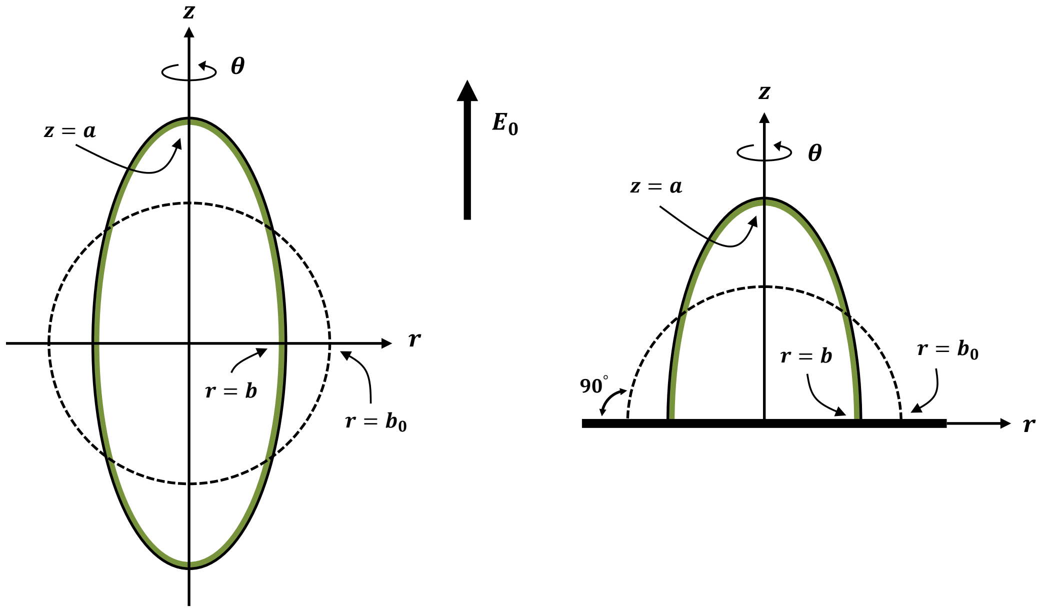

Figure 5-1: Fixed-volume droplets resolved in axisymmetric cylindrical coordinates. The case of a droplet in free-space (left) is mathematically equivalent to that of a droplet on a conducting plate so long as the corresponding contact angle is exactly 90°. This is due to the fact that the mid-plane of the free-space droplet (located along $z = 0$) is a plane of symmetry where $\vec{E} \cdot \vec{i}_r = 0$ by definition (notice that a perfectly conducting plate enforces the same field condition). Application of a uniform electrical field E_0 far downstream of the droplets disturbs their quiescent configurations (dashed curves), which are characterized by spherical radii of length b_0, and causes deformation along the direction of the field. The deformed droplets retain approximately spheroidal geometries for which the associated major and minor axes (denoted by a and b, respectively) are functions of the applied electrical stress. The corresponding aspect ratio a/b is a measure of the prevailing distortion and typically represented by the variable Z (not to be confused with the cylindrical coordinate z, which is always written in lower-case).

where E_n^v and E_n^l are again the normal components of the electric field on the vacuum and liquid sides of the interface, respectively, and where E_t is the tangential component. During the emission process we have shown that parts of the meniscus may experience depleted surface charge as a result of conduction limitations in the fluid. When the depletion is not too significant, however, and perhaps when the dielectric strength ϵ_r of the fluid is high, the droplet might be reasonably approximated as an equipotential structure. In that case, $E_n^l \sim E_t \sim 0$ leaving the vacuum field as the lone electrical stressor of the fluid. The simplified stress balance is

$$\frac{1}{2}\epsilon_0 \left(E_n^v\right)^2 + P_l = P_{st} \tag{5.2}$$

Of the terms here, the one involving E_n^v is easily the most involved, especially for generalized curvilinear geometries. Fortunately, the subset of spheroidal form factors are analytically tractable in an orthogonal system of prolate spheroidal coordinates. As we show in the appendix, the solution to Laplace's equation in that space yields

$$E_n^v = \frac{E_0}{\sqrt{1+(Z\cdot\tan\nu)^2}}\left[\frac{Z^2-1}{\frac{Z}{\sqrt{Z^2-1}}\ln\left(Z+\sqrt{Z^2-1}\right)-1}\right] \tag{5.3}$$

for the vacuum field acting on an equipotential spheroid. Here, Z is the aspect ratio a/b of the droplet (i.e. the ratio of the major and minor axes) and ν is a polar angle that ranges from $\nu = 0$ at the tip to $\nu = \pi/2$ at the mid-plane.

As for the surface tension and liquid pressure terms it is most appropriate to adopt the two-point stress method introduced by Taylor [3]. This calls for the stress to be balanced at both the tip of the meniscus and at the mid-plane, but not necessarily at points in between. Starting with the mid-plane, it can be verified from Eq. 5.3 that $E_n^v \to 0$ as $\nu \to \pi/2$ requiring that P_e fall out of the stress equation. The local surface tension is found by recalling that

$$\left(\frac{z}{a}\right)^2 + \left(\frac{r}{b}\right)^2 = 1 \tag{5.4}$$

is the equation of a spheroid resolved in axisymmetric cylindrical space. The first and second spatial derivatives of this equation are

$$\frac{z'}{a} = \frac{-r}{b\left(b^2-r^2\right)^{1/2}} \tag{5.5}$$

$$\frac{z''}{a} = \frac{-b}{\left(b^2-r^2\right)^{3/2}} \tag{5.6}$$

where the "primes" denote differentiation with respect to r. In general, the radius of curvature for projection of the spheroid on the $r-z$ plane is $R_1 = ||(1+(z')^2)^{3/2}/z''||$. Substituting the derivatives into this express gives

$$\frac{1}{R_1} = \frac{ab^4}{\left[b^2\left(b^2 - r^2\right) + a^2 r^2\right]^{3/2}} \tag{5.7}$$

At the mid-plane, $r \to b$ and reduces this relationship to $1/R_1 = b/a^2$. This is the first principal radius of curvature and the one residing in the $r - z$ plane. The second principal curvature is in the azimuthal direction and should be exactly b, the radius of the spheroidal waist. The total surface tension pressure at the mid-plane is then

$$P_{st}|_{mid} = \gamma\left(\frac{1}{R_1} + \frac{1}{R_2}\right) = \frac{\gamma}{b}\left(\frac{1+Z^2}{Z^2}\right) \tag{5.8}$$

where we have used the aspect ratio $Z = a/b$. Since there is no field this must be numerically equivalent to the hydrostatic pressure in the fluid (which is spatially uniform) at all times. Turning our attention to the tip, from Eq. 5.7 the local surface tension is

$$P_{st}|_{tip} = \frac{2\gamma Z}{b} \tag{5.9}$$

and we note that the electrical stress is, of course, nonzero now. The stress balance now reads

$$\underbrace{\frac{1}{2}\epsilon_0 E_0^2\left[\frac{Z^2-1}{\frac{Z}{\sqrt{Z^2-1}}\ln\left(Z+\sqrt{Z^2-1}\right)-1}\right]^2}_{P_e} + \underbrace{\frac{\gamma}{b}\left(\frac{1+Z^2}{Z^2}\right)}_{P_l} = \underbrace{\frac{2\gamma Z}{b}}_{P_st} \tag{5.10}$$

The base radius b in this expression is somewhat problematic as it must vary in order to satisfy volume conservation. We can address it, however, by integrating the equation of the spheroid in axisymmetric cylindrical space

$$V = 2\pi a\int_0^b r\sqrt{1-\left(\frac{r}{b}\right)^2}\cdot dr = \frac{2\pi ab^2}{3} \tag{5.11}$$

and noting that the product ab^2 is invariant regardless of any induced deformation. This condition requires that

$$b_0^3 = ab^2 \Rightarrow \frac{b}{b_0} = \frac{1}{Z^{1/3}} \tag{5.12}$$

where b_0 is the spherical radius of the undeformed droplet. Substituting this in the stress balance at the tip provides for an expression that we can use to estimate the elongation of the fluid as a function of the external field E_0

$$\frac{1}{2}\epsilon_0 E_0^2\left[\frac{Z^2-1}{\frac{Z}{\sqrt{Z^2-1}}\ln\left(Z+\sqrt{Z^2-1}\right)-1}\right]^2 + \frac{\gamma}{b_0}Z^{1/3}\left(\frac{1+Z^2}{Z^2}\right) - \frac{2\gamma}{b_0}Z^{4/3} = 0 \tag{5.13}$$

The emission part of the problem is subordinate to the deformation but still obeys the usual kinetic law. From Eq. 4.5

$$j = \frac{kE_n^v/\epsilon_r}{1 + \frac{hk}{\epsilon_0 \epsilon_r k_B T} \exp\left(\frac{1}{k_B T}\left\{\Delta G - \sqrt{\frac{q^3 E_n^v}{4\pi\epsilon_0}}\right\}\right)} \tag{5.14}$$

is the current density at the interface for a conduction-limited fluid. The total current is therefore the integral of this expression over the surface, $I = \int j \cdot dA$ with $dA = 2\pi r \cdot ds$ in axisymmetric cylindrical space. The differential distance along the interface follows from $ds^2 = dr^2 + dz^2$ and can be be expanded with the help of the expression for z' above

$$ds = dr\sqrt{1 + \left(\frac{dz}{dr}\right)^2} = dr\sqrt{\frac{1 + (r/b)^2 (Z^2 - 1)}{1 - (r/b)^2}} \tag{5.15}$$

The current is then

$$I = 2\pi \int_0^b jr\sqrt{\frac{1 + (r/b)^2 (Z^2 - 1)}{1 - (r/b)^2}} \cdot dr \tag{5.16}$$

Going forward it will be helpful to eliminate the r/b factors. To achieve this we now define $R = r/b$ and make this our variable of integration so that

$$I = 2\pi b^2 \int_0^1 jR\sqrt{\frac{1 + R^2 (Z^2 - 1)}{1 - R^2}} \cdot dR = 2\pi\left(\frac{b_0^2}{Z^{2/3}}\right) \int_0^1 jR\sqrt{\frac{1 + R^2 (Z^2 - 1)}{1 - R^2}} \cdot dR \tag{5.17}$$

where we have also invoked the volume conservation relationship $b = b_0/Z^{1/3}$. This completes the mathematical description of the emission problem for the fixed-volume droplet. Before proceeding, however, we will nondimensionalize the governing equations by electing the scales

$$\begin{aligned}
\hat{r} \rightarrow & \frac{r}{b_0} \\
\hat{E} \rightarrow & \frac{E}{E_c}, \text{ where } E_c = \frac{4\gamma}{\epsilon_0 b_0} \\
\hat{P_{st}} \rightarrow & \frac{P_{st}}{\left(\frac{2\gamma}{b_0}\right)} \\
\hat{P_l} \rightarrow & \frac{P_l}{\left(\frac{2\gamma}{b_0}\right)} \\
\hat{j} \rightarrow & \frac{j}{kE_c} \\
\hat{I} \rightarrow & \frac{I}{kE_c b_0^2}
\end{aligned}$$

Notice that the stresses are scaled by the nominal capillary pressure and that the fields are scaled by the critical value E_c. This is the field at which the electric pressure balances the capillary pressure, i.e. $\epsilon_0 E_c^2/2 = 2\gamma/b_0$. After implementing these we find that the problem is governed by

$$\hat{E}_0^2 \left[\frac{Z^2-1}{\frac{Z}{\sqrt{Z^2-1}}\ln\left(Z+\sqrt{Z^2-1}\right)-1}\right]^2 + \frac{Z^{1/3}}{2}\left(\frac{1+Z^2}{Z^2}\right) - Z^{4/3} = 0 \tag{5.18}$$

$$\hat{I} = \frac{2\pi}{Z^{2/3}}\int_0^1 \hat{j} R \sqrt{\frac{1+R^2\left(Z^2-1\right)}{1-R^2}} \cdot dR \tag{5.19}$$

at the interface, which is also subject to

$$\hat{j} = \frac{\hat{E}_n^v/\epsilon_r}{1+\chi\cdot\exp\left(\psi\left\{1-B^{1/4}\sqrt{\hat{E}_n^v}\right\}\right)} \tag{5.20}$$

$$\hat{E}_n^v = \hat{E}_0\sqrt{\frac{1-R^2}{1+R^2\left(Z^2-1\right)}}\left[\frac{Z^2-1}{\frac{Z}{\sqrt{Z^2-1}}\ln\left(Z+\sqrt{Z^2-1}\right)-1}\right] \tag{5.21}$$

The dimensionless groupings χ and ψ are those defined by Eqs. 4.10 and 4.11 in the previous chapter. The new grouping B is defined as b^*/b_0, where

$$b^* = r^* = \frac{\gamma q^6}{4\pi^2\epsilon_0^3\left(\Delta G\right)^4} \tag{5.22}$$

is the characteristic size of the charge evaporation area. B, therefore, can be interpreted as ratio of this size to that of the full meniscus. Also note that we have used the cylindrical transformations for prolate spheroidal space (see appendix)

$$\begin{aligned} r =& \alpha \sinh\mu \sin\nu \\ z =& \alpha \cosh\mu \cos\nu \end{aligned}$$

to substitute

$$\tan\nu = \frac{R}{\sqrt{1-R^2}} \tag{5.23}$$

in the expression for E_n^v.

5.1.1 Equilibria for conducting and dielectric droplets

To investigate equilibrium properties of the fixed-volume droplet in the most general way it makes sense to consider the electrical stress on a pure dielectric fluid of arbitrary strength ϵ_r. The Laplacian solution for this problem, developed in the appendix, suggests that the field on the vacuum side of the meniscus tip is

$$E_n^v|_{tip} = \frac{\epsilon_r E_0}{1 - \frac{\epsilon_r - 1}{Z^2-1}\left[1 + \frac{Z}{\sqrt{Z^2-1}} \cdot \ln\left\{\frac{1}{Z+\sqrt{Z^2-1}}\right\}\right]} \tag{5.24}$$

while the field on the liquid side is simply $E_n^l = E_n^v/\epsilon_r$ as a result of the vanishing surface charge. Notice that

$$\lim_{\epsilon_r \to \infty} E_n^v = \frac{E_0\left(Z^2-1\right)}{\frac{Z}{\sqrt{Z^2-1}} \cdot \ln\left\{Z + \sqrt{Z^2-1}\right\} - 1} \tag{5.25}$$

which, of course, is the solution for the perfectly conducting meniscus. Depending upon the structure of the field it is not always true that a material with unbounded permittivity will behave the same as one with infinite conductivity; in this instance, however, the cases are mathematically equivalent. The fact that this situations exists is helpful here as it will allow us to easily explore the stress responses of both conducting and dielectric drops at the same time. The task now is to formulate the electric pressure at the tip of the dielectric drop

$$P_e = \frac{\frac{1}{2}\epsilon_0 E_0^2\left[\epsilon_r\left(\epsilon_r - 1\right)\right]}{\left[1 - \frac{\epsilon_r-1}{Z^2-1}\left(1 + \frac{Z}{\sqrt{Z^2-1}} \cdot \ln\left\{\frac{1}{Z+\sqrt{Z^2-1}}\right\}\right)\right]^2} \tag{5.26}$$

and nondimensionalize in the same manner as before

$$\hat{P}_e = \frac{\hat{E}_0^2\left[\epsilon_r\left(\epsilon_r - 1\right)\right]}{\left[1 - \frac{\epsilon_r-1}{Z^2-1}\left(1 + \frac{Z}{\sqrt{Z^2-1}} \cdot \ln\left\{\frac{1}{Z+\sqrt{Z^2-1}}\right\}\right)\right]^2} \tag{5.27}$$

This is a more general expression that can be substituted in Eq. 5.18

$$\frac{\hat{E}_0^2\left[\epsilon_r\left(\epsilon_r - 1\right)\right]}{\left[1 - \frac{\epsilon_r-1}{Z^2-1}\left(1 + \frac{Z}{\sqrt{Z^2-1}} \cdot \ln\left\{\frac{1}{Z+\sqrt{Z^2-1}}\right\}\right)\right]^2} + \frac{Z^{1/3}}{2}\left(\frac{1+Z^2}{Z^2}\right) - Z^{4/3} = 0 \tag{5.28}$$

Eq. 5.28 now describes the relationship between the externally imposed electric field E_0 and the equilibrium deformation of an general fluid, as measured by the aspect ratio Z. The simplest way to solve it involves isolating the field on the left-hand side

$$\hat{E}_0^2 = \frac{Z^{4/3} - \frac{Z^{1/3}}{2}\left(\frac{1+Z^2}{Z^2}\right)}{\epsilon_r\left(\epsilon_r - 1\right)}\left[1 + \frac{\epsilon_r - 1}{Z^2-1}\left(\frac{Z}{\sqrt{Z^2-1}} \cdot \ln\left\{Z + \sqrt{Z^2-1}\right\} - 1\right)\right]^2 \tag{5.29}$$

and then calculating the value corresponding to the independent variable Z, which is arbitrary in this case.

Results from this process are shown in Fig. 5-2 for several values of dielectric strength ranging from $\epsilon_r = 5$ to the limiting case $\epsilon_r \to \infty$. These values increase in the counterclockwise direction, starting from the bottom curve, and offer rich insight

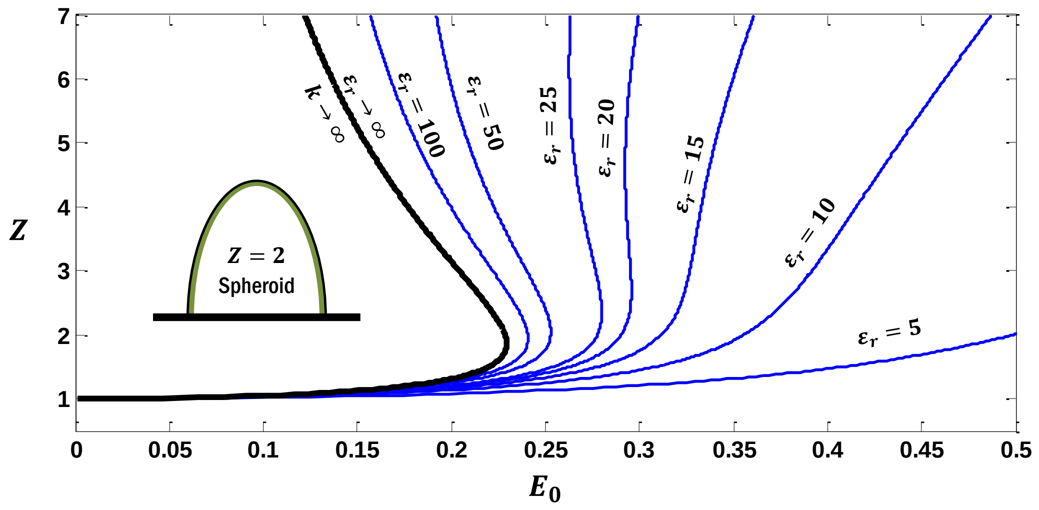

Figure 5-2: Equilibrium elongation values as a function of the dimensionless external electric field $\hat{E}_0$ for fixed-volume dielectric droplets. The monotonic growth of the weak dielectrics is very different from the multi-valued, turning point behavior of their high ϵ_r counterparts. In the limiting case, $\epsilon_r \to \infty$, the turning point precludes spheroidal solutions about $\hat{E}_0 \sim 0.228$ but an unbounded set of possible deformations is possible above the starting value $Z = 1$.

on the deformation behavior of fixed volume droplets. Other authors have arrived at similar results in the past through a variety of methods [3, 71].

From the plot we can distinguish three distinct groups of curves: the double-valued group, the hysteretic group, and the monotonic group. The first of these, the double-valued group, is populated by fluids with $\epsilon_r \gtrsim 25$ (at least within the pictured range) and includes the limiting $\epsilon_r \to \infty$ case. It is characterized by a multi-valued deformation curve involving a lower branch of modest Z and an upper branch of extreme protraction. In terms of the former, it begins with the undeformed or quiescent $Z = 1$ state and experiences a very subtle elongation as the external field is increased. We see that this elongation persists until some terminal value of the field is met, beyond which the fluid apparently cannot reach a mechanical equilibrium, at least with a spheroidal interface. In the limiting case, for example, this happens around $\hat{E}_0 \sim 0.228$ and $Z \sim 1.86$ (as shown in Fig. 5-3). Other interface modes could be possible for higher fields, however, and this is what led Taylor [3] to conclude that the so-called turning point must be the one at which the droplet begins to devolve into the characteristic cone that is known in that regime. Unfortunately, the results of Higuera [62] strongly suggest that steady evaporation is not supported by these modes and so we do not consider them any further here. Moving on to the upper branch, we see that solutions again exist for fields below the turning point but involve strong deformations. The fact that these satisfy the mechanical balance is very interesting, and in the next section we examine their stability to determine whether they are an artifact of the mathematics or something we should physically anticipate.

At the other end of the dielectric spectrum we have the monotonic group for which

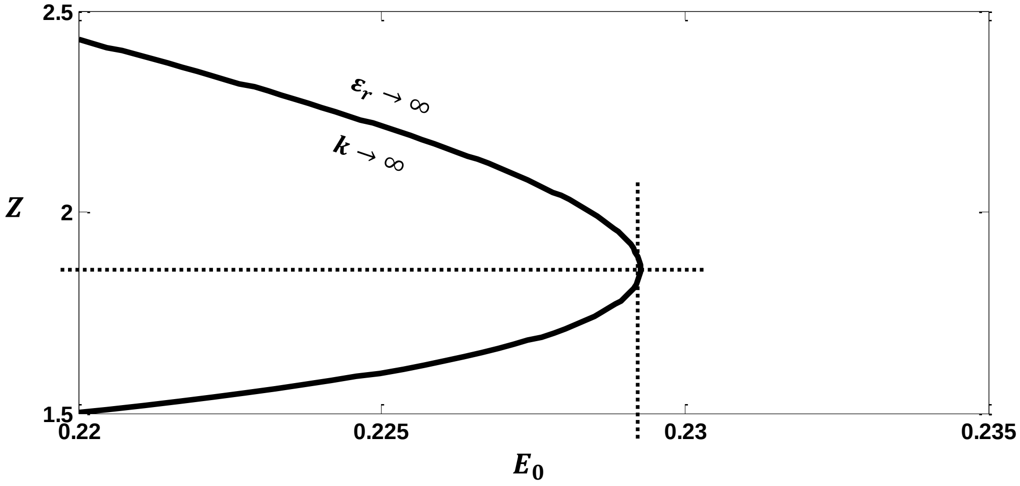

Figure 5-3: Detail of the turning point for the limiting case $\epsilon_r \to \infty$. The critical field is $\hat{E}_0 \sim 0.228$ and corresponds to the elongation $Z \sim 1.86$.

the elongation of the droplet is associated a single field value over $\hat{E}_0 \in [0, \infty]$. It corresponds to roughly $\epsilon_r \lesssim 20$ and likely has something to do with the arrangement of the field near the tip, where the low permittivity of the fluid must mitigate the stress of the electric pressure even when E_n^l is small (consider the $E_n^l \sim E_n^v/20$ case). Apparently, the meniscus is very sensitive to the structure of the surrounding field, which is something that should be kept in mind. In between this group and the double-valued family is the hysteretic group, corresponding to the range $20 \lesssim \epsilon_r \lesssim 25$. As shown in Fig. 5-4, a lower solution branch meets an initial turning point before reversing course at elevated Z and continuing to grow monotonically thereafter. Note that while it is possible that certain droplets with $\epsilon_r \gtrsim 25$ exhibit qualitatively similar hysteretic behavior (i.e. that their elongation curves return to positive slope at elevated Z), this would clearly need to occur in the presence of extreme protraction beyond the maximum $Z = 10$ that we have depicted. Such cases will not be rigorously considered here.

5.1.2 Stability

The stability of the deformed states depends on the behavior of the governing pressures in response to perturbations of the interfacial geometry. For the stress balance that determines the droplet shape we can write, in general

$$P_e + P_l - P_{st} = \Delta P \tag{5.30}$$

at the tip, where ΔP is a pressure difference that vanishes for an equilibrium configuration, i.e. $\Delta P \to 0$ for $Z \to Z_{eq}$. When an equilibrium is perturbed, however, ΔP may deviate in either the positive (outward forcing) or negative (inward forcing) direction and it is the nature of this excursion that determines stability. For example, if the equilibrium value of the droplet aspect ratio grows a small amount from Z_{eq} to

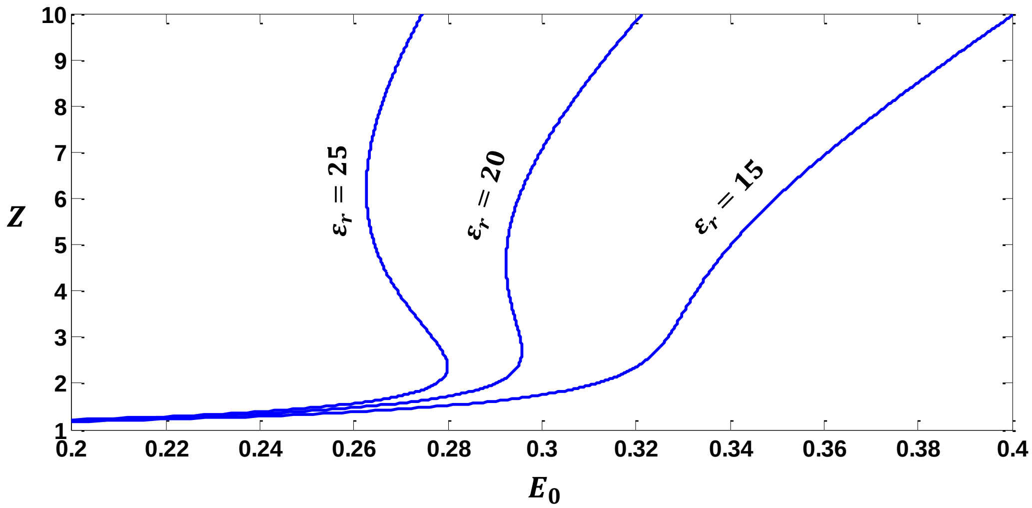

Figure 5-4: Detail for the hysteretic behavior of the curves corresponding to intermediate ϵ_r. After an initial turning point the curves reverse course and become monotonic again for high Z.

$Z_{eq} + \delta Z$ and $\Delta P(Z_{eq} + \delta Z)$ is positive, the extra pressure at the tip will tend to pull it out even further and likely create a runaway effect from which a steady interface cannot be recovered. On the other hand, if $\Delta P(Z_{eq} + \delta Z)$ is negative the excess pressure will tend to push the tip back in and restore the original configuration. To state this in a more formal mathematical way, consider the pressure at $Z = Z_{eq} + \delta Z$

$$P_e\left(Z_{eq} + \delta Z\right) + P_l\left(Z_{eq} + \delta Z\right) - P_{st}\left(Z_{eq} + \delta Z\right) = \Delta P\left(Z_{eq} + \delta Z\right) \tag{5.31}$$

with the field E_0 fixed. Since δZ is by definition very small, we can expand the pressures in a Taylor series and truncate after the linear term so that

$$\underbrace{\left[P_e\left(Z_{eq}\right) + \frac{\partial P_e}{\partial Z}\delta Z\right]}_{P_e(Z_{eq}+\delta Z)} + \underbrace{\left[P_l\left(Z_{eq}\right) + \frac{\partial P_l}{\partial Z}\delta Z\right]}_{P_l(Z_{eq}+\delta Z)} - \underbrace{\left[P_{st}\left(Z_{eq}\right) + \frac{\partial P_{st}}{\partial Z}\delta Z\right]}_{P_{st}(Z_{eq}+\delta Z)} = \underbrace{\Delta P\left(Z_{eq}\right) + \frac{\partial \Delta P}{\partial Z}\delta Z}_{\Delta P(Z_{eq}+\delta Z)} \tag{5.32}$$

After noting the equilibrium condition

$$P_e\left(Z_{eq}\right) + P_l\left(Z_{eq}\right) - P_{st}\left(Z_{eq}\right) = \Delta P\left(Z_{eq}\right) = 0 \tag{5.33}$$

and dividing through by δZ we get

$$\frac{\partial P_e}{\partial Z} + \frac{\partial P_l}{\partial Z} - \frac{\partial P_{st}}{\partial Z} = \frac{\partial \Delta P}{\partial Z} \tag{5.34}$$

The appropriate stability condition is, therefore

$$\left[\frac{\partial P_e}{\partial Z}+\frac{\partial P_l}{\partial Z}-\frac{\partial P_{st}}{\partial Z}\right]_{E_0(Z_{eq})}=\left.\frac{\partial \Delta P}{\partial Z}\right|_{E_0(Z_{eq})}<0 \tag{5.35}$$

While it is possible to arrive at closed-form analytical expressions for the derivatives in this relationship, they are far from trivial. We will consider them piecewise here and start with the electric pressure. From the pure dielectric condition $E_n^l = E_n^v/\epsilon_r$ we have

$$P_e=\frac{1}{2}\epsilon_0\left(\frac{\epsilon_r-1}{\epsilon_r}\right)\left(E_n^v\right)^2 \Rightarrow \frac{\partial P_e}{\partial Z}=\epsilon_0\left(\frac{\epsilon_r-1}{\epsilon_r}\right)E_n^v\cdot\frac{\partial E_n^v}{\partial Z} \tag{5.36}$$

where $E_n^v(Z)$ is given by Eq. 5.24. After extensive manipulation we find its derivative to be

$$\frac{\partial E_n^v}{\partial Z}=\frac{-\epsilon_r\left(\epsilon_r-1\right)E_0\frac{Z}{(Z^2-1)^2}\left[3-\frac{\ln\left\{Z+\sqrt{Z^2-1}\right\}}{\sqrt{Z^2-1}}\left(\frac{2Z^2+1}{Z}\right)\right]}{\left[1+\frac{\epsilon_r-1}{Z^2-1}\left(\frac{Z}{\sqrt{Z^2-1}}\ln\left\{Z+\sqrt{Z^2-1}\right\}-1\right)\right]^2} \tag{5.37}$$

The derivative of the electric pressure is now

$$\frac{\partial \hat{P}_e}{\partial Z}=\frac{-2\left(\epsilon_r-1\right)\frac{Z}{(Z^2-1)^2}\left[Z^{4/3}-\frac{Z^{1/3}}{2}\left(\frac{1+Z^2}{Z^2}\right)\right]\cdot\left[3-\frac{\ln\left\{Z+\sqrt{Z^2-1}\right\}}{\sqrt{Z^2-1}}\left(\frac{2Z^2+1}{Z}\right)\right]}{1+\frac{\epsilon_r-1}{Z^2-1}\left(\frac{Z}{\sqrt{Z^2-1}}\ln\left\{Z+\sqrt{Z^2-1}\right\}-1\right)} \tag{5.38}$$

in dimensionless form. Note that we invoked Eq. 5.29 to substitute for $E_0(Z_{eq})$ and write the derivative as a function of Z alone. The remaining terms are much more simple

$$\frac{\partial \hat{P}_l}{\partial Z}=\frac{Z^2-5}{6Z^{8/3}} \tag{5.39}$$

$$\frac{\partial \hat{P}_{st}}{\partial Z}=\frac{4}{3}Z^{1/3} \tag{5.40}$$

and yield the aggregate expression

$$\frac{\partial \Delta\hat{P}}{\partial Z}=\frac{-2\left(\epsilon_r-1\right)\frac{Z}{(Z^2-1)^2}\left[Z^{4/3}-\frac{Z^{1/3}}{2}\left(\frac{1+Z^2}{Z^2}\right)\right]\cdot\left[3-\frac{\ln\left\{Z+\sqrt{Z^2-1}\right\}}{\sqrt{Z^2-1}}\left(\frac{2Z^2+1}{Z}\right)\right]}{1+\frac{\epsilon_r-1}{Z^2-1}\left(\frac{Z}{\sqrt{Z^2-1}}\ln\left\{Z+\sqrt{Z^2-1}\right\}-1\right)}+\frac{Z^2-5}{6Z^{8/3}}-\frac{4}{3}Z^{1/3} \tag{5.41}$$

This relationship is plotted in Fig. 5-5 for several values of permittivity. In it we can see the curves transitioning from stable to unstable states as they change signs from negative to positive. For the limiting $\epsilon_r \to \infty$ case, for example, the sign change corresponds to $Z \approx 1.86$ which is the elongation at the turning point. This suggests that its lower solution branch is stable but not the upper one. Also notice

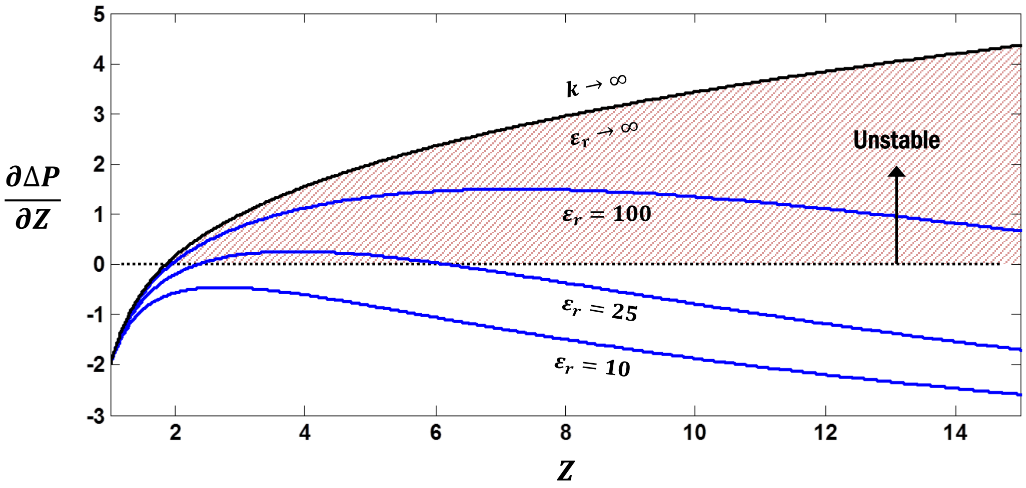

Figure 5-5: Stability curves for several values of dielectric strength ϵ_r. The region of positive $\partial\Delta P/\partial Z$ is unstable and occupied by most of the equilibrium elongations for the limiting $\epsilon_r \to \infty$ case. In fact, the location of neutral stability is $Z = 1.86$ and corresponds to the turning point. Its lower solution branch is stable, therefore, while its upper one is not.

that the $\epsilon_r = 25$ curve becomes unstable for an intermediate range of Z but recovers and begins to gain stability again. This is a very interesting phenomenon that we can learn more about by reproducing Fig. 5-2 and marking all of the sections of the elongation curves that are unstable. We do this in Fig. 5-6, where the stable sections are plotted in thin blue lines while the unstable sections are denoted by thick red ones. A subtle pattern is apparent, and without proving it rigorously here we note that it looks as though the sections with a negative slope are unstable while those with a positive slope are not. In mathematical terms

$$\frac{\partial Z_{eq}}{\partial \hat{E}_0} < 0 \Rightarrow \frac{\partial \Delta \hat{P}}{\partial Z} > 0 \tag{5.42}$$

$$\frac{\partial Z_{eq}}{\partial \hat{E}_0} > 0 \Rightarrow \frac{\partial \Delta \hat{P}}{\partial Z} < 0 \tag{5.43}$$

It may also be fair to speculate that the degree of stability (or proximity to neutral stability) correlates to the magnitude of the $Z - E_0$ slope. For example, a small positive slope likely indicates a high level of stability while a large positive slope could indicate a comparatively low level.

5.1.3 Field evaporation

Based on the stability results we can conclude that the maximum elongation for which we should expect steady evaporation to occur is roughly $Z \approx 1.86$, corresponding to

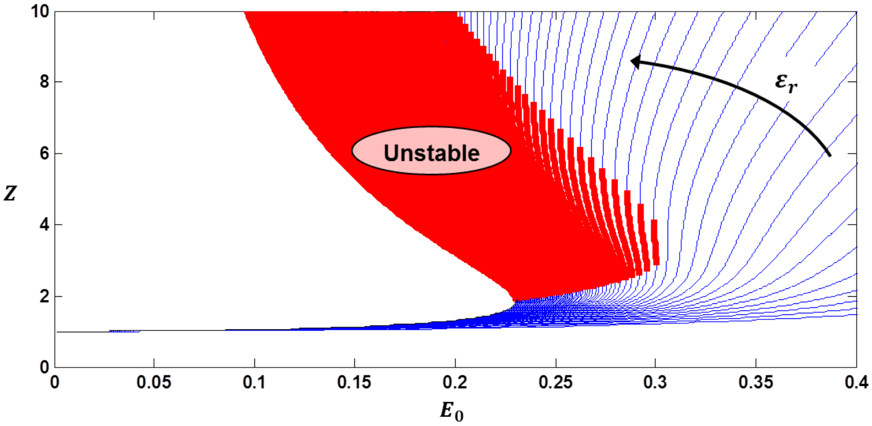

Figure 5-6: Equilibrium elongation map with ϵ_r as a parameter. The stable sections of each curve are plotted in thin blue while the unstable ones are shown in thick red. By inspection we can see that the areas of negative slope are the unstable ones.

the turning point for the limiting $\epsilon_r \to \infty$ case. This should be a fair approximation so long as the meniscus is not severely depleted of surface charge as we have already stated. Using this information we can examine the prevailing interfacial fields and estimate the magnitude of the emitted charge. For the former we wish to compare the vacuum field E_n^v with E^*, the characteristic field for strong evaporation. From Eq. 5.21 we have

$$\left.\frac{E_n^v}{E_0}\right|_{tip} = \frac{Z^2 - 1}{\frac{Z}{\sqrt{Z^2-1}} \cdot \ln\left\{Z + \sqrt{Z^2 - 1}\right\} - 1} \tag{5.44}$$

The ratio of the fields on the left-hand side of this expression is

$$\frac{E_n^v}{E^*}\frac{E^*}{E_c}\frac{E_c}{E_0} = \frac{E_n^v}{E^*}\frac{B^{-1/2}}{\hat{E}_0} \tag{5.45}$$

and this can be substituted to find

$$\frac{E_n^v}{E^*} = B^{1/2}\left[Z^{4/3} - \frac{Z^{1/3}}{2}\left(\frac{1+Z^2}{Z^2}\right)\right]^{1/2} \tag{5.46}$$

after invoking Eq. 5.29 for $\hat{E}_0$. In Fig. 5-7 we plot this relationship across the stable range $Z \in [1, 1.86)$ with the size ratio $B = b^*/b_0$ as a parameter. Based on the information it contains we can see that the maximum tip field E_n^v only approaches emission levels when b_0 (the radius of the undeformed droplet) is on the order of the characteristic scale b^* (recall that $b^* = r^*$). In other words, the spheroidal meniscus with fixed volume is only capable of supporting steady emission when the initial droplet is already as small as the size of the characteristic emission region for the working fluid. The present method alone is insufficient for resolving evaporation when the problem involves a disparity in scales. This is somewhat unfortunate, given

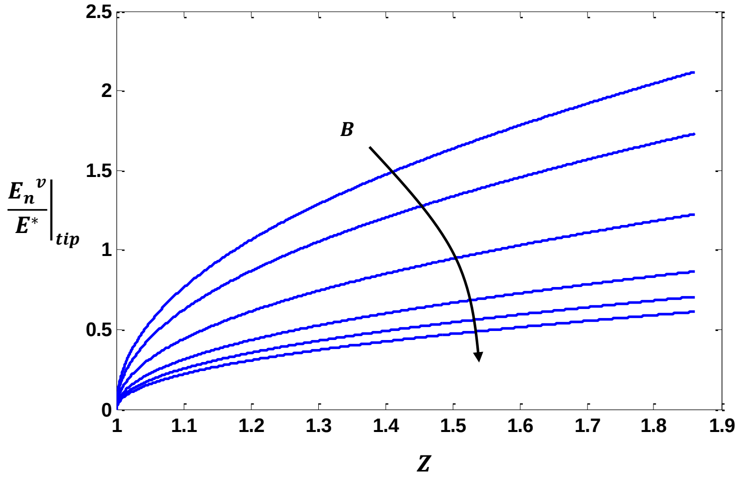

Figure 5-7: Electric field at the tip of a conducting spheroidal meniscus with fixed volume. The field is shown as a function of the elongation over the stable ranging that extends to $Z \sim 1.86$ with the size ratio B as a parameter. Values of $B = 3, 2, 1, 1/2, 1/3, 1/4$ are represented while the arrow indicates the direction of decreasing magnitude; i.e., the direction of increasing droplet size. From this information it is clear that $b_0 \sim b^*$ is a prerequisite for emission.

that many reports suggest emission can occur from much larger menisci [29, 30], but not necessarily prohibitive for continuing to explore issues of academic interest.

Notwithstanding the scale issue for the moment, we can consider the evaporated current by recalling Eqs. 5.19 thru 5.21. The results are plotted in Figs. 5-8 and 5-9 with B as a parameter once again. These assume a fluid with $\Delta G = 1$ eV, $\epsilon_r = 10$, $k = 1$ S/m, $\gamma = 5{\cdot}10^{-2}$ N/m, and $T = 300$ K so that χ and ψ are $\sim 10^{-3}$ and 40, respectively. In Fig. 5-8 we show the dimensionless evaporation as a function of the dimensionless field for several B between 3 and 1/4 across the range of ostensible stability. As expected, the smaller menisci start producing charge at smaller $\hat{E}_0$ because the actual field $E_0 \propto b_0^{-1/2}$.

In Fig. 5-9 we instead show estimated units of current (nanoamperes) as a function of the dimensionless field. Encouragingly, the curves delineated therein represent magnitudes $I \sim 10^{-7}$ A that are roughly consistent with empirical observations from similar fluids [29, 30]. Also, the curves indicate that the current might be retarded for very small menisci. While it makes obvious sense that big spheroidal droplets may not support significant emission, owing to the small fields that are attainable within the range of stable elongations, it is perhaps less clear that the larger current densities of their smaller counterparts are at some point offset by the decreasing area. This phenomenon apparently points to the existence of an optimal droplet size, i.e. one which maximizes the amount of evaporated current.

Fig. 5-9 suggests that the optimal size is likely somewhere between $B = 1$ and $B = 1/2$ assuming that all droplets obey the stable elongation properties of the limiting $\epsilon_r \to \infty$ case. We expect this to occur so long as significant charge depletion

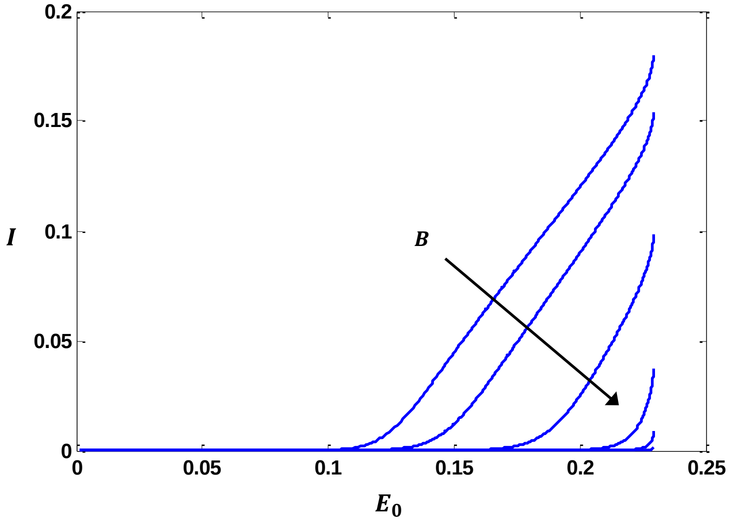

Figure 5-8: Dimensionless current as a function of dimensionless field for fixed-volume spheroidal droplets of conducting fluid. The arrow indicates the direction of decreasing B (i.e., increasing b_0), the size parameter for the meniscus. Values of $B = 3$, 2, 1, 1/2, 1/3, and 1/4 are represented. The results indicate that the size of the droplets must be of the order of the characteristic evaporation region for the fluid in order for steady emission to occur.

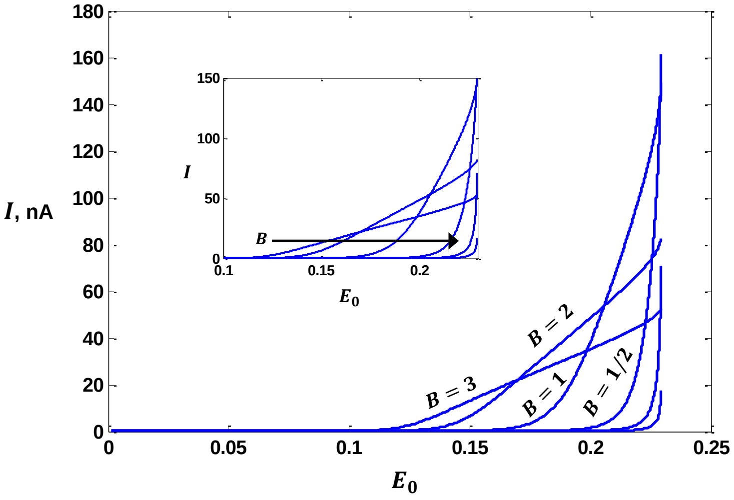

Figure 5-9: Dimensional current as a function of dimensionless field. Values of $B =$ 3, 2 , 1, 1/2, 1/3, and 1/4 are represented while the arrow indicates the direction of decreasing magnitude. The units of current, nanoamperes, suggest evaporation levels ($\sim 10^{-7}$ A) that are roughly consistent with empirical observations. Interestingly, it is also observed here that the evaporated current begins to decrease for very small menisci, which is likely the result of the smaller emission area offsetting the high fields and current densities. This, perhaps, points to an optimal droplet size when emission strength is the driving metric.

does not take place; however, in view of several of the fields observed in Fig. 5-7 it may not always be true that the interface is sufficiently near electrical relaxation. Consider the interfacial jump condition for surface charge $\sigma = \epsilon_0 E_n^v - \epsilon_0 \epsilon_r E_n^l$ where $E_n^l = j/k$ as a result of Ohm's law. The ratio of the surface charge to the fully relaxed value (the normal component of the displacement field in vacuum) is, therefore

$$\frac{\sigma}{\epsilon_0 E_n^v} = 1 - \frac{j\epsilon_r}{kE_n^v} \tag{5.47}$$

From Eq. 4.5, this becomes

$$\frac{\sigma}{\epsilon_0 E_n^v} = \frac{1}{1 + \frac{1}{\chi}\exp\left(-\psi\left\{1 - B^{1/4}\sqrt{\hat{E}_n^v}\right\}\right)} \tag{5.48}$$

after nondimensionalizing, where the normal field on the vacuum side of the interface

$$\hat{E}_n^v = \sqrt{\frac{1-R^2}{1+R^2\left(Z^2-1\right)}\left[Z^{4/3} - \frac{Z^{1/3}}{2}\left(\frac{1+Z^2}{Z^2}\right)\right]} \tag{5.49}$$

is a function of the scaled coordinate $R = r/b$. This relationship, Eq. 5.49, follows from Eqs. 5.21 and 5.29 and accounts only for the equilibrium elongations of the mensicus. As a result, it reaches a maximum in the vicinity of $Z \approx 1.86$, the largest stable deformation of the equipotential droplet.

In Fig. 5-10 we plot the surface charge ratio $\sigma/\epsilon_0 E_n^v$ across the span of the meniscus with its size B as a parameter. All calculations are carried out for $\chi = 10^{-3}$, $\psi = 40$, and the field/elongation corresponding to the turning point for the equipotential meniscus ($Z \to 1.86$). From the results it is clear that extensive swaths of the smaller menisci are very near full depletion of their interfacial charge while relaxation is only recovered in the vicinity of the anchoring point (the mid-plane) where the electrical field begins to vanish. Interestingly, even for the large menisci that are not producing much current we still see a modest degree of depletion near the tip, although it does not necessarily extend across much of the interface.

The fact that charge depletion is occurring is important because it means that the interface will begin to behave more like a dielectric than something that is perfectly conducting and equipotential. To illustrate this point, we define here an effective relative permittivity for the interface that is related to the vacuum field through

$$\left(\epsilon_r\right)^{eff} = \frac{E_n^v}{E_n^l} \tag{5.50}$$

which comes from the basic interfacial condition for a pure dielectric, $E_n^v = \epsilon_r E_n^l$. After noting that $E_n^l = j/k$ for the conduction-controlled meniscus and invoking Eq. 5.14 for the current density this becomes

$$\frac{\left(\epsilon_r\right)^{eff}}{\epsilon_r} = 1 + \chi \cdot \exp\left(\psi\left\{1 - B^{1/4}\sqrt{\hat{E}_n^v}\right\}\right) \tag{5.51}$$

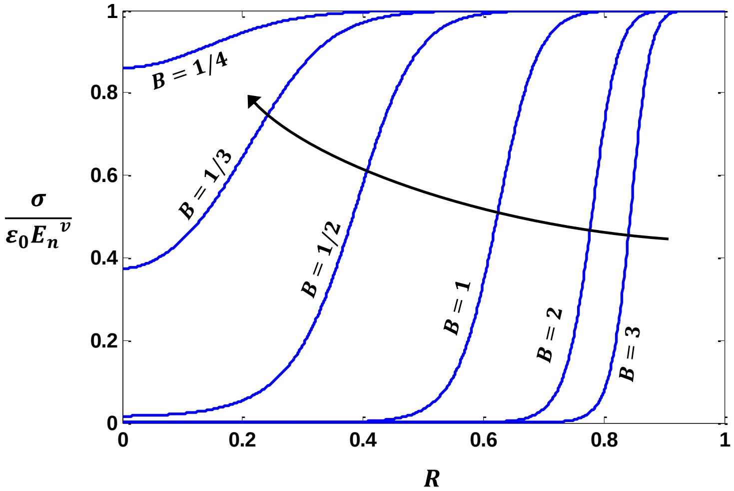

Figure 5-10: Ratio of interfacial charge to the normal component of the displacement field in vacuum (the fully relaxed value) across menisci of various sizes B in the vicinity of the turning point for an equipotential spheroid. The curves indicate that the smaller menisci, for which significant emission is observed (Fig. 5-9), are fairly depleted across much of the interface. For their large counterparts, a measure of depletion near the tip is also seen even though the currents they produce are more modest. This suggests that the interfaces could be giving way to dielectric behavior. All calculations assume $\chi = 10^{-3}$ and $\psi = 40$.

in dimensionless form. This relationship is plotted in Fig. 5-11 again at the equipotential turning point and with B as a parameter. Based on the curves it is clear that the smaller emitting droplets should behave like pure dielectric ones when the evaporation is strong. In view of this result, it makes sense to amend our initial hypothesis and admit the possibility that some of these droplets may trace paths through the $Z - \hat{E}_0$ plane that do not necessarily coincide with that of the limiting $\epsilon_r \to \infty$ or equipotential case. For example, when the field is low all droplets must obey the limiting elongation curve because no emission takes places. Providing that the initial droplet is small enough, emission will commence at an intermediate field (between $\hat{E}_0 = 0$ and $\hat{E}_0 \approx 0.228$) and the interface will start to behave more like a dielectric than a conductor, at least in areas that are local to charge depletion. As the first turning point is met, instability could be evaded as the droplet migrates to adjacent elongation curves. If the intrinsic permittivity of the fluid is somewhat high ($\epsilon_r \gtrsim 20$) instability will still ultimately be reached but at a higher $\hat{E}_0$. If it is fairly low, however ($\epsilon_r \lesssim 20$), it could be possible that the small droplet eventually traces one of the monotonically increasing elongation characteristics, which are apparently always stable, and never see a turning point. This would be rather amazing. We attempt to delineate one such possible trajectory in Fig. 5-12.

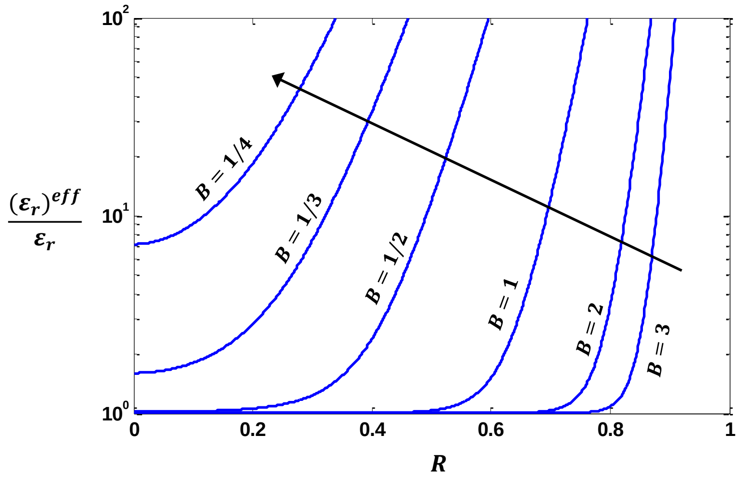

Figure 5-11: Ratio of effective permittivity to intrinsic permittivity across menisci of various sizes B near the turning point for an equipotential structure with $\chi = 10^{-3}$ and $\psi = 40$. As expected, the behavior of the smaller menisci may be very similar to pure dielectric droplets of fluid with the same intrinsic permittivity. Only near the anchoring point or mid-plane ($R \to 1$) where the field vanishes is conducting behavior recovered.

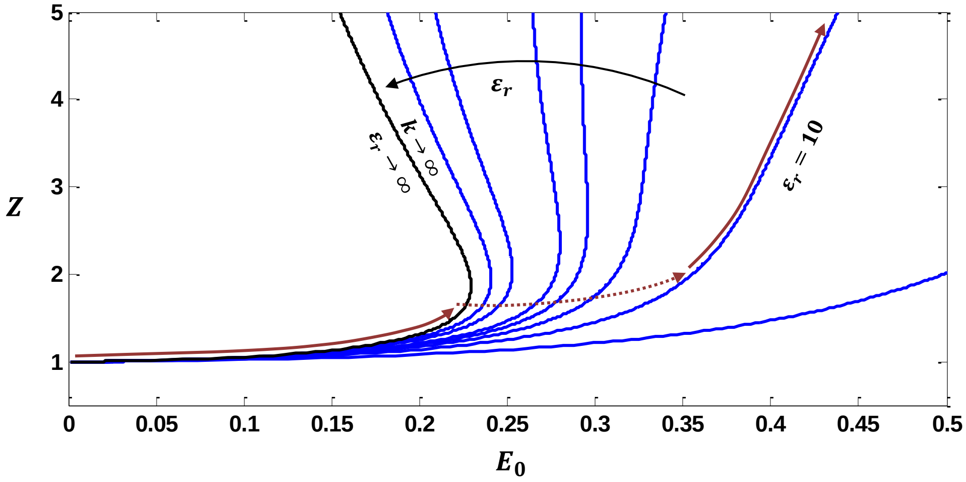

Figure 5-12: Notional path of a small, conduction-controlled meniscus through the equilibrium $\hat{E}_0 - Z$ plane. The conducting spheroid is initially relaxed for small fields and traces the limiting $\epsilon_r \to \infty$ curve. Emission commences as the dimensionless field is increased but before the first turning point is met. This results in a measure of charge depletion at the interface. Provided the depleted area is sufficiently broad, the meniscus begins migrating across adjacent elongation curves until it ultimately reaches the one corresponding to its intrinsic permittivity. In the pictured case, $\epsilon_r = 10$ for the fluid and the path of the droplet is delineated by the red line. The black arrow indicates the direction of increasing ϵ_r.

5.1.4 Discussion

The problem of the fixed-volume droplet is useful as a result of the fact that the attendant deformation modes closely resemble a family of prolate spheroids. A special system of coordinates makes electrical field solutions for these structures analytically convenient and we have shown that these can be used to study not only the equilibrium properties of the droplet but also the stability behavior. When the droplets follow the deformation curve of an equipotential meniscus we find that these characteristics result in evaporated currents on the order of what is often observed experimentally ($I \sim 10^{-7}$ A).

In spite of its convenience, the fixed-volume problem suffers several key issues. We briefly discuss these below.

- The first and foremost issue is that the present methods cannot resolve emission when there exists a disparity in the evaporation and meniscus anchor scales, i.e. when B is small. The literature would suggest that such a configuration is capable of supporting evaporation and so it stands to reason that we have yet to capture all of the important physics.

- We speculate in some cases that depletion of interfacial charge during emission could offer the droplets a mechanism through which instability behavior might be modified. Looking at the surface charge plots presented here, it would seem that the distribution of σ across the meniscus would in general be very complicated were that to occur. The present method is therefore unlikely to be sufficient for resolving such phenomena.

- The currents that we calculate as well as the properties of typical fluids point to something funny about the time scales for the fixed-volume problem. For example, consider that the flow rate out of the droplet is $\dot{m} \sim I(m/q)$ when emission is occurring. If $I \sim 10^{-7}$ A and $q/m \sim 10^{6}$ C/kg then this evaluates to $\dot{m} \sim 10^{-13}$ kg/s which at first appears very small. However, now consider that the total mass of the droplet is $m \sim \rho b_0^3$ where $\rho \sim 10^3$ kg/m^3 for most fluids and $b_0 \sim r^* \sim 10^{-8}$ - 10^{-9} m if emission is to actually occur. We can estimate the amount of time required for the drop to fully evaporate as $t \sim m/\dot{m}$ and find that this is but $t \sim 10^{-6}$ s. While 10^{-6} s might be long in comparison to the governing time scales (e.g. electrical relaxation) it is still very short in the grander scheme. Perhaps the fixed-volume droplet is not the best way to pose the evaporation problem.

- Finally, and perhaps most obviously, in practice there will often exist an hydraulic feed system capable of supplying the meniscus with fresh fluid in the event of evaporation. When that is the case, the volume of the droplet should not be constrained.

5.2 Free-volume problem

In practical situations it is often the case that an hydraulic feeding system is used to supply the meniscus with fresh fluid during evaporation. The particular system could be one of the emitter structures introduced early or anything capable of transporting fluid from an upstream reservoir. Unlike the previous problem, the nature of this architecture nullifies the volume constraint and permits the interface to adopt any shape that it needs, spheroidal or otherwise. In this section we will investigate the free-volume variation of the electrified meniscus problem but continue to focus on spheroidal morphologies in an effort to retain our analytic tools (see Fig. 5-13). Although the maintenance of spheroidal form factors will eventually lead to a non-trivial relationship between the feed pressure and the applied electric field, which is perhaps somewhat artificial, the results should still be insightful.

As for the mathematical framework, Eqs. 5.19 thru 5.21 for the emission properties of the fixed-volume droplet should still apply here. The remaining equation for a complete description of the interface is the one describing the stress balance at the tip (Eq. 5.18 in the fixed-volume case), which will require modification. We continue to observe the two-point stress balancing approach from Taylor [3] and recall that

$$P_{st}|_{mid} = \frac{\gamma}{b}\left(\frac{1+Z^2}{Z^2}\right) \tag{5.52}$$

for the surface tension at the mid-plane, which is also the hydrostatic pressure of the fluid as a result of the vanishing electrical traction. Since the lack of a volume constraint allows us to fix the anchor radius of the meniscus now, $b \to b_0$ in this expression. Similarly, the surface tension at the tip is

$$P_{st}|_{tip} = \frac{2\gamma Z}{b} \tag{5.53}$$

with $b \to b_0$. After substituting these into the stress balance we find that the dimensionless free-volume problem for a conducting fluid is governed by

$$\hat{E}_0^2\left[\frac{Z^2-1}{\frac{Z}{\sqrt{Z^2-1}}\ln\left(Z+\sqrt{Z^2-1}\right)-1}\right]^2 + \frac{1+Z^2}{2Z^2} - Z = 0 \tag{5.54}$$

$$\hat{I} = \frac{2\pi}{Z^{2/3}}\int_0^1 \hat{j}R\sqrt{\frac{1+R^2\left(Z^2-1\right)}{1-R^2}}\cdot dR \tag{5.55}$$

at the interface, which is also subject to

$$\hat{j} = \frac{\hat{E}_n^v/\epsilon_r}{1+\chi\cdot\exp\left(\psi\left\{1-B^{1/4}\sqrt{\hat{E}_n^v}\right\}\right)} \tag{5.56}$$

$$\hat{E}_n^v = \hat{E}_0\sqrt{\frac{1-R^2}{1+R^2\left(Z^2-1\right)}}\left[\frac{Z^2-1}{\frac{Z}{\sqrt{Z^2-1}}\ln\left(Z+\sqrt{Z^2-1}\right)-1}\right] \tag{5.57}$$

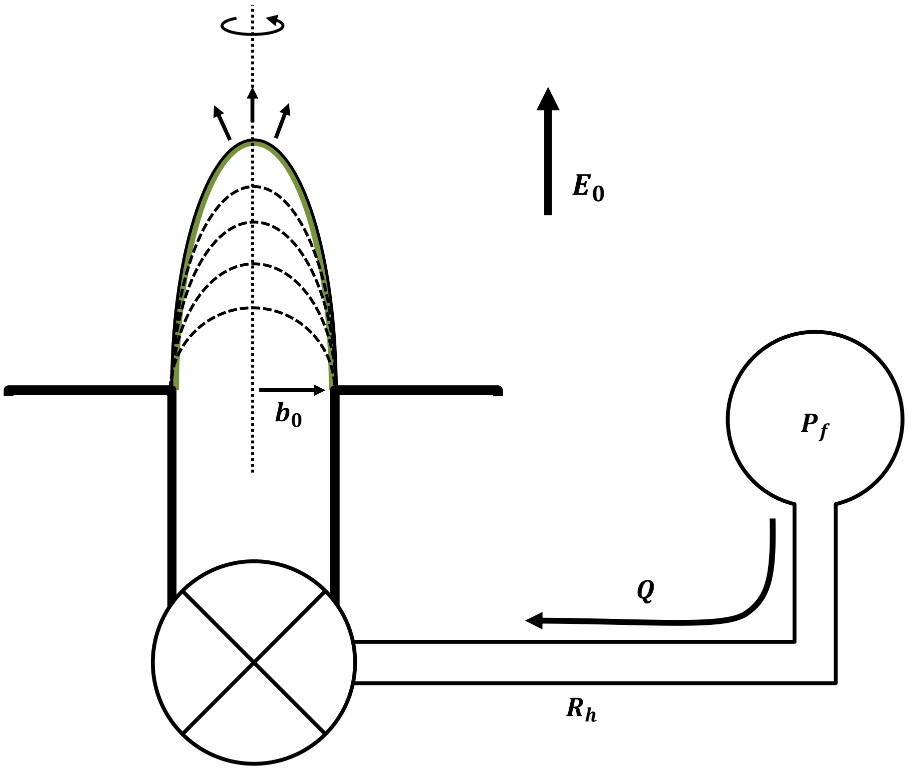

Figure 5-13: Diagram of free-volume spheroid problem. A meniscus is attached to some form of plate or the end of a tube and maintains a constant contact line radius, b_0. Elongation of the meniscus in response to the externally-applied field E_0 results in a sequence of growing spheroids (dashed curves) for which the internal fluid volume is no longer conserved. This is facilitated by communication of the meniscus with a liquid feeding system. The feeding system may comprise a fluid reservoir that is held at an arbitrary pressure, P_f, and a feeding line with a non-zero characteristic impedance, R_h. In the event of field evaporation from the meniscus tip, the interaction of the attendant flow rate Q with this impedance could create a corresponding pressure drop through the line. Also note that in order for the menisci to remain indefinitely spheroidal for this "free-volume" problem, a non-trivial relationship between the applied field E_0 and the pressure of the liquid immediately inside the meniscus, P_l (not pictured, but equivalent to P_f when $Q \to 0$ in the absence of emission), must be observed.

Notice that these relationships are nearly identical to those of the better-known fixed-volume problem, save for a slight modification in the form of the stress equation (Eq. 5.54). The extent to which this modifies the overall results will be examined in the forthcoming sections.

It is also interesting to highlight the fact that $Z = f(E_0)$ and $P_l = g(Z)$, which suggests that P_l is a function of the imposed electrical field rather than an arbitrary pressure that can be applied with the feeding system. Specifically, $P_l = P_l(E_0)$ is the relationship ensuring that the meniscus remains spheroidal at all times. The volume of the meniscus is similarly beholden to the field and may be of interest to us in certain instances. In general, it takes the form

$$V = \frac{2\pi}{3} a b^2 \tag{5.58}$$

When we nondimensionalize by the nominal value corresponding to $Z = 1$, or $V_0 = 2\pi/3 \cdot (b_0)^3$, this becomes

$$\hat{V} = Z \tag{5.59}$$

assuming, of course, that a fixed anchor radius b_0 prevails. Finally, we would be remiss without mentioning that in general $Z \in [0, \infty)$ for the free-volume interface, which includes a family of blunt spherical sections corresponding to $Z < 1$. We do not, however, anticipate that the attendant electrical fields will be of sufficient strength for evaporation when such equilibria prevail, unless the menisci are exceedingly small ($B \gg 1$). In view of this we will restrict our attention to cases of prolate spheroids in what follows.

5.2.1 Equilibria for conducting and dielectric menisci

As with the fixed-volume case we will study the equilibria for conducting and pure dielectric menisci simultaneously. After substituting the more general expression for the electric pressure acting on a dielectric we arrive at the stress balance

$$\frac{\hat{E}_0^2\left[\epsilon_r\left(\epsilon_r-1\right)\right]}{\left[1-\frac{\epsilon_r-1}{Z^2-1}\left(1+\frac{Z}{\sqrt{Z^2-1}}\cdot\ln\left\{\frac{1}{Z+\sqrt{Z^2-1}}\right\}\right)\right]^2}+\frac{1}{2}\left(\frac{1+Z^2}{Z^2}\right)-Z=0 \tag{5.60}$$

which is defined at the tip of the meniscus. We solve this relationship by arranging it so that $\hat{E}_0$ is the dependent variable

$$\hat{E}_0^2=\frac{\left[Z-\frac{1}{2}\left(\frac{1+Z^2}{Z^2}\right)\right]}{\epsilon_r\left(\epsilon_r-1\right)}\left[1+\frac{\epsilon_r-1}{Z^2-1}\left(\frac{Z}{\sqrt{Z^2-1}}\cdot\ln\left\{Z+\sqrt{Z^2-1}\right\}-1\right)\right]^2 \tag{5.61}$$

The equilibrium $\hat{E}_0 - Z$ relationship is plotted in Fig. 5-14 for select values of fluid permittivity. From the results it is obvious that the equilibria for the free-volume

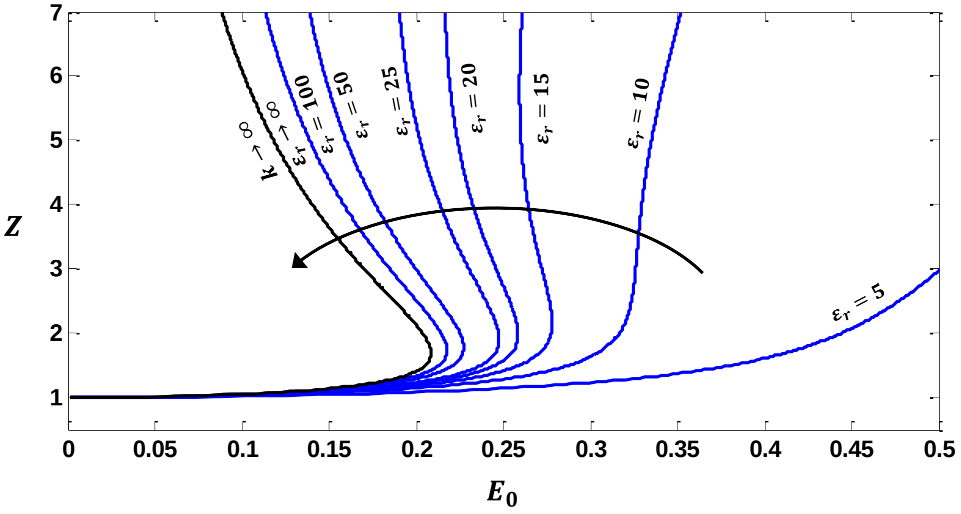

Figure 5-14: Equilibrium elongation curves as a function of the dimensionless field for free-volume menisci of pure dielectric fluids with various permittivities ϵ_r. The limiting $\epsilon_r \to \infty$ case is mathematically equivalent to case of a conducting fluid with an equipotential interface. As with the fixed-volume problem, turning points are seen for permittivities above a certain threshold. The results are slightly shifted but still within the same quantitative neighborhood.

problem are very similar to their fixed-volume counterparts, if not slightly shifted. For example, consider the elongation curve for the limiting $\epsilon_r \to \infty$ case, which is delineated in Fig. 5-15 and plotted alongside the corresponding one from the fixed-volume solution. Both the dimensionless field at the first turning point ($\hat{E}_0 \approx 0.21$) and the corresponding elongation ($Z \approx 1.68$) occur at incrementally lower but still similar values.

As we have pointed out, for the free-volume problem there is a non-trivial relationship between the hydraulic pressure that must be applied by the feeding system and the imposed electric field $\hat{E}_0$. This is plotted for select ϵ_r in Fig. 5-16. For small fields the elongation $Z \to 1$ while the fluid pressure $\hat{P}_l \to 1$ also. This says that the feed system must apply a force equivalent to the capillary pressure when the meniscus is perfectly hemispherical, as we would expect. For nonzero increasing $\hat{E}_0$ the fluid pressure begins to drop and ultimately asymptotes to $\hat{P}_l = 0.5$ in all cases when $Z \to \infty$. Notice that the dielectrics ϵ_r with multi-valued elongation curves also exhibit multi-valued $\hat{P}_l$ curves.

Finally, we will examine here the distribution of the various stresses across the interface as Taylor has done for the fixed-volume problem (see [3]). Given that we are balancing the stresses at only two locations, the tip and the mid-plane, it makes sense that small but nonzero pressure differences could arise at points in between. To check these, consider the pressure balance

$$\Delta P\left(R\right) = P_e\left(R\right) + P_l - P_{st}\left(R\right) \tag{5.62}$$

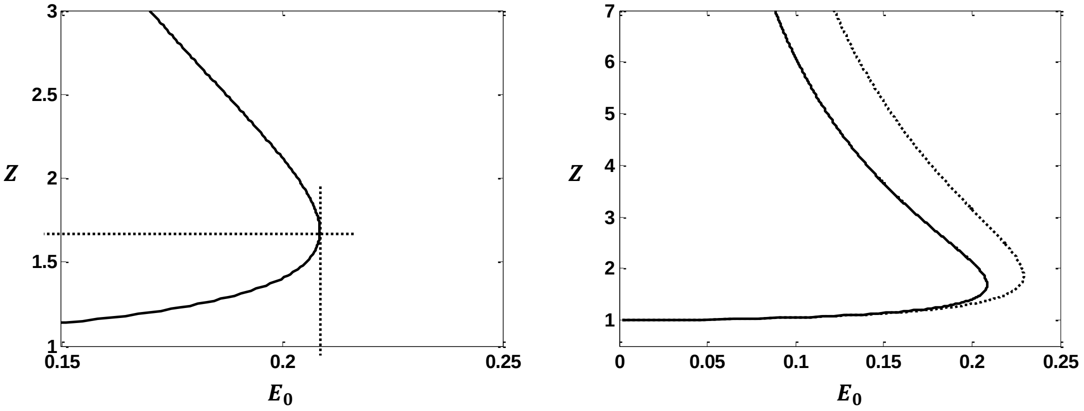

Figure 5-15: Equilibrium elongation characteristics as a function of the dimensionless field $\hat{E}_0$. (**Left**) Detail for the turning point of the limiting $\epsilon_r \to \infty$ case. This occurs in the vicinity of $\hat{E}_0 \approx 0.21$ where the elongation is $Z \approx 1.68$. (**Right**) Comparison of the limiting $\epsilon_r \to \infty$ elongation curves for the free-volume (solid) and fixed-volume (dashed) cases. The free-volume solution is slightly shifted with respect to its fixed-volume counterpart.

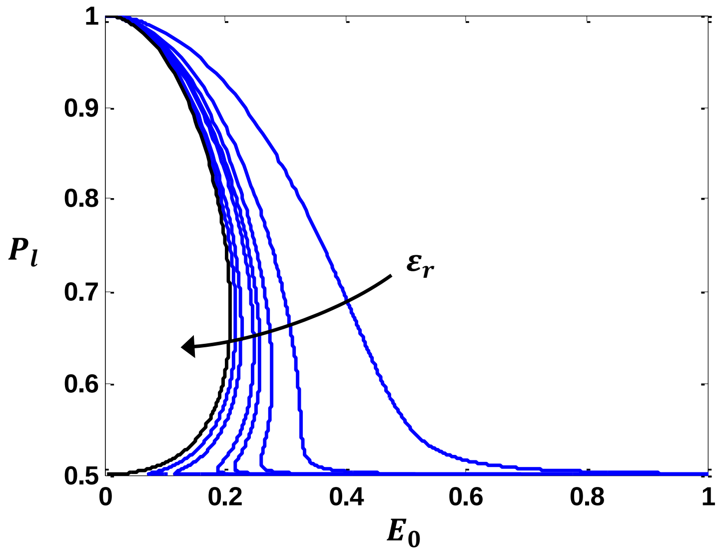

Figure 5-16: Dimensionless fluid pressure as a function of dimensionless electric field $\hat{E}_0$ for pure dielectric menisci of various permittivity ϵ_r. Values of ϵ_r = 5, 10, 15, 20, 25, 50, 100, and ∞ are represented, with the arrow indicating the direction of increasing magnitude. For small fields, $\hat{E}_0 \to 0$, the liquid pressure converges to $\hat{P}_l = 1$ in all instances. This is the capillary pressure and corresponds to the case of a hemispherical interface. As the field is increased the pressure must be lowered in order to maintain the spheroidal morphology, asymptoting at $\hat{P}_l \to 0.5$ for $Z \to \infty$. The multi-valued elongation curves are also typified by multi-valued $\hat{P}_l$ curves.

written as a function of $R = r/b_0$, a parameter describing points along the spheroidal interface. Let us now expand each of the terms on the right-hand side individually. For the electric pressure, we can see from Eq. 5.21 how the normal component of the vacuum field at the interface varies with R

$$E_n^v \propto \sqrt{\frac{1-R^2}{1+R^2\left(Z^2-1\right)}} \tag{5.63}$$

This is to be appended to the electric pressure expression of Eq. 5.27 after squaring it (recall $P_e \propto (E_n^v)^2$)

$$\hat{P}_e = \frac{\hat{E}_0^2\left[\epsilon_r\left(\epsilon_r-1\right)\right]}{\left[1-\frac{\epsilon_r-1}{Z^2-1}\left(1+\frac{Z}{\sqrt{Z^2-1}}\cdot\ln\left\{\frac{1}{Z+\sqrt{Z^2-1}}\right\}\right)\right]^2}\cdot\left[\frac{1-R^2}{1+R^2\left(Z^2-1\right)}\right] \tag{5.64}$$

In order to isolate the equilibrium elongations we can look to Eq. 5.61 and substitute for $\hat{E}_0^2$. This yields the result

$$\hat{P}_e\left(R\right) = \left[Z-\frac{1}{2}\left(\frac{1+Z^2}{Z^2}\right)\right]\left[\frac{1-R^2}{1+R^2\left(Z^2-1\right)}\right] \tag{5.65}$$

The liquid pressure, by contrast, is spatially uniform

$$\hat{P}_l\left(R\right) = \frac{1}{2}\left(\frac{1+Z^2}{Z^2}\right) \tag{5.66}$$

For the surface tension we can invoke its general form, $P_{st} = -\gamma\nabla\cdot\vec{n}$ where $\vec{n}$ is the unit normal on the interface, and consult the appendix where we find

$$\nabla\cdot\vec{n} = \frac{\left(1+h_r^2\right)h_r + r\cdot h_{rr}}{r\left(1+h_r^2\right)^{3/2}} \tag{5.67}$$

for axisymmetric cylindrical space. Here, h_r and h_{rr} are the first and second spatial derivatives given by Eqs. 5.5 and 5.6. Substituting for these yields

$$\nabla\cdot\vec{n} = -\frac{Z}{b_0}\frac{2+R^2\left(Z^2-1\right)}{\left[1+R^2\left(Z^2-1\right)\right]^{3/2}} \tag{5.68}$$

and so the dimensionless surface tension across the interface is simply

$$\hat{P}_{st}\left(R\right) = \frac{Z}{2}\frac{2+R^2\left(Z^2-1\right)}{\left[1+R^2\left(Z^2-1\right)\right]^{3/2}} \tag{5.69}$$

To visualize the net pressure we plot the ratio

$$\frac{\Delta P\left(R\right)}{P_{st}\left(R\right)} = \frac{P_e\left(R\right)+P_l}{P_{st}\left(R\right)} - 1 \tag{5.70}$$

in Fig. 5-17, which compares the net pressure at points across the interface to the

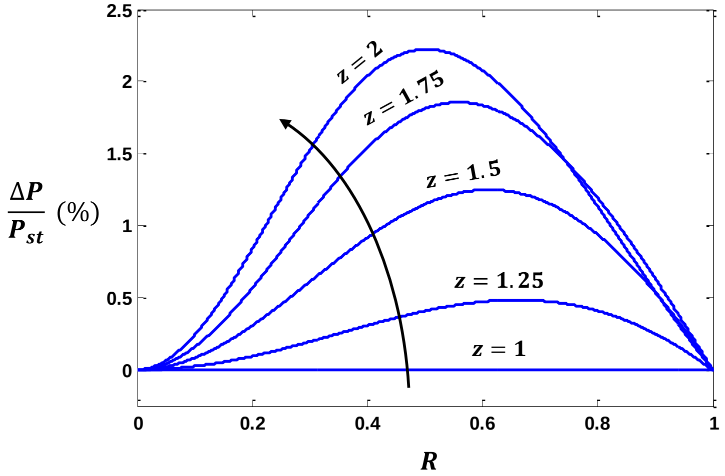

Figure 5-17: Percentage net pressure along the interface of a spheroidal protrusion for several equilibrium elongations. While ΔP is an increasing function of the elongation it is never very large for the range of Z under consideration. As a result, it is likely that real menisci subjected to similar stressing conditions would adopt very similar (nearly spheroidal) shapes.

magnitude of the local surface tension. We do this for select equilibrium elongations Z in the vicinity of and below the first turning point for the equipotential case. The results show that the maximum pressure difference occurs somewhere along the meniscus where $R \approx 1/2$ and that it is apparently an increasing function of Z. It does not, however, grow to appreciable values. This would seem to support the notion that real menisci subjected to similar stressing conditions would likely adopt very similar shapes. Also, note that $\Delta P \to 0$ at the balancing points $R = 0$ and $R = 1$ like we would expect and that similar curves for the fixed-volume case can be found elsewhere [3].

5.2.2 Stability

The stability condition for the free-volume problem is the same as before

$$\left[\frac{\partial P_e}{\partial Z} + \frac{\partial P_l}{\partial Z} - \frac{\partial P_{st}}{\partial Z}\right]_{E_0(Z_{eq})} = \left.\frac{\partial \Delta P}{\partial Z}\right|_{E_0(Z_{eq})} < 0 \qquad (5.71)$$

The individual terms, however, require slight modification. After discarding the volume constraint we find

$$\frac{\partial \hat{P}_e}{\partial Z} = \frac{-2\left(\epsilon_r - 1\right)\frac{Z}{(Z^2-1)^2}\left[Z - \frac{1}{2}\left(\frac{1+Z^2}{Z^2}\right)\right]\cdot\left[3 - \frac{\ln\left\{Z+\sqrt{Z^2-1}\right\}}{\sqrt{Z^2-1}}\left(\frac{2Z^2+1}{Z}\right)\right]}{1 + \frac{\epsilon_r-1}{Z^2-1}\left(\frac{Z}{\sqrt{Z^2-1}}\ln\left\{Z + \sqrt{Z^2-1}\right\} - 1\right)} \qquad (5.72)$$

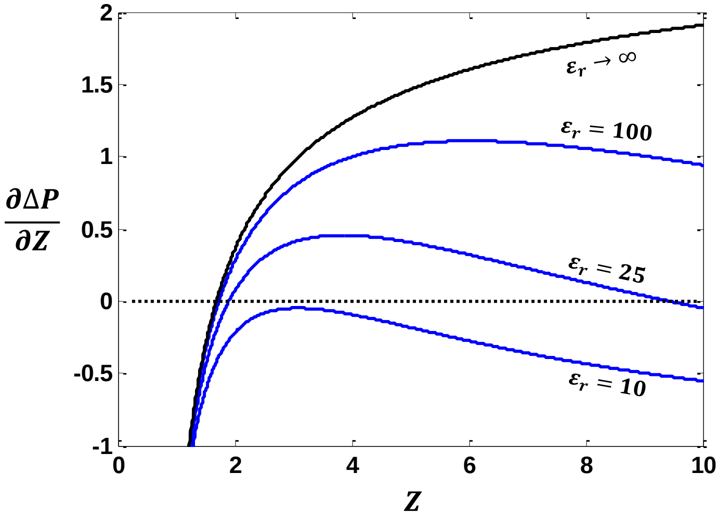

Figure 5-18: Derivative of the dimensionless net pressure $\Delta\hat{P}$ as a function of equilibrium elongation Z. The elongations for which $\partial(\Delta\hat{P})/\partial Z$ is positive are unstable while those for which it is negative are stable. As with the fixed-volume problem, the turning point for the limiting $\epsilon_r \to \infty$ case marks the transition from stable equilibria (lower solution branch) to unstable equilibria (upper solution branch).

$$\frac{\partial \hat{P}_l}{\partial Z} = -\frac{1}{Z^3} \tag{5.73}$$

$$\frac{\partial \hat{P}_{st}}{\partial Z} = 1 \tag{5.74}$$

Notice that the change in liquid pressure for increasing Z is now negative-definite, which was not the case for the fixed-volume problem. This is a byproduct of the anchor fixation. In Fig. 5-18 we plot the derivative of the dimensionless pressure, $\partial(\Delta\hat{P})/\partial Z$, while in Fig. 5-19 we show a map of the unstable regions. From the results we can see that the stability behavior is qualitatively similar to that of the fixed-volume problem, where stability was conferred only for elongations residing along the parts of the equilibrium characteristics with positive slopes.

5.2.3 Field evaporation

The equilibrium and stability results for the free-volume problem are very similar to those of its fixed-volume counterpart, and so it stands to reason that the emission properties will also be akin. Unfortunately, this suggests that B will need to be at least on the order of unity, if not somewhat higher, in order for the attainable electric fields at the spheroidal interface to begin approaching E^*. In other words, the size b_0 of the meniscus still cannot be much larger than that of the characteristic emission zone r^*.

Consider a case involving a spheroidal meniscus with $b_0 \gg r^*$. Even if emission does somehow take place, the region of charge depletion will be very small and most

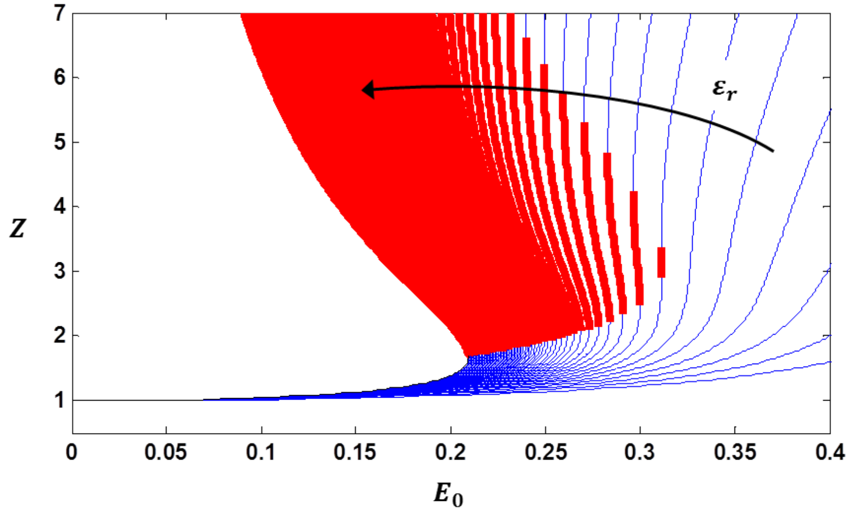

Figure 5-19: Map of instability region within the equilibrium $\hat{E}_0 - Z$ plane. The unstable equilibria coincide with the sections of the elongation curves that have negative slope.

of the interface will remain in the vicinity of electrical relaxation. As a result, we can approximate the structure as an equipotential and assume that it obeys the limiting $\epsilon_r \to \infty$ elongation curve. From Eq. 5.21 we have that $E_n^v \sim E_c$ at the tip of the meniscus when $Z \sim 1.7$ and $\hat{E}_0 \sim 0.2$ near the turning point. The ratio of E_c to the characteristic emission field E^* is proportional to the size parameter, $E_c/E^* \sim \sqrt{B}$, which says that emission cannot be supported when B is small, just as expected. While this prevents us from quantitatively explaining emission for situations involving a scale disparity, as is often the case in practice, it is still useful for narrowing the part of the parameter space across which evaporation might occur. For example, the value of the liquid pressure at the turning point, which corresponds to the maximum vacuum field, is $\hat{P}_l \sim 0.67$. Given that this value is inversely proportional to the field (the liquid pressure goes up when the field goes down, and vice versa), this is very likely an upper bound for the allowable fluid pressure. Under real circumstances, and when other conditions are appropriate, evaporation may occur when $\hat{P}_l$ is lower than ~ 0.67 but certainly not when it is higher.

Now that we have an upper bound for the pressure of the fluid in the meniscus we can draw a connection to the pressure that is used by the feed system to provide a supply of liquid. These two are numerically equivalent when no evaporation is ongoing but

$$P_l \sim P_f - Q \cdot R_h \tag{5.75}$$

when there is flow. Here, P_f is the feed pressure in the fluid reservoir, Q is the volumetric flow rate being pumped by the feed system, and R_h is its characteristic hydraulic impedance (recall Fig. 5-13). In the event that the feed system is a long, slender tube (a capillary, perhaps), the impedance is

$$R_h \approx \frac{8\mu L}{\pi r^4} \tag{5.76}$$

as a result of Poiseuille, where L is the length of the tube, r is its radius, and μ is the dynamic viscosity of the fluid. After noting the relationship between the current and the volumetric flow, $Q \sim I\rho^{-1}(q/m)^{-1}$, we rearrange Eq. 5.75 to find

$$\hat{P}_l \sim \hat{P}_f - \hat{I} \cdot \underbrace{\left[\frac{kR_h}{\rho\,(q/m)}\sqrt{\frac{b_0^5}{\epsilon_0\gamma}}\right]}_{\hat{R}_h} \tag{5.77}$$

Recall from earlier that the dimensionless current is

$$\hat{I} = \frac{I}{kE_c b_0^2} \tag{5.78}$$

For a fluid with $k \sim 1$ S/m, $\gamma \sim 5{\cdot}10^{-2}$ N/m, and $b_0 \sim 10^{-5}$ - 10^{-6} m, the dimensionless current could be anywhere from $\hat{I} \sim 10^{-3}$ - 10^{-5} when $I \sim 10^{-6}$ - 10^{-8} A. The hydraulic impedance R_h is arbitrary but could range from nearly zero all the way to $R_h \sim 10^{22}$ N-s/m^5, if not higher. When $\rho \sim 10^3$ kg/m^3 and $q/m \sim 10^6$ C/kg, this could perhaps put $\hat{R}_h$ near 10^8 in extreme cases.

In Fig. 5-20 we plot the relationship between $\hat{P}_f$ and $\hat{R}_h$ when $\hat{P}_l \rightarrow 0.67$ with I as a parameter. This is for a fluid with the intrinsic properties listed above and an anchor radius of $b_0 = 10^{-5}$ m. The individual curves correspond to a selection of typical currents and loosely demarcate the upper bounds of the allowable feeding pressure when pure ion evaporation is the objective. Pressures above the curves will lead to stresses in the meniscus higher than the limiting $\hat{P}_l = 0.67$ and likely precipitate destabilization. Conversely, a subspace of the region below the curves could confer stable ion evaporation, although the present methods are insufficient for accurately outlining it.

5.2.4 Discussion

The equilibria and stability properties of the free-volume problem are quantitatively similar to those of its fixed-volume counterpart, though slightly shifted. As a result, the emission behavior is also akin and suggests that menisci with spheroidal form factors are incapable of supporting evaporation when a disparity in scales exists, i.e. when B is much less than unity. This is unfortunate because it precludes the present methods from describing important phenomena from the literature, where it is believed that currents as high as hundreds of nA are possible with ionic liquids even when b_0 is orders of magnitude larger than r^* ($B^{-1} \sim 10^2$ - 10^3, perhaps, as b_0 can be tens of microns).

To further underscore the deficiencies of the analytical spheroid approach, we might revisit the work of Romero-Sanz [29] where a pure ion current of $\sim$ 200 nA was reported for the popular ionic liquid EMI-BF4 ($k \sim 1$ S/m; $\gamma \sim 5{\cdot}10^{-2}$ N/m; $\mu \sim 4{\cdot}10^{-2}$ Pa-s; $q/m \sim 10^6$ C/kg). Consider that the emission configuration involved

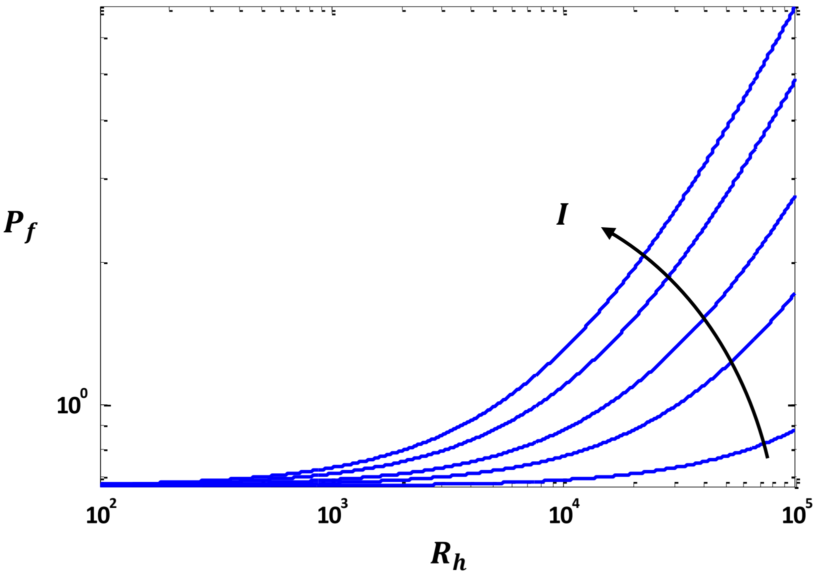

Figure 5-20: Relationship between $\hat{P}_f$ and $\hat{R}_h$ at the limiting liquid pressure $\hat{P}_l = 0.67$ for a fluid with typical ionic liquid properties. The individual curves correspond to currents of 10 nA, 50 nA, 100 nA, 200 nA, and 300 nA while the arrow indicates the direction of increasing magnitude. These represent estimates for the upper bounds on the allowable feed pressure for ion evaporation.

a ~ 1400V bias stressing a b_0 =10^{-5} m capillary extending approximately L =$3{\cdot}10^{-1}$ m. The upstream end of the tube connected to a reservoir where a P_f =3700 Pa pressure (~ 28 Torr) was used to drive the prevailing flow. Based on these numbers we calculated a dimensionless feed pressure of $\hat{P}_f \approx 0.37$, which is already below both the estimated maximum of 0.67 and the minimum of 0.5 that is asymptotically approached by spheroids with strong elongation. The modest impedance of the tube ($R_h \approx 3{\cdot}10^{18}$ N-s/m^5 $\Rightarrow \hat{R}_h \approx 1500$) did not substantially modify the pressure of the fluid in the meniscus ($\hat{I} \approx 4{\cdot}10^{-5} \Rightarrow \hat{I} \cdot \hat{R}_h \approx 6{\cdot}10^{-2}$), but the fact that $\hat{P}_l$ was well below 0.5 points to the likelihood that a very different deformation mode had been activated. Furthermore, if we estimate that the driving field for the capillary (which is admittedly a little different than the one for the flat plate configuration we have considered) might go like $E_0 \sim V/b_0$, then we calculate $E_0 \sim 1400{\cdot}10^5$ V/m and the dimensionless strength $\hat{E}_0 \sim 3$, which is quite amazing! Compare this to the field $\hat{E}_0 \approx 0.2$ at the turning point of the equipotential spheroid.

It should be obvious at this point that the analytical approach is incapable of sufficiently resolving the physics that are important to ion evaporation. The spectrum of potential deformation modes is presumably very rich and not restricted to the small subset of spheroidal morphologies that have been considered thus far. In the remaining chapters we will attempt to reconcile the discrepancies between our theoretical predictions and empirical observations through numerical recourse.

Chapter 6

Generalized free-volume problem

Owing to the deficiencies of the spheroidal approach we seek to generalize the model of the electrified ionic liquid meniscus. Note that this will also afford us the opportunity to incorporate the additional physics outlined in previous chapters (e.g. viscous stresses and Ohmic heating), which could be important. The model will involve a free-volume fluid column that is attached to a flat plate of finite thickness and biased with respect to a downstream surface so that a uniform electric field can prevail far from the liquid-vacuum interface (Fig. 6-1). Technically speaking, the plate could be either a perfect conductor or an ideal dielectric (no free charges) in order to capture effects related to the choice of substrate material. As recent studies on porous glass and aluminum oxide show, e.g. Coffman [58], it is believed that these could play a potentially measurable role in the process of emission (see Lozano [74] for estimates related to dielectric anchoring media of relative permittivity $\epsilon_r \sim 5$ - 10, which are typical of many porous ceramics [75, 76]). In terms of the liquid column, it will obey a constant contact line at the interface with the plate, i.e. it will have a prescribed radius, while the contact angle will remain unconstrained. This is essentially the situation that prevails for a well-defined tube which terminates in the plane of a perfectly non-wetting plate. In what follows, we will attempt to use the combination of these conditions for simulating steady ion emission from electrified ionic liquids over a range of field and media conditions.

To formulate the problem we will model the ionic liquid populating the meniscus as a simple quasi-neutral fluid so that we may utilize the Navier-Stokes and Laplace equations in the fluid bulk. While these physics may or may not be admissible in the charge separation layer that develops at the interface when an electric field is applied, this region should be small. From Poisson, observe that

$$\Delta E \sim \frac{-e\left(n_+ - n_-\right)}{\epsilon}\delta \tag{6.1}$$

local to the interface. In the limit of complete charge separation the thickness of the non-neutral layer goes something like $\delta \sim \epsilon E/\left(en_+\right)$, which evaluates to submolecular scale ($\delta \sim 10^{-10}$ m) when fields characteristic of ion emission ($E \sim 10^9$ V/m) and bulk number densities ($n_+ \sim 10^{28}$ m^{-3}) are present, and remains small even in cases when the latter is somehow rarefied. This suggests that we can view

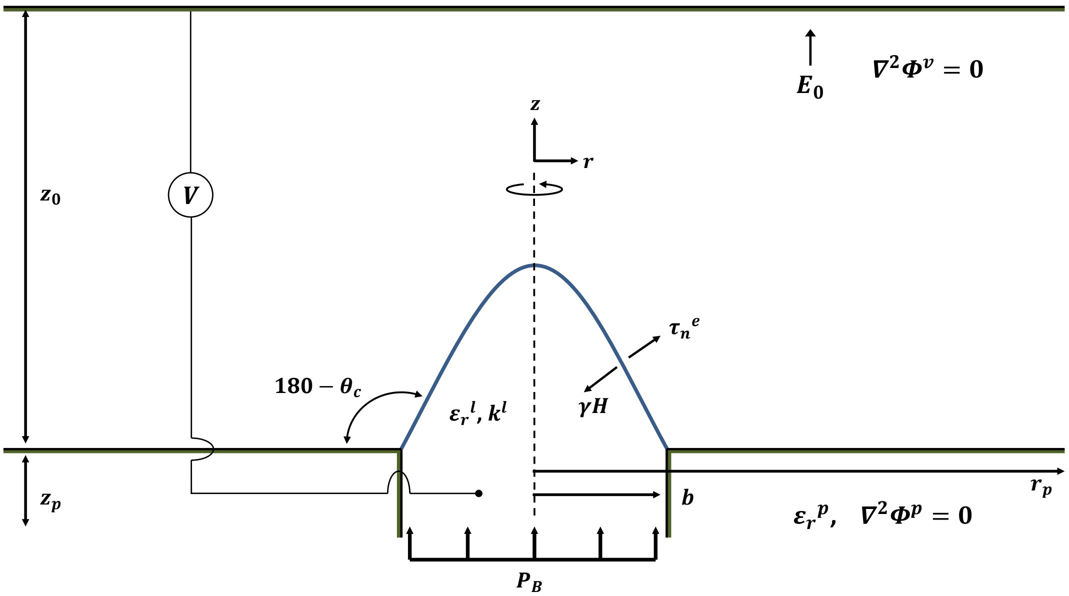

Figure 6-1: Diagram of solution domain for an electrified ionic liquid meniscus model. Two Laplacian regions bracket a fluid interface of prescribed waist radius, b_0. The anchoring plate has thickness z_p, radius r_p, and can be either a perfect conductor or ideal dielectric. Fluid enters the region of the plate at a pressure P_B, based on upstream conditions, and feeds a meniscus in mechanical equilibrium.

the electrified layer as an infinitesimal transition region bracketed by vacuum on one side and bulk fluid on the other. The nominal jump condition for the charge density $\sigma = \epsilon_0 E_n^v - \epsilon E_n^l$, where E_n^v is the normal component of the field on the vacuum side and E_n^l is normal component on the liquid side, is then easily invoked. The same is true of Ohm's law for the fluid, $j^l = kE^l$, where k is the bulk conductivity (Si/m).

The structure of the following sections is designed to introduce a set of equations that form a rigorous and coherent mathematical framework while also outlining a feasible approach for implementing the requisite numerics. In the sections that immediately follow we start by presenting the full complement of physical equations in their dimensional forms. The appropriate boundary conditions are derived and discussed where necessary, after which we offer a collection of logical scales and use them to nondimensionalize the problem. Several substrate considerations are then investigated as a means of abbreviating the rather rich parameter space that results. Finally, we develop a conceptual approach for solving the multiphysical problem in a self-consistent manner and discuss the way in which it might be integrated with Comsol, a commercial finite-element package.

6.1 Full equation set

The full equation set is developed here by first investigating the bulk equations and then deriving the corresponding boundary conditions. Physical exposition is offered where necessary, as several of the latter can be sources of confusion.

6.1.1 Bulk physics

Vacuum & plate regions

We start by considering the vacuum and plate regions, both of which are governed by Laplace

$$\nabla^2\Phi^v = 0 \tag{6.2}$$

$$\nabla^2\Phi^p = 0 \tag{6.3}$$

For the former, this owes to the fact that we are choosing to explicitly neglect space charge effects *a priori*, as these would require iterative and possibly expensive calculations. They would ideally be accounted for; however, from the earlier chapters we recall that $E_{sc}/E^* \sim 0$ is likely a good approximation in most instances. Laplace, therefore, seems to be justified here, especially in view of the anticipated numerical difficulties. Also note that the superscripts v, p, and l will henceforth be used to distinguish the vacuum, plate, and liquid regions, respectively.

Liquid region

The fluid region is somewhat more complicated in that it will involve coupled electrical, hydrodynamic, and heat transfer relationships when we choose to invoke all of the contributing physics that we have identified to this point. For example, the governing equation for the electrical effects should be charge conservation, $\nabla \cdot \vec{j} = 0$ where $\vec{j}$ is the current density vector. From Ohm we have that $\vec{j} = k\vec{E}^l$ and so

$$\nabla \cdot \left(k\vec{E}^l\right) = 0 \tag{6.4}$$

is in general the appropriate relationship for charge conservation. When there is no heating of the fluid, notice that the electrical conductivity of the fluid should be constant, i.e. $k \rightarrow k_0$ where k_0 is the nominal value (S/m) at some reference temperature T_0. When this is the case, charge conservation $\nabla \cdot \vec{j} = 0$ is simply reduced to Laplace. Recall that in the present case, however, we wish to incorporate heating effects and so the more general relationship, Eq. 6.4, should apply more strictly as it allows for $k = k(T)$.

For the hydrodynamics, it stands to reason from our Reynolds number estimates that the Stokes relationship, $\nabla p = \nabla \cdot (\mu \nabla \vec{u})$, should be a very good approximation to the relationship governing the flow. Unfortunately, the finite-element (FEM) package available to us (Comsol) does not support perfectly creeping flow and so we will be forced to retain the inertial term in the Navier-Stokes momentum equation. While this is not a substantial issue (indeed, the inertial term could offer incrementally better accuracy), it is possible that it could eventually slow our calculations. Nevertheless, after invoking mass conservation for the fluid ($\rho \to \rho_0$, a constant) we find that its motion must obey

$$\nabla \cdot \vec{u} = 0 \tag{6.5}$$

$$\rho \left(\vec{u} \cdot \nabla\right) \vec{u} = \nabla \cdot \left[-p\boldsymbol{I} + \boldsymbol{\tau}\right] \tag{6.6}$$

where $\vec{u}$ is the velocity vector of the flow and p is the hydrostatic pressure. Note that these equations assume that the flow is time-independent, as it should be for the steady evaporation solutions we are seeking. The viscous stress tensor, $\boldsymbol{\tau}$, relates the strain rate of the flow to its viscous forces. For Newtonian fluids it is given by

$$\boldsymbol{\tau} = \mu \left[\nabla\vec{u} + \left(\nabla\vec{u}\right)^T\right] \tag{6.7}$$

which can be expanded in several coordinate systems of interest (see appendix).

We also endeavor here to account for effects due to heating in the fluid, which we could be important as we have already shown. To achieve this we first require a thermal balance that can describe the spatial distribution of steady temperatures. Owing to the motion of the fluid, which is of course a prerequisite for Ohmic heating, both conduction and convection are capable of transporting thermal energy. In view of this, the appropriate balance should be

$$\rho c_p \left(\vec{u} \cdot \nabla T\right) = k_T \nabla^2 T + \dot{q} \tag{6.8}$$

where c_p is the heat capacity of the fluid at constant pressure (J/kg-K), T is the temperature (K), k_T is the intrinsic thermal conductivity (W/m-K), and $\dot{q}$ is the internal generation rate (W/m^3). Note that this assumes a constant isotropic k_T, which should roughly be the case for many ionic liquids. If the generation is purely Ohmic (we will ignore viscous generation, which should be weak as a result of the tenuous flow), then $\dot{q} = j^2/k$ where j is the local current density (A/m^2). After substituting this we arrive at

$$\nabla^2 T + \frac{1}{k_T}\frac{j^2}{k} - \frac{\rho c_p}{k_T}\left(\vec{u} \cdot \nabla T\right) = 0 \tag{6.9}$$

which is our final working form for the thermal balance.

6.1.2 Interfacial and boundary conditions

Liquid-vacuum interface

The normal and tangential components of the stress acting on the fluid interface are, respectively

$$\boldsymbol{\tau}_n^e - \vec{n} \cdot \boldsymbol{\tau} \cdot \vec{n} = \gamma \nabla \cdot \vec{n} \tag{6.10}$$

$$\vec{t} \cdot \boldsymbol{\tau} \cdot \vec{n} = \boldsymbol{\tau}_t^e \tag{6.11}$$

Here, $\boldsymbol{\tau}$ is the viscous tensor and $\boldsymbol{\tau}\cdot\vec{n}$ is the fluid traction vector $\vec{T}$ on the interface where $\vec{n}$ is the unit normal (note that $\vec{t}$ is the unit tangent). The factors $\vec{n}\cdot\boldsymbol{\tau}\cdot\vec{n}$ and $\vec{t}\cdot\boldsymbol{\tau}\cdot\vec{n}$ are, therefore, the projections of the traction vector on either direction. The electrical stress $\boldsymbol{\tau}^e$ follows from the Maxwell tensor (see, for example, Landau & Lifshitz [77], Melcher [78], Zahn [79])

$$\boldsymbol{\tau}^e_{ij} = \epsilon E_i E_j - \frac{\epsilon}{2}\delta_{ij} E_k E_k \tag{6.12}$$

where the repeated indices in the last term on the right-hand side indicate the Einstein summation convention. This leads to

$$\boldsymbol{\tau}^e_n = \frac{1}{2}\epsilon_0\left[\left(E^v_n\right)^2 - \epsilon_r\left(E^l_n\right)^2\right] + \frac{1}{2}\epsilon_0\left(\epsilon_r - 1\right)E_t^2 \tag{6.13}$$

$$\boldsymbol{\tau}^e_t = \epsilon_0 E^v_n E_t - \epsilon E^l_n E_t = \sigma E_t \tag{6.14}$$

for the normal and tangential components of the electrical stress at the interface. Note that only viscous forces are available for balancing the latter, which differs from the normal direction where surface tension forces play an important role.

In addition to these stresses, the surface charge at the interface is governed by the usual jump condition for regions of dissimilar permittivity

$$\sigma = \epsilon_0 E^v_n - \epsilon_0\epsilon_r E^l_n \tag{6.15}$$

The prevailing surface charge may or may not be in the vicinity of the fully relaxed value (equal to the normal component of the displacement field on the vacuum side, $\epsilon_0 E^v_n$), as we have shown, and this is important because the evaporation is in part a function of σ

$$j_e = \sigma\frac{k_B T}{h}\exp\left(\frac{-1}{k_B T}\left\{\Delta G - \sqrt{\frac{q^3 E^v_n}{4\pi\epsilon_0}}\right\}\right) \tag{6.16}$$

Notice that the introduction of the jump condition and this kinetic law for the evaporated current density (two relationships) gives us only two of j_e, σ, and the liquid field E^l_n. It says nothing of the third, and so we require an additional relationship if we are to uniquely solve the set of equations at hand. We can do this by writing a steady-state transport equation at the interface

$$j_e = \underbrace{j_{cond}}_{kE^l_n} + j_{conv} \tag{6.17}$$

This suggests that the current evaporated on the vacuum side must be balanced by a corresponding flow of charge on the liquid side of the interface. This flow is composed of two parts: a conducted component and a convected component. Of these, observe that only the former can prevail in the bulk, where quasineutrality in the fluid precludes net charge from being transported by internal flows. At the interface, however, charge separation (i.e. the surface charge) is available for entrainment by the passing flow and so convection is possible. The conducted part of the interfacial current, j_{cond}, is simply the familiar Ohmic value kE_n^l. Expressions for the convected part, on the other hand, are sometimes confusing and so we offer here a fundamental and intuitive derivation.

Consider the axisymmetric meniscus illustrated in Fig. 6-2, where evaporation of charge is taking place in the steady-state. If we allow s to be a parameter describing the distance along the interface between the axis of symmetry and an arbitrary point (say, s_0), we can isolate a cylindrical section bracketed by s_0 and $s_0 + \Delta s$ and perform a basic current balance. The locally evaporated current on the vacuum side is simply $j_e(\Delta A)$ while the current conducted to the liquid side of interface is $kE_n^l(\Delta A)$. In both cases, the differential area of the section is $\Delta A = 2\pi r(\Delta s)$ where r is the local cylindrical radius. The convected contribution to the balance is somewhat trickier and depends on three parameters: (1) the speed of the flow tangent to the local interface, v_t; (2) the magnitude of the local surface charge, σ; and (3) the circumference of the projection of the local interface on the $r - \theta$ plane, assuming we are resolving the interface in cylindrical space. The product of these three things, $v_t \cdot \sigma \cdot 2\pi r$, determines the locally convected current (units of Amperes rather than a current *density*). From the figure we can see that flow moving toward the tip of the meniscus requires that a current of

$$v_t\left(s_0 + \Delta s\right) \cdot \sigma\left(s_0 + \Delta s\right) \cdot 2\pi r\left(s_0 + \Delta s\right)$$

enter the bottom of our differential section where $s = s_0 + \Delta s$. By the same token, a current of

$$v_t\left(s_0\right) \cdot \sigma\left(s_0\right) \cdot 2\pi r\left(s_0\right)$$

must be leaving the top of the section. We can now collect the difference between these two currents and formulate the aggregate balance

$$\frac{\partial \sigma}{\partial t}\left(\Delta A\right) = kE_n^l\left(\Delta A\right) - j_e\left(\Delta A\right) - \left[v_t\left(s_0 + \Delta s\right) \cdot \sigma\left(s_0 + \Delta s\right) \cdot 2\pi r\left(s_0 + \Delta s\right) - v_t\left(s_0\right) \cdot \sigma\left(s_0\right) \cdot 2\pi r\left(s_0\right)\right] \tag{6.18}$$

which is general and accounts for transients in the local charge. After dividing through by the sectional area this becomes

$$\frac{\partial \sigma}{\partial t} = kE_n^l - j_e - \frac{1}{r}\left[\frac{v_t\left(s_0 + \Delta s\right) \cdot \sigma\left(s_0 + \Delta s\right) \cdot 2\pi r\left(s_0 + \Delta s\right) - v_t\left(s_0\right) \cdot \sigma\left(s_0\right) \cdot 2\pi r\left(s_0\right)}{\Delta s}\right] \tag{6.19}$$

where the last term on the right-hand side can be converted to a partial derivative through the fundamental theorem of calculus. Taking the limit as $\Delta s \to 0$

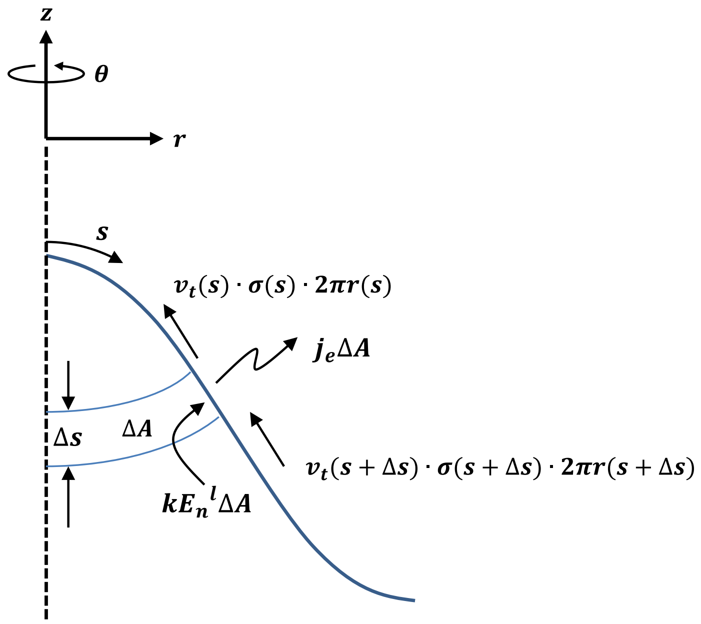

Figure 6-2: Prevailing currents for an arbitrary cylindrical slice of an axisymmetric electrified meniscus. The evaporative current is balanced by conducted and convected charge in the fluid. Note that the latter is strictly a surface phenomenon which does not take place in the bulk where quasineutrality prevents flows from transporting net charge.

$$\lim_{\Delta s\to 0}\frac{\partial\sigma}{\partial t}=kE_n^l-j_e-\frac{1}{r}\frac{\partial}{\partial s}\left(v_t\sigma r\right)\tag{6.20}$$

For steady evaporation, $\partial\sigma/\partial t\to 0$ and we find

$$j_e=\underbrace{kE_n^l}_{j_{cond}}-\underbrace{\frac{1}{r}\frac{\partial}{\partial s}\left(v_t\sigma r\right)}_{j_{conv}}\tag{6.21}$$

The second term on the right-hand side of this expression is what we refer to as the convected current contribution.

The transport equation, Eq. 6.21, is presented in a cylindrical form and represents the motion of all charges at the interface. It could be of use, however, to recast it since its given form is most easily evaluated in a local $\vec{n}-\vec{t}$ coordinate system rather than a global one. To do this, we might look to Higuera [62] where the alternative representation

$$\frac{D\sigma}{Dt}=\frac{\partial\sigma}{\partial t}+\vec{u}\cdot\nabla\sigma=\sigma\left(\vec{n}\cdot\nabla\vec{u}\cdot\vec{n}\right)+kE_n^l-j_e\tag{6.22}$$

is offered. Apparently, this is partially derived from Batchelor [81], in which the first term on the right-hand side is interpreted as an effect related to the surface strain (which makes some sense given the presence of the $\nabla\vec{u}$ tensor factor). In the steady-state this relationship reduces to

$$j_e = \underbrace{kE_n^l}_{j_{cond}} + \underbrace{\sigma\left(\vec{n} \cdot \nabla \vec{u} \cdot \vec{n}\right) - \vec{u} \cdot \nabla \sigma}_{j_{conv}} \tag{6.23}$$

This is similar to the transport equation derived above but differs slightly in the representation of the convected current. We do, however, believe it to be equivalent. Therefore, in view of its greater notational formalism and amenability to arbitrary coordinate systems we will sometimes make use of it throughout the remainder of this thesis.

Finally, to complete the interfacial conditions we must say something of the thermal behavior. Consider now the small section of the electrified fluid interface delineated in Fig. 6-3. Just beneath the surface resides a differential control volume of cross-sectional area ΔA (into the page) and thickness Δn in the direction normal to the surface. We can derive a representative interfacial condition by writing a heat balance in this volume. In general, this is

$$\rho c_p \frac{\partial T}{\partial t}\left(\Delta A \cdot \Delta n\right) = \dot{q}\left(\Delta A \cdot \Delta n\right) - k_T \nabla T\left(\Delta A\right) + \rho c_p\left[u\left(n_0 + \Delta n\right) T\left(n_0 + \Delta n\right) - u\left(n_0\right) T\left(n_0\right)\right]\left(\Delta A\right) \tag{6.24}$$

where $\dot{q}$ is the generation internal to the control volume (W/m^3) and $k_T \nabla T$ is the heat conducted away from its inward face (W/m^2). The terms involving the fluid velocity u describe the thermal energy convected into $(\rho c_p u(n_0 + \Delta n) T(n_0 + \Delta n))$ and out of $(\rho c_p u(n_0) T(n_0))$ the volume. After dividing through by the area the balance becomes

$$\rho c_p \frac{\partial T}{\partial t}\left(\Delta n\right) = \dot{q}\left(\Delta n\right) - k_T \nabla T + \rho c_p\left[u\left(n_0 + \Delta n\right) T\left(n_0 + \Delta n\right) - u\left(n_0\right) T\left(n_0\right)\right] \tag{6.25}$$

and since we are interested in the condition at the interface we can now take the limit as $\Delta n \to 0$. The result is

$$\lim_{\Delta n \to 0}\left\{\rho c_p \frac{\partial T}{\partial t}\left(\Delta n\right) = \dot{q}\left(\Delta n\right) - k_T \nabla T + \rho c_p\left[u\left(n_0 + \Delta n\right) T\left(n_0 + \Delta n\right) - u\left(n_0\right) T\left(n_0\right)\right]\right\}$$
$$\Rightarrow \vec{n} \cdot \nabla T = 0 \tag{6.26}$$

In other words, the interface should act like a thermal insulator. Notice, however, that this is simply an approximation (but probably a very good one still) owing to the fact that we have neglected the possibilities of thermal radiation and the consumption of latent heat. The former of these, at least, should be very small when the temperature excursions are not too great. Observe that

$$q_{rad} \approx \sigma_B\left[\left(T_0 + \Delta T\right)^4 - T_0^4\right] \tag{6.27}$$

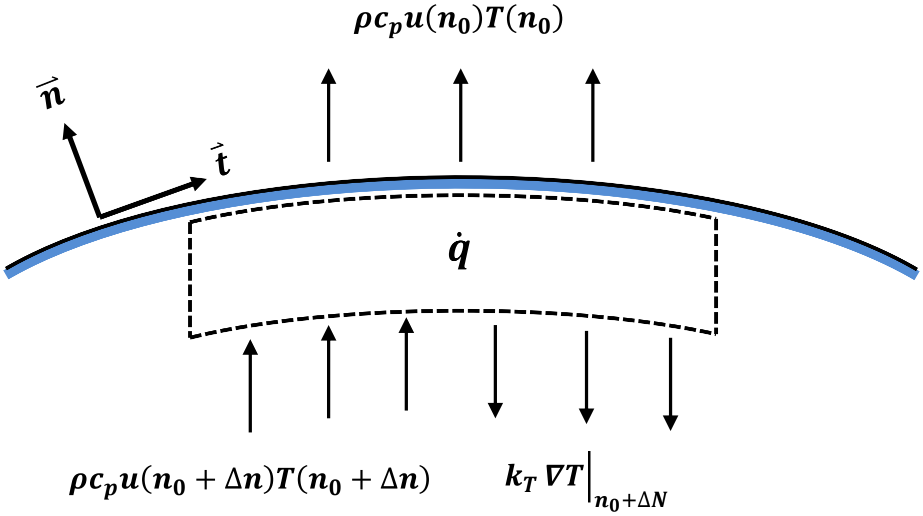

Figure 6-3: Thermal transport and generation processes near an electrified meniscus. Internal generation heats a small control volume while conduction and convection redistribute heat in several directions. A system of local $\vec{n} - \vec{t}$ coordinates is shown for the surface.

where q_{rad} is the radiative transfer density (W/m^2), σ_B is the Stefan-Boltzmann constant ($5.67 \cdot 10^{-8}$ W$\cdot$m$^{-2}\cdot$K^{-4}), T_0 is some reference temperature for the quiescent fluid and its surroundings, and ΔT is the temperature increment in the emission zone of the meniscus due to Ohmic heating. When ΔT is not too substantial, i.e. $\Delta T \ll T_0$

$$q_{rad} \approx 4\sigma_B T_0^3 \left(\Delta T\right) \tag{6.28}$$

which can be compared with, for example, the thermal conduction. Assuming that $q_{cond} \sim k_T \Delta T / r^*$

$$\frac{q_{rad}}{q_{cond}} \sim \frac{\sigma_B r^* T_0^3}{k_T} \tag{6.29}$$

For many ionic liquids it is likely that $r^* \sim 10^{-8}$ m, $T_0 \sim 3 \cdot 10^2$ K, and $k_T \sim 10^{-1}$ W/m-K. Using these values suggests that the ratio of the radiation transfer to the conduction transfer is likely no more than 10^{-6} in most cases, which would seem to justify its exclusion.

The extent of the role played by the latent heat, on the other hand, is less clear. In evaporative processes that are strictly thermal, i.e. those that are not electrically assisted, it is understood that the phase transition of excited species, charged or otherwise, must be accompanied by the consumption of an additional amount of energy. This is known as the latent heat, which, thermodynamically speaking, is an intrinsic property of the evaporating substance. In situations where field assistance is not insignificant, as in the room temperature evaporation of electrified ionic liquids, it is believed that the strong pull of the field effectively "plucks" charged particles from the surface of the fluid. Thermal excitation does play some part, however, and this is evidenced by the kinetic law of Iribarne and Thomson [7]. With this in mind, the extent to which latent heat should be consumed is rather unclear.

For the sake of argument, let us assume for the moment that particles evaporating from an electrified ionic liquid do consume full measures of the latent heat. When this is the case, an additional "cooling" term should be added to the heat balance of the form

$$q''_L = \frac{\dot{m}}{A} L_v \tag{6.30}$$

where q''_L is the heat flux associated with the consumption of latent heat (W/m^2), $\dot{m}/A$ is the specific evaporation rate (kg/m^2-s), and L_v is the latent heat (J/kg). During ion evaporation we might approximate $\dot{m}/A$ as $\sim j/(q/m) \sim kE^*\epsilon_r^{-1}(q/m)^{-1}$ and so this expression becomes

$$q''_L \sim \frac{kE^*}{\epsilon_r\,(q/m)} L_v \tag{6.31}$$

When we compare this to, for example, the characteristic conduction flux we find

$$\frac{q''_L}{q''_{cond}} \sim \frac{kE^* r^* L_v}{\epsilon_r\,(q/m)\,k_T \Delta T} \tag{6.32}$$

For a fluid with $k \sim 1$ S/m, $E^* \sim 10^9$ V/m, $r^* \sim 10^{-8}$ m, $\epsilon_r \sim 10$, $q/m \sim 10^6$ C/kg, $k_T \sim 10^{-1}$ W/m-K, and $L_v \sim 10^6$ J/kg (which could be more or less representative of a fluid like EMI-BF4; see [88, 89]), this evaluates to roughly

$$\frac{q''_L}{q''_{cond}} \sim \frac{10}{\Delta T} \tag{6.33}$$

When the thermal excursion ΔT is small, the latent heat would obviously dominate. Conversely, when it is of a more typical order, say $\Delta T \sim 10^0$-10^1 K, the latent heat contribution could be comparable to the that of conduction but certainly not extreme. In view of this finding and the uncertainty that would come with invoking latent heat factors, the thermal balances used throughout the rest of this thesis will explicitly neglect them.

Boundaries

We will address the hydrodynamic boundaries first, as these will require some cleaving of the global modeling domain. Ideally, we would like to capture effects on the meniscus stemming from events as far upstream as the origin (reservoir) of the evaporating fluid. The ramifications of the hydraulic configuration there are of particular interest as we often have much more direct control over the upstream hydraulics than we do over what happens very near to the menisci.

Consider the conceptual modeling domain illustrated in Fig. 6-4, which includes a fluid reservoir and a feeding tube for delivering liquid to the plate upon which our meniscus is anchored. Under very rigorous circumstances we might attempt to

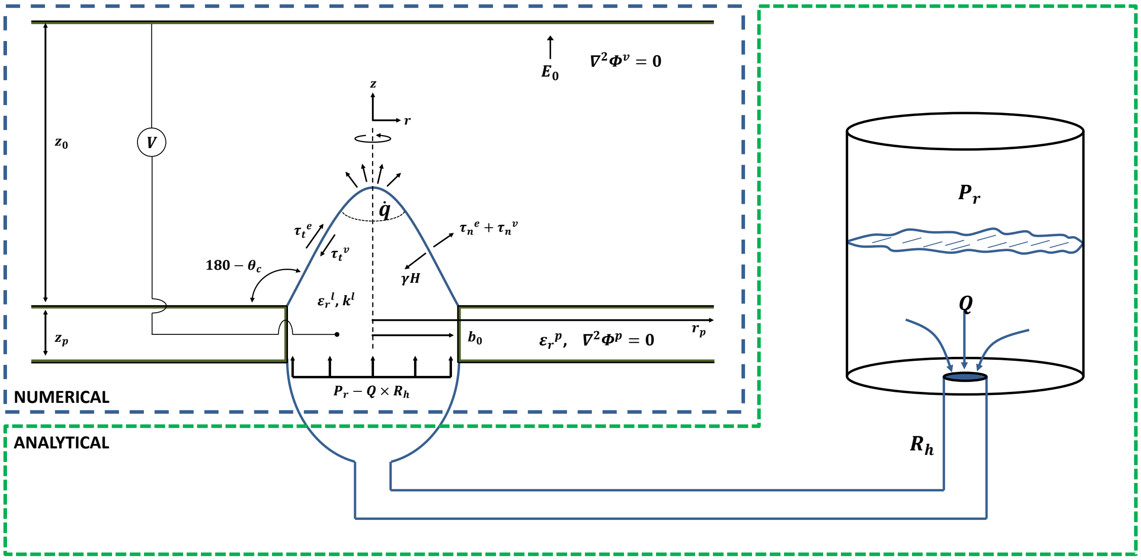

Figure 6-4: Schematic illustration of global modeling domain, including a computational space that is local to the meniscus and an upstream feeding system that is handled analytically. The feeding system (green enclosure) is a "black box" from the perspective of our numerical calculations. Its simplified architecture includes a reservoir that is held at pressure P_r and a characteristic impedance R_h (Pa-s/m^3) such that it supplies fluid to the bottom of our computational channel at a pressure $P_r - Q \times R_h$.

numerically model this system in its entirety; in other words, we would discretize all of the space in-between and including the reservoir and the meniscus regions. It is likely, however, that the physics taking place in the feeding system (upstream of the plate) should be rather straightforward and amenable to characterization by analytical means. In the specific case of a long tube, for example, the upstream flow field should very nearly resemble that of Poiseuille, for which we have a well-known solution. With this in mind, we will endeavor to ease our eventual numerical burden by segregating the upstream feeding system from the more nuanced region in which the meniscus itself resides. The former will be treated analytically while the latter, which is essentially the region delineated in Fig. 6-1, will be handled computationally.

The hydraulic boundary at the bottom of the computational domain ($z = -z_p$ in Fig. 6-1 when the origin is coincident with the top surface of the plate) is the one that requires specification now. We can assume that the reservoir is pressurized to P_{res} (or P_r) and that the feeding line (tube, porous material, etc.) is characterized by an hydraulic impedance R_h (N-s/m^5). In general then, the fluid being fed to the meniscus enters the bottom of the plate at a pressure

$$P_B = P_r - Q \cdot R_h \tag{6.34}$$

where Q is the volumetric flow rate. When steady emission prevails, we recognize that this is related to the current as $Q = I\rho^{-1}(q/m)^{-1}$. Substituting this gives

$$P_B = P_r - \frac{IR_h}{\rho\,(q/m)} \tag{6.35}$$

Eq. 6.35 is at this point a passable hydraulic boundary condition for the bottom of the fluid column in the computational domain. The condition for the sidewalls of the plate ($r = b_0$, $-z_p < z < 0$) are much easier. We can simply take

$$\vec{u} \cdot \vec{i}_r = 0 \tag{6.36}$$

$$\vec{u} \cdot \vec{i}_z = 0 \tag{6.37}$$

which ensures that fluid neither passes into the plate nor “slips” alongside it.

For the thermal calculations we are again only interested in the liquid column within the computational domain. Along the bottom of the column ($0 < r < b_0$, $z = -z_p$) and along the sidewalls of the plate ($r = b_0$, $-z_p < z < 0$) we can adopt a static reference temperature T_0, which should be a good approximation so long as the plate is a good thermal sink. Mathematically, these conditions state

$$T\,(r < b_0, z = -z_p) = T_0 \tag{6.38}$$

$$T\,(r = b_0, -z_p < z < 0) = T_0 \tag{6.39}$$

Only the electrical conditions remain now. Regardless of the nature of the plate we can set a reference potential along the bottom of the computational domain and bias the top plate with respect to this value. The vertical edges of the domain should obey a Neumann condition and together these state

$$\Phi\,(r, z = -z_p) = \Phi_0 \tag{6.40}$$

$$\Phi\,(r, z = z_0) = \Phi_0 + V \tag{6.41}$$

$$\left.\frac{\partial \Phi}{\partial r}\right|_{r=r_p} = 0 \tag{6.42}$$

For the remaining surfaces of the plate, these should be at the reference potential if it is a conductor. When it is a dielectric, the vacuum-exposed surface should satisfy the condition of vanishing σ and the liquid surface should be at full electrical relaxation (at least approximately, since we would expect the flow to be very weak in the tube). Mathematically we have that

$$\Phi\,(r = b_0, -z_p < z < 0) = \Phi_0 \tag{6.43}$$

$$\Phi\,(b_0 < r < r_p, z = 0) = \Phi_0 \tag{6.44}$$

when the plate is a conductor; and

$$\Phi^{l}\left(r=b_0,-z_p<z<0\right)=\Phi^{p}\left(r=b_0,-z_p<z<0\right) \tag{6.45}$$

$$\sigma=-\epsilon_0\epsilon_p\left.\frac{\partial\Phi^{p}}{\partial r}\right|_{r=b_0} \tag{6.46}$$

$$\Phi^{v}\left(r>b_0,z=0\right)=\Phi^{p}\left(r>b_0,z=0\right) \tag{6.47}$$

$$\left.\frac{\partial\Phi^{v}}{\partial z}\right|_{z=0}=\epsilon_p\left.\frac{\partial\Phi^{p}}{\partial z}\right|_{z=0} \tag{6.48}$$

when the plate is a dielectric with permittivity ϵ_r.

6.1.3 Summary

After examining the relevant physics we find the vacuum and plate regions are governed by Laplace's equation while the liquid is subject to a more general form of charge concentration owing to possible thermal excursions and modifications to the nominal electrical conductivity there. The flow of fluid should obey the Stokes relationship for the viscous limit, although limitations in our numerical software call for the inclusion of an inertial term from the more general Navier-Stokes momentum balance.

In summary, the collection of governing relationships (bulk/volume equations, interfacial equations, and boundary conditions) defining the computational part of the problem are

$$\nabla^2\Phi^{v}=0 \tag{6.49}$$

$$\nabla^2\Phi^{p}=0 \tag{6.50}$$

in the vacuum and plate regions, respectively;

$$\nabla\cdot\vec{j}=0,\ \ \text{where } \vec{j}=k\vec{E}^{l} \tag{6.51}$$

$$\rho\left(\vec{u}\cdot\nabla\right)\vec{u}=\nabla\cdot\left[-p\boldsymbol{I}+\mu\left(\nabla\vec{u}+\left(\nabla\vec{u}\right)^{T}\right)\right] \tag{6.52}$$

$$k_T\nabla^2T+\frac{j^2}{k}-\rho c_p\left(\vec{u}\cdot\nabla T\right)=0 \tag{6.53}$$

in the liquid region;

$$\boldsymbol{\tau}_n^e - \vec{n} \cdot \boldsymbol{\tau} \cdot \vec{n} = \gamma \nabla \cdot \vec{n} \tag{6.54}$$

$$\vec{t} \cdot \boldsymbol{\tau} \cdot \vec{n} = \boldsymbol{\tau}_t^e \tag{6.55}$$

$$\sigma = \epsilon_0 \left(\vec{E}^v \cdot \vec{n} \right) - \epsilon_0 \epsilon_r \left(\vec{E}^l \cdot \vec{n} \right) \tag{6.56}$$

$$j_e = \sigma \frac{k_B T}{h} \exp \left(\frac{-1}{k_B T} \left\{ \Delta G - \sqrt{\frac{q^3 \vec{E}^v \cdot \vec{n}}{4\pi\epsilon_0}} \right\} \right) \tag{6.57}$$

$$j_e = k \left(\vec{E}^l \cdot \vec{n} \right) + \sigma \left(\vec{n} \cdot \nabla \vec{u} \cdot \vec{n} \right) - \vec{u} \cdot \nabla \sigma \tag{6.58}$$

$$I = \int j_e \cdot dA \tag{6.59}$$

$$\vec{n} \cdot \nabla T = 0 \tag{6.60}$$

at the liquid-vacuum interface;

$$\Phi^l = \Phi_0 \tag{6.61}$$

$$P^l = P_r - \frac{I R_h}{\rho \left(q/m \right)} \tag{6.62}$$

$$T^l = T_0 \tag{6.63}$$

at the base of the fluid column in the computational domain ($0 < r < b_0$, $z = -z_p$);

$$\vec{u} \cdot \vec{i}_r = 0 \tag{6.64}$$

$$\vec{u} \cdot \vec{i}_z = 0 \tag{6.65}$$

$$T^l = T_0 \tag{6.66}$$

on the sidewalls of the fluid channel ($r = b_0$, $-z_p < z < 0$);

$$\Phi = \Phi_0 \tag{6.67}$$

$$\Phi^v = \Phi_0 + V \tag{6.68}$$

$$\vec{E} \cdot \vec{i}_r = 0 \tag{6.69}$$

on the bottom of the domain ($z = -z_p$), the top of the domain ($z = z_0$), and the radial edge of the domain ($r = r_p$), respectively;

$$\Phi = \Phi_0 \tag{6.70}$$

on the vertical ($r = b_0$, $-z_p < z < 0$) and horizontal ($b_0 < r < r_p$, $z = 0$) surfaces of the plate, when it is a conductor; and

$$\Phi^l = \Phi^p \tag{6.71}$$

$$\sigma = \epsilon_0 \epsilon_p \left(\vec{E}^p \cdot \vec{i}_r \right) \tag{6.72}$$

$$\Phi^v = \Phi^p \tag{6.73}$$

$$\left(\vec{E}^v \cdot \vec{i}_z \right) = \epsilon_p \left(\vec{E}^p \cdot \vec{i}_z \right) \tag{6.74}$$

on the vertical and horizontal surfaces of the plate, when it is a dielectric with relative permittivity ϵ_p.

6.2 Nondimensionalization

Before nondimensionalizing the problem we will need to clarify the intrinsic fluid properties that may vary as a function of temperature, namely the electrical conductivity $k(T)$ and the viscosity $\mu(T)$. For the former, we adopt the linear approximation

$$k\left(T\right) = k_0 + k'\left(T - T_0\right) \tag{6.75}$$

where k_0 is the nominal conductivity (S/m) at the reference temperature T_0 (K) and k' is a thermal sensitivity (S/m-K). This should be more than sufficient over a range of at least tens of Kelvin in the vicinity of room temperature for many ionic liquids. As a point of reference, for the popular fluid EMI-BF4 the thermal sensitivity $k' \sim 0.04$ S/m-K in the neighborhood of room temperature [90, 91]. With respect to the viscosity, it is often a good approximation to take $\mu(T)k(T)$ as a constant since both of these parameters depend on temperature in a roughly linear way over wide ranges but vary in proportionally opposite directions (i.e. $\mu \sim T^{-1}$ while $k \sim T$). If we evaluate this constant at the reference temperature, $\mu(T)k(T) \to \mu_0 k_0$ and so we can write

$$\mu = \frac{\mu_0 k_0}{k_0 + k'\Delta T} \tag{6.76}$$

We make use of both of these relationships for nondimensionalization. The scales that we elect for this process are

$$\hat{L} \to \frac{L}{b_0} \tag{6.77}$$

$$\hat{A} \to \frac{A}{b_0^2} \tag{6.78}$$

$$\hat{P} \to \frac{P}{P_c}, \text{ where } P_c = \frac{2\gamma}{b_0} \tag{6.79}$$

$$\hat{E} \to \frac{E}{E_c}, \text{ where } E_c = \sqrt{\frac{4\gamma}{\epsilon_0 b_0}} \tag{6.80}$$

$$\hat{\sigma} \to \frac{\sigma}{\epsilon_0 E_c} \tag{6.81}$$

$$\hat{j} \to \frac{j}{k_0 E_c} \tag{6.82}$$

$$\hat{I} \to \frac{I}{k_0 E_c b_0^2} \tag{6.83}$$

$$\hat{u} \to \frac{u}{(\gamma/\mu_0)} \tag{6.84}$$

$$\hat{T} \to \frac{T}{T_0} \tag{6.85}$$

Lengths are scaled by the radius of the contact line, b_0; areas are scaled by b_0^2; stresses are scaled by the capillary pressure, P_c; fields are scales by a "critical" value satisfying the balance $\epsilon_0 E_c^2/2 = P_c$; charge densities are scales by the corresponding displacement field, $\epsilon_0 E_c$; current densities by $k_0 E_c$; currents by $k_0 E_c b_0^2$; velocities by the viscous-capillary speed, γ/μ_0; and temperatures by the reference value, T_0. After applying these to the governing equations we find that the dimensionless problem is subject to

$$\hat{\nabla}^2 \hat{\Phi}^v = 0 \tag{6.86}$$

$$\hat{\nabla}^2 \hat{\Phi}^p = 0 \tag{6.87}$$

in the vacuum and plate regions, respectively;

$$\hat{\nabla} \cdot \hat{j} = 0 \tag{6.88}$$

$$\frac{R_E}{B} \left(\hat{u} \cdot \hat{\nabla} \right) \hat{u} = \hat{\nabla} \cdot \left[\hat{p} \boldsymbol{I} + \frac{1/2}{1 + \Lambda \left(\hat{T} - 1 \right)} \left(\hat{\nabla} \hat{u} + \left(\hat{\nabla} \hat{u} \right)^T \right) \right] \tag{6.89}$$

$$B \cdot C_c^T \left(\hat{\nabla}^2 \hat{T} \right) + \frac{\hat{j}^2}{1 + \Lambda \left(\hat{T} - 1 \right)} - C_u^T \left(\hat{u} \cdot \hat{\nabla} \hat{T} \right) = 0 \tag{6.90}$$

in the liquid region;

$$\left[\left(\hat{E}_n^v\right)^2 - \epsilon_r\left(\hat{E}_n^l\right)^2 + (\epsilon_r - 1)\hat{E}_t^2\right] - \left[-\hat{p} + \frac{1}{2}\frac{\vec{n}\cdot\left(\hat{\nabla}\hat{u} + \left(\hat{\nabla}\hat{u}\right)^T\right)\cdot\vec{n}}{1+\Lambda\left(\hat{T}-1\right)}\right] = \frac{1}{2}\hat{\nabla}\cdot\vec{n} \tag{6.91}$$

$$\frac{\vec{t}\cdot\left(\hat{\nabla}\hat{u} + \left(\hat{\nabla}\hat{u}\right)^T\right)\cdot\vec{n}}{1+\Lambda\left(\hat{T}-1\right)} = 4\hat{\sigma}\hat{E}_t \tag{6.92}$$

$$\hat{\sigma} = \hat{E}_n^v - \epsilon_r\hat{E}_n^l \tag{6.93}$$

$$\hat{j}_e = \frac{\hat{\sigma}\hat{T}}{\epsilon_r\chi}\exp\left(\frac{-\psi}{\hat{T}}\left\{1 - B^{1/4}\sqrt{\hat{E}_n^v}\right\}\right) \tag{6.94}$$

$$\hat{j}_e = \left[1+\Lambda\left(\hat{T}-1\right)\right]\hat{E}_n^l + C_u^e(B)\left[\hat{\sigma}\left(\vec{n}\cdot\hat{\nabla}\hat{u}\cdot\vec{n}\right) - \hat{u}\cdot\hat{\nabla}\hat{\sigma}\right] \tag{6.95}$$

$$\hat{I} = \int \hat{j}_e \cdot d\hat{A} \tag{6.96}$$

$$\vec{n}\cdot\hat{\nabla}\hat{T} = 0 \tag{6.97}$$

at the liquid-vacuum interface;

$$\hat{\Phi}^l = \hat{\Phi}_0 \tag{6.98}$$

$$\hat{P}^l = \hat{P}_r - C_R\hat{I} \tag{6.99}$$

$$\hat{T}^l = \hat{T}_0 \tag{6.100}$$

at the base of the fluid column in the computational domain ($0 < \hat{r} < 1$, $\hat{z} = -\hat{z}_p$);

$$\hat{u}\cdot\vec{i}_r = 0 \tag{6.101}$$

$$\hat{u}\cdot\vec{i}_z = 0 \tag{6.102}$$

$$\hat{T}^l = \hat{T}_0 \tag{6.103}$$

on the sidewalls of the fluid channel ($\hat{r} = 1$, $-\hat{z}_p < \hat{z} < 0$);

$$\hat{\Phi} = \hat{\Phi}_0 \tag{6.104}$$

$$\hat{\Phi}^v = \hat{\Phi}_0 + \hat{V} \tag{6.105}$$

$$\hat{E}\cdot\vec{i}_r = 0 \tag{6.106}$$

on the bottom of the domain ($\hat{z} = -\hat{z}_p$), the top of the domain ($\hat{z} = \hat{z}_0$), and the radial edge of the domain ($\hat{r} = \hat{r}_p$), respectively;

$$\hat{\Phi} = \hat{\Phi}_0 \tag{6.107}$$

on the vertical ($\hat{r} = 1$, $-\hat{z}_p < \hat{z} < 0$) and horizontal ($1 < \hat{r} < \hat{r}_p$, $\hat{z} = 0$) surfaces of the plate, when it is a conductor; and

$$\hat{\Phi}^l = \hat{\Phi}^p \tag{6.108}$$

$$\hat{\sigma} = \epsilon_p \hat{E}^p \cdot \vec{i}_r \tag{6.109}$$

$$\hat{\Phi}^v = \hat{\Phi}^p \tag{6.110}$$

$$\hat{E}^v \cdot \vec{i}_z = \epsilon_p \hat{E}^p \cdot \vec{i}_z \tag{6.111}$$

on the vertical and horizontal surfaces of the plate, when it is a dielectric with relative permittivity ϵ_p. The problem, therefore, is contingent upon the selection of 16 unique parameters

$$\begin{array}{llll}
\hat{E}_0 & \epsilon_r & \epsilon_p & \hat{r}_p \\
\hat{z}_p & \hat{z}_0 & B = \dfrac{r^*}{b_0} & R_E = \dfrac{\rho \gamma r^*}{2\mu_0^2} \\
\Lambda = \dfrac{k' T_0}{k_0} & C_c^T = \dfrac{\epsilon_0 k_T T_0}{4 k_0 \gamma r^*} & C_u^T = \dfrac{\epsilon_0 \rho c_p T_0}{4 \mu_0 k_0} & C_u^e = \dfrac{\epsilon_0 \gamma}{\mu_0 k_0 r^*} \\
\chi = \dfrac{h k_0}{\epsilon_0 \epsilon_r k_B T_0} & \psi = \dfrac{\Delta G}{k_B T_0} & C_R = \dfrac{k_0 E_c b_0^3 R_h}{2 \gamma \rho \, (q/m)} & \hat{P}_r
\end{array}$$

The physics of the present problem are clearly very rich and likely restrict reasonably efforts to map the parameter space to investigations of but a few important degrees of freedom. Of course, this naturally raises the question as to which ones are "important". As an example, one way to begin narrowing the parameter space could be to select physical values corresponding to a single liquid (k_0, ΔG, γ, etc.) and hold these constant, which is essentially what we do when we conduct experiments in the laboratory. When this is the case, we can see that ϵ_r, R_E, Λ, C_c^T, C_u^T, C_u^e, χ, and ψ all become static parameters. This leaves us with 8 free values, of which another two can be eliminated if we wish to study a meniscus that is isolated at infinity. Since this simply requires an absence of boundary influences, we can choose $\hat{r}_p$ and $\hat{z}_0$ arbitrarily large and not have to worry about the sensitivity of the solution with respect to these so long as they are both $\gg 1$.

We are now faced with a six-dimensional spaced (defined by $\hat{E}_0$, ϵ_p, $\hat{z}_p$, B, C_R, $\hat{P}_r$) that may or may not still be too expansive for us to reasonably explore through numerics, depending upon the speed of the routines that we will develop. Before we get to that point though, in the next few sections we will consider several substrate issues and determine the relative importance of ϵ_p and $\hat{z}_p$ to our fundamental study.

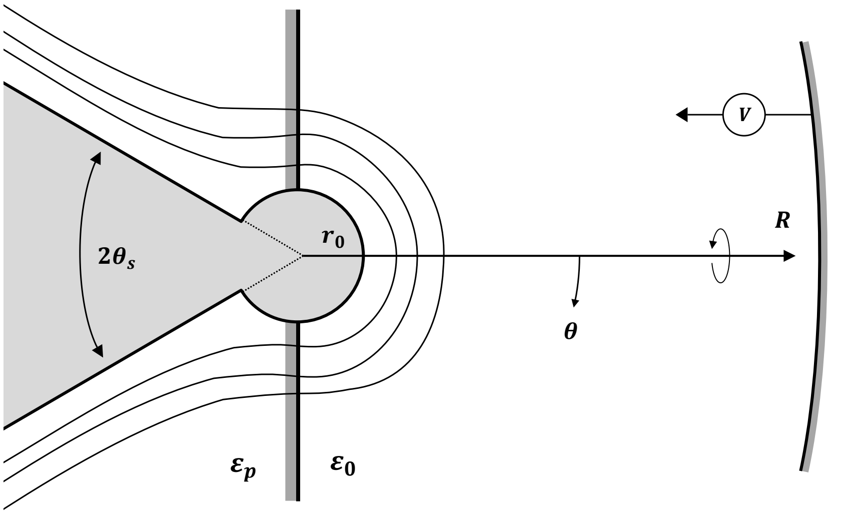

Figure 6-5: Sphere-on-cone (SOC) model. A sphere (radius r_0) and an infinite conical shaft (half-angle θ_s) are superimposed to create a field-amplifier structure that has a closed-form analytical solution to the Laplace equation. Several equipotential surfaces are shown between the solid assembly and a distant counter-electrode (radius R along the zenith line). The presence of a substrate material with unique permittivity ($\epsilon_p \neq \epsilon_0$) surrounding the cone structure is admissible.

6.3 Substrate considerations

In this section we consider two issues that are central to dielectric substrate media: (1) the manner in which they modify the structure of the field acting on the meniscus, and (2) the singularity that they promote along the contact line. The results will be useful for informing choices of substrate material during our numerical investigation.

6.3.1 Dielectric plate amplification

In order to study structural modifications to the interfacial electric field through analytical means we might consider the simple case of a purely hemispherical meniscus and look to the well-known sphere-on-cone (SOC) model [85, 86, 87, 74]. This offers closed-form solutions to Laplace's equation for a family of spherically-capped conical structures that are subject to electrical stress (Fig. 6-5). As we show in the appendix, solutions to Laplace in spherical space are of the product variety, $\Phi(r,\theta) = R(r)\cdot\Theta(\theta)$, where $R(r)$ and $\Theta(\theta)$ are of the form

$$R\left(r\right) = A_n r^n + B_n r^{-(n+1)}$$
$$\Theta\left(\theta\right) = C_n P_n\left(\cos\theta\right) + D_n Q_n\left(\cos\theta\right)$$

P_n and Q_n are the Legendre functions of the first and second kind, respectively, while n is the separation constant that results from segregating the r and θ dependencies (essentially the eigenvalue of the differential operator). Typically we take $n \in \mathbb{Z}^+$ (i.e. $n = 0, 1, 2, ...$) so that the Legendre functions simplify to their familiar polynomial forms and construct the series

$$\Phi\left(r, \theta\right) = \sum_{n=0}^{\infty} \left[A_n r^n + B_n r^{-(n+1)}\right] \cdot \left[C_n P_n\left(\cos\theta\right) + D_n Q_n\left(\cos\theta\right)\right] \tag{6.112}$$

which can be useful for non-standard geometries but not always convenient. As it turns out, in the case of the SOC we have license to abbreviate this series to a single term so long as we can assign the reference potential $\Phi = 0$ to the boundary defined by the sphere-cone superposition. When we do this we get

$$\Phi\left(r, \theta\right) = \left[A r^n + B r^{-(n+1)}\right] \cdot \left[C \cdot P_n\left(\cos\theta\right) + D \cdot Q_n\left(\cos\theta\right)\right] \tag{6.113}$$

where the separation constant n could, in general, be of fractional magnitude now. Its only constraint is that it must satisfy

$$C \cdot P_n\left(\cos\theta\right) + D \cdot Q_n\left(\cos\theta\right) = 0 \tag{6.114}$$

for $\theta \to \pi - \theta_s$ in order to preserve the boundary along the cone. In the traditional situation where the SOC is surrounded by only vacuum we can remove Q_n from this balance because it is singular along the zenith line ($\theta \to 0$). At present, however, we wish to investigate the slightly different scenario in which the body of the SOC is enveloped by a dielectric material of potentially disparate permittivity ($\epsilon_p \neq \epsilon_0$) leaving only the hemispherical cap exposed to vacuum. To do this we can invoke unique field solutions for each of the two regions in the problem (i.e., the vacuum region and the plate/substrate region) by writing

$$\Phi\left(r, \theta\right) = \begin{cases} \left[A r^n + B r^{-(n+1)}\right] P_n\left(\cos\theta\right) = \Phi^v, \ \theta \in [0, \pi/2] \\ \left[C r^n + D r^{-(n+1)}\right] \left[P_n\left(\cos\theta\right) + E \cdot Q_n\left(\cos\theta\right)\right] = \Phi^p, \ \theta \in [\pi/2, \pi - \theta_s] \end{cases} \tag{6.115}$$

where n is common to both fields. Notice that Q_n is now omitted for the vacuum part of the solution, Φ^v, but retained for the part inside the plate, Φ^p. In both regions the potential field needs to satisfy the reference value on the sphere, $\Phi(r_0, \theta) = 0$ where r_0 is the radius of the cap. Applying this condition gives

$$\Phi^v\left(r, \theta\right) = A r_0^n \left[\left(\frac{r}{r_0}\right)^n - \left(\frac{r_0}{r}\right)^{n+1}\right] P_n\left(\cos\theta\right) \tag{6.116}$$

$$\Phi^p\left(r, \theta\right) = C r_0^n \left[\left(\frac{r}{r_0}\right)^n - \left(\frac{r_0}{r}\right)^{n+1}\right] \left[P_n\left(\cos\theta\right) + E \cdot Q_n\left(\cos\theta\right)\right] \tag{6.117}$$

The four remaining constants (A, C, E, and n) are identified by enforcing the constraints

$$\Phi^v\left(R,0\right)=V,\text{ where } R\gg r_0 \tag{6.118}$$

$$\Phi^v\left(r,\pi/2\right)=\Phi^p\left(r,\pi/2\right) \tag{6.119}$$

$$\frac{1}{r}\left.\frac{\partial\Phi^v}{\partial\theta}\right|_{\theta=\pi/2}=\frac{\epsilon_p}{r}\left.\frac{\partial\Phi^p}{\partial\theta}\right|_{\theta=\pi/2} \tag{6.120}$$

$$\Phi^d\left(r,\pi-\theta_s\right)=0 \tag{6.121}$$

These provide a counter-electrode through which an electrical bias can be imposed (condition 6.118) and ensure that the conical shaft of the SOC remains at the appropriate potential (condition 6.121). Eqs. 6.119 and 6.120 represent the interfacial conditions for a perfect dielectric (constant voltage and normal displacement field across the surface) and are applied at the mid-plane where the vacuum region meets the plate. After inserting these we find the system of governing equations

$$V=Ar_0^n\left[\left(\frac{R}{r_0}\right)^n-\left(\frac{r_0}{R}\right)^{n+1}\right]\approx AR^n \tag{6.122}$$

$$AP_n\left(0\right)=C\left[P_n\left(0\right)+E\cdot Q_n\left(0\right)\right] \tag{6.123}$$

$$AP_n'\left(0\right)=\epsilon_pC\left[P_n'\left(0\right)+E\cdot Q_n'\left(0\right)\right] \tag{6.124}$$

$$0=P_n\left(0\right)+E\cdot Q_n\left(0\right) \tag{6.125}$$

where the "primes" denote partial differentiation $\partial/\partial\theta$. Note that these involve special values of the Legendre functions given by (see [82, 83])

$$P_n\left(0\right)=\frac{1}{\sqrt{\pi}}\cos\left(\frac{\pi n}{2}\right)\frac{\Gamma\left(\frac{n+1}{2}\right)}{\Gamma\left(\frac{n+2}{2}\right)} \tag{6.126}$$

$$P_n'\left(0\right)=-\frac{2}{\sqrt{\pi}}\sin\left(\frac{\pi n}{2}\right)\frac{\Gamma\left(\frac{n+2}{2}\right)}{\Gamma\left(\frac{n+1}{2}\right)} \tag{6.127}$$

$$Q_n\left(0\right)=-\frac{\sqrt{\pi}}{2}\sin\left(\frac{\pi n}{2}\right)\frac{\Gamma\left(\frac{n+1}{2}\right)}{\Gamma\left(\frac{n+2}{2}\right)} \tag{6.128}$$

$$Q_n'\left(0\right)=-\sqrt{\pi}\cos\left(\frac{\pi n}{2}\right)\frac{\Gamma\left(\frac{n+2}{2}\right)}{\Gamma\left(\frac{n+1}{2}\right)} \tag{6.129}$$

Since we are primarily interested in the vacuum fields acting on our notional meniscus (the exposed part of the spherical cap from the SOC), we can now restrict our attention to Φ^v. From above, this is

$$\Phi^v=V\left(\frac{r}{R}\right)^n\left[1-\left(\frac{r_0}{r}\right)^{2n+1}\right]P_n\left(\cos\theta\right) \tag{6.130}$$

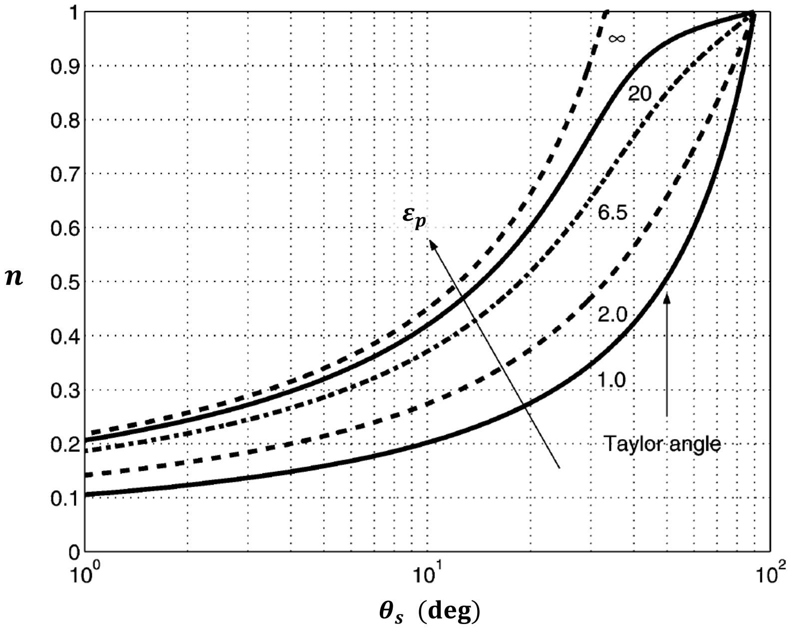

Figure 6-6: Map of $n = n(\epsilon_p, \theta_s)$ as a function of θ_s with the permittivity ϵ_p as a parameter. The values $\epsilon_p = 1$, 2, 6.5, 20, and ∞ are represented and increase in the direction of the arrow. Reproduced from Lozano [74].

which varies with the properties of the plate through n alone. Similarly, for the interfacial electric fields produced by this distribution of potentials we have

$$E_n^v = -\left.\frac{\partial \Phi^v}{\partial r}\right|_{r_0} = -\frac{V}{R}\left(\frac{R}{r_0}\right)^{1-n}(2n+1)\,P_n\left(\cos\theta\right) \tag{6.131}$$

where the "n" in E_n^v is understood to denote the normal component of the vacuum field along the arc $r = r_0$ and not the eigenvalue of the differential operator (or separation constant) used previously. Assuming that the spatially uniform and axially-oriented field existing far from the interface goes like $E_0 \sim -V/R$, we find the corresponding dimensionless form

$$\frac{E_n^v}{E_0} = (2n+1)\left(\frac{R}{r_0}\right)^{1-n} P_n\left(\cos\theta\right) \tag{6.132}$$

Note that this is very similar to the result that we obtain in the appendix for the traditional pure vacuum case ($\epsilon_p \to \epsilon_0$) with the lone exception that n is now subject to the constraints 6.118-6.121 rather than $P_n(\cos(\pi - \theta_s))$. In order to ascertain the effect that the dielectric has on the meniscus field we need to solve for $n = n(\epsilon_p, \theta_s)$. Instead of performing this directly, we refer to Lozano [74] where the same problem is considered and it is shown that the separation constant ranges from $n \sim 0.1$ (for the degenerate case $\theta_s \to 0$ and $\epsilon_p \to 1$) to $n = 1$ (for all ϵ_p when $\theta_s \to \pi/2$). A reproduction of this result is shown in Fig. 6-6.

In Fig. 6-7 we plot the interfacial electric field as a function of n and θ in several

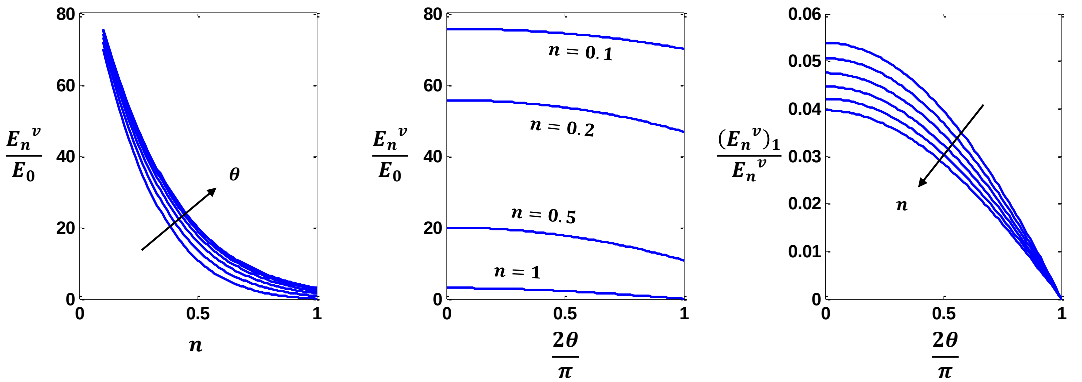

Figure 6-7: Representations of the normal electric field acting on the cap of a sphere-on-cone (SOC) immersed in a dielectric plate. Dimensionless field strengths are shown for various n (separation constant) and θ. **Left:** Dimensionless normal field as a function of n with polar angle θ as a parameter. The arrow delineates the direction of decreasing value for $\theta =$[0,15,30,45,60,75,90]. **Center:** Dimensionless field as a function of polar angle θ with n as a parameter. The curves show that field distributions are structurally similar but amplified for decreasing n (signifying a narrowing shaft and/or weakening ϵ_p). Notice that the field along the interface of the plate, $\theta = \pi/2$, does not vanish even when $n \sim 0.2$ (the value corresponding to $\epsilon_p \to \infty$ in the degenerate case $\theta_s \to 0$). **Right:** Ratio of the field for the conducting plate case, $n = 1$ (shown as $(E_n^v)_1$ here), to fields of other n as a function of polar angle θ. The arrow indicates the direction of decreasing separation constant for $n =$[0.1 0.12 0.14 0.16 0.18 0.2], a range that spans the approximate set of solutions for all ϵ_p in the degenerate case $\theta_s \to 0$.

different ways. For example, in Fig. 6-7 (left) we show how E_n^v/E_0 varies for n with θ as a parameter. From the curves we can see that small n correspond to strong amplifications, which we anticipate based on the fact that n is a measure of the "sharpness" of the SOC; i.e. small n represent narrow conical shafts (small θ_s) while large n represent comparatively broad conical shafts (large θ_s). In Figs. 6-7 (center) and 6-7 (right) we first show changes in E_n^v/E_0 across the meniscus/interface and then $(E_n^v)_{n=1}/E_n^v$ in order to show the ratio of the limiting case $\theta_s \to \pi/2$ (corresponding to $n = 1$, a flat conducting plate) to solutions of other n. In doing so we primarily focus on a subset of n in the range from $0.1 \sim 0.2$ where the results of Lozano [74] suggest that all solutions should reside when the shaft is degenerate ($\theta_s \to 0$), including the one for $\epsilon_p \to \infty$ (for reference, this corresponds to $n \sim 0.2$ under these conditions). From the curves we see that the field distributions are structurally similar but amplified to various degrees depending upon the dielectric strength of the plate material. Interestingly, this is also true of the $\epsilon_p \to \infty$ case which we may have initially expected to reduce to the $n = 1$ solution. As we recall, in the chapter on spheroidal menisci the $\epsilon \to \infty$ and equipotential fluids were mathematically identical. Given the present revelation, however, it appears as though the relationship between perfectly polarizable and perfectly conducting materials is not always trivial. The organization of the boundaries, it turns out, must also have a say in determining their behaviors.

In any event, it is rather amazing that the $\epsilon_p \to \infty$ material is able to permit a nonzero field on the contact line ($\theta = \pi/2$) and in Fig. 6-8 we underscore this by plotting $E_n^v/(E_n^v)_{n=1}$ across the meniscus with n as a parameter. While it is clear that a key difference between dielectric and conducting plates is that the former support a nonzero field at the contact line and the latter do not, the essential conclusion for present purposes is that the prevailing interfacial fields are otherwise structurally similar, at least near the zenith where we know the important physics to be concentrated. Going forward, this could be a useful observation in that it might allow us to restrict our attention to conducting substrates so long as we can show that these do not obscure critical physics in the vicinity of the contact line.

6.3.2 Contact line singularity

It is interesting that the modulus of the electric field along the contact line need not be identically zero when the meniscus is attached to a dielectric plate, regardless of its polarizability. In the last section we considered a perfectly hemispherical interface that ensured a smooth 90° junction with the substrate material but in general the contact could be discontinuous. If it is true that the field does not vanish in its vicinity, these more general geometries could have important consequences for the global problem since discontinuous boundaries are commonly characterized by singularities.

In order to investigate the ramifications of a discontinuous contact we will consider a meniscus that is fed by a vertical column of fluid and anchored by a plate of arbitrary permittivity ϵ_p (Fig. 6-9). By zooming in on the contact line we see that the fluid makes an angle θ^l with the horizontal and is very likely characterized by a locally uniform potential. So long as $B \ll 1$ (recall that the size ratio $B = r^*/b_0$ is a measure

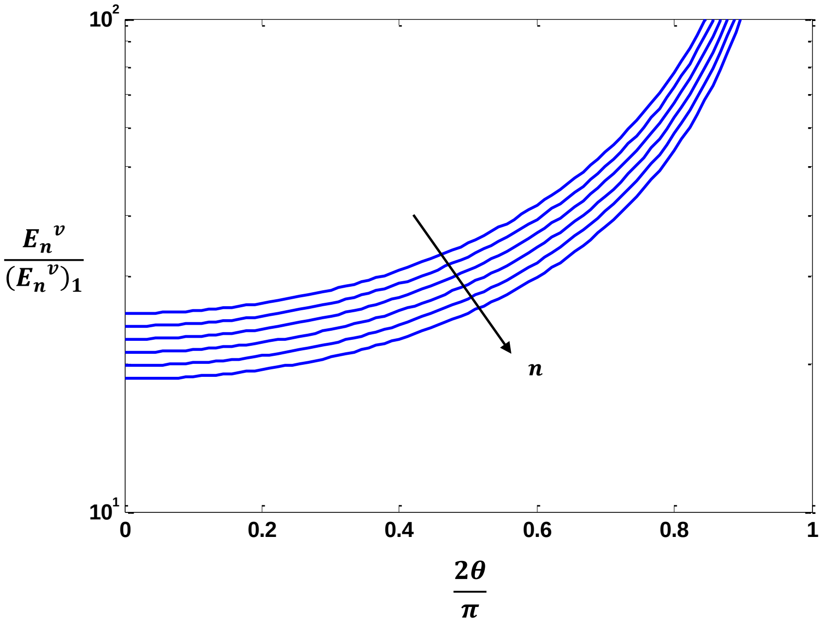

Figure 6-8: Ratio of normal electric field for arbitrary n to the field in the limiting $n = 1$ case as a function of polar angle θ. The arrow indicates the direction of increasing separation constant for parameter values n =[0.10 0.12 0.14 0.16 0.18 0.20]. Notice that the relative field behaviors are divergent near the contact line but structurally similar in the vicinity of the meniscus tip where we know important evaporation phenomena to be focused, particularly when $B \ll 1$. This is evidenced by the modest slopes observed in the corresponding region of the plot (small θ).

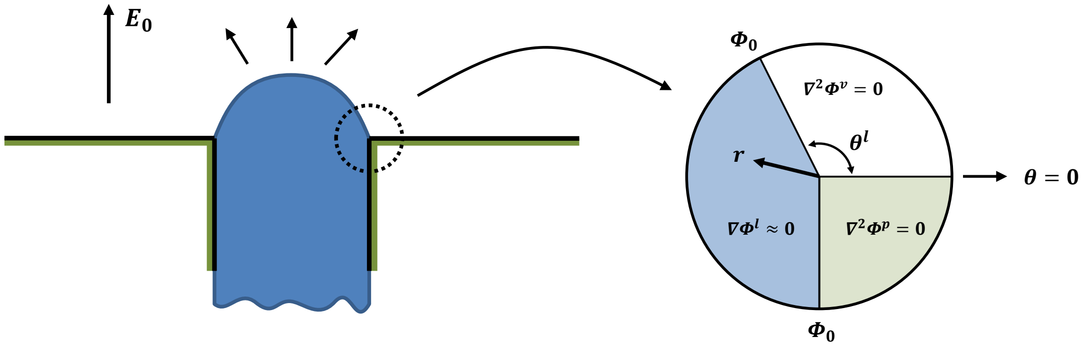

Figure 6-9: Geometric aspects of a discontinuous contact line. (**Left**): Electrically stressed meniscus supported by a dielectric plate. (**Right**): Zoomed view of the contact region where in general a geometric discontinuity might exist between the boundary of the fluid column and the part of the liquid-vacuum interface extending up toward the tip. Boundary and volume conditions are shown for a representative mathematical framework resolved in 2D polar coordinates. Owing to charge relaxation, the liquid boundaries are equipotential while the adjacent volumes simply obey Laplace.

of the scale of the contact line in relation to the characteristic emission area), this owes to the fact that the interface must be essentially fully relaxed even if emission is taking place far downstream at the location of the meniscus tip. Assuming that similar evaporation is not occurring nearby (more on this in the next section), the ratio of the local particle residence time τ^l_{res} to the electric relaxation time τ_e should be a fair measure of relaxation; i.e., a ratio $\gg 1$ should signify full relaxation in this case. Since $\tau^l_{res} \sim r/u$ and $u \propto r^{-2}$, the residence time must go like $\tau^l_{res} \propto r^3$ (where r is measured from the tip so that the contact line resides near $r \sim b_0$) and grow very rapidly away from the tip, where we have already shown that it still may not be comparable to τ_e (see chapter on orders of magnitude and scaling). As a result, the condition of equipotentiality for the fluid would seem to withstand scrutiny as a first approximation.

We can now construct a mathematical framework and examine the contact fields in greater quantitative detail. Very near to the contact it is probably fair to represent the problem in two-dimensional space so that we can invoke the polar Laplacian

$$\nabla^2\Phi = \frac{1}{r}\frac{\partial}{\partial r}\left(r\frac{\partial\Phi}{\partial r}\right) + \frac{1}{r^2}\frac{\partial^2\Phi}{\partial\theta^2} + \underbrace{\frac{\partial^2\Phi}{\partial z^2}}_{\approx 0} = 0 \tag{6.133}$$

where r is now the polar radius for a coordinate system centered about the contact point and θ is the corresponding angle (with the respect to the horizontal). As is conventional, we adopt here a product solution to this equation that is of the form $\Phi(r,\theta) = \boldsymbol{R}(r)\cdot\boldsymbol{\Theta}(\theta)$. After substituting this we find

$$\underbrace{\frac{r}{\boldsymbol{R}}\frac{d}{dr}\left(r\frac{d\boldsymbol{R}}{dr}\right)}_{m^2} + \underbrace{\frac{1}{\boldsymbol{\Theta}}\frac{d^2\boldsymbol{\Theta}}{d\theta^2}}_{-m^2} = 0 \tag{6.134}$$

The variables have been fully separated between the two terms and so the equality can only be satisfied when they differ by the constant m^2. Starting with the first term on the left, introducing this factor gives

$$\frac{d^2\boldsymbol{R}}{dr^2} + \frac{1}{r}\frac{d\boldsymbol{R}}{dr} - \frac{m^2}{r^2}\boldsymbol{R} = 0 \tag{6.135}$$

Trying solutions of the form $\boldsymbol{R} = Ar^n$ shows that $n = \pm m$. $\boldsymbol{R}$ must, therefore, take the general structure

$$\boldsymbol{R} = Ar^n + Br^{-n} \tag{6.136}$$

Similarly, for the second term in Eq. 6.134 we find

$$\frac{d^2\boldsymbol{\Theta}}{d\theta^2} + m^2\boldsymbol{\Theta} = 0 \tag{6.137}$$

which, by inspection, gives

$$\boldsymbol{\Theta} = C\sin(m\theta) + D\cos(m\theta) \tag{6.138}$$

for the general form of $\mathbf{\Theta}$. The boundary conditions for the simple problem illustrated in Fig. 6-9 are that the potential along the liquid surfaces must equal some reference value while the interface between the dielectric plate and vacuum should behave in the usual charge-free way (continuity in the normal component of the displacement field but discontinuity for the tangential part). Mathematically, these require that

$$\Phi^v\big|_{\theta=\theta^l} = \Phi_0 \tag{6.139}$$

$$\Phi^p\big|_{\theta=-\pi/2} = \Phi_0 \tag{6.140}$$

$$\Phi^v = \Phi^p, \text{ along } \theta = 0 \tag{6.141}$$

$$\left.\frac{\partial \Phi^v}{\partial \theta}\right|_{\theta=0} = \epsilon_p \left.\frac{\partial \Phi^p}{\partial \theta}\right|_{\theta=0} \tag{6.142}$$

Here, the superscripts v and p represents the fields in the vacuum and plate regions, respectively, while the dielectric strength of the latter is ϵ_p. The first two of these conditions are immediately satisfied if we choose

$$\Phi^v = r^m \sin\left[m\left(\theta^l - \theta\right)\right] \tag{6.143}$$

$$\Phi^p = C r^m \sin\left[m\left(\frac{\pi}{2} + \theta\right)\right] \tag{6.144}$$

for the two Laplacian regions. Notice that two constants, C and m, remain to be identified now. The condition for continuity of the potential at the dielectric interface, Eq. 6.141, yields the first of these

$$r^m \sin\left(m\theta^l\right) = C r^m \sin\left(\frac{\pi m}{2}\right) \Rightarrow C = \frac{\sin\left(m\theta^l\right)}{\sin\left(\frac{\pi m}{2}\right)} \tag{6.145}$$

and after substituting this relationship and imposing Eq. 6.142 we find that the separation constant is subject to

$$\tan\left(\frac{\pi m}{2}\right) + \epsilon_p \tan\left(m\theta^l\right) = 0 \tag{6.146}$$

Resolution of the field behavior near the discontinuous contact point is now contingent upon finding solutions to Eq. 6.146. Noting that the periodic nature of this relationship will facilitate a multitude of mathematically satisfactory m, we anticipate that only a small subset of these will be physically viable. These will likely be of the simple, low-order variety with $m \in (0, 1]$. To develop a more strict sense for the range of feasible m we might consider an equipotential Φ_c in the vicinity of the contact point

$$\Phi^v = r^m \sin\left[m\left(\theta^l - \theta\right)\right] = \Phi_c \tag{6.147}$$

As $\theta \to \theta^l$ the distance between the contact point and the curve traced by Φ_c will tend to infinity as we might expect. If we now begin to reduce θ the distance of the equipotential should begin to shrink and approach a finite value r as $\theta \to 0$ so that it may penetrate the dielectric. To observe the radial behavior of this curve we can reformulate Eq. 6.147 so that

$$r^m = \frac{\Phi_c}{\sin\left[m\left(\theta^l - \theta\right)\right]} \tag{6.148}$$

In the most extreme case (that of a conducting plate), r might become unbounded again as we reduce θ, but only at exactly $\theta = 0$. Based on this observation we can see that physical solutions for m are those which prevent Eq. 6.148 from becoming singular on $\theta \in (0, \theta^l)$. This requires that $m(\theta^l - \theta) < \pi$, where the left-hand side reaches a maximum as $\theta \to 0$. The relationship

$$m < \frac{\pi}{\theta^l} \tag{6.149}$$

is, therefore, the one that ensures "real" solutions. Recalling Eq. 6.146, we note that the function $f = \tan(\pi m/2) + \epsilon_p \tan(m\theta^l)$ is positive definite for small m (assuming, of course, that the separation constant is positive) and only crosses the line $f = 0$ between subsequent singularities (precluding $m = 0$, which is the trivial solution). From the cosine factors in the denominator, these occur at

$$m = n, \ \mathrm{n} = 1, 3, 5, ... \tag{6.150}$$

$$m = \frac{\pi n}{2\theta^l}, \ \mathrm{n} = 1, 3, 5, ... \tag{6.151}$$

Solutions to Eq. 6.146 that satisfy relationship 6.149 are sought between the two smallest of these singular m-values. The results from this process are plotted in Fig. 6-10 as a function of the scaled angle $2\theta^l/\pi$ and with the dielectric strength ϵ_p as a parameter. The limiting case $\epsilon_p \to \infty$ is shown in solid black and is characterized by two discontinuous branches. For $\theta^l < \pi$, the simplest solution involves $\tan(\pi m/2) \to -\infty$ and requires that $m \to 1$ from the top. In other words, $m \to 1^+$ and remains constant for all θ^l in this range. For $\theta^l > \pi$, the solution $m = \pi/\theta^l$ becomes appropriate. Note that this is identical to the boundary for "physical" solutions which is also shown by a dashed line. The remaining curves represent finite ϵ_p and show that the field at the contact line is generally bounded for $\theta^l < \pi/2$. This is because $\partial\Phi^v/\partial r \propto r^{m-1}$ and m is greater than unity for these angles. On the other hand, m dips below unity when $\theta^l < \pi/2$ and this suggests that the contact line begins to harbor a divergent field, albeit one of the relatively weak variety. As it turns out, the field is still integrable over the polar radius r. Observe that

$$\int_0^r \left(r'\right)^{m-1} dr' \to \frac{1}{m} r^m \tag{6.152}$$

which is always finite, regardless of the integration bounds. Recognizing that the same is true for the square of the field, we see that it should still be possible to com-

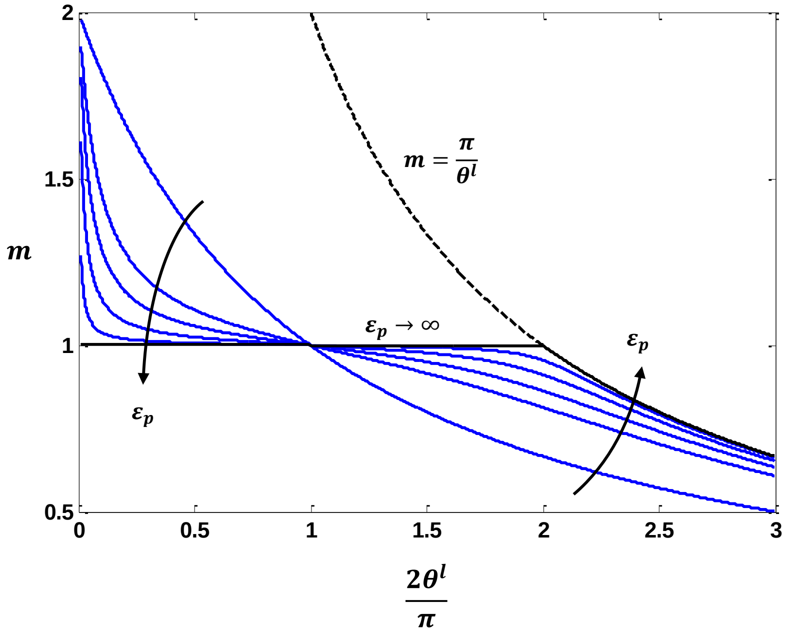

Figure 6-10: Simple solutions to the problem of a discontinuous contact line in polar coordinates. The separation constant m is plotted as a function of the scaled contact angle $2\theta^l/\pi$ with ϵ_p as a parameter. The arrows indicate the direction of increasing value for $\epsilon_p =$[1,5,10,25,100,∞] while the dashed line represents the upper bound for "physical" solutions. Recognizing that the field at the liquid interface $E_n^v \propto r^{m-1}$, we see from the curves that $\theta^l < \pi/2$ ensures unconditionally bounded fields. On the other hand, when $\theta^l > \pi/2$ the m dip below unity and give rise to a singular field at the contact point where $r \to 0$. This is the case for all permittivities but the limiting value $\epsilon_p \to \infty$, which does not support a singularity until $\theta^l > \pi$.

pute currents, force densities, etc. along the contact line in spite of its inconvenient behavior. In particular, the former is of interest for present purposes (the current) and in the next section we consider whether or not the singularity could meaningfully contribute to evaporation.

6.3.3 Emission from the contact line

The singular fields we have found suggest that evaporation of the liquid might occur not just at the tip of the meniscus but also around its contact line. In order to determine whether the fractional contribution of the current emanating from the latter is significant we need to revisit the model from the last section. The way it is formulated omits any characteristic lengths or fields and so we first need to rectify this by writing the modified distributions

$$\Phi^v = Ar^m \sin\left[m\left(\theta^l - \theta\right)\right] \tag{6.153}$$

$$\Phi^p = Br^m \sin\left[m\left(\frac{\pi}{2} + \theta\right)\right] \tag{6.154}$$

where A is a new constant that we can use to enforce an additional boundary condition. Before introducing this condition, notice that these field distributions still allow for $\Phi = 0$ on the liquid surfaces ($\theta = \theta^l$ and $\theta = -\pi/2$) and, similarly, that a dielectric interface at $\theta = 0$ with

$$\Phi^v = \Phi^p \tag{6.155}$$

$$\frac{\partial \Phi^v}{\partial \theta} = \epsilon_p \frac{\partial \Phi^p}{\partial \theta} \tag{6.156}$$

still requires the separation constant m to obey

$$\tan\left(\frac{\pi m}{2}\right) + \epsilon_p \tan\left(m\theta^l\right) = 0 \tag{6.157}$$

just as before. In view of this, the values presented in Fig. 6-10 should be germane to what follows. The task now is to resolve the new constant A through an appropriate boundary imposition. This is facilitated in part by noting that the influences of the strong fields surrounding the contact line are likely very localized. Anecdotally, this notion would seem to be supported by photographic images of steady Taylor cones atop capillary tubes where the structure of the anchoring region is not noticeably perturbed in spite of sharp geometric transitions between the liquid and the feeding tube [92, 93]. Given that these interfaces seem to globally adhere to the nominal Taylor angle, even near the anchoring point where there could be locally divergent fields, the conclusion must be that the length scale over which these fall off must be very small in comparison to the characteristic scale of the full meniscus. With this in mind, we might formulate the condition

$$E_n^v\left(r = \alpha b_0\right) \sim \sqrt{\frac{4\gamma}{\epsilon_0 b_0}} \tag{6.158}$$

where $\alpha < 1$ is some number ensuring that the characteristic length scale for field dilution is smaller than the characteristic scale of the meniscus, b_0. The term on the right-hand side is the characteristic field corresponding to the contact radius while E_n^v follows from

$$E_n^v = -\frac{1}{r}\left.\frac{\partial \Phi^v}{\partial \theta}\right|_{\theta=\theta^l} = \frac{mA}{r^{1-m}} \tag{6.159}$$

Notice that $m < 1$, which is prerequisite for singular fields, already ensures that the effects of the contact line vanish very far away, where $r \to \infty$. The function of the boundary condition (and specifically the number α), therefore, is simply to mediate the rate at which attenuation should occur. After applying it we find

$$\sqrt{\frac{4\gamma}{\epsilon_0 b_0}} = \frac{mA}{(\alpha b_0)^{1-m}} \Rightarrow A = \frac{(\alpha b_0)^{1-m}}{m}\sqrt{\frac{4\gamma}{\epsilon_0 b_0}} \tag{6.160}$$

and so the field along the interface becomes

$$E_n^v = \left(\frac{\alpha b_0}{r}\right)^{1-m}\sqrt{\frac{4\gamma}{\epsilon_0 b_0}} \tag{6.161}$$

This is a distribution that we can now use to estimate the current produced by evaporation along the contact line. Recalling the conduction limitations discussed in the earlier chapters we can assume $j \sim kE_n^v/\epsilon_r$ for the prevailing current density. Combining this with the differential area $dA \sim 2\pi b_0 dr$ gives

$$dI \sim 2\pi b_0 \frac{k}{\epsilon_r}\sqrt{\frac{4\gamma}{\epsilon_0 b_0}}\left(\frac{\alpha b_0}{r}\right)^{1-m} dr \tag{6.162}$$

for the differential current contribution. The aggregated current emanating from the contact region should be the integral of Eq. 6.162 from $r = 0$ to $r = r_c^*$, where the latter is the location at which the contact field approaches the characteristic one for ion evaporation, E^*. From Eq. 6.161 we have that

$$E^* \sim \left(\frac{\alpha b_0}{r_c^*}\right)^{1-m}\sqrt{\frac{4\gamma}{\epsilon_0 b_0}} \tag{6.163}$$

The critical field E^* is related to the curvature at the tip of an evaporating meniscus. Since $E^* \sim \sqrt{4\gamma/\epsilon_0 r^*}$, where r^* is the scale for the tip, we can substitute and find

$$r_c^* \sim \alpha b_0 \left(\frac{r^*}{b_0}\right)^{\frac{1}{2(1-m)}} \tag{6.164}$$

The ratio of this length to r^* is then

$$\frac{r_c^*}{r^*} \sim \alpha\left(\frac{r^*}{b_0}\right)^{\frac{2m-1}{2(1-m)}} = \alpha B^{\frac{2m-1}{2(1-m)}} \tag{6.165}$$

The case of $B \gtrsim 1$ is trivial for the present purposes and has already been investigated to an extent. We are primarily interested in the less certain situation in which the scale of the full meniscus is much larger than that of the usual emission area at its apex. By definition, this requires that $B \ll 1$. When this case prevails, the exponent in Eq. 6.165 becomes very important. For example, in the event that $m \to 1/2$ (corresponding to the strongest singularities we might expect to see, relatively speaking), $(2m-1)/(2m-2) \to 0$ and the ratio of the scales is essentially tantamount to α, which is mostly unknown still. Depending upon how small it is, this may or may not make r_c^* much less than r^*. At the opposite end of the spectrum, however, where $m \to 1$ for less divergent fields, we see that the exponent $(2m-1)/(2m-2) \to \infty$

causing r_c^* to vanish. Obviously, this would preclude any meaningful emission.

Although we now have some qualitative sense for how big the emission zone around the contact line could be, the relative current that could be evaporated there remains unclear. This owes to the disparity in activated areas (observe that $A \sim 2\pi b_0 r_c^*$ around the contact line while $A \sim 2\pi (r^*)^2$ at the tip) and also the drastic difference in driving fields ($E \to \infty$ over parts of the contact line while $E \sim E^*$ at the tip). To resolve the issue definitively we can now integrate Eq. 6.162 over the appropriate span

$$I_c^* \sim 2\pi b_0 \frac{k}{\epsilon_r} \sqrt{\frac{4\gamma}{\epsilon_0 b_0}} \left(\alpha b_0\right)^{1-m} \int_0^{r_c^*} r^{m-1} dr \tag{6.166}$$

which results in

$$I_c^* \sim 2\pi b_0 \frac{k}{\epsilon_r} \sqrt{\frac{4\gamma}{\epsilon_0 b_0}} \left(\alpha b_0\right)^{1-m} \cdot \frac{\left(r_c^*\right)^m}{m} \tag{6.167}$$

After substituting for r_c^*

$$I_c^* \sim 2\pi b_0^2 \frac{\alpha k}{m \epsilon_r} \sqrt{\frac{4\gamma}{\epsilon_0 b_0}} B^{\frac{m}{2(1-m)}} \tag{6.168}$$

In an effort to compare this to the characteristic current that might be produced at the tip of the meniscus, I^*, we can write

$$I^* \sim 2\pi \left(r^*\right)^2 k E^* \sim 2\pi \left(r^*\right)^2 \frac{k}{\epsilon_r} \sqrt{\frac{4\gamma}{\epsilon_0 r^*}} \tag{6.169}$$

If we now take the ratio of I_c^* to this current we find

$$\frac{I_c^*}{I^*} \sim \frac{\alpha}{m} B^{\frac{4m-3}{2(1-m)}} \tag{6.170}$$

The number α is somewhat unknown but it is probably safe to say that even if α/m approaches unity, corresponding to a very strong singularity, it can never be much greater. In all likelihood it could be that $\alpha/m \ll 1$ very often; however, the attendant ambiguity requires that we seek recourse if we are to quantify the ratio from Eq. 6.170 in any way. Fortunately, the exponent over B leads to a high degree of nonlinearity that we can exploit to examine the essential behavior of I_c^*/I^* with greater certainty. Notice that when $m \to 1/2$ in extreme cases, the exponent $(4m-3)/(2-2m) \to -1$ and B ends up being inverted. Since we are considering the regime in which $B \ll 1$, this would suggest that the current emanating from the contact line could actually be measurable in comparison to that which originates from the tip of the meniscus, or even dominate. At the other end of the spectrum, however, when $m \to 1$ we see $(4m-3)/(2-2m) \to \infty$ which says that the contact current is completely suppressed. It would appear then that m, and therefore the contact angle θ^l, are critical in determining the emission behavior.

In Fig. 6-11 we plot the nonlinear term B^f, where f is the exponent $(4m-3)/(2-2m)$, as a function of the separation constant m with the scale ratio B as a parameter.

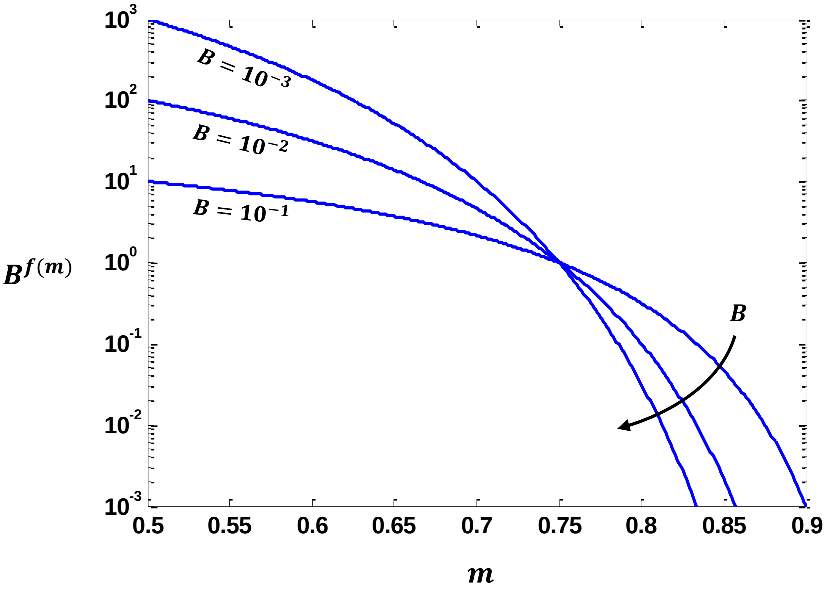

Figure 6-11: Nonlinear function $B^{f(m)}$ as a function of m with the meniscus scale factor B as a parameter. The exponent $f(m)$ is defined as $f(m) = (4m-3)/(2-2m)$ while the arrow indicates the direction of decreasing B for several values that are explicitly shown. There is a crossover field value $m = 3/4$ above which B^f is strongly suppressed and below which it is amplified.

As expected we see that small m could amplify the contribution of the contact current while larger m must suppress it very strongly. Also notice that in all cases there is a crossover value $m = 3/4$ at which $B^f \to B^0 \to 1$.

The problem now calls for us to revisit the $m - \theta^l$ relationship so that we can determine the conditions under which m will be greater than the crossover field and the conditions under which it will be smaller. These should tell us when to anticipate emission from the contact line. In Fig. 6-12 we plot the subset of solutions to Eq. 6.146 corresponding to $\theta^l \in [\pi/2, \pi]$. Notice, however, that unlike Fig. 6-10 the abscissa is now θ_c. We define this here as

$$\theta_c = \theta^l - \frac{\pi}{2} \tag{6.171}$$

It is shown in units of degrees and might be interpreted as the internal half-angle of the meniscus in the event that it is a perfect cone. For example, $\theta_c = 49.2°$ would indicate a classical Taylor structure. Based on the results we can see that for nearly all ϵ_p the m-values remain above 3/4, at least within the range of delineated contact angles. The lone exception is $\epsilon_p = 1$ (a vacuum surrounding) which crosses over at $\theta_c \approx 60°$. This suggests that ideal Taylor cones are likely immune to contact evaporation regardless of the anchoring media. Also note that $\epsilon_p \sim$ 5-10 is loosely representative of many dielectrics of interest and that contact emission from these would appear to be strongly suppressed.

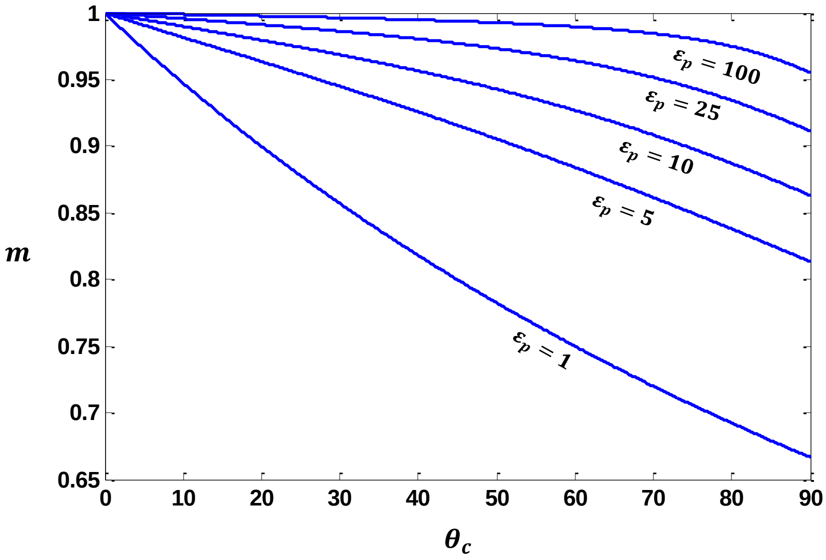

Figure 6-12: Separation constant m as a function of cone angle $\theta_c \in [0, \pi/2]$ (shown in units of degrees) with ϵ_p as a parameter. The results suggest that contact emission from many dielectric plate media is likely strongly suppressed as m is well above the crossover value of 3/4 in nearly all cases. The lone exception involves $\epsilon_p = 1$, where $m = 3/4$ corresponds to $\theta_c \approx 60^\circ$, an angle greater than that of the classical Taylor structure.

6.4 Numerical methodology

The results from the last several sections suggest that the fields surrounding menisci attached to dielectric anchoring media have slight morphological differences when compared to those of perfectly conducting plates. This is particularly true of the region in the immediate vicinity of the contact line, where dielectric materials seem to permit a field that is not only non-zero, but possibly singular. In spite of this, we have shown that attendant evaporation should be relatively limited in comparison to the currents that are characteristic of the meniscus tip, at least in the case of ionic liquid working fluids.

With these issues in mind, we will choose here to further reduce the rich parameter space of the generalized free-volume problem by restricting our attention to conducting anchoring media. Although this may preclude us from identifying some of the finer nuances of certain emission architectures (e.g. menisci at the end of thin, dielectric capillary tubes), it is likely that we will still capture the essential physics. In the sections that follow we outline a procedure for using a commercial finite-element (FEM) package, Comsol, to solve the reduced problem in a self-consistent way. This begins with a brief conceptual overview of the numerical protocol and continues with discussions on how the various facets of the model (volume equations, boundary conditions, etc.) are integrated within Comsol's specific software environment. To conclude, we address the inherently iterative nature of the process with the introduction of an interfacial propagation strategy.

6.4.1 Overview

Figure 6-13 presents a conceptual overview of the numerical process we will use to identify steady, axisymmetric solutions to the generalized free-volume problem. We will work in a cylindrical domain similar to that which is shown in Fig. 6-1 (origin of the vertical axis coincident with the plane defined by the top of the plate) and start by specifying several parameters of interest (i.e. values for the various degrees of freedom in the parameter space). These include the downstream field $\hat{E}_0$, the feeding or reservoir pressure $\hat{P}_r$, the feed impedance C_r, as well as a fixed set of intrinsic fluid properties (nominal conductivity, surface tension, solvation energy, etc.). Additionally, we will input an initial "guess" as to the topographical profile of the interface and any useful information from previous simulations that might help expedite convergence for the run at hand.

Once all of the parameters have been chosen, including the geometry, the process calls for us to solve the various physics in sequence. While some packages like Comsol offer multi- or coupled-physics simulation capabilities that theoretically allow for these to be solved concurrently, for logistical and computational reasons it will be easiest for us to utilize the piecemeal approach. This begins with the solution of the electrical equations, where we solve Laplace in the vacuum region and charge conservation $\nabla \cdot \vec{j} = 0$ in the liquid (also note that the potential in the plate is now spatially uniform since we are considering conducting substrates, and that this obviates the need for numerical treatment in the attendant subdomain). This is followed by solu-

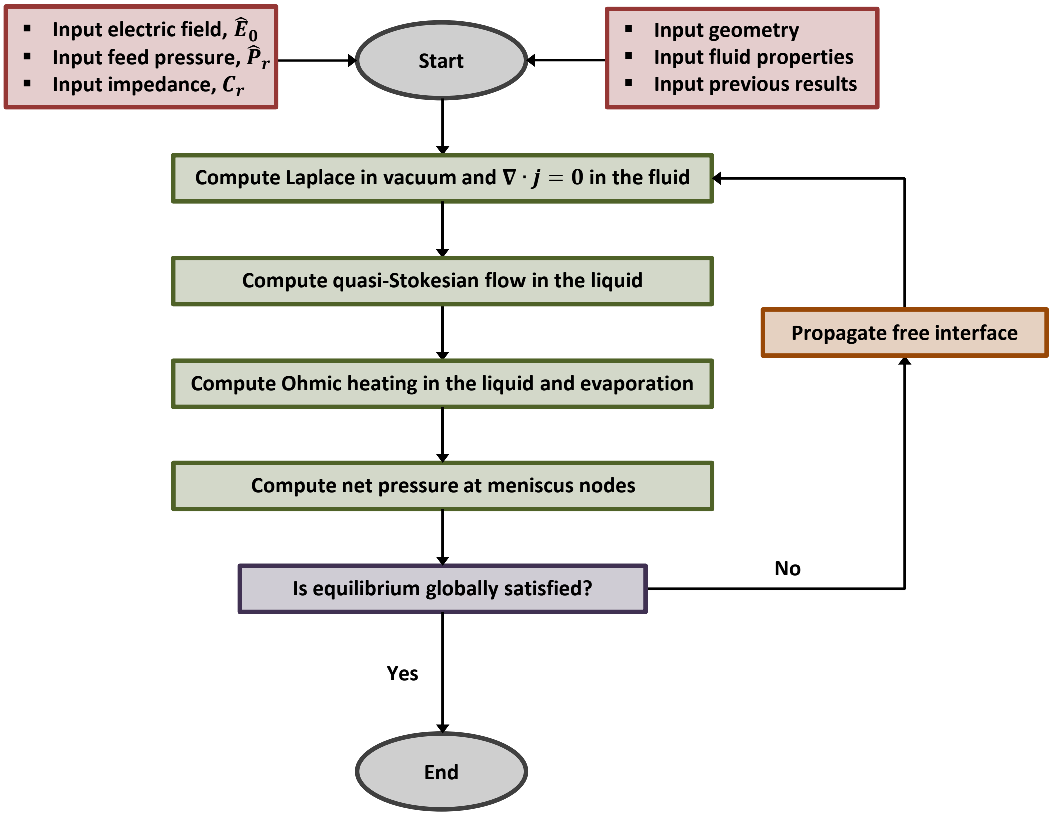

Figure 6-13: Conceptual framework for numerical solution procedure to the generalized free-volume problem. We start by specifying topographical characteristics of the free-interface and values of interest from the parameter space. The computational scheme then proceeds with sequential FEM solutions to the various physics (electrical, hydraulic, heat transfer) and an integrated estimate of the instantaneous current. The results are used to investigate the mechanical balance at the interface before propagating it if necessary.

tions to the Navier-Stokes and heat transfer relations in the liquid. After all of the volume physics have been handled, at which point we should have all of the necessary electrical/hydraulic/thermal field information, we can invoke the kinetic evaporation law at the interface and perform a surface integration to determine an approximate current. This will be used in part to determine the distribution of net stress across the interface before iterating (in the event that the interface requires perturbation) or terminating the loop (in the event that global equilibrium has been reached). Also note that the notion of a "net" pressure, which we have yet to introduce, is specific to our steady-state approach and will be expounded upon as part of the interfacial propagation discussion at the end of this chapter.

6.4.2 Comsol integration

Solutions to all of the volume physics will be carried out in the Comsol environment. In this section we detail specific aspects of the relevant solver configurations, which include but are not limited to boundary declarations and mesh construction. It should also be pointed out that Comsol requires us to work in physical units, and that as a result we will often reference dimensional quantities during this process. Keep in mind, however, that these dimensional calculations will be restricted to only the subroutines involving FEM. In other words, we will convert to units before calling Comsol and then immediately convert back to dimensionless values before examining the stress balance and propagating the interface, if necessary, since these will be managed elsewhere (Matlab).

Electrodynamics

For the electrical calculations we start by setting the voltage on the downstream counter-electrode. Assuming we want to impose a uniform downstream field E_0, this requires that

$$\Phi^v \left(z = z_0\right) = -V = E_0 z_0 \tag{6.172}$$

where z_0 is the distance between the plate and the top electrode. Given that the field far from the meniscus should approach E_0 asymptotically, this Dirichlet condition should provide for a reasonable facsimile of a uniform, axially-directed field in the corresponding vicinity so long as $z_0 \gg b_0$. To isolate the meniscus at infinity we will also take

$$\vec{n} \cdot \vec{E}^v = 0 \tag{6.173}$$

along the vertical edge of the solution domain at $r = r_p$. Here, $\vec{n}$ is the unit normal for the corresponding surface and $r_p \gg b_0$. All remaining boundaries, excepting that of the meniscus, are set to the reference potential $\Phi_0 = 0$.

The specifications for the liquid-vacuum interface and charge conservation in the fluid are somewhat more involved. With respect to the former, the easiest approach is to specify the distribution of surface charge densities. From the earlier discussion on charge transport we have that $j_e = kE_n^l + j_{conv}$, which says that the local flux of evaporating charges must be balanced by local conduction and convection. Recalling the kinetic evaporation law, we can rewrite this in terms of σ as

$$\sigma = \frac{h}{k_B T} \exp\left(\frac{1}{k_B T}\left\{\Delta G - \sqrt{\frac{q^3 E_n^v}{4\pi\epsilon_0}}\right\}\right) \cdot \left[kE_n^l + j_{conv}\right] \tag{6.174}$$

Note that Comsol provides access to the normal and tangential unit vectors on each surface, internal or otherwise. In axisymmetric cylindrical space it defines these as

$$\vec{n} = n_r \vec{i}_r + n_z \vec{i}_z \tag{6.175}$$

$$\vec{t} = t_r \vec{i}_r + t_z \vec{i}_z \tag{6.176}$$

and so anytime we require, for example, E_n^v and E_n^l we are writing

$$E_n^v = E_r^v \cdot n_r + E_z^v \cdot n_z \tag{6.177}$$

$$E_n^l = E_r^l \cdot n_r + E_z^l \cdot n_z \tag{6.178}$$

where $\vec{E}^v = E_r^v \vec{i}_r + E_z^v \vec{i}_z$ and $\vec{E}^l = E_r^l \vec{i}_r + E_z^l \vec{i}_z$ are the fields stored by Comsol for the vacuum and liquid regions, respectively. Also notice that the convection current j_{conv} is left in its unexpanded form. This is because we solve the electrical equations before the hydraulic ones during each iteration, and the fact that the convected current is some function of the latter. In view of this we specify it as an external input and provide $j_{conv} = j_{conv}(r)$ to the electrical solver where $j_{conv}(r)$ is a radially-resolved estimation taken from the most recent iteration. For example, during the $(i-1)$ iteration we calculate from Eq. 6.21

$$j_{conv}^{i-1} = -\frac{1}{r}\frac{\partial}{\partial s}\left(v_t \sigma r\right) \tag{6.179}$$

which becomes the input to the interfacial condition of Eq. 6.174 for the i^{th} iteration. Near the tip, we address the apparent singularity by expanding this relationship so that

$$-\frac{1}{r}\frac{\partial}{\partial s}\left(v_t \sigma r\right) \rightarrow -\frac{\partial}{\partial s}\left(v_t \sigma\right) - \frac{v_t \sigma}{r}\frac{\partial r}{\partial s} \tag{6.180}$$

In the limit as $r \rightarrow 0$ we have $\partial r / \partial s \rightarrow 1$ and $v_t \rightarrow 0$ by symmetry. Recognizing that

$$\lim_{r \rightarrow 0} \frac{v_t \sigma}{r} \rightarrow \frac{\sigma \frac{\partial v_t}{\partial r} + v_t \frac{\partial \sigma}{\partial r}}{1} \rightarrow \sigma \frac{\partial v_t}{\partial r} \tag{6.181}$$

after application of L'Hôpital's, this result gives

$$\lim_{r\to 0} j_{conv} \to -2\sigma \frac{\partial v_t}{\partial r} \tag{6.182}$$

at the exact tip of the meniscus. Repeated application of this procedure should offer numerical convergence for the σ condition in our FEM calculations, especially in view of the small convection contribution that we anticipate.

The final condition that needs to be accounted for is charge conservation $\nabla \cdot \vec{j} = 0$ in the fluid. We do this by invoking Ohm's law $\vec{j} = k\vec{E}^l$ and expanding so that

$$\nabla \cdot \vec{j} = 0 \to k\nabla \cdot \vec{E}^l + (\nabla k) \cdot \vec{E}^l = 0 \tag{6.183}$$

As before, we take a linear approximation for thermally-induced modifications to the prevailing electrical conductivity, $k = k_0 + k'\Delta T$. Substituting this

$$\nabla \cdot \vec{E}^l = -\frac{k'\left(\nabla T\right) \cdot \vec{E}^l}{k_0 + k'\Delta T} \tag{6.184}$$

The module in Comsol that directly handles currents is somewhat inconvenient. In lieu of it, we wish to make use of the basic electrostatic interface. This can be done by recognizing that the right-hand side of Eq. 6.184 looks similar to a space charge (ρ_f) since $\nabla \cdot \vec{E} = \rho_f/\epsilon$. With this is mind, we give as an external input to the electrostatic interface

$$\rho_f\left(r, z\right) = -\epsilon_0\epsilon_r \frac{k'\left(\nabla T\right) \cdot \vec{E}^l}{k_0 + k'\Delta T} \tag{6.185}$$

where the temperature map $T(r, z) = T(r, z)^{i-1}$ is again an estimation from the previous iteration in the numerical sequence. This satisfies charge continuity *per se* and requires no further attention.

Hydrodynamics

Hydrodynamics calculations are restricted to the liquid subdomain, where we will make use of the laminar flow module in Comsol. The first condition that needs to be imposed is the pressure along the bottom horizontal boundary of the fluid channel. Owing to the linearity of the Stokes equation, in all cases we will take the reference value $P = 0$. The astute reader may note that, in general, this represents a shift from condition reflected in Eq. 6.35. We will address this issue while discussing interfacial propagation in the corresponding section.

In cylindrical space, the laminar flow module offers the built-in velocity vector

$$\vec{u} = u\vec{i}_r + v\vec{i}_\theta + w\vec{i}_z \tag{6.186}$$

The next condition that must be satisfied is "no-slip" along the vertical wall of the channel. In terms of the velocity components, this requires

$$u = 0, \text{ and} \tag{6.187}$$

$$w = 0 \tag{6.188}$$

at that boundary, which we enforce with Comsol's built-in option. The final condition defining the flow field involves the liquid-vacuum interface, where we might specify two of three potential constraints. These involve (1) the normal component of interfacial traction vector, $\vec{n} \cdot \boldsymbol{\tau} \cdot \vec{n}$; (2) the tangential component of the interfacial traction vector, $\vec{t} \cdot \boldsymbol{\tau} \cdot \vec{n}$; or (3) the normal component of the flow velocity, $\vec{u} \cdot \vec{n} = u \cdot n_r + w \cdot n_z$. In studies of the dynamics of the surface motion it is most appropriate to use the first two of these and to take $\vec{n} \cdot \boldsymbol{\tau} \cdot \vec{n}$ directly from the stress balance. For present purposes, however, we are only interested in steady solutions and so it will be easiest to make use of the latter two. From the appendix, the fluid stress in axisymmetric cylindrical space reduces to

$$\boldsymbol{\tau} = -p\boldsymbol{I} + \mu \begin{pmatrix} 2\frac{\partial u}{\partial r} & \left(\frac{\partial u}{\partial z} + \frac{\partial w}{\partial r}\right) \\ \left(\frac{\partial u}{\partial z} + \frac{\partial w}{\partial r}\right) & 2\frac{\partial w}{\partial z} \end{pmatrix} \tag{6.189}$$

where u_r and u_z (or w_r and w_z) will be used to denote the respective spatial derivatives hereafter. For the tangential stress, the hydrostatic pressure term drops out and we find that

$$\vec{t} \cdot \boldsymbol{\tau} \cdot \vec{n} = 2\left(u_r n_r t_r + w_z n_z t_z\right) + \left(u_z + w_r\right)\left(n_z t_r + n_r t_z\right) \tag{6.190}$$

Therefore, to handle the electrical shear we specify in Comsol

$$\sigma\left(E_r^v t_r + E_z^v t_z\right) = 2\left(u_r n_r t_r + w_z n_z t_z\right) + \left(u_z + w_r\right)\left(n_z t_r + n_r t_z\right) \tag{6.191}$$

where σ is the value calculated from the electrical equations during the current iteration. For the next condition, that of the normal flow at the interface, we recognize that only evaporation can cause $\vec{u} \cdot \vec{n} \neq 0$ in the steady-state. Observe that, when the evaporation is nonzero the flow immediately inside the interface must be

$$\vec{u} \cdot \vec{n} = \frac{j_e}{\rho\left(q/m\right)} \tag{6.192}$$

in order to satisfy mass continuity, where j_e is the local flux of emitted charge (A/m^2). With this in mind, we offer to Comsol the ancillary condition

$$u n_r + w n_z = \frac{j_e}{\rho\left(q/m\right)} \tag{6.193}$$

again using the j_e calculated from the current iteration.

Heat transfer

The heat transfer calculations are also restricted to the liquid subdomain. The boundary conditions are very simple and involve the Dirichlet specifications $T = T_0$, where T_0 is a fixed reference, along the bottom and vertical walls of the fluid channel in the computational domain. The meniscus is a thermal insulator to first approximation and requires that $\nabla T = 0$ along its boundary. This is easily applied with a built-in option provided by Comsol.

For the transport equation in the volume, we simply use

$$\dot{q} = \left[k_0 + k'\left(T - T_0\right)\right] \vec{E}^l \cdot \vec{E}^l \tag{6.194}$$

as the source term (W/m^3), where the field $\vec{E}^l$ comes from the electrical calculation in the current iteration. Similarly, the convection term uses $\vec{u}$ from the hydraulic step in the current iteration.

Meshing

For convenience and efficiency we take advantage of Comsol's built-in meshing engine to discretize the solution domain. Generation requires declaration of no more than four sizing parameters. These include

- **hmax:** the maximum allowable element size in the domain;
- **hmin:** the minimum allowable element size in the domain;
- **hgrad:** the maximum allowable growth rate between adjacent elements (e.g. hgrad=2 allows for an element to be twice as large as a neighbor); and
- **hcurve:** a factor controlling the maximum allowable element size along a curved boundary (e.g. hcurve=0.1 requires all elements along a curved boundary to be less than ten times smaller than the local radius of curvature of that boundary).

For accuracy we create one mesh for the electrostatic calculations and another for the hydraulic and heat transfer calculations during each computational cycle. This is helpful in that it allows us to populate a denser mesh for the hydraulics, which benefit more from the smaller elements, without slowing down the electrical counterpart. Nominal settings for the electrical mesh are $hmax = b_0/4$ (where b_0 is the meniscus contact radius), $hmin = 10^{-11}$ (arbitrarily small so as not to limit resolution near the meniscus tip), $hgrad = 1.25$, and $hcurve = 0.01$. We also call for a single "adaption" in which we offer the functional $E^v \times E^v$ along the liquid-vacuum interface. This allows Comsol to selectively distribute additional elements near the interface to minimize an internal estimate of the error for the functional. It effectively serves as a systematic mesh refinement step that, within reason, maximizes accuracy in the calculation of the vacuum fields that govern the meniscus. Nominal settings for the hydraulic and heat transfer mesh are $hmax = b_0/25$, $hmin = 10^{-11}$, $hgrad = 1.25$, $hcurve = 0.005$, and include no adaption step.

6.4.3 Interfacial propagation

In a previous section we modified the pressure at the base of the liquid channel in the computational domain and applied the reference value $P = 0$ instead of using the more correct condition described by Eq. 6.35. While we did this for convenience, it should only retain validity as long as we still communicate the actual pressure of the fluid coming from the feeding system to the meniscus in some way. To see how this can be done, consider the stress tensor for the liquid

$$\boldsymbol{\tau} = -p\boldsymbol{I} + \mu\left(\nabla\vec{u} + (\nabla\vec{u})^T\right) \tag{6.195}$$

At the interface, the p-term can be viewed as a record of the accumulated hydrostatic pressure between that location and as far upstream as the generating reservoir. In view of this, we can expand it by writing

$$\boldsymbol{\tau} = -\underbrace{\left(P_r - \frac{IR_h}{\rho\,(q/m)} - \Delta P_m\right)}_{P_B - \Delta P_m}\boldsymbol{I} + \mu\left(\nabla\vec{u} + (\nabla\vec{u})^T\right) \tag{6.196}$$

which shows that the hydrostatic pressure acting on the interface is simply the algebraic sum of P_B and an additional drop accrued within the small channel of fluid immediately beneath the meniscus (i.e., the drop between the bottom of the liquid column in the computational domain and the liquid-vacuum interface). The former of these could be of any magnitude owing to the arbitrary nature of the impedance R_h but we expect that latter to always be relatively insignificant as a result of the small capillary number $C_a \sim \mu u^*/\gamma$ that is typical of emission from pure ionic liquids. With this in mind, we isolate the comparatively important implications of the feed system by changing the balance of normal stresses at the interface so that

$$\boldsymbol{\tau}_n^e + \underbrace{P_r - \frac{IR_h}{\rho\,(q/m)}}_{P_B} - \vec{n}\cdot\boldsymbol{\tau}^m\cdot\vec{n} = \gamma\nabla\cdot\vec{n} \tag{6.197}$$

where $\vec{n}\cdot\boldsymbol{\tau}^m\cdot\vec{n}$ is now understood to mean the part of the fluid stress generated in the small channel of the computational domain only. For clarity, the modified tensor is given by

$$\boldsymbol{\tau}^m = -\Delta P_m\boldsymbol{I} + \mu\left(\nabla\vec{u} + (\nabla\vec{u})^T\right) \tag{6.198}$$

During FEM calculations, ΔP_m will be the algebraic difference between the hydrostatic pressure found at the interface and whichever reference pressure is provided for the fluid at the base of the channel. Consequently, it should be clear that the reference choice $P = 0$ given at that location is simply for numerical convenience.

With respect to the modified balance of normal stresses at the interface, Eq. 6.197, the surface tension during each computational iteration will be established by the chosen geometry, whatever that happens to be. The electrical stress will follow from the prevailing field distributions and P_B will be calculated using the instantaneous evaporation current (the integral of j_e over the meniscus). The remaining term in the balance, $\vec{n} \cdot \boldsymbol{\tau}^m \cdot \vec{n}$, will be calculated using the steady-state boundary conditions we have already discussed: namely, viscous balancing of the electrical shear on the interface and a distribution of normal velocities $\vec{u} \cdot \vec{n}$ tantamount to the local evaporation-induced speed $j_e/(\rho q/m)$. Unless the interface is of the exact equilibrium configuration, constructing the balance in this way will in general lead to a distribution of "net" pressures or "residues" such that

$$\boldsymbol{\tau}_n^e + P_B - \vec{n} \cdot \boldsymbol{\tau}^m \cdot \vec{n} - \gamma \nabla \cdot \vec{n} = \Delta P_d \tag{6.199}$$

This is a direct byproduct of the fact that we use steady-state boundary conditions to identify the fluid stresses. When the problem does not satisfy an exact mechanical equilibrium (which is what Eq. 6.197 represents), the interface should move and so ΔP_d can be interpreted as the pressure controlling the "dynamic", or transient, behavior of the meniscus. Although the dynamics of electrified menisci are sometimes of interest (see, for example, Higuera [62] or Suvorov [84]), we have already firmly established that in the present study we would like to focus solely upon solutions of the steady variety. Noting that these require $\Delta P_d \to 0$ at all points along the meniscus, in what follows we briefly introduce an interfacial perturbation method that will be useful in approaching this condition sequentially during our numerical iterations.

Consider an interface with an arbitrary distribution of surface tension pressures P_{st}^i, where i denotes the i^{th} computational iteration and $P_{st}^i = P_{st}^i(r)$ is a vector quantity of values defined at N discrete points r_j $(j = 1, 2, ..., N)$ between the symmetry axis and the contact line. In order to determine the spatial profile of the meniscus characterized by this distribution, $z = h(r)$, we can recall that $P_{st} = -\gamma \nabla \cdot \vec{n}$ and refer to the appendix where we show that for axisymmetric cylindrical space

$$P_{st} = -\gamma \nabla \cdot \vec{n} = -\gamma \left[\frac{\left(1 + h_r^2\right) h_r + r \cdot h_{rr}}{r \left(1 + h_r^2\right)^{3/2}} \right] \tag{6.200}$$

where the subscripted variables h_r and h_{rr} denote the first and second spatial derivatives of $z = h(r)$ with respect to the cylindrical radius. After rearranging this relationship we arrive at the 2nd-order nonlinear ODE

$$h_{rr} + \frac{\left(1 + h_r^2\right) h_r}{r} + \left(1 + h_r^2\right)^{3/2} \frac{P_{st}}{\gamma} = 0 \tag{6.201}$$

which can easily be integrated numerically for any distribution $P_{st} = P_{st}^i(r)$ (using, for example, the built-in Matlab Runge-Kutta solver ODE45). When we do this for the i^{th} iteration we find a profile $z = h^i(r)$ that can be used to conduct the necessary electrical/hydraulic/heating calculations before determining an attendant imbalance $\Delta P_d^i(r)$ from Eq. 6.199. The question now is how to begin driving $\Delta P_d^i \to 0$ globally, and one possible avenue is to modify slightly the distribution of surface tension stresses in order to cancel out a measure of the local net pressure. In other words, for the $(i + 1)$ iteration we might take

$$P_{st}^{i+1} = P_{st}^{i} + \beta \Delta P_d^i \tag{6.202}$$

where β is some relaxation parameter $\beta \in (0, 1]$ that can be used to control the rate at which we approach equilibrium during the iteration process and/or the numerical stability. In situations where the equilibrium interface is very well-defined and stable (when it is not too stressed by the field or significantly distorted) it might be safe to take β close to unity; however, during emission and when $B \ll 1$ the strong nonlinearity of the physics will undoubtedly necessitate $\beta \ll 1$ in order to circumvent numerical hiccups.

We expect that the judicious choice of β will provide for gradual reduction of excess pressure at the interface as we iterate in time. While we ideally desire to identify equilibrium configurations in which ΔP_d is identically zero at every observation point on the meniscus, in reality this will not be possible because of limitations such as machine precision and computational cost, among others. Finding the various equilibria is therefore an exercise in approximation that will require us to possess some notion of "closeness" to the real solutions and a corresponding termination condition that prevents us from having to iterate indefinitely. To develop one, albeit in a relatively crude way, we point to that fact that the low Reynolds numbers typified by emission from ionic liquids suggests the interplay between pressure and viscous forces (as formalized in the Stokes equation). By considering a hypothetical meniscus, or maybe some small section thereon, that is slightly statically imbalanced and subject to the dynamic pressure ΔP_d we can write

$$\Delta P_d \sim \mu \frac{u}{r} \tag{6.203}$$

where u is a measure of the local propagation speed for the interface and r is its characteristic length scale. Rearranged, this gives that $u \sim r\Delta P_d/\mu$. A good condition for proximity to an exact equilibrium might be that the distance traveled by the unbalanced one over some characteristic time scale should be much less than the local r. In other words,

$$u\tau \ll r \Rightarrow \frac{r\Delta P_d}{\mu}\tau \ll r \Rightarrow \frac{\Delta P_d}{\mu}\tau \ll 1 \tag{6.204}$$

From our earlier analyses we saw that the viscous-capillary time $\tau_v \sim \mu r/\gamma$ for the meniscus is likely the limiting one. If we insert this now for τ in the preceding relationship we find

$$\frac{\Delta P_d}{\mu}\frac{\mu r}{\gamma} \ll 1 \Rightarrow \frac{\Delta P_d}{(\gamma/r)} \ll 1 \tag{6.205}$$

which says that when the local pressure imbalance is small in comparison to the local capillary pressure the interface could be very near an equilibrium. This seems to make good sense but in practice we will sometimes find that the actual Laplace pressure (i.e., $\gamma\nabla \cdot \vec{n}$ rather than the approximate γ/r) can change signs somewhere between the tip and the anchoring location. This is because the fluid pressure, which can be below the vacuum level, in some places requires a negative Laplace pressure to compensate it, especially in regions of weak electrical field like the contact point. In order to avoid attendant numerical complication we could perhaps adopt the more conservative condition that the net local pressure must be small in comparison to the capillary pressure of the full meniscus since this will be the smallest characteristic surface tension for the problem. The termination condition is then

$$\frac{\Delta P_d}{P_c} = \Delta \hat{P}_d \leq P_\beta \tag{6.206}$$

where P_β is a number much less than one. When this condition is satisfied at all observation points r_j across the meniscus we can conclude that an approximate equilibrium has been reached.

6.5 Stability

The balance of normal stresses at the interface reads

$$\hat{\boldsymbol{\tau}}_n^e - \hat{\boldsymbol{\tau}}_n^v = \hat{\boldsymbol{\tau}}^{st} \tag{6.207}$$

where $\hat{\boldsymbol{\tau}}_n^v$ is the fluid stress (hydrostatic plus viscous) and $\hat{\boldsymbol{\tau}}^{st}$ is the surface tension, in all cases static or dynamic. When a mechanical equilibrium is reached, the balance becomes

$$\hat{\boldsymbol{\tau}}_{n,0}^e - \hat{\boldsymbol{\tau}}_{n,0}^v - \hat{\boldsymbol{\tau}}_0^{st} = 0 \tag{6.208}$$

where $\hat{\boldsymbol{\tau}}_{n,0}^v$ is by definition the steady part of the fluid stress. Now imagine a scenario in which an interface that is initially at rest is subjected to a distribution of morphological perturbations such that $\hat{\boldsymbol{\tau}}^{st} \to \hat{\boldsymbol{\tau}}_0^{st} + \delta\hat{\boldsymbol{\tau}}^{st}$. Owing to these surface perturbations, the electrical and hydraulic stresses will also experience slight excursions that lead to the modified balance

$$\underbrace{\hat{\boldsymbol{\tau}}_{n,0}^e - \hat{\boldsymbol{\tau}}_{n,0}^v - \hat{\boldsymbol{\tau}}_0^{st}}_{=0} + \delta\hat{\boldsymbol{\tau}}_n^e - \delta\hat{\boldsymbol{\tau}}_n^v - \delta\hat{\boldsymbol{\tau}}^{st} = \Delta\hat{P} \tag{6.209}$$

After subtracting out the equilibrium solution and dividing through by $\delta\hat{\boldsymbol{\tau}}^{st}$ we can see

$$\frac{\delta\hat{\boldsymbol{\tau}}_n^e}{\delta\hat{\boldsymbol{\tau}}^{st}} - \frac{\delta\hat{\boldsymbol{\tau}}_n^v}{\delta\hat{\boldsymbol{\tau}}^{st}} - 1 = \frac{\Delta\hat{P}}{\delta\hat{\boldsymbol{\tau}}^{st}} \tag{6.210}$$

Similar to what we found for the spheroidal problem, this tells us that the condition for stability is

$$\frac{\Delta\hat{P}}{\delta\hat{\boldsymbol{\tau}}^{st}} \leq 0 \Rightarrow \frac{\delta\hat{\boldsymbol{\tau}}_n^e}{\delta\hat{\boldsymbol{\tau}}^{st}} - \frac{\delta\hat{\boldsymbol{\tau}}_n^v}{\delta\hat{\boldsymbol{\tau}}^{st}} \leq 1 \tag{6.211}$$

although the condition must now be met at all points r_j that we are observing along the meniscus; i.e.

$$\left.\frac{\delta\hat{\boldsymbol{\tau}}_n^e}{\delta\hat{\boldsymbol{\tau}}^{st}}\right|_{r_j} - \left.\frac{\delta\hat{\boldsymbol{\tau}}_n^v}{\delta\hat{\boldsymbol{\tau}}^{st}}\right|_{r_j} \leq 1 \tag{6.212}$$

where $j = 1, 2, ..., N$. In other words, the excess or "dynamic" pressure $\Delta\hat{P}$ distributed around the interface must work to suppress the prevailing perturbations rather than exacerbate them.

In addition to physical stability it will be important to consider issues of a related numerical nature. For example, we will want to know whether our chosen iteration scheme will remain stable for (1) all instances in which physical stability of the interface should be expected to prevail, and (2) for instances in which equilibria exist but under physically unstable conditions, e.g. the upper solution branch of fixed-volume droplets in free space. To probe this problem, consider a situation in which we run our meniscus model for a given set of parameters and reach a perfect equilibrium at the $i-1^{st}$ computational iteration. During the next (i^{th}) iteration a small set of morphological perturbations $\delta\hat{\boldsymbol{\tau}}^{st}$ are introduced by either numerical error or external means (for example, by the human user). The stress balance for this iteration becomes

$$\delta\hat{\boldsymbol{\tau}}_n^{e,i} - \delta\hat{\boldsymbol{\tau}}_n^{v,i} - \delta\hat{\boldsymbol{\tau}}^{st,i} = \Delta\hat{P}^i \tag{6.213}$$

For this particular instance, the algebraic difference between the electrical and fluid stresses is $\delta\hat{\boldsymbol{\tau}}_n^{e,i} - \delta\hat{\boldsymbol{\tau}}_n^{v,i} = \chi(\delta\hat{\boldsymbol{\tau}}^{st,i})$, which permits us to write

$$(\chi - 1)\,\delta\hat{\boldsymbol{\tau}}^{st,i} = \Delta\hat{P}^i \tag{6.214}$$

Recalling our scheme for updating the interface, this requires for the following iteration that

$$\hat{\boldsymbol{\tau}}^{st,i+1} = \hat{\boldsymbol{\tau}}^{st,i} + \beta\,(\chi - 1)\,\delta\hat{\boldsymbol{\tau}}^{st,i} \tag{6.215}$$

The first two surface tension stress can be expanded in the form $\hat{\boldsymbol{\tau}}^{st,l} \to \hat{\boldsymbol{\tau}}_0^{st,l} + \delta\hat{\boldsymbol{\tau}}^{st,l}$. Applying this gives

$$\delta\hat{\boldsymbol{\tau}}^{st,i+1} = \delta\hat{\boldsymbol{\tau}}^{st,i}\,[1 + \beta\,(\chi - 1)] \tag{6.216}$$

from which we can easily identify the ratio of perturbation magnitudes from one iteration to the next

$$\frac{\delta\hat{\boldsymbol{\tau}}^{st,i+1}}{\delta\hat{\boldsymbol{\tau}}^{st,i}} = 1 + \beta\,(\chi - 1) \tag{6.217}$$

Physical stability requires $\chi < 1$ and from Eq. 6.217 we see that our numerical scheme will tend to suppress perturbations for such a condition. Conversely, physical stability will be lost for $\chi > 1$ and numerical stability will suffer concurrently. As a result, we should expect to find stable equilibria if and where they exist, and numerical deterioration otherwise.

On a final note, while the preceding methods should be more than sufficient for satisfying the scope of the study at hand, in the future it might be desirable to decouple the numerical and physical stabilities. In other words, it could be useful to make use of a routine that is capable of identifying unstable equilibria. Achieving this will likely require us to cast the stress balance equation as a nonlinear root-find problem, similar to what Wohlhuter [71] has done. For example, consider a meniscus that is not in static equilibrium so that its instantaneous normal stresses look like

$$\hat{\boldsymbol{\tau}}_n^{e,i} - \hat{\boldsymbol{\tau}}_n^{v,i} - \hat{\boldsymbol{\tau}}^{st,i} = \Delta \hat{P}^i \tag{6.218}$$

during the i^{th} computational iteration. For the $(i+1)^{st}$ iteration we can attempt to perturb the morphology such that

$$\underbrace{\hat{\boldsymbol{\tau}}_n^{e,i} - \hat{\boldsymbol{\tau}}_n^{v,i} - \hat{\boldsymbol{\tau}}^{st,i}}_{\Delta \hat{P}^i} + \delta\hat{\boldsymbol{\tau}}_n^{e,i} - \delta\hat{\boldsymbol{\tau}}_n^{v,i} - \delta\hat{\boldsymbol{\tau}}^{st,i} = 0 \tag{6.219}$$

which directly drives the excess pressure to zero at every point across the meniscus. Before we can solve for the appropriate distribution of perturbations we need to note that

$$\left.\delta\hat{\boldsymbol{\tau}}_n^{e,i}\right|_{r_j} \approx \sum_n \frac{\partial \hat{\boldsymbol{\tau}}_n^{e,i}(r_j)}{\partial \hat{\boldsymbol{\tau}}^{st,i}(r_n)} \delta\hat{\boldsymbol{\tau}}^{st,i}(r_n) \tag{6.220}$$

$$\left.\delta\hat{\boldsymbol{\tau}}_n^{v,i}\right|_{r_j} \approx \sum_n \frac{\partial \hat{\boldsymbol{\tau}}_n^{v,i}(r_j)}{\partial \hat{\boldsymbol{\tau}}^{st,i}(r_n)} \delta\hat{\boldsymbol{\tau}}^{st,i}(r_n) \tag{6.221}$$

These follow from a Taylor expansion truncated to linear order. After substituting these, at any point r_j we can write

$$\Delta \hat{P}^i(r_j) + \sum_n \left[\frac{\partial \hat{\boldsymbol{\tau}}_n^{e,i}(r_j)}{\partial \hat{\boldsymbol{\tau}}^{st,i}(r_n)} - \frac{\partial \hat{\boldsymbol{\tau}}_n^{v,i}(r_j)}{\partial \hat{\boldsymbol{\tau}}^{st,i}(r_n)} \right] \delta\hat{\boldsymbol{\tau}}^{st,i}(r_n) - \delta\hat{\boldsymbol{\tau}}^{st,i}(r_j) = 0 \tag{6.222}$$

In matrix form this equation reads

$$\begin{pmatrix} \Delta \hat{P}^i(r_1) \\ \Delta \hat{P}^i(r_2) \\ \vdots \\ \Delta \hat{P}^i(r_N) \end{pmatrix} + \left(\boldsymbol{J}_e\left(\hat{\boldsymbol{\tau}}^{st,i}\right) - \boldsymbol{J}_v\left(\hat{\boldsymbol{\tau}}^{st,i}\right) \right) \begin{pmatrix} \delta\hat{\boldsymbol{\tau}}^{st,i}(r_1) \\ \delta\hat{\boldsymbol{\tau}}^{st,i}(r_2) \\ \vdots \\ \delta\hat{\boldsymbol{\tau}}^{st,i}(r_N) \end{pmatrix} - \boldsymbol{I} \begin{pmatrix} \delta\hat{\boldsymbol{\tau}}^{st,i}(r_1) \\ \delta\hat{\boldsymbol{\tau}}^{st,i}(r_2) \\ \vdots \\ \delta\hat{\boldsymbol{\tau}}^{st,i}(r_N) \end{pmatrix} = \begin{pmatrix} 0 \\ 0 \\ \vdots \\ 0 \end{pmatrix} \tag{6.223}$$

where $\boldsymbol{J}_e\left(\hat{\boldsymbol{\tau}}^{st,i}\right)$ is the Jacobian matrix of the electric stress tensor

$$\boldsymbol{J}_e\left(\hat{\boldsymbol{\tau}}^{st,i}\right) = \begin{pmatrix} \frac{\partial \hat{\boldsymbol{\tau}}_n^{e,i}(r_1)}{\partial \hat{\boldsymbol{\tau}}^{st,i}(r_1)} & \frac{\partial \hat{\boldsymbol{\tau}}_n^{e,i}(r_1)}{\partial \hat{\boldsymbol{\tau}}^{st,i}(r_2)} & \cdots & \frac{\partial \hat{\boldsymbol{\tau}}_n^{e,i}(r_1)}{\partial \hat{\boldsymbol{\tau}}^{st,i}(r_N)} \\ \frac{\partial \hat{\boldsymbol{\tau}}_n^{e,i}(r_2)}{\partial \hat{\boldsymbol{\tau}}^{st,i}(r_1)} & \frac{\partial \hat{\boldsymbol{\tau}}_n^{e,i}(r_2)}{\partial \hat{\boldsymbol{\tau}}^{st,i}(r_2)} & \cdots & \frac{\partial \hat{\boldsymbol{\tau}}_n^{e,i}(r_2)}{\partial \hat{\boldsymbol{\tau}}^{st,i}(r_N)} \\ \vdots & \vdots & \ddots & \vdots \\ \frac{\partial \hat{\boldsymbol{\tau}}_n^{e,i}(r_N)}{\partial \hat{\boldsymbol{\tau}}^{st,i}(r_1)} & \frac{\partial \hat{\boldsymbol{\tau}}_n^{e,i}(r_N)}{\partial \hat{\boldsymbol{\tau}}^{st,i}(r_2)} & \cdots & \frac{\partial \hat{\boldsymbol{\tau}}_n^{e,i}(r_N)}{\partial \hat{\boldsymbol{\tau}}^{st,i}(r_N)} \end{pmatrix} \tag{6.224}$$

and $\boldsymbol{J}_v\left(\hat{\boldsymbol{\tau}}^{st,i}\right)$ is the corresponding Jacobian for the fluid stress. We solve Eq. 6.223 by first rearranging to the form

$$\left(\boldsymbol{I} + \boldsymbol{J}_v\left(\hat{\boldsymbol{\tau}}^{st,i}\right) - \boldsymbol{J}_e\left(\hat{\boldsymbol{\tau}}^{st,i}\right)\right) \begin{pmatrix} \delta\hat{\boldsymbol{\tau}}^{st,i}(r_1) \\ \delta\hat{\boldsymbol{\tau}}^{st,i}(r_2) \\ \vdots \\ \delta\hat{\boldsymbol{\tau}}^{st,i}(r_N) \end{pmatrix} = \begin{pmatrix} \Delta\hat{P}^i(r_1) \\ \Delta\hat{P}^i(r_2) \\ \vdots \\ \Delta\hat{P}^i(r_N) \end{pmatrix} \tag{6.225}$$

and then finding

$$\begin{pmatrix} \delta\hat{\boldsymbol{\tau}}^{st,i}(r_1) \\ \delta\hat{\boldsymbol{\tau}}^{st,i}(r_2) \\ \vdots \\ \delta\hat{\boldsymbol{\tau}}^{st,i}(r_N) \end{pmatrix} = \left(\boldsymbol{I} + \boldsymbol{J}_v\left(\hat{\boldsymbol{\tau}}^{st,i}\right) - \boldsymbol{J}_e\left(\hat{\boldsymbol{\tau}}^{st,i}\right)\right)^{-1} \begin{pmatrix} \Delta\hat{P}^i(r_1) \\ \Delta\hat{P}^i(r_2) \\ \vdots \\ \Delta\hat{P}^i(r_N) \end{pmatrix} \tag{6.226}$$

Since $\hat{\boldsymbol{\tau}}^{st,i+1} = \hat{\boldsymbol{\tau}}^{st,i} + \delta\hat{\boldsymbol{\tau}}^{st,i}$, we now have that

$$\hat{\boldsymbol{\tau}}^{st,i+1} = \hat{\boldsymbol{\tau}}^{st,i} + \left(\boldsymbol{I} + \boldsymbol{J}_v\left(\hat{\boldsymbol{\tau}}^{st,i}\right) - \boldsymbol{J}_e\left(\hat{\boldsymbol{\tau}}^{st,i}\right)\right)^{-1} \Delta\hat{P}^i \tag{6.227}$$

By inspection we see that this is very similar to the present propagation equation save for the fact that β is now replaced with $(\boldsymbol{I} + \boldsymbol{J}_v\left(\hat{\boldsymbol{\tau}}^{st,i}\right) - \boldsymbol{J}_e\left(\hat{\boldsymbol{\tau}}^{st,i}\right))^{-1}$, which will in general vary from point to point along the meniscus and also from iteration to iteration.

The difficulty in deploying such a method is in calculating the various Jacobian matrices, which is why we will not use it for the present studies. Moreover, the fact that it can identify unstable equilibria necessitates the use of a separate analysis to determine physical stability. Notwithstanding those issues, it is important to keep in mind that it could be of great interest in the future, particularly in view of the fast convergence properties it is likely to exhibit [71].

Chapter 7

Validation

During the literature review we highlighted the fact that while many studies have been carried out on the equilibria and stability properties of both conducting and dielectric liquids, the overwhelming majority of these focus on situations of constrained volume. Among these, we also learned that only the investigations reported by Higuera [62] considered the possibility of kinetic emission in any detail, at least as it pertains to moderately conducting fluids such as ionic liquids. In the preceding chapter we have developed a rigorous meniscus model that purposefully avoids any volumetric constraints and incorporates the influences of a liquid feeding system. Along with potential heating effects, which were explicitly disregarded in the Higuera [62] work, we believe that these lend the present model to a much more physical and realistic description of the problem of steady electrically-assisted evaporation. This is due to the fact that in practice we typically elect to work with some form of electrospray emitter (be it a capillary, a porous needle, or an externally-wetted tip) that is connected to a reservoir of fluid rather than simply discrete droplets.

In an ideal world we would be able to immediately benchmark our model against some well-known theoretical result; however, the lack of any free-volume numerical investigations in the literature makes this very difficult. While attempting to exactly reproduce an empirical finding is one alternative, there are apparently no existing studies that do a sufficient job of reporting precise experimental parameters (meniscus size, liquid properties, electrode configurations, feeding impedance and back pressure, etc.) in a detailed way. As a result, we must at this point resign ourselves to only validating aspects of the current model that are relevant to the problem of a fixed-volume droplet since that is the only meniscus configuration that has been rigorously modeled to date. After making the appropriate concessions we will be able to quantitatively verify the electrostatic and interfacial propagation components of our model, i.e., the ability to calculate electric fields, formulate a balance of normal stresses, and use the interfacial relaxation method introduced in the last chapter to slowly approach stable, equilibrated morphologies. Once we have shown this, we will begin to explore the parameter space of the full free-volume model in the following chapter before comparing the corresponding results with known empirical behaviors in an attempt to qualitatively assess the merits of the remaining components of the model, i.e., the evaporative components.

In what follows we will make slight modifications to the full model to adapt it to the fixed-volume droplet problem. In most cases this will also be accompanied by suppression of the emission physics (for example, by setting $\Delta G \to \infty$ so that finite fields will not extract charge) so that conditions in the comparison studies can we replicated. The appropriate balance of normal stresses will be

$$\boldsymbol{\tau}_n^e + P_l = \gamma \nabla \cdot \vec{n} \tag{7.1}$$

where P_l is the hydrostatic pressure in the droplet (recall the chapter on fixed-volume spheroids). The interfacial relaxation procedure introduced in Section 6.4.3 will be used in conjunction with this balance to identify equilibrated droplet structures.

We will first attempt to model stressed dielectric droplets in free-space, the results of which can be compared to the analytical spheroids that were presented in Chapter 5. Recall that the construction of those results was predicated upon Taylor's two-point stress balancing method (i.e., balancing stresses at the droplet tip and at the droplet waist) and the assumption of exact spheroidal morphologies. Sufficient reproduction of the droplet shapes and elongations from Chapter 5 should confirm our ability to (1) calculate accurate fields at a vacuum-dielectric interface, and (2) utilize our relaxation method for the identification of various equilibria. Given that the analytical results also speak to the locations of turning point and unstable equilibria, this exercise will also be useful in showing that our methods are restricted to physically stable interface configurations.

Second, we will attempt to reproduce several of the numerical results reported by Wohlhuter [71]. As the reader may recall from the literature review, Wohlhuter calculates equilibria for dielectric droplets resting on plates where either the contact angle (which can be arbitrarily chosen over $\theta \in [0, \pi/2]$) or radius (alternatively referred to as a the contact line) is made invariant. The results contained therein are useful in the sense that a very high-accuracy Jacobian method (similar in spirit to the one presented in Section 6.5 of this thesis) was used to quickly identify equilibria in connection with a small numerical tolerance. We will compare meniscus elongations computed with our methods to those in the reference, where they are given to two decimal places, to quantitatively assess the accuracy of the relaxation technique. As we will show, strong agreement is observed.

Finally, we will attempt to reproduce several of the numerical results reported in the seminal study of Higuera [62]. There, the author uses a time-resolved marching technique to propagate interfaces for constant contact line droplets (droplets on plates with fixed attachment radii) and calculate equilibria in the presence of evaporation. Effects due to flow in the meniscus (hydraulic stressing) and charge depletion at the interface were included. While at first glance it would appear as though comparison to the Higuera [62] results may offer a new opportunity to confirm our ability to accurately calculate flow fields and surface charges, we will show that neither hydraulic stresses (due to a low Capillary number) nor charge depletion (due to a high dielectric constant) had any effect on the important findings (e.g. droplet morphology and emission strength). We will achieve this by calculating equilibria for non-evaporating droplets of a corresponding dielectric strength ($\epsilon_r = 50$) and introducing emission estimations as a post-processing step. Comparison with the Higuera [62] findings will, therefore, primarily serve to provide additional confirmation that our relaxation method for interfacial propagation is equipped to identify stable equilibria while the contact line is fixed in place.

To summarize, the model developed for this thesis is a unique entry in the theoretical landscape in the sense that it describes free-volume menisci and incorporates several effects (namely Ohmic heating) that were disregarded in the only other model of an IL source [62]. Owing to its richness, we cannot directly validate every aspect of it *a priori*, i.e., before using it to explore the parameter space of interest. Unfortunately, little recourse is offered by empirical studies as a result of the fact that important conditions (e.g. feeding impedance and electrode configuration) are not commonly reported in sufficient detail. With this in mind, we make the concession here to temporarily suppress the emission physics in our model and make a slight modification to the balance of normal stresses to engender compatibility with the well-investigated problem of fixed-volume droplets. Comparison of results from our modified model with several well-known findings from the literature will help us to (1) prove that we can accurately calculate electric fields and formulate a balance of stresses, and (2) utilize the relaxation method for interfacial propagation to identify stable equilibria. In the following chapter we will use the full free-volume model (i.e., the dimensionless one presented in Section 6.2) to begin collecting new results, which will later be compared against empirical emission behaviors.

7.1 Free-space dielectric droplets

For the problem of the free-space dielectric droplet we will ignore the possibilities of charge evaporation and dynamical flow in accordance with existing literary conventions. In reference to parameter space of the full model presented in the previous chapter, this is tantamount to setting B, R_E, Λ, C_c^T, C_u^T, C_u^e, χ, C_R, and $\hat{P}_r$ all equal to zero along with $\psi \to \infty$ (see Section 6.2). Under these conditions the governing set of equations reduces to

$$\hat{\nabla}^2 \hat{\Phi}^v = 0 \tag{7.2}$$

$$\hat{\nabla}^2 \hat{\Phi}^l = 0 \tag{7.3}$$

in the vacuum and liquid regions, respectively; and

$$\hat{\boldsymbol{\tau}}_n^e + \hat{p} = \frac{1}{2} \hat{\nabla} \cdot \vec{n} \tag{7.4}$$

on the interface. The mid-plane is defined by the reference potential, i.e. $\hat{\Phi} = 0$. Unlike the free-volume case, the hydrostatic pressure of the liquid comprising the meniscus, $\hat{p}$, is now fully coupled to the prevailing fields by way of the interfacial structure. This pressure, along with the corresponding interface geometry, is calculated for arbitrary $\hat{E}_0$ in an iterative fashion. As before, we do this in axisymmetric cylindrical space and start by assuming a surface tension profile and a corresponding shape $\hat{z} = h(\hat{r})$ that defines the fixed volume

$$\hat{v} = 2\pi \int h\left(\hat{r}\right)\hat{r} \cdot d\hat{r} \tag{7.5}$$

Because the waist of the droplet is free to contract now, the scaling length is taken as the radius r_0 of the undeformed structure. We next calculate the prevailing electrical fields and assess the mechanical balance at the interface. When it is not sufficiently satisfied we prepare for a subsequent iteration by updating the surface tension (i.e., Laplace pressure) profile such that

$$\vec{P_{st}}^{\,i+1} = \vec{P_e}^{\,i-1} + \beta_{CV}\left(\vec{P_e}^{\,i} - \vec{P_e}^{\,i-1}\right) + P_f \tag{7.6}$$

where i is the iteration index and P_e is the normal component of the electrical stress. β_{CV} is a relaxation parameter that can be used to ensure "slow" evolution of the meniscus and the constant-volume analog to the β from our last chapter. The fluid pressure P_f, which is spatially uniform, is at this point unknown. We determine it through a sublayer of iterations in which we integrate the differential relationship of the surface, Eq. 6.201, until we find the exact value satisfying the given contact angle constraint. For the free-space droplet this is $\pi/2$, i.e. the surface must be orthogonal to the plane of symmetry. In general, the new meniscus shape will not initially enclose the exact volume prescribed through $\hat{v}$. This is rectified by scaling all spatial coordinates by a value $\alpha_{CV} \in (0, 1]$ such that

$$\alpha_{CV}^3 = \frac{\hat{v}}{2\pi \int \hat{z}\hat{r} \cdot d\hat{r}} \tag{7.7}$$

where $\hat{z} = h(\hat{r})$ corresponds to the initial distribution $\vec{P_{st}}^{\,i+1}$ calculated for the subsequent iteration. To incorporate the volume constraint we now impose the following modifications

$$\vec{P_{st}}^{\,i+1} \to \frac{1}{\alpha}\vec{P_{st}}^{\,i+1} \tag{7.8}$$

$$P_f^{i+1} \to \frac{1}{\alpha}P_f^{i+1} \tag{7.9}$$

$$\hat{z} \to \alpha\hat{z} \tag{7.10}$$

$$\hat{r} \to \alpha\hat{r} \tag{7.11}$$

where the values on the right-hand side are those calculated for the contact angle constraint only (i.e. calculated *before* enforcing the volume constraint) while the scaled values on the left-hand side reflect *both* contact angle and volume constraints. The latter are the values that we pass along to the next iteration where we calculate the fields, check the mechanical balance, and repeat the process in kind until a converged solution is reached.

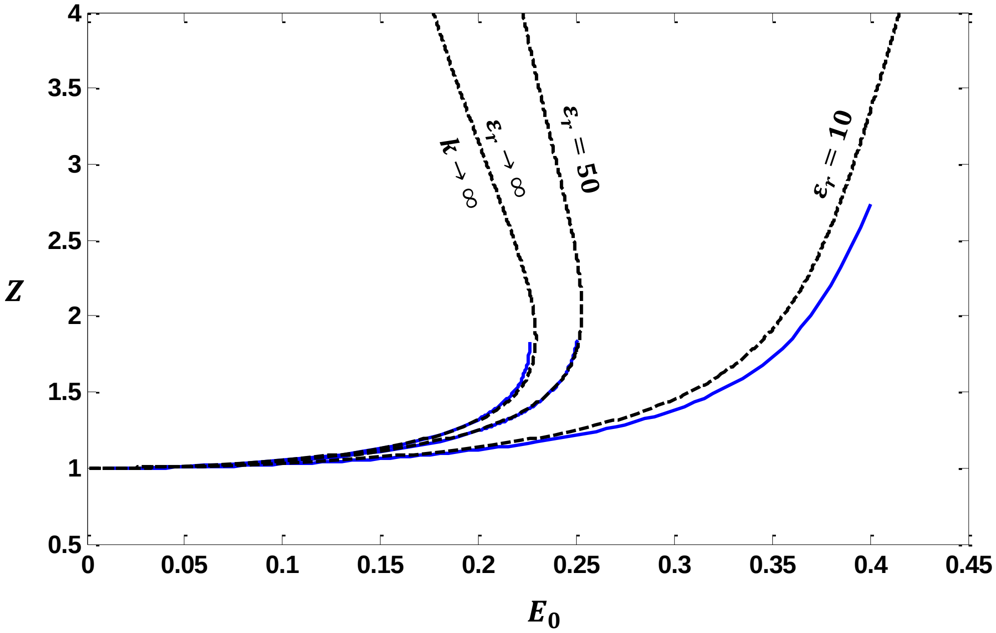

Figure 7-1: Overview of simulated (blue) and approximated (dashed) elongation curves for several fixed-volume dielectric droplets as functions of dimensionless field $\hat{E}_0$. Three cases of permittivity are shown: $\epsilon_r \to \infty$, $\epsilon_r = 50$, and $\epsilon_r = 10$. Solutions for the first two cases terminate at the turning point, beyond which the computational routine began to oscillate and did not identify any equilibria. The results seem to suggest that our numerical methodology is sound, at least insofar as the electrostatics and propagation components are concerned.

In Figs. 7-1-7-3 we show equilibrium results for the free droplet problem with $\hat{v} = 2\pi/3$. All calculations involve $N = 10^3$ observation points equally-spaced across the meniscus between $\hat{r} = 0$ and the contact location. The Comsol electrostatics mesh is set so that $\hat{h}_{max} = 1$, $\hat{h}_{min} = 10^{-4}$, $\hat{h}_{grad} = 1.25$, and $\hat{h}_{curve} = 10^{-2}$ while a single adaption is allowed. The relaxation parameter $\beta_{CV} = 0.5$ and the termination condition is set to $P_\beta = 10^{-3}$.

Figure 7-1 delineates a comparison of three simulated elongation curves ($\epsilon_r \to \infty$, $\epsilon_r = 50$, and $\epsilon_r = 10$) with the corresponding analytical approximations developed in the earlier chapter on spheroids. The results appear to agree very well over the range of dimensionless field $\hat{E}_0$ investigated, which is rather remarkable given the assumptions that were invoked for the closed-form model. Small discrepancies, where present, are likely attributable to the slight distribution of net pressure between the droplet apex and waist that occurs for a perfectly spheroidal topography. Apparently, this effect is more pronounced for small permittivity and possibly minimized as $\epsilon_r \to \infty$. For the two cases of high permittivity, the solutions terminate at the calculated turning point, beyond which our numerical routine began to oscillate and no equilibrium could be identified. No turning point was seen for the case $\epsilon_r = 10$ and so the solutions were arbitrarily cut off at $\hat{E}_0 = 0.4$.

Figure 7-2 provides zoomed views of the individual elongation curves with ϵ_r

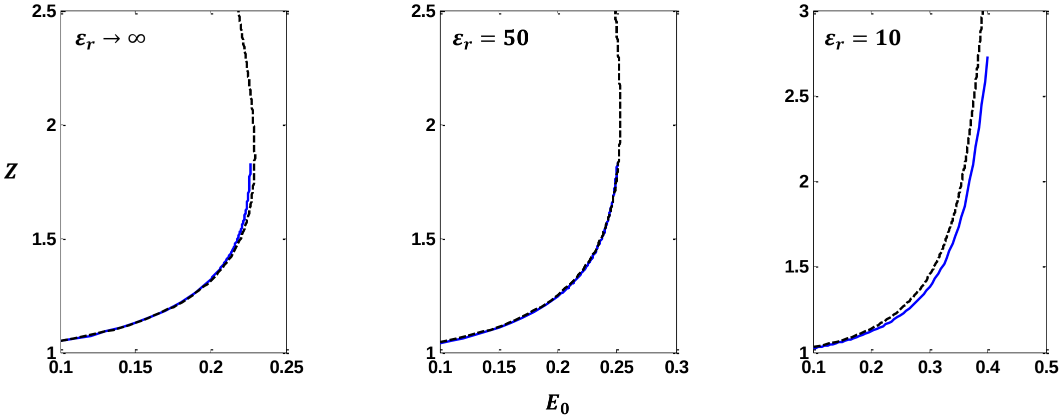

Figure 7-2: Zoomed comparisons of simulated (blue) and approximated (dashed) elongation curves for the free droplet problem. As before, the equilibrium elongation Z is plotted as a function of dimensionless field $\hat{E}_0$. Cases $\epsilon_r \to \infty$, ϵ_r =50, and ϵ_r =10 are shown from left to right. The curves further highlight the good agreement between simulated and approximated solutions, particularly in the first two cases where there are excellent quantitative similarities near the turning points.

decreasing from left to right. In the first two cases, this serves to highlight the quantitative similarities between the simulated and approximated turning point characteristics. Figure 7-3 compares several of the simulated interfacial geometries with perfect spheroids of equal aspect ratio. The results strongly suggest that fixed-volume droplets retain nearly spheroidal morphologies throughout the elongation process, exactly as we noted earlier.

7.2 Plate-attached dielectric droplets (Wohlhuter)

The comparison between the numerical results and the analytical model is qualitatively useful but fails to provide a strong quantitative measure of our solution accuracy since the latter is based on an approximation. A better comparison might be to invoke other numerical results in the literature and for this we can turn to Wohlhuter [71], where deformation modes of fixed-volume droplets are described sans any synthetic interface constraints.

Wohlhuter presents in detail the deformation properties of a dielectric droplet ($\epsilon_r = 21$) that is attached to a conducting plate and subjected to an externally-imposed electrical field. Two cases of attachment condition are considered (fixed contact angle, FCA, and fixed contact line/radius, FCL) along with three fluid volumes. This yields a test matrix with six distinct droplets, three of which we reproduce here for the sake of comparison. These include (1) the case of a fixed orthogonal contact angle droplet with $\hat{v} = 2\pi/3$, which is similar to what we studied in the previous section; (2) the case of a fixed contact line droplet with $\hat{v} = 2\pi/3$; and (3) the case of a fixed contact line droplet with $\hat{v} = 0.1173$.

For the fixed contact angle problem we will make use of the procedure described

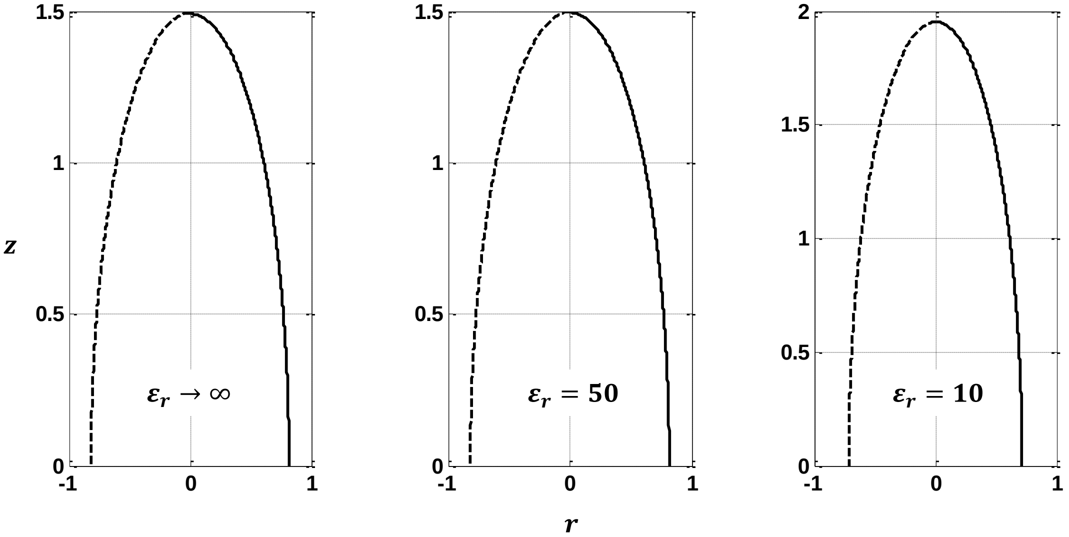

Figure 7-3: Comparison of simulated topographies (solid curves) and perfect spheroids (dashed curves) for select elongations. The interfaces are plotted using the dimensionless coordinates $\hat{r}$ and $\hat{z}$ and include, from left to right, $\epsilon_r \rightarrow \infty$, ϵ_r =50, and ϵ_r =10. The results confirm that fixed-volume droplets under electrical stress in free space are almost identically spheroidal.

in the previous section. For those involving a fixed contact line we will modify it by using the hydrostatic fluid pressure to satisfy the volume constraint directly and removing the scaling step. In other words, after calculating $\vec{P_e}^i$ for the i^{th} computational iteration we will take

$$\vec{P_{st}}^{i+1} = \vec{P_e}^{i-1} + \beta_{CV}\left(\vec{P_e}^{i} - \vec{P_e}^{i-1}\right) + P_f \tag{7.12}$$

and perform a sub-iteration loop over the fluid pressure P_f until the appropriate value is identified. This is the value for which the meniscus profile $\hat{z} = h(\hat{r})$ corresponding to the distribution $\vec{P_{st}}^{i+1}$ has a volume integral (Eq. 7.5) equal to the prescribed quantity.

In all cases, Wohlhuter makes use of the unit sphere, prior to any stressing, to modulate the effective droplet volume. This is achieved by shifting the sphere a specific distance in either the positive or negative z-direction (i.e. translation of the sphere with respect to the plane of the plate is used to prescribe the droplet volume, which is possible since the droplets will exhibit spherical morphologies in the unstressed limit). A quantity D, measured between the horizontal plane of the conducting plate and the center of the unit sphere, is used to signify this displacement (Fig. 7-4). The two volumes we will consider are reported by Wohlhuter as $D = 0$ and $D = -0.8$. By inspection it is easy to see that the former is tantamount to $\hat{v} = 2\pi/3$. For the latter, consider that the general equation for the vertically-displaced unit circle is

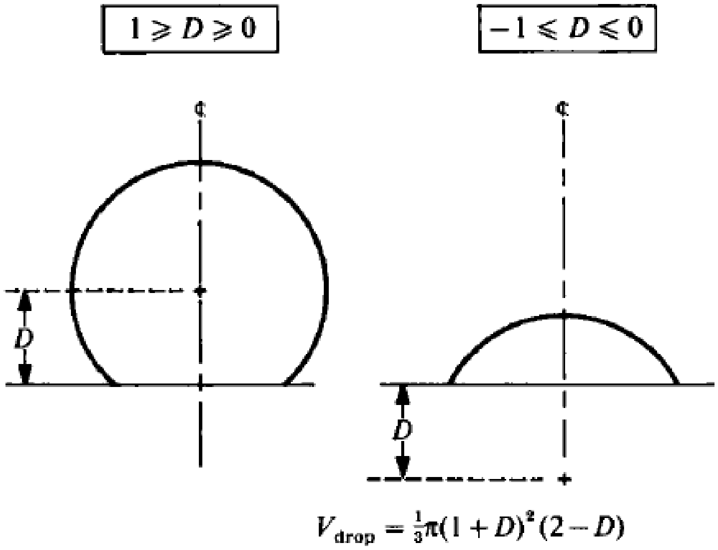

Figure 7-4: Illustration of unit circle displacement method used to simulate various droplet volumes. The unit circle is displaced a vertical distance D to affect droplets that are either larger ($D > 0$) or smaller ($D < 0$) than the nominal hemispherical case ($D = 0$). Reproduced from Wohlhuter [71].

$$\hat{r}^2 + (\hat{z} - D)^2 = 1 \Rightarrow \hat{z} = \sqrt{1 - \hat{r}^2} + D \tag{7.13}$$

When the displacement is negative, this is equivalent to

$$\hat{z} = \sqrt{1 - \hat{r}^2} - |D| \tag{7.14}$$

The height of the unperturbed sphere is $\hat{z}_0 = 1 - |D|$ and it has a radial footprint on the plate of $\hat{r}_{CL} = 1 - D^2$. The enclosed volume is found by integrating

$$\hat{v} = 2\pi \int_0^{\hat{r}_{CL}} \hat{r} \left(\sqrt{1 - \hat{r}^2} - |D|\right) d\hat{r} = \frac{\pi}{3} \left(|D|^3 - 3|D| + 2\right) \tag{7.15}$$

For $D = -0.8$ it is easy to confirm that this evaluates to $\hat{v} = 0.1173$, which is why we have cited that volume. Figure 7-5 delineates computed elongation curves for a dielectric droplet ($\epsilon_r = 21$) with $\hat{z}_0 = \hat{z}_p = 20$. These are plotted as functions of the root of the so-called electric bond number ($N_e^{1/2} = \sqrt{2} \times \hat{E}_0$), which is used by Wohlhuter, while corresponding results from the reference are shown on the right. Using the present methods we have identified for each case a lower branch of ostensibly stable solutions extending between a region of vanishing electrical stress and the turning point. For small fields the computational scheme converges very quickly but near the turning point we observe an increasing number of oscillations and an attendant growth in the required solution time. This issue has precluded us from computing any solutions above turning point, where the oscillations typically lead to divergence, and is likely related to the stability of the interface. Notwithstanding this

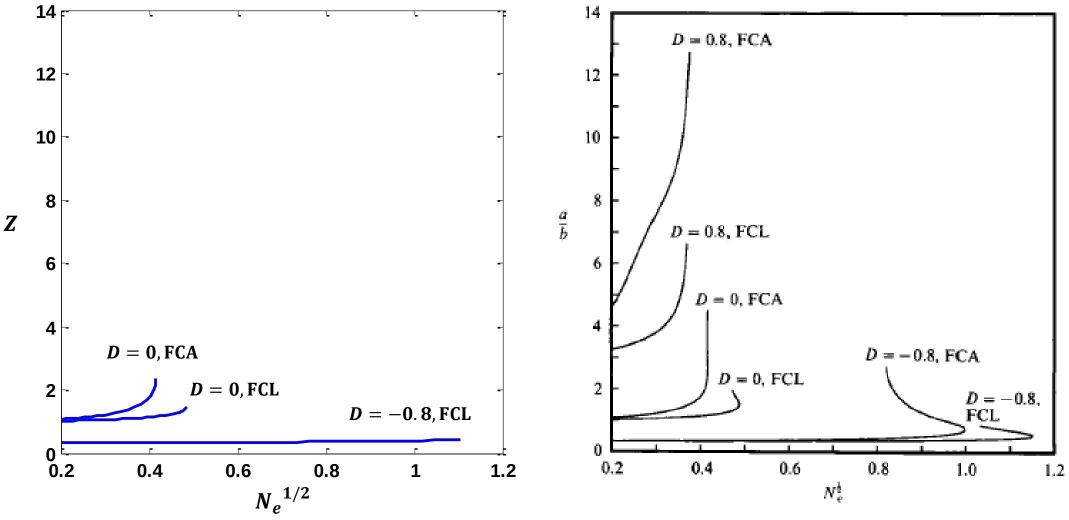

Figure 7-5: Comparison of several elongation curves with the results described in Wohlhuter [71]. Each case corresponds to a dielectric droplet with $\epsilon_r = 21$ situated on a conducting plate. The boundary geometry is defined by $\hat{z}_0 = \hat{z}_p = 20$ while the contact arrangement is given by either FCA (fixed contact angle) or FCL (fixed contact line). N_e is the so-called electric bond number used in the reference. Its root is related to $\hat{E}_0$ through a simple constant, i.e. $N_e^{1/2} = \sqrt{2} \times \hat{E}_0$.

inherent limitation in our method, the stable solutions we have computed appear to agree very well with the results from the reference.

Figures 7-6 to 7-8 delineate comparisons between specific solution points. In each case Wohlhuter provides equilibrium shapes for several elongations above and below the turning point. While we cannot reproduce the former because of stability, the elongations we calculate for the stable instances agree with Wohlhuter to all decimal places given in the reference.

7.3 High-B emission from plate-attached droplets (Higuera)

The model presented by Higuera [62] is unique in that it describes not only the steady morphologies of fixed volume droplets but also the attendant evaporation when the governing properties are representative of ionic liquids. As a further measure of the present formulation we might try to reproduce several of the results provided therein, especially those pertaining to emission behavior.

Higuera investigates the situation of a fixed-volume droplet anchored to a conducting plate with a fixed contact line. The mathematical framework used to describe the problem is fundamentally similar to the one constructed for this thesis but differs in its dimensionless form. Noting that the Higuera model does not admit thermal phenomena, it is shown in the reference that the problem resides in a six-dimensional

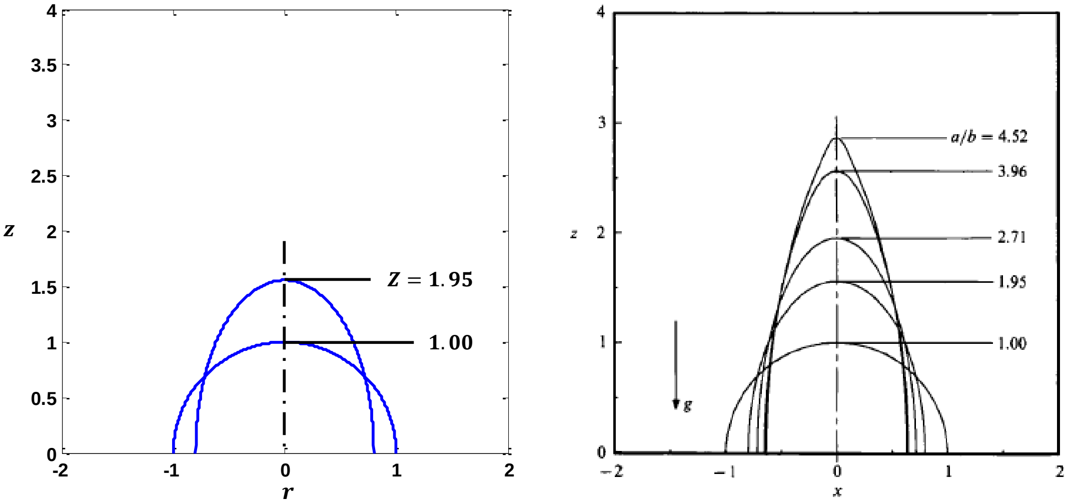

Figure 7-6: Comparison of dielectric droplet shapes for $\epsilon_r = 21$ and $\hat{z}_0 = \hat{z}_p = 20$ with fixed contact angle (90°). **Left:** Shapes calculated with present methods. Dimensionless fields $N_e^{1/2}$ for the given elongations are 0 for $Z = 1.00$ and 0.4088 for $Z = 1.95$. **Right:** Shapes reproduced from Wohlhuter [71]. Dimensionless fields $N_e^{1/2}$ for the given elongations are 0 for $Z = 1.00$; 0.4088 for $Z = 1.95$; 0.4172 for $Z = 2.71$; 0.4163 for $Z = 3.96$; and 0.4172 for $Z = 4.52$.

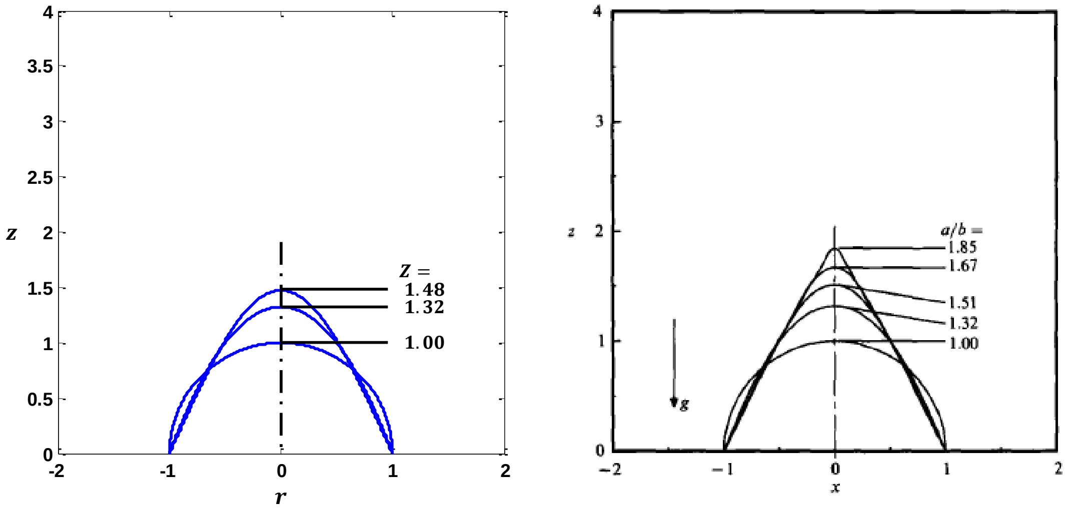

Figure 7-7: Comparison of dielectric droplet shapes for $\epsilon_r = 21$ and $\hat{z}_0 = \hat{z}_p = 20$ with fixed contact line ($\hat{r}_{CL} = 1$). **Left:** Shapes calculated with present methods. Dimensionless fields $N_e^{1/2}$ for the given elongations are 0 for $Z = 1.00$; 0.4744 for $Z = 1.32$; and 0.4870 for $Z = 1.48$. **Right:** Shapes reproduced from Wohlhuter [71]. Dimensionless fields $N_e^{1/2}$ for the given elongations are 0 for $Z = 1.00$; 0.4744 for $Z = 1.32$; 0.4880 for $Z = 1.51$; 0.4838 for $Z = 1.67$; and 0.4753 for $Z = 1.85$.

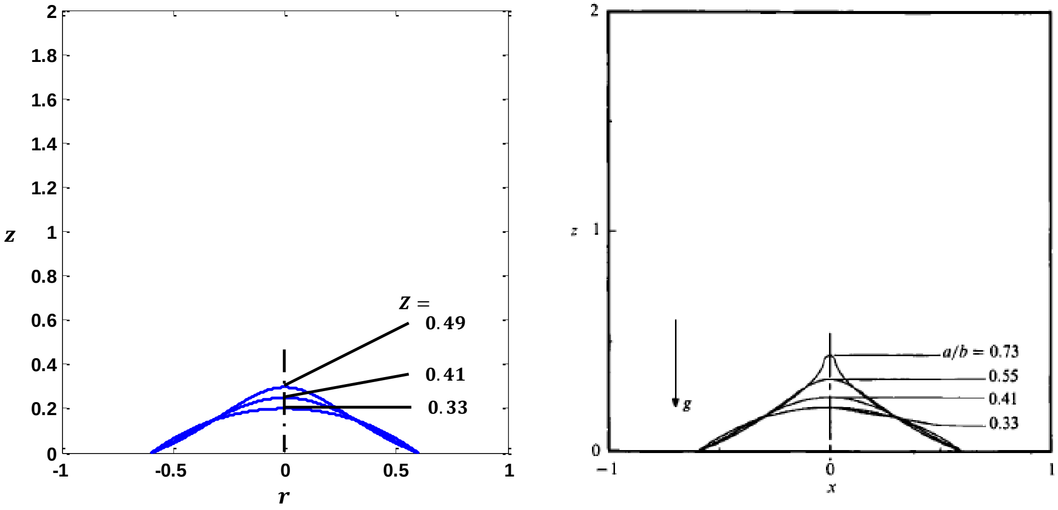

Figure 7-8: Comparison of dielectric droplet shapes for $\epsilon_r = 21$ and $\hat{z}_0 = \hat{z}_p = 20$ with fixed contact line ($\hat{r}_{CL} = 0.6$). **Left:** Shapes calculated with present methods. Dimensionless fields $N_e^{1/2}$ for the given elongations are 0 for $Z = 0.33$; 1.0469 for $Z = 0.41$; and 1.1400 for $Z = 0.49$. **Right:** Shapes reproduced from Wohlhuter [71]. Dimensionless fields $N_e^{1/2}$ for the given elongations are 0 for $Z = 0.33$; 1.0469 for $Z = 0.41$; 1.1531 for $Z = 0.55$; and 1.0833 for $Z = 0.73$.

parameter space defined by

$$\begin{aligned} \Lambda_H &= \frac{\mu r_0 k}{\epsilon_0 \gamma} & & \epsilon_r \\ B_H &= \frac{E_0}{E_H} & \mathcal{V}_H &= \frac{V}{r_0^3} \\ D_H &= \frac{\mu r_0 k_B T}{\gamma h} \exp\left(-\frac{\Delta G}{k_B T}\right) & \beta_H &= \frac{1}{k_B T}\left(\frac{q^3 E_H}{4\pi\epsilon_0}\right)^{1/2} \end{aligned}$$

where E_H is the field scale

$$E_H = \left(\frac{\gamma}{\epsilon_0 r_0}\right)^{1/2} = \frac{1}{2} E_c \tag{7.16}$$

Before we begin to reproduce any results it will be helpful to understand the emission regime that they represent, i.e. to determine whether $B \sim 10^0$ or $B \ll 1$. The task now is to recast B in terms of the parameters used by Higuera. Recall from our formulation that the size parameter is given by $B = r^*/r_0$ where

$$r^* \sim \frac{4\gamma}{\epsilon_0}\left(\frac{q^3}{4\pi\epsilon_0 \Delta G^2}\right)^2 \tag{7.17}$$

Using $r_0 = r^*/B$ we can substitute in β_H to find

$$\beta_H = \frac{\Delta G}{k_B T}\left(\frac{B}{4}\right)^{1/4} \tag{7.18}$$

The prefactor in this expression, $\Delta G/k_B T$, can be determined through the quantity D_H. Rearranging that parameter gives

$$D_H = \frac{\epsilon_0 \Lambda_H}{k}\frac{k_B T}{h}\exp\left(-\frac{\Delta G}{k_B T}\right) \Rightarrow \frac{\Delta G}{k_B T} = \ln\left(\frac{\epsilon_0 \Lambda_H}{k D_H}\frac{k_B T}{h}\right) \tag{7.19}$$

which can itself be substituted in Eq. 7.18. The final result is that

$$B = \frac{4\beta_H^4}{\left[\ln\left(\frac{\epsilon_0 \Lambda_H}{k D_H}\frac{k_B T}{h}\right)\right]^4} \tag{7.20}$$

For most of the results in the reference Higuera takes Λ_H =10^4, D_H =10^{-3}, and β_H =10. Since $k \sim 10^0$ for ionic liquids we find $B \sim 0.24$ near room temperature. This says that the contact line is somewhat larger than the characteristic size of the emission region, even if not quite so large as we are accustomed to seeing in practice (where $B \ll 1$ at the end of a large capillary tube, for example). We can conclude, therefore, that any depletion of charge should primarily be restricted to the tip of the droplet. Indeed, this appears to be reflected in several of the plots that are offered by the author.

In addition to B it will be of utility to have a sense for the prevailing capillary number, $C_a = u^* \mu/\gamma$. Recall that this is tantamount to

$$C_a = \frac{kE^*}{\rho\,(q/m)}\frac{\mu}{\gamma} \tag{7.21}$$

since $u \sim j/(\rho \cdot q/m)$ on the liquid side of the interface. Although the author does not provide the volumetric charge density $\rho(q/m)$ it is explicitly noted that the meniscus is essentially hydrostatic. This is important because it implies a very low capillary number and marginalization of any flow-induced stresses. In fact, in the limit as the meniscus becomes identically hydrostatic, we should expect to recover morphological solutions resembling those from earlier sections that do not involve any emission at all. After factoring in the prevailing B, which likely ensures charge relaxation over most of the meniscus, it is fair to speculate whether evaporation had anything to do with the structures reported in the reference.

Based on this speculation we hypothesize here that the equilibrium topographies in Higuera [62] were essentially those of an electrically-relaxed droplet of fixed-volume (no emission) and that any emission, where present, could have been reasonably approximated through a post-processing step. In terms of methodology, the process could have been to (1) determine the equilibrium shapes of a perfectly conducting droplet using appropriate steps; and (2) integrate the conduction-controlled current density over the computed interfaces to find the attendant evaporation level.

In Figures 7-9 thru 7-12 we present the results of this process and compare them to those reported by Higuera [62]. Figure 7-9 delineates elongation curves for droplets of various volume as functions of the dimensionless field B_H. The results of Higuera are reproduced on the right and include six volumes ranging from $\mathcal{V}_H = 0.5$ to $\mathcal{V}_H = 3.0$ (increments of $\mathcal{V}_H = 0.5$). Among these, the two largest volumes ($\mathcal{V}_H = 3.0$ and 0.25) are omitted in our calculations because their quiescent equilibria involve contact angles with the plate that cannot be resolved through our specific cylindrical coordinate scheme. Elongation curves for the remaining four droplet volumes have been identified with our methods and are given on the left. To compute these, the quiescent interface is first identified as an appropriate spherical section. Without any electrical stressing the meniscus will belong to the sphere defined by

$$\hat{r}^2 + (\hat{z} - \hat{z}_0)^2 = \hat{r}_0^2 \Rightarrow \hat{z} = \sqrt{\hat{r}_0^2 - \hat{r}^2} + \hat{z}_0 \tag{7.22}$$

where $\hat{z}_0$ is some fraction of $\hat{r}_0$, i.e. $\hat{z}_0 = \chi_0 \hat{r}_0$. If we impose the condition that the meniscus must pass through $\hat{r} = 1$, the contact point, we find that $\chi_0 \hat{r}_0 = \sqrt{\hat{r}_0^2 - 1}$ and Eq. 7.22 becomes

$$\hat{z} = \sqrt{\hat{r}_0^2 - \hat{r}^2} - \sqrt{\hat{r}_0^2 - 1} \tag{7.23}$$

The attendant droplet volume is tantamount to the integral

$$\mathcal{V}_H = 2\pi \int_0^1 \hat{r} \left[\sqrt{\hat{r}_0^2 - \hat{r}^2} - \sqrt{\hat{r}_0^2 - 1}\right] d\hat{r} \tag{7.24}$$

which evaluates to

$$\mathcal{V}_H = \frac{\pi}{3}\left[2\hat{r}_0^3 - 2\left(\hat{r}_0^2 - 1\right)^{3/2} - 3\sqrt{\hat{r}_0^2 - 1}\right] \tag{7.25}$$

For a given $\mathcal{V}_H$ we identify the quiescent interface by solving this relationship for the appropriate spherical radius. Once this is known, equilibria for non-zero electrical stress are determined in a manner similar to that which is discussed in the last section. From Fig. 7-9 we can see that the elongations of the equipotential droplets are nearly identical to those provided by the reference, save for the $\mathcal{V}_H = 0.5$ case in which we calculate a maximum stable field that is incrementally elevated. This confers a small but noticeable increase in the maximum elongation which is fleshed out to some small degree in Fig. 7-10 where the limiting topographies are plotted. The extent to which this small, albeit non-zero discrepancy can be attributed to either flow effects or numerical artifacts is unclear. Notwithstanding it, however, the results would otherwise seem to agree very nicely.

In Figures 7-11(a) and 7-11(b) we compare the dimensionless electric field at the tip and the dimensionless charge density at the tip, respectively. For the latter case our calculation is predicated upon the hydrostatic assumption so that we may neglect convective surface currents and formulate a balance between emission and conduction alone. In the notation of Higuera, this is

$$\underbrace{D_H \sigma \exp\left(\beta_H \sqrt{\hat{E}_n^v}\right)}_{j_e} = \underbrace{\Lambda_H \hat{E}_n^l}_{j_{cond}} \tag{7.26}$$

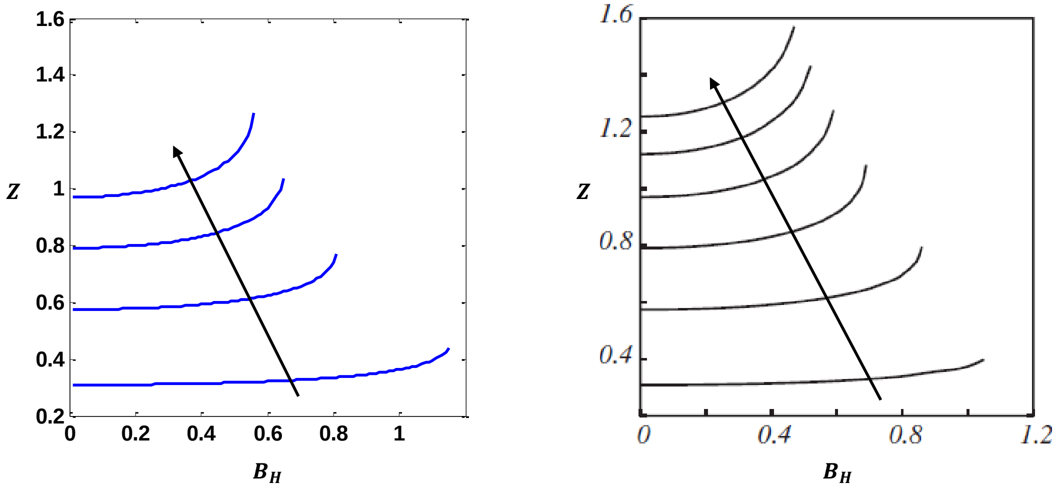

Figure 7-9: Comparison of elongation curves for active-emission droplets of fixed-volume attached to conducting plates with a static contact line. **Left:** Elongations calculated with present methods. Delineated volumes are $\mathcal{V}_H = 0.5, 1.0, 1.5, 2.0$ increasing in the direction of the arrow. **Right:** Elongations reproduced from Higuera [62]. Delineated volumes are $\mathcal{V}_H = 0.5, 1.0, 1.5, 2.0, 2.5, 3.0$ increasing in the direction of the arrow.

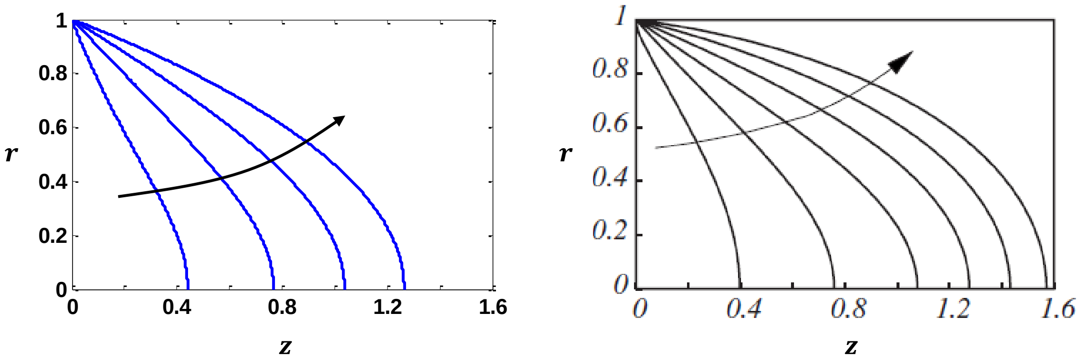

Figure 7-10: Comparison of limiting topographies for active-emission droplets of fixed-volume attached to conducting plates with a static contact line. **Left:** Limiting topographies calculated with present methods. Delineated volumes are $\mathcal{V}_H = 0.5, 1.0, 1.5, 2.0$ increasing in the direction of the arrow. **Right:** Limiting topographies reproduced from Higuera [62]. Delineated volumes are $\mathcal{V}_H = 0.5, 1.0, 1.5, 2.0, 2.5, 3.0$ increasing in the direction of the arrow.

where all quantities are dimensionless. After invoking the interfacial jump condition

$$\sigma = \hat{E}_n^v - \epsilon_r \hat{E}_n^l \Rightarrow \hat{E}_n^l = \frac{1}{\epsilon_r}\left(\hat{E}_n^v - \sigma\right) \tag{7.27}$$

we solve this to find

$$\sigma = \frac{\Lambda_H \hat{E}_n^v}{\epsilon_r D_H \exp\left(\beta_H \sqrt{\hat{E}_n^v}\right) + \Lambda_H} \tag{7.28}$$

The astute reader will now recognize that the equipotential menisci we are using do not permit any fields to form within the body of the liquid. In this case, the surface charge density is simply $\sigma = \hat{E}_n^v$ in spite of any emission. While that is true, we refer to the earlier chapter on spheroidal interfaces where we showed that highly polar droplets (say, $\epsilon_r \gtrsim 50$) are characterized by stable equilibria that are nearly identical to those of a perfectly conducting fluid, suggesting that the vacuum field is not significantly changed when the droplet permittivity sufficiently suppresses the small but non-zero liquid field. With that in mind, we can assume as a first approximation that a real fluid with depleted surface charge has a vacuum field that is equivalent to that of a conducting fluid of similar shape (what we have calculated) and an internal field governed by the interfacial jump condition so long as ϵ_r is large. Given that Higuera has taken $\epsilon_r = 50$ it would seem that Eq. 7.28 should provide a very reasonable estimate when $\hat{E}_n^v$ is borrowed from our conducting meniscus solutions. The correspondence between the curves in Fig. 7-11(left) and Fig. 7-11(right) appear to confirm this.

In a similar spirit we can approximate the evaporation density j_e across the interface. When this is nondimensionalized by $\epsilon_0 E_H \gamma a/\mu$ as in the reference, we find, again the notation of Higuera

$$j_e = \frac{\sigma D_H}{a^2} \exp\left(\beta_H \sqrt{\hat{E}_n^v}\right) \tag{7.29}$$

The total current is now the integral of this density over the full surface. The result is that

$$I_e = \int_0^1 \frac{\Lambda_H \hat{E}_n^v D_H \exp\left(\beta_H \sqrt{\hat{E}_n^v}\right)}{\epsilon_r D_H \exp\left(\beta_H \sqrt{\hat{E}_n^v}\right) + \Lambda_H} \times d\hat{A} \tag{7.30}$$

where the differential area is given by

$$d\hat{A} = 2\pi \hat{r} \sqrt{d\hat{r}^2 + d\hat{z}^2} \tag{7.31}$$

Evaporation curves are plotted in Figure 7-12 where we again observe good correspondence between our calculations (left) and those from the reference (right). A slight extension of the evaporation tail is noted for the $\mathcal{V}_H = 0.5$ droplet but this can be attributed to the elevated field that we have already addressed.

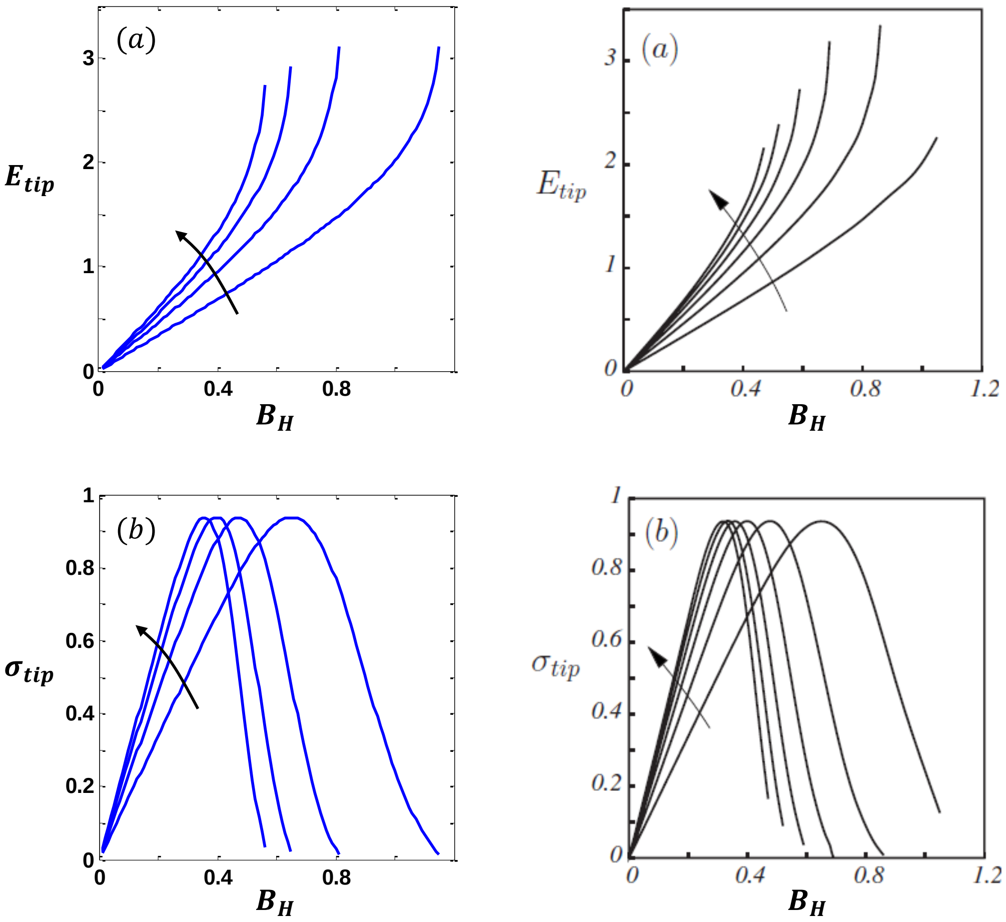

Figure 7-11: Comparison of apex properties for active-emission droplets of fixed-volume attached to conducting plates with a static contact line. The top figures, (a), delineate the tip field on the vacuum side while the bottom figures, (b), delineate the local density of surface charge. These are plotted as functions of the dimensionless field B_H used by Higuera [62], which is related to ours through $B_H = 2\hat{E}_0$. **Left:** Apex properties calculated with present methods. Delineated volumes are $\mathcal{V}_H = 0.5, 1.0, 1.5, 2.0$ increasing in the direction of the arrow. **Right:** Apex properties reproduced from Higuera [62]. Delineated volumes are $\mathcal{V}_H = 0.5, 1.0, 1.5, 2.0, 2.5, 3.0$ increasing in the direction of the arrow.

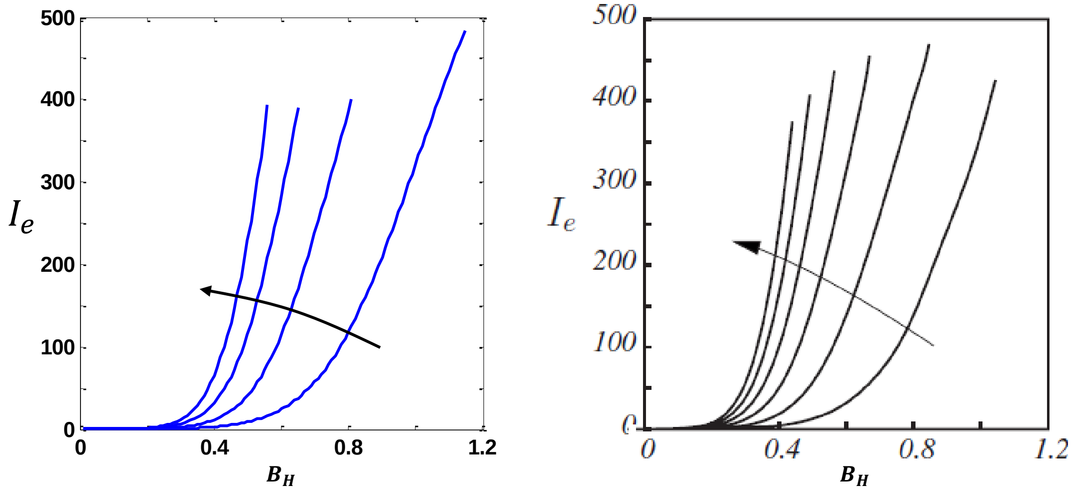

Figure 7-12: Comparison of evaporation curves for active-emission droplets of fixed-volume attached to conducting plates with a static contact line. **Left:** Evaporation curves calculated with present methods. Delineated volumes are $\mathcal{V}_H = 0.5, 1.0, 1.5, 2.0$ increasing in the direction of the arrow. **Right:** Evaporation curves reproduced from Higuera [62]. Delineated volumes are $\mathcal{V}_H = 0.5, 1.0, 1.5, 2.0, 2.5, 3.0$ increasing in the direction of the arrow.

7.4 Discussion

Using analytical approximations for electrically-stressed droplets in free space we have confirmed that our numerical methods are capable of capturing stable equilibria very accurately, at least when no emission is present. This notion is corroborated through direct quantitative comparison of results that were obtained with our model (for several droplet configurations) to known values developed in the literature using high-accuracy Jacobian (Wohlhuter [71]) and time-resolved (Higuera [62]) methods.

Estimates of emission from conducting droplets have been compared to the results of Higuera [62] with good agreement. During this process we have shown that the menisci of moderate B in the reference (recall that $B \sim 1/5$ rather than $B \ll 1$) were primarily beholden to the normal turning point behavior of fixed-volume droplets. Because the emission dynamics did not significantly influence the problem, we calculated our estimates as a post-processing step rather than in the strictly self-consistent manner afforded by the full model.

Chapter 8

Equilibria and evaporation

In this chapter we will invoke the full meniscus model, as presented earlier, and use it to explore equilibria and evaporation of ionic liquids under various conditions. Owing to previous work on solutions for the regime of moderate-B (Higuera [62]), emphasis will be placed on low-B scenarios during this process; i.e. we will concentrate on menisci that are much larger than the estimated size of the evaporation zone. Such configurations will also afford better resolution of laboratory conditions, where large tubes or emitter tips are often used to facilitate electrospraying.

The first section will investigate a branch of stable solutions corresponding to low electric fields. These terminate at familiar "turning points" and represent the free-volume analog to the well-known lower equilibrium branch of its fixed-volume counterpart. The following section will introduce for the first time a new branch of ostensibly stable solutions, corresponding to much higher fields, that begin to support meaningful evaporation. As we will show, these are apparently enabled by the physics of the flow. To conclude, we offer a brief qualitative comparison between the modeled menisci and known empirical behaviors.

Unless otherwise noted, in all cases we adopt static fluid properties that are loosely representative of pure ionic liquids, such as the popular EMI-BF4, near room temperature. These include ϵ_r =10; k_0 =1 S/m; k' =0.04 S/m-K; q/m =10^6 C/kg; T_0 =300 K; μ_0 =0.037 Pa-s; k_T =0.2 W/m-K; c_p =1500 J/kg-K; γ =0.05 N/m; ΔG =1 eV; and ρ =10^3 kg/m^3. This selection of parameters sets the following dimensionless quantities: R_E =853×10^{-6}; Λ =12; C_c^T =0.0569; C_u^T =0.0269; C_u^e =256×10^{-6}; χ =181×10^{-5}; in addition to ψ =38.6. The domain specifications are $\hat{r}_p = \hat{z}_0$ =20, similar to Wohlhuter [71], and $\hat{z}_p$ =1. All remaining values (i.e. $\hat{E}_0$, B, C_R, $\hat{P}_r$) are elected with discretion but explicitly noted where appropriate.

For the numerical routine, nominal values for the number of observation points evenly spaced across the radial dimension of the meniscus N, the relaxation parameter β, and the termination threshold P_β are 10^3, 0.5, and 10^{-3}, respectively. These may, however, be modified in certain instances to suit the needs of a given solution. Also, there are now two independent meshes: one for the electrical calculations and another for the fluid and thermal calculations. The former is set to $\hat{h}_{max}$ =0.25, h_{min} =10^{-10}, h_{grad} =1.25, and h_{curve} =10^{-2} while the latter substitutes $\hat{h}_{max}$ =0.04 and h_{curve} =5×10^{-3}.

8.1 Lower equilibrium branch

We will begin our study of free-volume menisci by investigating the behavior attendant to small fields before gradually increasing the stresses ($\hat{E}_0$ and $\hat{P}_r$) to see what happens. During this process it will be simplest to fix the remaining parameters B and C_R. As a starting point for the former, we arbitrarily select a dimensional meniscus size of b_0 =10^{-6} m. Given the aforementioned fluid properties, a value of

$$r^* = \frac{\gamma q^6}{4\pi^2 \epsilon_0^3 \Delta G^4} = 46.7nm \tag{8.1}$$

is calculated for the characteristic evaporation zone. This yields the dimensionless size parameter $B = r^*/b_0$ =0.047, i.e. the contact line is approximately 21.4 times wider than the part of the tip that we should expect to support evaporation.

At this point it is difficult to have any intuition as to sensible values for the scaled hydraulic impedance C_R. It would at first seem attractive to take $C_R = 0$, the so-called friction-less feed system, for numerical convenience but empirical indications suggest that much higher values could be a prerequisite for steady evaporation. In order to get ourselves into the proper ballpark then, we might look instead to the seminal work of Romero-Sanz [29] and attempt to glean a measure of insight. In the study described therein, it is noted that a somewhat larger capillary with radius b_0 =10^{-5} m and length L =0.3 m is used to achieve pure evaporation with EMI-BF4 (for which the dynamic viscosity μ_0 ∼0.037 Pa-s). Assuming Poiseuille flow, the corresponding impedance of this line is numerically equivalent to

$$R_h = \frac{8\mu_0 L}{\pi b_0^4} = 2.83 \times 10^{18} Pa - s/m^3 \tag{8.2}$$

which gives C_R =1340 in our dimensionless notation. With this in mind, we will elect C_R =10^3 for the initial survey of low fields.

The figures that follow present several important results, including the corresponding variations in $\hat{E}_0$ and $\hat{P}_r$. Figure 8-1 delineates computed elongation curves as functions of the applied field. Perhaps unsurprisingly, these exhibit familiar turning point behavior and bear a strong qualitative resemblance to earlier results for other menisci. Figure 8-2 depicts limiting shapes, approximately representative of the static stability threshold, for each of the back-pressures we have considered.

Emission properties for the calculated menisci are elucidated in Figure 8-3, where the vacuum field at the tip is shown as a function of $\hat{E}_0$. Interestingly, we can see that the maximum attainable field is only on the order of $\hat{E}_{tip} \sim 10^0$, and roughly corresponds to the case of a vanishing back-pressure. To understand the implications for evaporation, consider that

$$\hat{E}_{tip} \sim 1 \Rightarrow E_{tip} \sim E_c = \sqrt{\frac{4\gamma}{\epsilon_0 b_0}} \tag{8.3}$$

which can easily be related to the critical field E^*

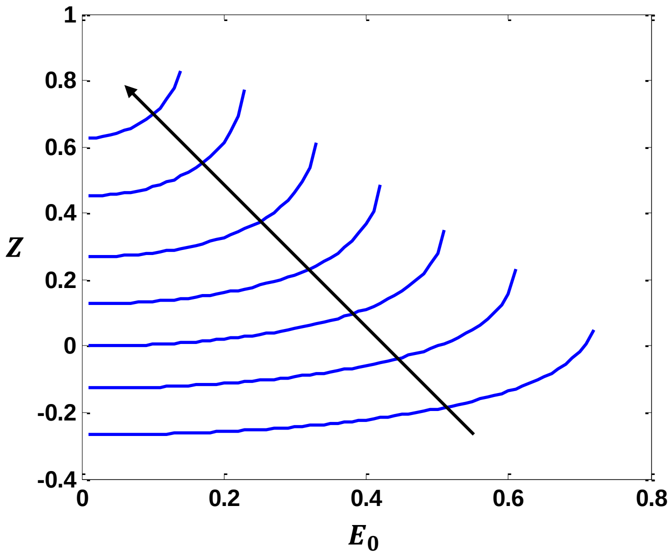

Figure 8-1: Elongation curves corresponding to lower branch of free-volume equilibria. The elongations are plotted as a function of the dimensionless field $\hat{E}_0$ with the reservoir pressure $\hat{P}_r$ as a parameter. Delineated values are $\hat{P}_r$ =-0.50, -0.25, 0.00, 0.25, 0.50, 0.75, and 0.90 with the arrow indicating the direction of increasing value. Notice that the curves are qualitatively familiar and exhibit so-called turning point behavior.

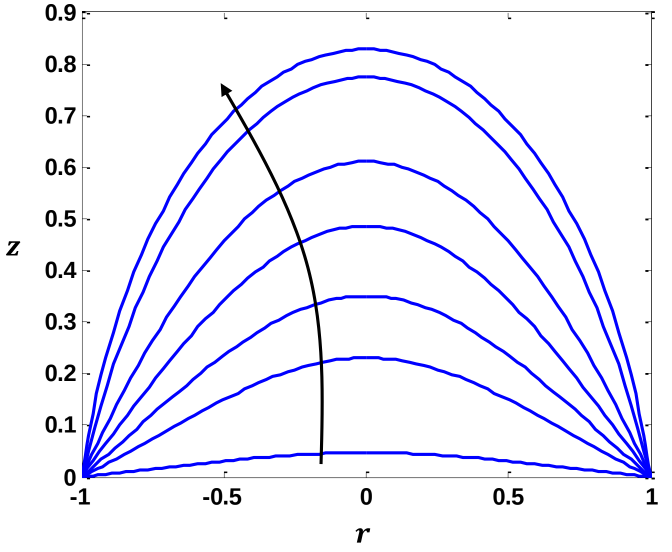

Figure 8-2: Limiting menisci for lower branch of free-volume equilibria. The menisci are plotted in dimensionless $\hat{r}-\hat{z}$ space and correspond to the turning point locations from Fig. 8-1. Delineated back-pressures are $\hat{P}_r$ =-0.50, -0.25, 0.00, 0.25, 0.50, 0.75, and 0.90 with the arrow indicating the direction of increasing value.

$$\frac{E_{tip}}{E^*} \sim \sqrt{\frac{4\gamma}{\epsilon_0 b_0}} \times \sqrt{\frac{\epsilon_0 r^*}{4\gamma}} = \sqrt{\frac{r^*}{b_0}} = B^{1/2} \tag{8.4}$$

In the regime involving $B \ll 1$, this indicates that the interfacial fields corresponding to this ordinary branch of solutions will never be high enough for meaningful evaporation. This was confirmed in the simulations, where currents were observed in the range from 10^{-16} - 10^{-12} A for the 1-micron meniscus but not beyond. Owing to these nearly immeasurable magnitudes, our choice of C_R was apparently moot.

In spite of our complex and very substantial efforts to this point, it is still difficult to reconcile these rigorous results with empirical observations suggesting that pure evaporation can indeed be feasible in an extremely low-B regime. As in the spheroidal case, it appears as though free-volume menisci residing along the normal solution branch (i.e. the one for which $\hat{E}_0$ is low) are subject to similar restrictions. If we are to eventually identify evaporative situations, as we suspect that we should be able to, it stands to reason then that we will need to search for previously uncharted branches. This will be the topic of the following section.

Before we begin that search, there are potentially useful results still to be gleaned from the lower solution branch. Figure 8-4, for example, delineates one such result. The contact angle, defined here as the liquid-side angle between the interface and plane of the plate, is shown as a function of the applied field with $\hat{P}_r$ as a parameter. As we can see, this angle tends to increase with the field and also climbs dramatically in response to added back-pressure. Since we can expect the contact line to be pinned at b_0 so long as θ_c is less than the so-called wetting angle θ_w [94], the utility of this result is a demarcation of the feeding and stressing conditions for which the meniscus should be confined to the modeled fluid port. For example, with a system that is perfectly wetting ($\theta_w \to 0$) it is clear that any back-pressure $\hat{P}_r > 0$ will immediately result in spillage that breaks the interface, causing fluid to rapidly spread across the plate (Fig. 8-5). The same is likely true of smaller back-pressures if the field is sufficiently high; for example, in the case where $\hat{P}_r = -0.25$ and $\hat{E}_0 \gtrsim 0.50$.

When the feeding port in the plate is part of a larger emitter tip, it is expected that these "leaky" conditions will lead to a thin layer of conformal fluid covering the structure. In this event, the fluid could resemble that of an externally-wetted tip (insofar as its coverage of the tip, at least) but exhibit different hydraulics as a result of the internal feeding. While this may at first seem interesting, it is becoming increasingly evident that larger menisci may have a much more difficult time supporting pure evaporation. If this is indeed true, spillage will only serve to increase the effective meniscus size, reducing in some way the ability for the tip to produce monodisperse ions in steady fashion.

8.2 Upper equilibrum branch

The results of the previous section should embody the full family of "normal" solutions for menisci involving $B \ll 1$, i.e. “egg-shaped” solutions that are qualitatively similar to those that we have already seen. We can surmise this based on the familiar

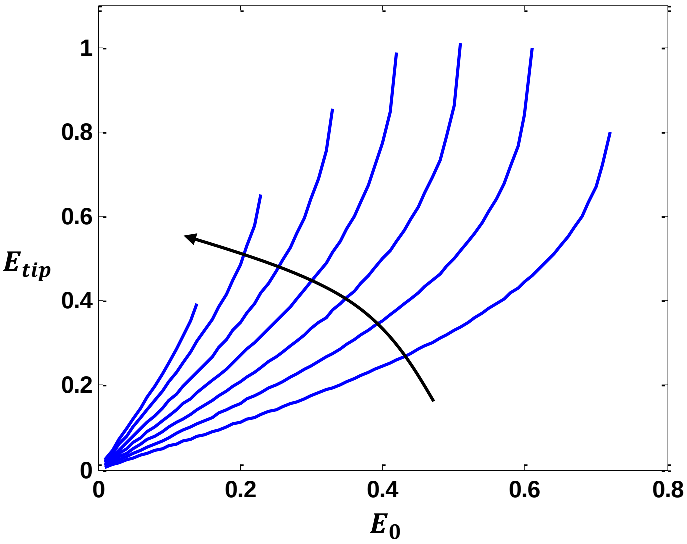

Figure 8-3: Apex fields for free-volume menisci residing on lower solution branch. The dimensionless vacuum field $\hat{E}_{tip}$ is shown as a function of the applied field $\hat{E}_0$ with the reservoir pressure as a parameter. Delineated values are $\hat{P}_r$ =-0.50, -0.25, 0.00, 0.25, 0.50, 0.75, and 0.90 with the arrow indicating the direction of increasing magnitude. Notice that the field reaches a maximum near the turning point of the $\hat{P}_r$ =0 case and corresponds to approximately E_c, precluding meaningful evaporation when $b_0 \gg r^*$.

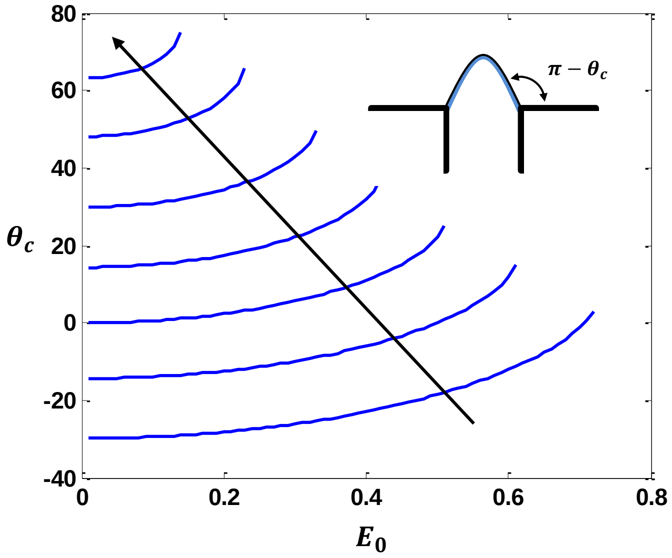

Figure 8-4: Contact angles for free-volume menisci residing on lower solution branch. The contact angle is defined as the angle inside the liquid between the interface and the plane of the anchoring plate. It is shown (units of degrees) as a function of the applied field $\hat{E}_0$ with the reservoir pressure as a parameter. Delineated values are $\hat{P}_r$ =-0.50, -0.25, 0.00, 0.25, 0.50, 0.75, and 0.90 with the arrow indicating the direction of increasing magnitude.

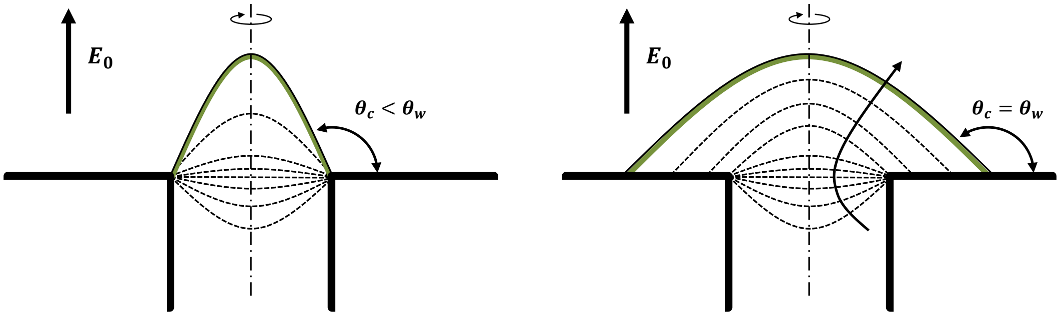

Figure 8-5: Contact line pinning for a free-volume meniscus. **Left:** The contact line is pinned to the fluid port so long as angle the interface makes with the plate is less than the wetting angle, i.e. $\theta_c < \theta_w$. **Right:** The contact line is permitted to wander when $\theta_c \to \theta_w$. It is possible that this leads to a situation in which the plate becomes covered with a thin layer of liquid.

turning point behavior observed in the elongation curves of Fig. 8-1, which would seem to significantly temper the possibility that additional solutions of the same type exist beyond the noted limits of stability. However, as we have also suggested, this conclusion is very difficult to reconcile with empirical phenomena since the lower branch was not found to support meaningful emission.

With this in mind, it makes sense now to hypothesize the existence of high-field solutions that do in fact support the strong emission we anticipate, but from interfacial configurations that are possibly very different from the ones to which we have become accustomed. Owing to the lower turning points, it seems fair to speculate that the emission physics themselves (namely the interaction of evaporation-induced flow with an upstream impedance) are responsible for conferring stability on this new and previously uncharted branch.

8.2.1 First solution & numerical recalibration

In an effort to elucidate this elusive solution family, we might start by electing to investigate the same fluid that was used to probe the lower branch. For consistency, we can conserve $B = 0.047$ and $C_R = 10^3$ while judiciously prescribing the reservoir pressure $\hat{P}_r = 0$ in view of Fig. 8-3, which suggests that this is a good candidate for maximizing the field at the tip of the meniscus. On the other hand, the choice of appropriate $\hat{E}_0$ is rather arbitrary and uninformed but should obviously be larger than the limiting field $\hat{E}_0 \sim 0.51$ found for the lower turning point. As an exercise in educated conjecture, we can therefore choose $\hat{E}_0 = 0.70$ to satisfy this condition while offering at the same time a small buffer that does not push the field to farcical levels.

Before searching for a solution we will also need to identify an initial meniscus shape that is at least reasonably close to the equilibrium one so that our numerical routine does not diverge. As with the field, this is again an exercise in guesswork since it is difficult to have intuition for what the interface might eventually resemble. While it is unlikely that the Taylor archetype will prevail, owing to an important dependence on the hydrostatic condition of the meniscus now (which, of course, is neglected in the classical derivation of Taylor's structure), a pseudo-conic is probably a good starting point so long as the tip is sufficiently rounded. To develop such a shape we will first consider the corresponding distribution of surface tension (i.e., Laplace pressure) since this is an input to the model. In general we have that $P_{st} = -\gamma(\nabla \cdot \vec{n})$, where $\nabla \cdot \vec{n}$ is the divergence of the local normal at the interface. From the appendix, this takes the form

$$\nabla \cdot \vec{n} = \frac{(1 + h_r^2)\, h_r + r \times h_{rr}}{r\,(1 + h_r^2)^{3/2}} \tag{8.5}$$

in cylindrical coordinates, where the spatial profile of the meniscus is given by $z = h(r)$ and the subscripts denote the first and second spatial derivatives with respect to the cylindrical radius r. After converting this to our dimensionless notation we find

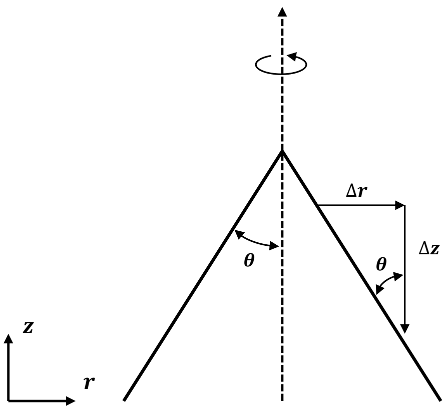

Figure 8-6: Relationship between the half-angle of an axisymmetric cone in cylindrical space and the slope of its projection on the $r - z$ plane. From $dz/dr = h_r$ we have that $h_r = -\cot\theta$.

$$\hat{P}_{st} = -\frac{1}{2}\left[\frac{\left(1+\hat{h}_r^2\right)\hat{h}_r + \hat{r}\times\hat{h}_{rr}}{\hat{r}\left(1+\hat{h}_r^2\right)^{3/2}}\right] \tag{8.6}$$

For a conical protrusion, h_r must be a constant while $h_{rr} \to 0$. This reduces Eq. 8.6 to

$$\hat{P}_{st} = -\frac{1}{2}\frac{\hat{h}_r}{\hat{r}\left(1+\hat{h}_r^2\right)^{1/2}} \tag{8.7}$$

The slope of the profile h_r will now depend on half-angle of the cone we choose (see Fig. 8-6). The trigonometric relationship is $h_r = -\cot\theta$ since the cone requires $h_r < 0$ by definition, and so the surface tension becomes

$$\hat{P}_{st} = \frac{\cos\theta}{2\hat{r}} \tag{8.8}$$

after a measure of algebraic manipulation. Of course, $P_{st} \to \infty$ for $r \to 0$ as we would expect for a perfectly sharp conical tip, but such a singularity is something that should be avoided, particularly in numerical computation. In situations where steady evaporation prevails it is likely that a rounded apex exists in lieu of a sharp point. From earlier chapters we know that the characteristic scale of this cap is r^* and so the corresponding tension must be $P_{st} \sim 2\gamma/r^*$. In dimensionless quantities this amounts to

$$\hat{P}_{st} \sim \frac{r_0}{r^*} = B^{-1} \tag{8.9}$$

Since we have already prescribed $B = 0.047$ we now see that $\hat{P}_{st} \sim 20$ should be expected in the vicinity of an equilibrated tip. Just to be sure that we are starting our

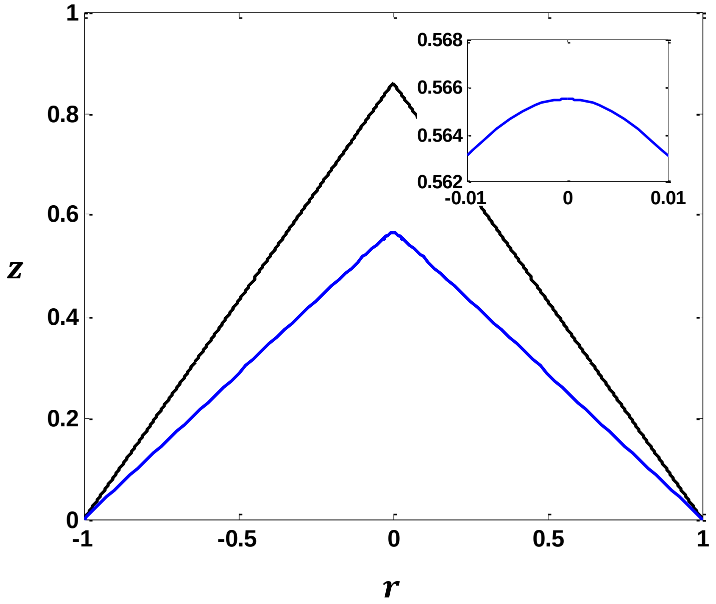

Figure 8-7: Starting shape for calculations to identify first solution along upper equilibrium branch. The initial guess (blue) is shown alongside a classical Taylor structure (black) while the inset highlights the roundedness of the cap. Coordinates are given in dimensionless $\hat{r} - \hat{z}$ space.

numerical process with a situation of active emission, however, it might make sense to "sharpen" this tip, even if only incrementally. As a result, in a semi-arbitrary manner we now choose $\hat{P}_{st} = 50$ for the cap and $\theta = 60°$ for the conical half-angle that will exist far from the apex. Mating these two conditions gives

$$\hat{P}_{st} = \begin{cases} 50 & , \ \frac{\cos\theta}{2\hat{r}} \geq 50 \\ \frac{\cos\theta}{2\hat{r}} & , \ \text{otherwise} \end{cases} \tag{8.10}$$

The shape that is produced by this distribution of tension is shown in Fig. 8-7 alongside a classical Taylor structure for comparison. The inset delineates the rounded part of the cap very near to the axis of symmetry.

With a starting shape in hand we can begin to search for an equilibrium solution at the specific point we have identified in the parameter space. Before we start, it is worth mentioning that we may or may not require a "slow" iterative evolution of the meniscus since we are now anticipating emission that will in general have a very nonlinear (i.e. exponential) dependency on the prevailing fields. To be safe, we can investigate cases of $\beta = 0.50$ and $\beta = 0.05$ in parallel while maintaining our $P_\beta = 10^{-3}$ termination condition.

Figure 8-8 shows semi-converged solutions for both cases. On the left, the dashed blue line delineates the starting point for $\beta = 0.5$ while the lower blue line signifies an interface that is apparently very close to an equilibrium but still slightly beyond the

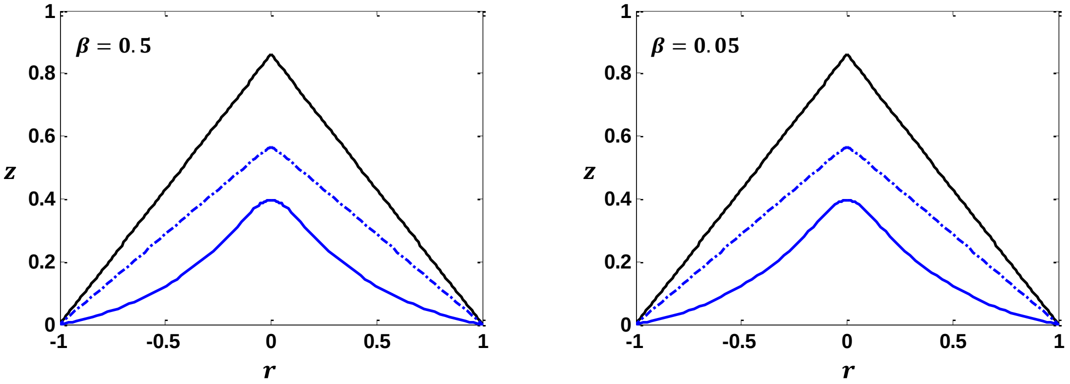

Figure 8-8: Semi-converged morphologies for first solution along upper branch with $\beta = 0.50$ and $\beta = 0.05$. The initial guess (blue dash) is shown above near-equilibrium menisci (solid blue) with a classical Taylor structure (black) for comparison. In the $\beta = 0.50$ case (left), the near-equilibrium structure is reached very quickly but the termination condition cannot be satisfied after many additional iterations. The $\beta = 0.05$ case (right) approaches an almost identical structure fairly slowly but does achieve full convergence.

termination threshold. On the right, the lower blue curve indicates a fully converged solution (termination condition satisfied) found with the smaller $\beta = 0.05$. These were reached after $i = 100$ iterations for $\beta = 0.50$ (arbitrarily stopped due to asymptoting excess pressure) and $i = 272$ iterations for $\beta = 0.05$.

To clarify several important convergence properties, Figures 8-9 and 8-10 delineate the tip height (left) and dimensionless current (right) computed during each computational iteration. For $\beta = 0.50$ (Fig. 8-9), we can see that the tip height oscillates to some degree but otherwise approaches a constant value $\hat{z}_{tip} \sim 0.40$ very quickly. The same is true of the dimensionless current, where it might be noted that for the fluid in question the value $\hat{I} \sim 5{\times}10^{-4}$ corresponds to roughly 80 nA. By comparison, it is clear that the $\beta = 0.05$ case (Fig. 8-10) yields what amounts to identical values, albeit after significantly more iteration cycles.

Figures 8-11 ($\beta = 0.5$) and 8-12 ($\beta = 0.05$) delineate the maximum absolute value of $\Delta\hat{P}$ across the menisci during each iteration (left graphs). Again, these show that the $\beta = 0.5$ case very rapidly approaches a converged condition, but now we can see how it “dances” right around $P_\beta = 10^{-3}$ for many iterations without actually reaching it at any point. As a result, the solver was manually terminated after 100 computational cycles. For $\beta = 0.05$, on the other hand, the termination condition is indeed reached, although it is clear that the threshold is approached extremely methodically.

In an ideal world the deliberateness of $\beta = 0.05$ would not be an issue. Much to the contrary, it would likely be a virtue, and we would take β arbitrarily small in connection with an infinitely dense mesh in order to capture the important physics perfectly well. In the real world, however, making the relaxation parameter small and

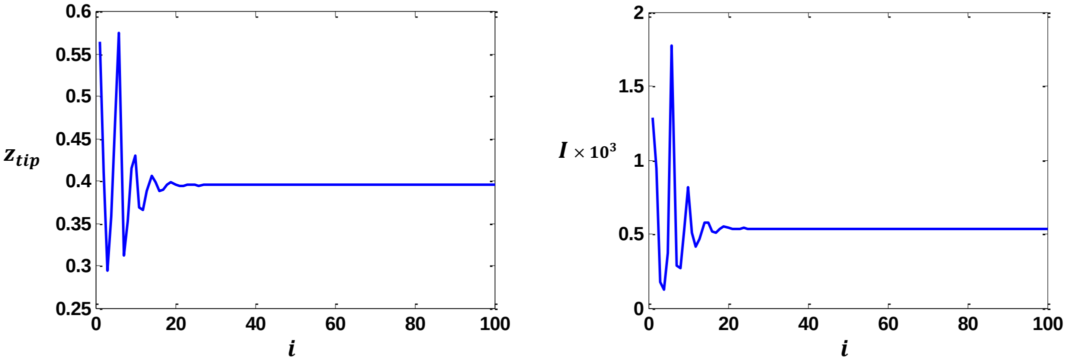

Figure 8-9: Elongation and evaporation convergence for first upper branch solution with $\beta = 0.50$. **Left:** The elongation of the meniscus (tip height) is shown as a function of the iteration index i. **Right:** The calculated dimensionless current is similarly offered. Note for the elected fluid and contact conditions that $\hat{I} \approx 5\times10^{-4}$ corresponds to roughly 80 nA.

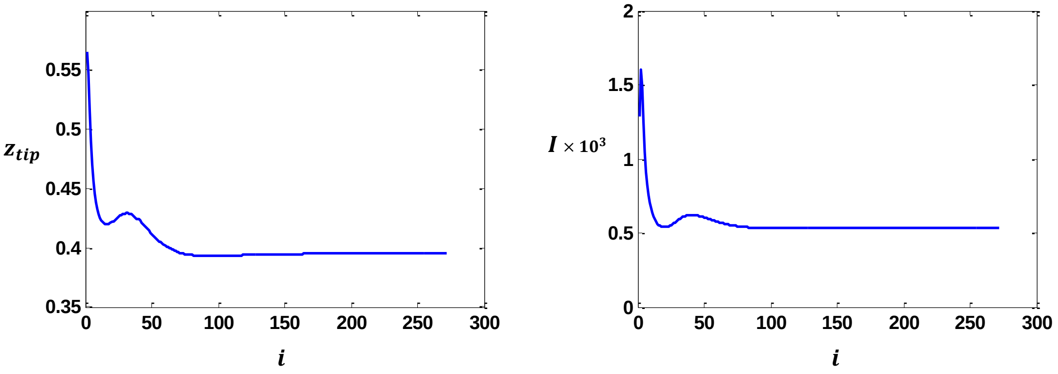

Figure 8-10: Elongation and evaporation convergence for first upper branch solution with $\beta = 0.05$. **Left:** The elongation of the meniscus (tip height) is shown as a function of the iteration index i. **Right:** The calculated dimensionless current is similarly offered. Note for the elected fluid and contact conditions that $\hat{I} \approx 5\times10^{-4}$ corresponds to roughly 80 nA.

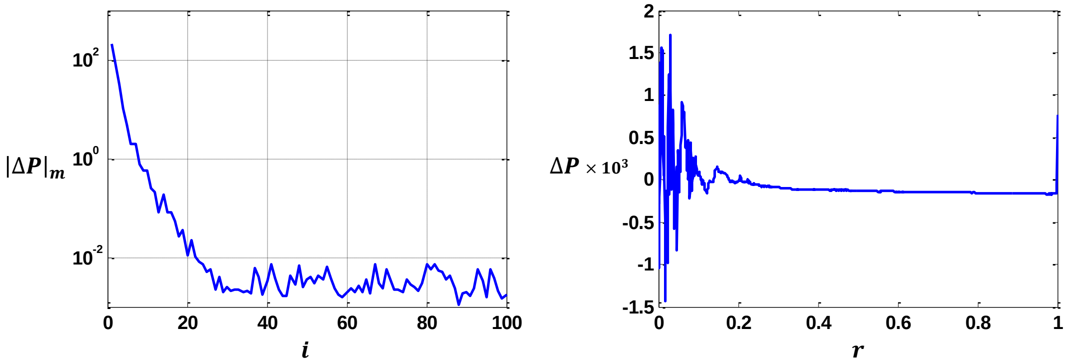

Figure 8-11: Convergence of excess pressure and final interfacial distribution for first upper branch solution with $\beta = 0.50$. **Left:** Maximum absolute value of $\Delta \hat{P}$ along the meniscus during each computational iteration. **Right:** Distribution of excess pressure as a function of $\hat{r}$ across the interface for the final computational iteration ($i = 100$).

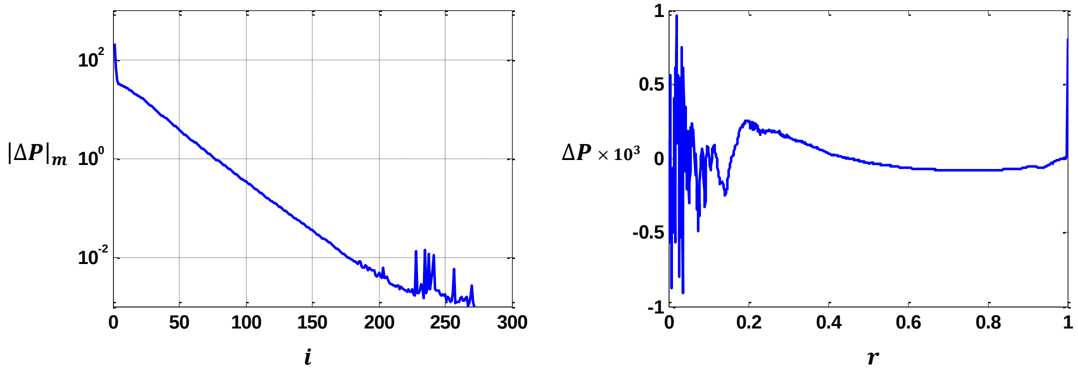

Figure 8-12: Convergence of excess pressure and final interfacial distribution for first upper branch solution with $\beta = 0.05$. **Left:** Maximum absolute value of $\Delta \hat{P}$ along the meniscus during each computational iteration. **Right:** Distribution of excess pressure as a function of $\hat{r}$ across the interface for the final computational iteration ($i = 272$).

supplementing the mesh has nontrivial consequences, i.e. this increases the number of required iterations (small β) and also the computational time per iteration (mesh density). Since each iteration already costs roughly one minute of real time, neither of these options are particularly compelling. We have an obvious and vested interest in maintaining the mesh as it is while using $\beta = 0.50$, but we need to rectify our present inability to satisfy the chosen P_β before we can move on to exploring the broader parameter space.

Based on the collection of presented convergence behaviors for the $\beta = 0.50$ case, it is clear that the real equilibrium solution was actually identified in spite of the fact that the termination condition was not quite satisfied. This is a first indication that P_β can be relaxed in some way without loss of accuracy. In other words, the existing termination condition is unnecessarily stringent. To develop a better sense for what might be going on, we refer to Figs. 8-11 and 8-12 (right), which show the distributions of $\Delta\hat{P}_d$ across the menisci for both β during the final iteration ($i = 100$ and $i = 272$ for $\beta = 0.5$ and $\beta = 0.05$, respectively). From the curves contained therein it is evident that we are experiencing a small amount of noise near the activated (emitting) apices. Owing to the multiphysical and nonlinear nature of the processes that are now concentrated there, this is perhaps to be expected. What is important to point out, however, is that unlike the "egg-shaped" interfaces from the lower solution branch and the earlier chapters, for which the governing stresses are on the order of $2\gamma/r_0$ at most, the emitting part of the meniscus is now unfairly penalized by the chosen form of P_β. This is because the important stresses on the activated tip (these scale like $\sim B^{-1}$) can be large in comparison to the nominal capillary pressure, which suggests that the attendant noise could be too great for the static termination value.

As an alternative, it would seem reasonable to compare the distribution of ΔP_d to the other local pressures (electrical, interfacial, etc.) in lieu of simply $2\gamma/r0$. For example, a given ΔP_d could be compared to the local max-norm, $|\boldsymbol{\tau}|_m$, defined by

$$|\boldsymbol{\tau}|_m = \max\left\{|\boldsymbol{\tau}_n^e|, |\gamma\nabla\cdot\vec{n}|, |\boldsymbol{\tau}_n^v|\right\} \tag{8.11}$$

where the three stresses on the right-hand side are the normal electric stress, the surface tension stress, and the normal viscous stress, respectively. This leads to the modified termination condition

$$\frac{|\Delta P_d|}{|\boldsymbol{\tau}|_m} \leq |P_\beta| \tag{8.12}$$

in which the denominator is understood to be the max-norm of the pressures local to the ΔP_d in question. With this formulation, we should expect a fair assessment of equilibrium proximity, even for instances where $B \ll 1$, and the ability to use the faster $beta = 0.5$ value. For example, in the present case of $\hat{E}_0 = 0.7$ this condition with $|P_\beta| = 10^{-2}$ would have stopped the $\beta = 0.5$ simulation after iteration $i = 22$, where the integrated current and tip elongation differed from the final $\beta = 0.05$ result (the one for iteration $i = 272$) by no more than 1% and 0.1%, respectively. As a result, we will adopt $|P_\beta| = 10^{-2}$ going forward and hope that it will afford us the

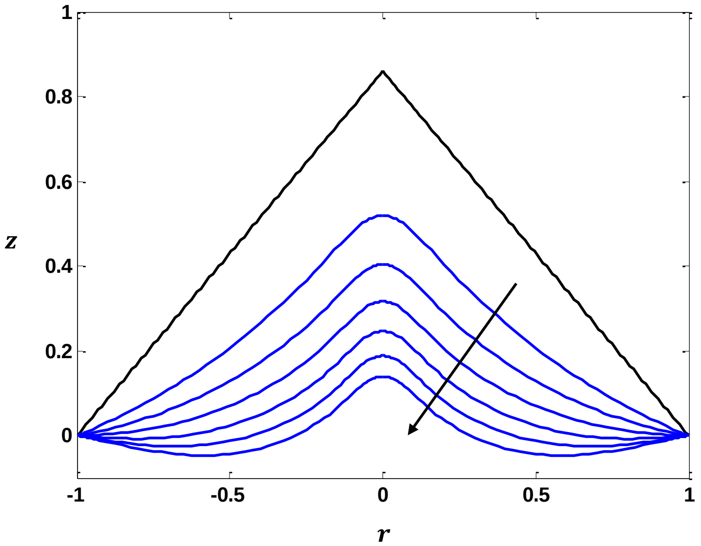

Figure 8-13: Select shapes for the first set of upper equilibrium solutions (variations in $\hat{E}_0$) plotted in dimensionless $\hat{r}$-$\hat{z}$ space. A Taylor structure (black) is shown alongside menisci for $\hat{E}_0 = [0.59, 0.69, 0.79, 0.89, 0.99, 1.09]$, where the arrow indicates the direction of increasing field. The results indicate an inverse proportionality between the field and the elongation (and also the volume), in addition to the notion that the Taylor structure may not be the appropriate archetype for ion evaporation.

opportunity to explore an interesting subregion of the global parameter space in a practical amount of time.

8.2.2 Variations in $\hat{E}_0$ ($B = 0.047$, $C_R = 10^3$, $\hat{P}_r = 0$)

Our first submapping task is to explore variations in the field $\hat{E}_0$ while conserving the set of complimentary parameters ($B = 0.047$, $C_R = 10^3$, $\hat{P}_r = 0$). Starting with the initial $\hat{E}_0 = 0.70$ solution, we achieve this by making incremental excursions in either direction ($\Delta\hat{E}_0 = 0.01$) until new solutions can no longer be identified within the given tolerance.

Using this method we calculate equilibria spanning the domain from $\hat{E}_0 = 0.59$ to $\hat{E}_0 = 1.09$. Figure 8-13 delineates a selection of corresponding shapes alongside a classical Taylor structure for comparison. The arrow indicates the direction of increasing field. As we can see, for small fields the meniscus begins to approach something that might be construed as a pseudo-conic but never quite resembles Taylor. On the opposite end of the spectrum, the physics of the higher fields apparently cause the interface to be sucked into its feeding tube, for lack of a better description. At $\hat{E}_0 = 1.09$ in particular, this results in a meniscus that is very unlike the classical Taylor structure, and a first indication that such “cones” might not be the proper archetype for low-B ion evaporation.

In Figure 8-14 we plot the elongation curve for the upper equilibria in order to

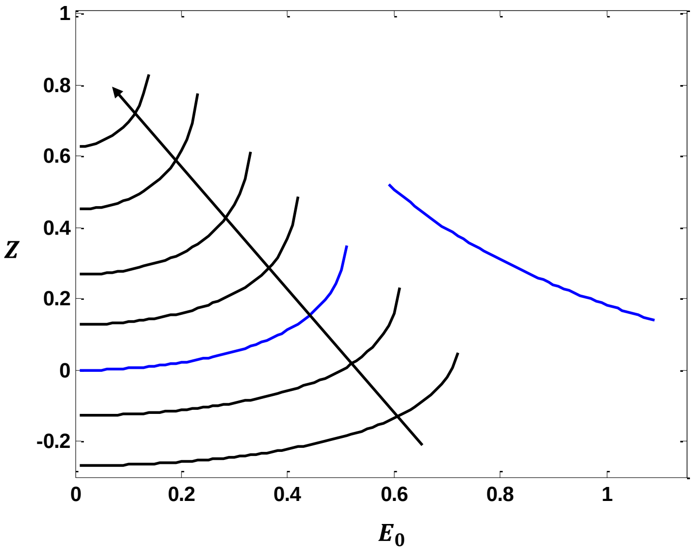

Figure 8-14: Comparison of elongation curves between upper and lower branches. The elongation Z is given as a function of $\hat{E}_0$. The lower branch (left curves) is the same as that delineated in Fig. 8-1, where the arrow indicates the direction of increasing reservoir pressure $\hat{P}_r$. Along both branches, the case $\hat{P}_r = 0$ is plotted in blue. The results highlight the inverse proportionality between the field and elongation (also the volume).

develop a better sense for where these new solutions reside in comparison to those of the lower branch. Beyond the turning point that terminates the latter there exists a small gap in the field for which we have not identified any menisci. It is possible that this region corresponds to known electrospray regimes (or at least relatives of known regimes, e.g. the pulsating regimes described by Cloupeau and Prunet-Foch [95, 96]) that are unstable. At $\hat{E}_0 = 0.59$ the upper elongation curve commences and immediately distinguishes itself from its lower counterpart in the sense that it exhibits a negative slope. In other words, the field and the elongation show the inverse proportionality that we noted in Fig. 8-13. This is very interesting and also explicable by way of the emission physics that are now present but did not contribute to the lower branch. For clarity, we plot the tip fields in Figure 8-15 where we can see that the sharpness of the upper branch confers much higher E_n^v. The inset delineates the relationship between this field and the critical one, E^*, and indicates that we must now be supporting fields that are appropriate for ion evaporation.

Figure 8-16 shows the integrated dimensionless current as a function of the field $\hat{E}_0$. Units are offered in the inset, corresponding to the particular fluid we have chosen, and these suggest that very meaningful evaporation is now taking place. For example, for the lower fields we see several tens of nanoamperes ($I \lesssim 50$ nA at the low extreme) and for the higher fields we see several hundred nanoamperes ($I \gtrsim 180$ nA at the high extreme). At first glance these would seem to agree at least qualitatively with laboratory observations as they exhibit reasonable magnitude, i.e., hundreds of nA,

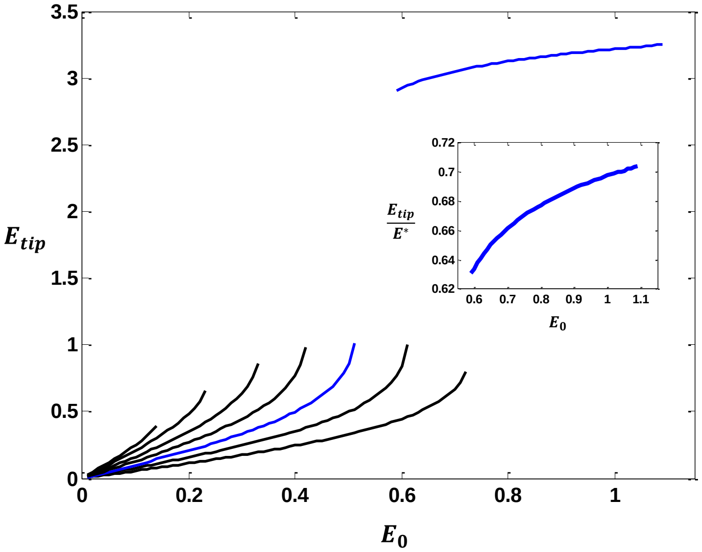

Figure 8-15: Comparison of apex field between upper and lower branches. The dimensionless tip field $\hat{E}_{tip}$ is given as a function of $\hat{E}_0$. The lower branch (lower left curves) is the same as that delineated in Fig. 8-3, where $\hat{P}_r$ decreases from left to right. Along both branches, the case $\hat{P}_r = 0$ is plotted in blue. The results highlight the substantial increase in field that is observed for the upper equilibria. This owes to improved meniscus sharpness and likely affords meaningful emission. The latter is evidenced by the inset, which depicts the relationship between the tip field and the critical one E^*.

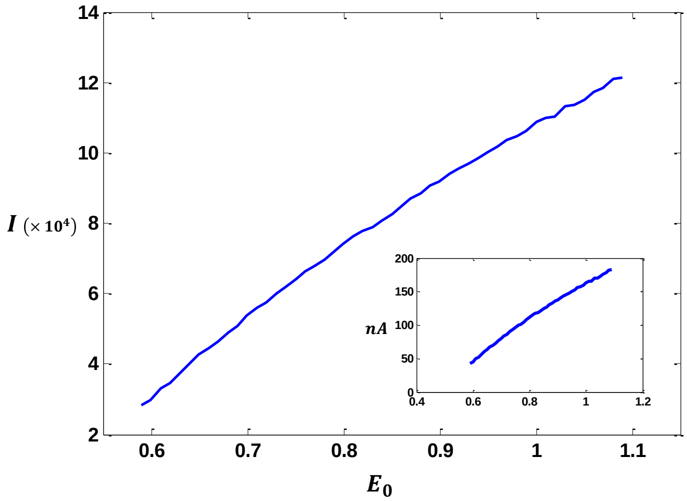

Figure 8-16: Calculated current for first solutions along upper equilibrium branch. The dimensionless current $\hat{I}$ is plotted as a function of $\hat{E}_0$ while the inset offers units (nA) corresponding to the prototype fluid. Along with reasonable magnitudes (several tens of nA to several hundred), a linear relationship between the current and the field is observed. These appear to at least qualitatively agree with known empirical phenomena.

and a measure of linearity with respect to the applied field [54, 56]. Moreover, they now provide a physical explanation for the interesting elongation behavior: as the current increases with the field, interaction of the attendant flow with the upstream impedance reduces the nearly hydrostatic pressure in the meniscus such that it is pulled toward the plane defining the end of the tube (as seen in Figs. 8-13 and 8-14).

8.2.3 Select solution characteristics ($\hat{E}_0 = 1.00$, $B = 0.047$, $C_R = 10^3$, $\hat{P}_r = 0$)

In an effort to further our investigation of the upper equilibria we will present here a collection of interesting results for the specific solution identified at $\hat{E}_0 = 1.00$. We believe that these will at least qualitatively embody the characteristics of many of the additional solutions we hope to uncover later on.

Mechanical

Figure 8-17 shows the distributions of dimensionless normal stress across the interface, i.e. as a function of $\hat{r}$. The electric pressure $\boldsymbol{\tau}_n^e$ is the dominant pressure and it is primarily compensated by the surface stresses $\gamma\nabla \cdot \vec{n}$, as expected. At this point it should be clear as to why we separated the hydraulic tensor: the "suction" ($Q \times R_h$) created by pressure loss in the upstream feeding duct is apparently meaningful while the stress accumulated in the meniscus itself ($\vec{n} \cdot \boldsymbol{\tau}^m \cdot \vec{n}$) is exceedingly small. This means that the meniscus is very nearly hydrostatic, which should not come as a

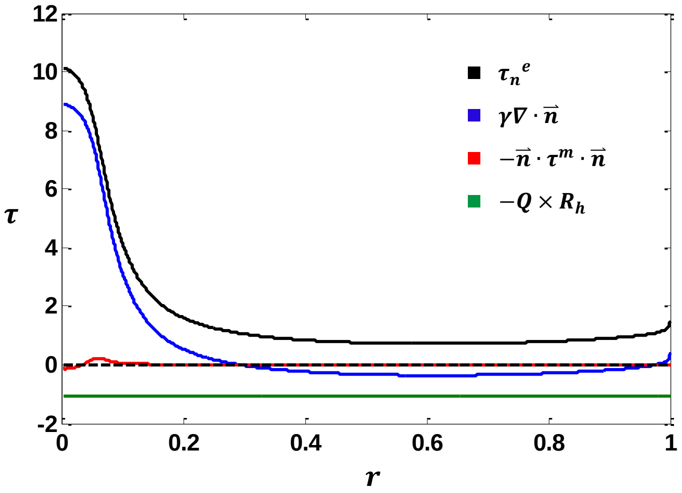

Figure 8-17: Distribution of dimensionless normal surface stresses as a function of $\hat{r}$ across the meniscus. The electrical, interfacial, and hydraulic stresses are indicated in the legend while the excess pressure ΔP_d is shown as a dashed black line. These results strongly suggest a hydrostatic meniscus for which the electrical traction is dominant.

surprise in view of the small Capillary number $\mu u^*/\gamma$, at a pressure that is dictated by the upstream impedance.

From Figure 8-17 we can see that the excess pressure ΔP_d (dashed black) is very small in comparison to the other important pressures, as it should be. For clarity, an expanded view is offered in Figure 8-18 where we show the quotient of the attendant distribution and the max-norm $|\boldsymbol{\tau}|_m$. It is clear that our convergence criterion has been satisfied.

Electrical

The jump condition for electrical surface charge is $\sigma = \epsilon_0 E_n^v - \epsilon_0 \epsilon_r E_n^l$ and so we can write

$$\frac{\sigma}{\epsilon_0 E_n^v} = 1 - \epsilon_r \frac{E_n^l}{E_n^v} = 1 - \epsilon_r \frac{\hat{E}_n^l}{\hat{E}_n^v} \tag{8.13}$$

as a measure of the local surface relaxation. This relationship is plotted in Fig. 8-19 as a function of the dimensionless radial coordinate $\hat{r}$, where we can see that full relaxation prevails across most of the meniscus and gives way to charge depletion only in the vicinity of a small activated region near the tip. Based on the inset it is clear that this region is roughly $0.05 = 1/20^{th}$ the size of the contact line, corresponding with very nicely to earlier estimations of r^* for the elected fluid.

As we have already discussed, local depletion of surface charge is an expected byproduct of conduction limitations in the fluid. This will in general lead to field permeation that should affect the potential of the meniscus near its tip. In Fig. 8-20

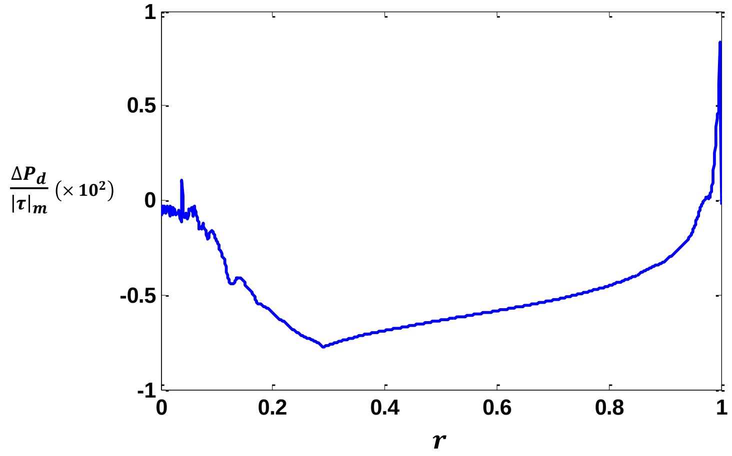

Figure 8-18: Distribution of scaled excess pressure as a function of $\hat{r}$ across the meniscus. The results clearly indicate satisfaction of the given convergence criterion.

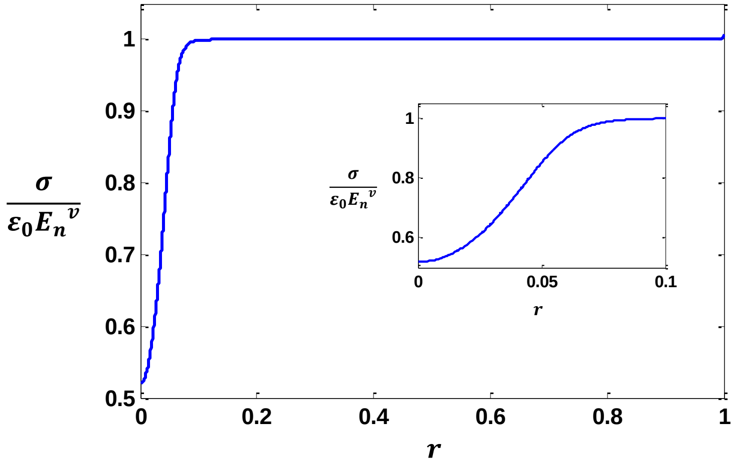

Figure 8-19: Ratio of surface charge to the normal component of the displacement field in vacuum as a function of $\hat{r}$. The meniscus is very nearly fully relaxed outside of a small, activated region near the tip. The inset elucidates this region and indicates that its size corresponds to the estimated r^*.

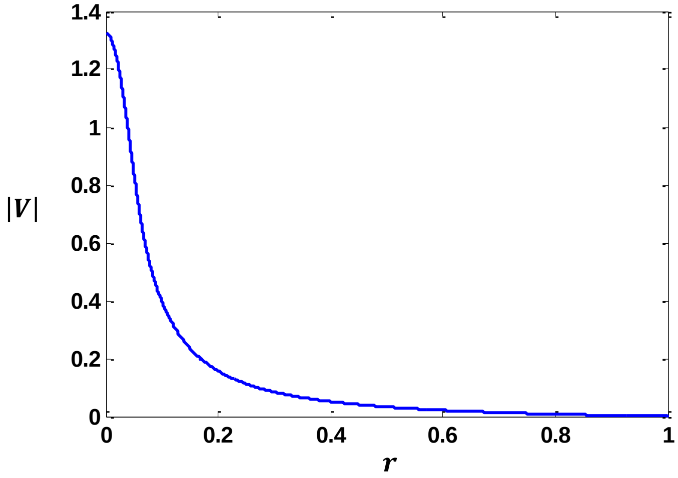

Figure 8-20: Magnitude of potential drop across the meniscus. The modulus $|V|$ is shown as a function of $\hat{r}$ and given in units of volts (based on the prototype fluid). A loss of the expected order is indicated.

we plot the modulus of the potential drop along the meniscus (i.e., the potential of the interface with respect to the reference value Φ_0 at the base) as a function of $\hat{r}$. From the curve we can see that the drop concentrates around the apex, albeit less strongly than for the charge depletion, and exhibits an order ($\sim 10^0$ V) that again agrees very nicely with previous estimates.

In Fig. 8-21 we further elucidate transport issues by plotting the convected (j_{conv}) and conducted (kE_n^l) currents as functions of $\hat{r}$. Without proper context it would at first appear that the convected contribution (j_{conv} $\sim 10^3$ A/m^2) is substantial; however, in comparison to the scale of its conducted counterpart it is obvious that convection plays a rather meaningless role in this instance. As we have already postulated, we believe this to be a very general result for evaporating ionic liquids.

In Figs. 8-22 and 8-23 we plot the dimensionless potential and electric field (axial component E_z^v) distributions along the vacuum axis of the computational domain, respectively. From the insets we can see that the field and potential quickly decrease as we move away from the tip before asymptoting to the parallel-plate values. This is not surprising as we would in general expect that the fields very near to the tip might behave like those of a spherical diode. The corresponding scale for the transition from this local spherical behavior to the one-dimensional solution is apparently b_0 (i.e. that of the contact line), which seems reasonable.

In addition to the preceding results it might be useful to shed additional light on the corresponding space charge characteristics. While we have already performed an order-of-magnitude analysis in an earlier chapter, a slightly more rigorous investigation seems warranted in view of the fact that this aspect of ionic liquid sources is often dismissed. Unlike their liquid metal counterparts, for which it is known that space charge does indeed play a decided role, ionic liquids typically produce more modest

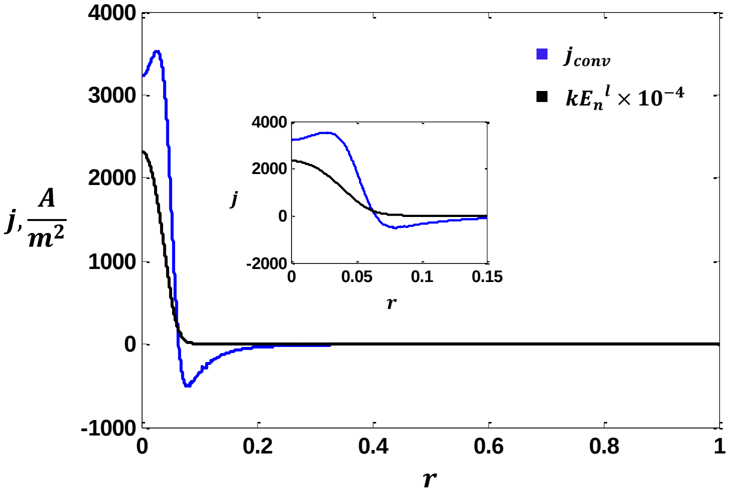

Figure 8-21: Comparison of convected and conducted current values across the meniscus. The convected contribution j_{conv} is shown alongside its conducted counterpart kE_n^l as a function of $\hat{r}$. The latter is strongly scaled ($\times 10^{-4}$) to fit in the plot, which suggests that convection is largely insubstantial in the process of ionic liquid evaporation.

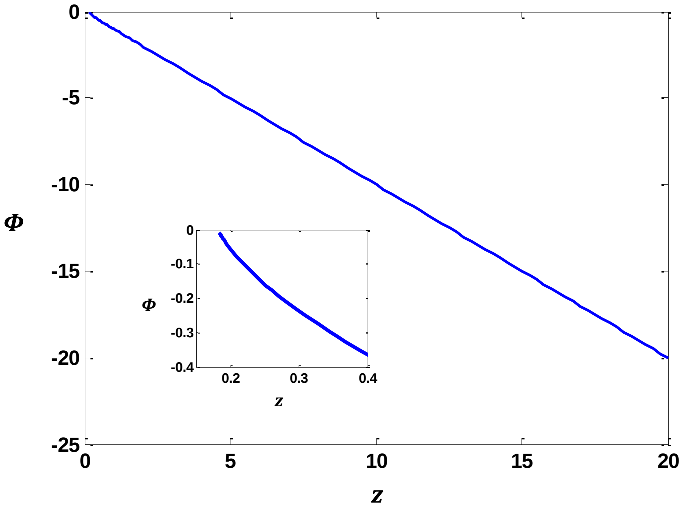

Figure 8-22: Dimensionless potential distribution along the vacuum part of the computational axis. The dimensional potential Φ^v is scaled by $E_c \times b_0$ and shown as a function of $\hat{z}$. The inset delineates behavior very near to the tip and indicates a fast transition from nonlinear behavior to the parallel-plate solution.

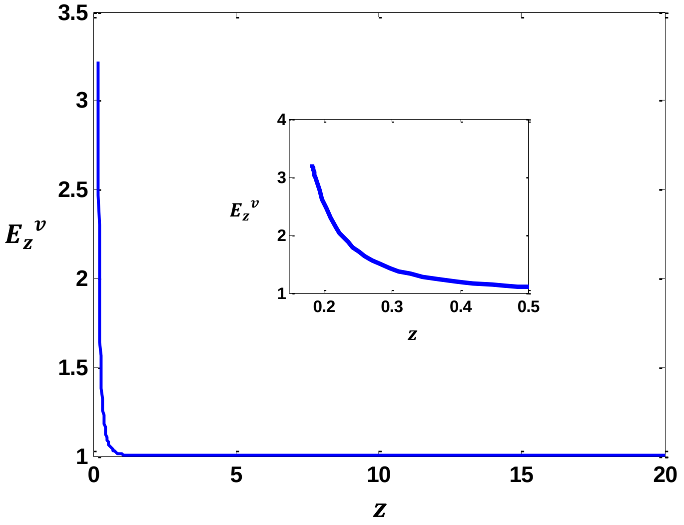

Figure 8-23: Dimensionless field distribution along the vacuum part of the computational axis. The axial field E_z^v is scaled by E_c and shown as a function of $\hat{z}$. The inset delineates behavior very near to the tip and appears to show behavior that is similar to that of a spherical diode. The attendant nonlinearity in the field gives way to the parallel-plate solution over a distance $\Delta\hat{z} \sim 0.5 - 1.0$, indicating that b_0 is likely the appropriate scale.

currents. Owing to the spherical behavior that is local to the tip, we might approach such an investigation by first considering the spherical Poisson equation, i.e.

$$\nabla^2\Phi^v = \frac{1}{r^2}\frac{d}{dr}\left(r^2\frac{d\Phi^v}{dr}\right) = \frac{d^2\Phi^v}{dr^2} + \frac{2}{r}\frac{d\Phi^v}{dr} = \frac{-\rho}{\epsilon_0} \tag{8.14}$$

where we have intentionally omitted θ (polar) and ϕ (azimuthal) dependencies for reasons of symmetry (or at least quasi-symmetry, as in the case of the former). Also note that r is now the spherical radius for a coordinate system that is centered about the active part of the meniscus tip (see Fig. 8-24). The volumetric charge in vacuum is related to the quotient of the spatially varying current density and propagation speed, $\rho = j/v$. In contrast to 1D space charge calculations, for the spherical diode it is necessary for the current density to vary with r in situations where continuity must strictly apply. Noting that the total current $I \sim 4\pi r^2 j$ is invariant, we can write

$$j = j_0\left(\frac{r_0}{r}\right)^2 \tag{8.15}$$

where r_0 and j_0 are the radius and current density for the inner electrode, respectively. If we assign the reference potential $\Phi^v = 0$ to the same electrode, the usual balance between kinetic and electrostatic potential energy gives

$$v = \sqrt{2\frac{q}{m}\left(-\Phi^v\right)} \tag{8.16}$$

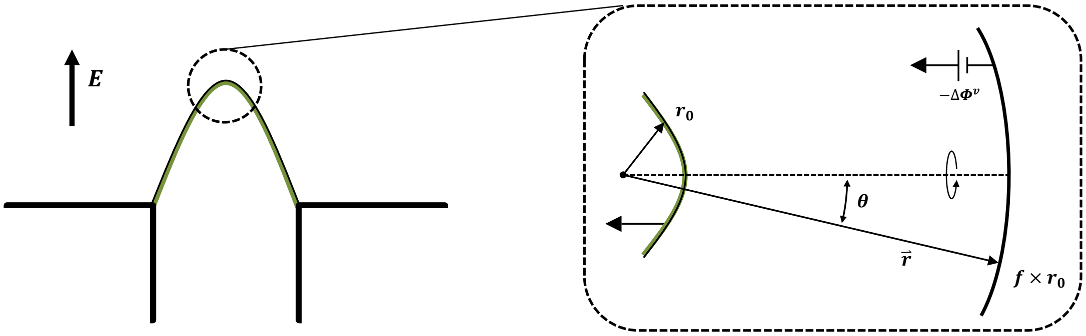

Figure 8-24: Sketch of approximate spherical diode representation near the tip of an activated meniscus. A spherical coordinate system is colocated with the center of the evaporating region such that the radial coordinate $r = r_0$ is coincident with its surface. An approximate potential drop $-\Delta\Phi^v$ exists at a location $r = f \times r_0$.

for the charge velocity. Substituting these in the spherical Poisson now

$$\frac{d^2\Phi^v}{dr^2} + \frac{2}{r}\frac{d\Phi^v}{dr} = -\frac{j_0}{\epsilon_0}\left(\frac{r_0}{r}\right)^2 \frac{1}{\sqrt{2\frac{q}{m}\left(-\Phi^v\right)}} \tag{8.17}$$

We can nondimensionalize Eq. 8.17 by electing the scales

$$\tilde{r} \to \frac{r}{r_0} \tag{8.18}$$

$$\tilde{\Phi}^v \to \frac{\Phi^v}{\Delta\Phi^v} \tag{8.19}$$

where we have invoked the tilde for the dimensionless values to avoid confusion with other dimensionless equation sets. Here, $\Delta\Phi^v$ is the potential difference that is enforced across the diode. After introducing these quantities we find

$$\frac{d^2\tilde{\Phi}^v}{d\tilde{r}^2} + \frac{2}{\tilde{r}}\frac{d\tilde{\Phi}^v}{d\tilde{r}} + \frac{\chi_s}{\tilde{r}^2\sqrt{-\tilde{\Phi}^v}} = 0, \text{ where } \chi_s = \frac{j_0 r_0^2}{\epsilon_0 \Delta\Phi^v \sqrt{2\frac{q}{m}\Delta\Phi^v}} \tag{8.20}$$

When the current density j_0 in the diode goes to zero, such that χ_s vanishes (note that χ_s may be interpreted as the charge loading in the diode), Eq. 8.20 reduces to the spherical Laplacian. If the outer electrode exists a distance $\tilde{r} = f$ from the origin, it can be shown that the corresponding solution is

$$\left(\Phi^v\right)_L = -\left(1 - \frac{1}{\tilde{r}}\right)\left(\frac{f}{f-1}\right) \tag{8.21}$$

For the Laplacian field on the inner electrode, this gives

$$\tilde{E}_r^v\left(\tilde{r} = 1, \chi_s = 0\right) = \frac{f}{f-1} \tag{8.22}$$

Our primary interest relates to how evaporated charge may or may not affect the mechanics of the activated tip. With this in mind, we have solved Eq. 8.20 numerically for various charge factors χ_s and diode ratios f. Figure 8-25, where we have plotted the former as a function of the field ratio $\widetilde{E}_p/\widetilde{E}_L$ (i.e. the Poisson field divided by its Laplacian counterpart) with the latter as a parameter, delineates a family of select solutions. Based on the results we can clearly see that $\chi_s \rightarrow 0$ leads to the homogeneous field while decreasing f amplifies the space charge limit. To confirm that this is correct we can consider instances of small diode ratio, where $f-1 \ll 1$ suggests that we should recover the well-known Child-Langmuir result for 1D space charge limited current

$$j_{CL} = \frac{4}{9}\epsilon_0\sqrt{2\frac{q}{m}}\frac{(\Delta\Phi^v)^{3/2}}{D^2} \tag{8.23}$$

For the diodes, the spacing $D \approx (f-1)r_0$ and so the limiting current is

$$j_0 = \chi_2\left(f-1\right)^2 \times \epsilon_0\sqrt{2\frac{q}{m}}\frac{(\Phi^v)^{3/2}}{D^2} \tag{8.24}$$

By inspection we see that recovery of Child-Langmuir requires $\chi_s(f-1)^2 \rightarrow 4/9$, or $\chi_s \rightarrow 4/9(f-1)^{-2}$. The right-most curve in Fig. 8-25 corresponds to $f-1 = 10^{-2}$ and terminates at $\chi_s = 4516$ for $E_p/E_L = 0$. This gives $\chi_s(f-1)^2 \approx 4.06/9$ and indicates that we are converging to the appropriate physics.

In terms of the present $\hat{E}_0 = 1.00$ meniscus, the dimensionless surface tension (i.e. Laplace pressure) is $\hat{P}_{st} = 8.9$ at the tip, suggesting that $r_0 \sim 10^{-7}$ m might be an appropriate but conservative scale. Similarly, we find that $j_0 \sim 2\times10^7$ A/m^2 and observe from Figs. 8-22 and 8-23 that the pseudo-diode region likely extends to a point between $\hat{z} = 0.5$ and $\hat{z} = 1$ where the potential has dropped 100-150V. Based on considerations for the so-called perveance of the beam (see Lozano [21]), it is probably fair to assume that this is also the extent of the region of space charge that will influence the Poisson field at the tip. With that in mind, we take $f \approx 10$ and $\Delta\Phi^v \approx 150$V to calculate $\chi_s \approx 10^{-2}$. This yields $E_p/E_L \approx 0.96$, or space charge that reduces the Laplacian field by approximately 4%, which is very much in line with the more crude estimate of 1-10% that was arrived at in an earlier chapter.

Hydraulic

In Fig. 8-26 we plot the normal and tangential components of the fluid velocity at the interface. These are scaled by the critical velocity, $u^* \sim kE^*/[\epsilon_r\rho(q/m)]$, that was discussed in earlier chapters. We can see that the tangential velocity (blue) gradually increases as the tip is approached, reaching a maximum near the edge of the activated region and sharply decreasing thereafter. By continuity, $\vec{u}\cdot\vec{t} \rightarrow 0$ as $\hat{r} \rightarrow 0$. Conversely, the normal component (black) of the flow is essentially vanishing for all points outside of the activated region but sharply increasing within it, reaching a maximum on the central axis (where the vacuum field is also at its highest) as we would expect.

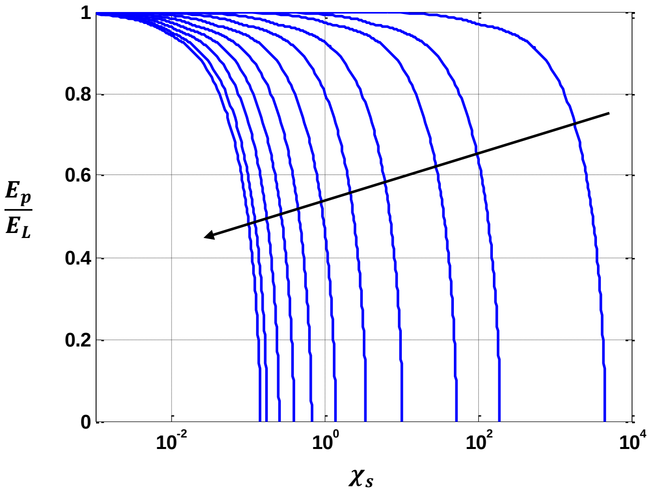

Figure 8-25: Influence of space charge on the field of an idealized spherical diode. The ratio of Poisson to Laplacian fields, E_p/E_L, is plotted as a function of the charge loading χ_s with the diode ratio f as a parameter. The delineated values are $f = [50, 25, 10, 5, 3, 2, 1.5, 1.25, 1.1, 1.05, 1.01]$, increasing in the direction of the arrow.

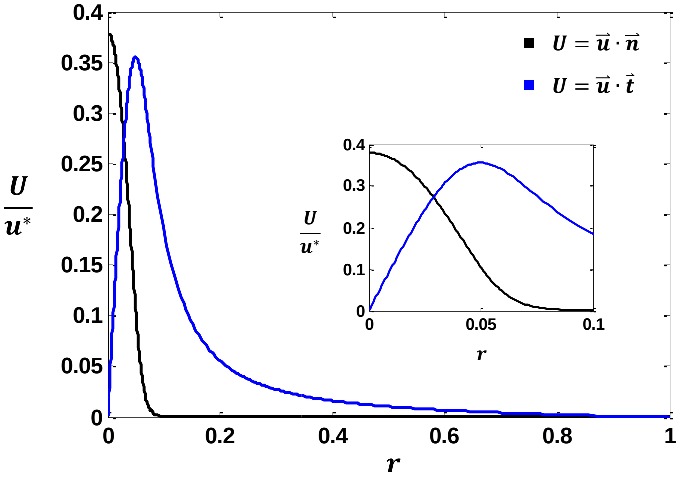

Figure 8-26: Normal $(\vec{u} \cdot \vec{n})$ and tangential $(\vec{u} \cdot \vec{t})$ components of the interfacial flow. These are plotted as a function of $\hat{r}$ and scaled by the critical velocity $u^* \sim kE^*/[\epsilon_r \rho(q/m)]$. The tangential flow increases steadily until the edge of the activated region, after which it falls off sharply. Conversely, the normal flow is essentially zero until the edge of the same region, which marks the beginning of a fast ascent to its maximum at $\hat{r} = 0$. The inset delineates a zoomed view of these behaviors.

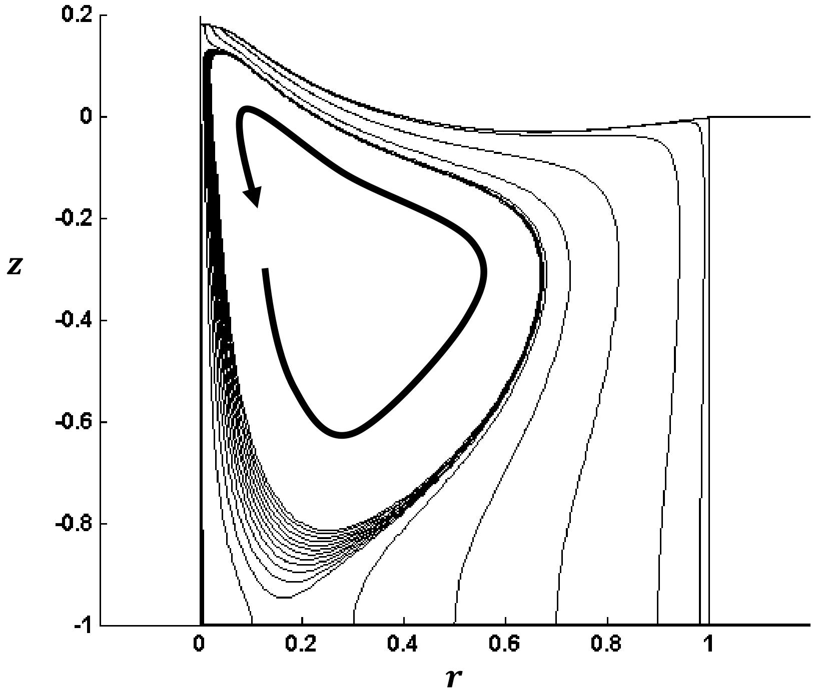

Figure 8-27: Select streamlines for steady flow within the liquid column of the computational domain. Electrical shear at the interface appears to force a pattern of circulation in the body of the liquid, where the inscribed arrow delineates the corresponding direction. Coordinates are given in dimensionless $\hat{r} - \hat{z}$ space.

Figure 8-27 delineates several streamlines of the prevailing flow within the fluid column that we have modeled computationally. Very interestingly, we appear to capture a large region of recirculation in the body of the channel. Streamlines emerge from the bottom of the column (corresponding to the point at which the upstream feed system dumps fluid into our computational arena), veer in a radial direction toward the wall that defines the edge of the anchoring plate, and then begin to hug the interface itself as they approach the evaporation area. Owing to an added "kick" that can be attributed to electrical shear (recall, $\boldsymbol{\tau}_t^e = \sigma E_t$), fluid apparently reaches the latter area at a rate that exceeds emission. As a result, some of the fluid is turned back in a way that creates circulation. Although such a phenomenon is known in the context of cone-jet sprays [97, 98], to the best of our knowledge this is the first time that it has been uncovered for pure ion emission.

Thermal

Figs. 8-28 and 8-29 delineate the surface and bulk temperature distributions, respectively. Where applicable, units are based on the noted reference value T_0 =300 K. From the results we can see that thermal excursions due to Ohmic heating are largely restricted to the vicinity of the activated tip, just as expected. The maximum

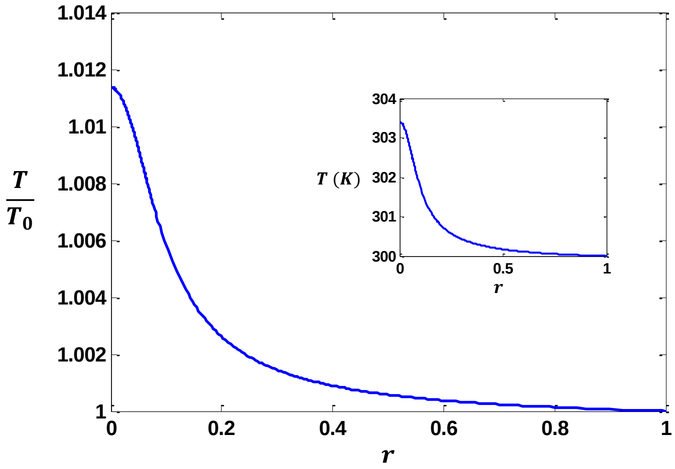

Figure 8-28: Temperature distribution along the interface as a function of $\hat{r}$. The dimensionless $\hat{T}$ suggests that thermal excursions are relatively restricted to the vicinity of the activated tip a reach a maximum $\sim$ 1.5% boost on the axis. This represents $\Delta T \sim 4$ K for a reference value T_0 =300 K.

increment corresponds to roughly $\sim$ 4 K and resides on the central axis. Based on the sensitivity of the liquid conductivity (k' =0.04 S/m-K for the elected fluid), the conclusion must be that the nominal k =1 S/m is locally augmented by a value $\Delta k \sim$ 0.16 S/m. This represents a 16% boost.

8.3 Preliminary subspace mapping of upper equilibria

In the last section we demonstrated the existence of a previously unknown family of equilibrium solutions (i.e., the upper equilibria) but restricted our attention to a fixed meniscus size and feeding impedance in the process. In this section we will endeavor to begin relaxing those condition so that we may explore aspects of the three-dimensional subspace defined by the parameters $\hat{E}_0$, B, and C_R. For convenience we will continue to maintain $\hat{P}_r = 0$ since it is our belief that the feeding pressure is possibly the least important of the parameters under present consideration.

The contents of this section will be organized in the following way. To start, we will map the $\hat{E}_0$-B plane for fixed $C_R = 10^3$ and emphasize the region of low-B as we are primarily interested in situations of large scale disparity. Ideally we would attempt to rigorously map areas approaching $B \sim 1$; however, we anticipate large computational costs that will necessitate judicious selection of solution points. In other words, time will limit us to the investigation of but a few key parameter combinations.

Once we have mapped a sufficient portion of the $\hat{E}_0$-B plane we will elect a single point of interest and begin to explore variations in the impedance C_R. In the limit as $C_R \to \infty$ we will recover a constant volume problem, which, by definition, cannot

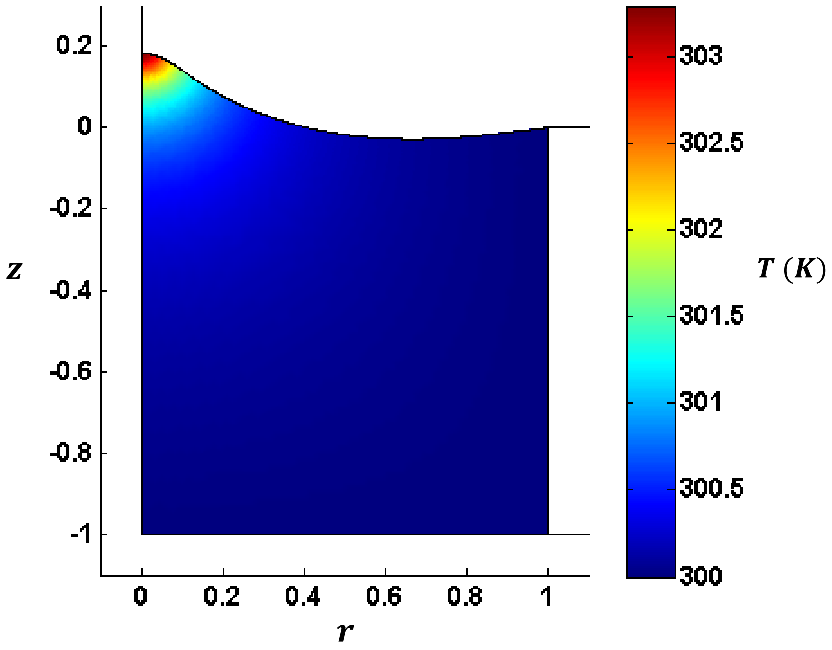

Figure 8-29: Spatial distribution of temperature in the liquid column. Coordinates are shown in dimensionless $\hat{r} - \hat{z}$ space while temperature is given in units of Kelvin (assuming the fluid properties we have already reported). Again, thermal excursions are observed to primarily reside in a region about the activated tip. Little to no penetration into the bulk of the fluid is apparent.

support steady emission. Similarly, the limit $C_R \to 0$ is tantamount to a constant feeding pressure problem, for which it is unlikely that steady upper equilibria exist (we believe that the impedance itself is a critical stabilizer in this regime and so its absence would seem to preclude solutions). With this in mind, it is expected that these explorations will yield solutions over a finite range of impedance. After defining this range for the single $\hat{E}_0$-B point we will select one or two additional C_R values (for example, $C_R = 3 \times 10^3$ like we calculate for the Romero-Sanz [29] experiments) and attempt to map the corresponding $\hat{E}_0$-B planes for comparison.

Finally, it is also our belief that the liquid permittivity ϵ_r plays a non-trivial role in determining the existence of the upper equilibria in spite of the fact that it is often overlooked in the evaporation literature. While many authors discuss the conductivity k (S/m) and an associated threshold for evaporation (i.e., a minimum conductivity for pure ion evaporation), it is really the ratio k/ϵ_r that governs both charge relaxation in the meniscus and electrical stresses at the interface. Even in the case of a fluid that exhibits the relatively high conductivity of $k \sim 1$ S/m, which is common among ILs that are empirically known to support evaporation, it is possible that a concurrently large ϵ_r could offset associated benefits to some degree. Indeed, it is clear that many ILs have much lower permittivities ($\epsilon_r \sim$ 10-20) than highly doped organic solvents ($\epsilon_r \sim 100$) that are much more fickle despite comparable k. It would, therefore, come as no surprise if this disparity were determined to be the genesis of the very different evaporation behaviors that are typically observed. To begin elucidating this possibility, we will again elect an interesting point in $\hat{E}_0$-B-C_R space and slowly vary ϵ_r to explore the range of feasible permittivity. In doing so we will maintain constant k since this is essentially what we do in the laboratory when we switch from an IL to a doped organic solvent of very similar conductivity, all other things being roughly equal.

8.3.1 Mapping of $\hat{E}_0$-B plane ($C_R = 10^3$)

Figure 8-30 depicts a modestly populated map of the $\hat{E}_0$-B plane for $C_R = 10^3$, where the blue circles represent specific points at which we have calculated solutions. These were determined by slowly varying the dimensionless field for the five scale ratios $B^{-1} = [21.3, 53.2, 85.1, 95.7, 106.4]$ (corresponding to $b_0 = 1\mu$m, 2.5μm, 4.0μm, 4.5μm, and 5.0μm for the prototype fluid), and also varying B at fixed $\hat{E}_0 = [0.62, 0.70]$. For the $B^{-1} = 21.3$ line we have used the relaxation parameter $\beta = 0.5$ while all other solutions were found with $\beta = 0.05$. In connection with small step sizes, the latter helped to avoid inadvertent numerical runaway, particularly in the region of very high scale disparity.

Excepting the vertical $\hat{E}_0 = 0.62$ solution group, the ends of all other blue lines correspond to points at which we have observed indefinite interfacial oscillations that precluded convergence to within the stated tolerance. In most instances solutions could be identified after 50-100 computational cycles. Qualitatively we observed that points near the center of each line required the fewest iterations and that additional calculations were needed as we moved away from these points. Variations in the given directions were, therefore, arbitrarily terminated after 500-1000 cycles (i.e., greater than ten times the notional average) were completed without convergence. This phenomenon of increasing iterations as we move toward the ends of the solution groups is qualitatively similar to what was seen in the benchmarking tests and the lower equilibria studies as so-called turning points were approached. With that in mind, it is likely that the number of required iterations could be a measure of the physical stability associated with a particular point in the parameter space, relatively speaking.

The lone exception to this termination practice is the low-B end of the $\hat{E}_0 = 0.62$ line, where continued increase in B^{-1} was not possible as a result of a meshing error in Comsol. In order to sufficiently resolve the physics near the meniscus tip we require elements in its vicinity to be roughly 10^2 times smaller than the local interface scale. Given that B^{-1} is already exceeding 100 in these studies, and that the vacuum region of the solution domain is at least 10 times larger than the contact line to ensure that a uniform field prevails downstream, it is clear that the difference between the smallest scale in the computational problem (the scale for the elements at the meniscus tip) and the largest (the scale for the vacuum region) is in the neighborhood of 5 orders of magnitude. Apparently, this is near the threshold of what the Comsol meshing engine can handle, meaning that further exploration of high B^{-1} will not be possible without special measures.

Accepting that the observed oscillatory behavior near the ends of the solution groups is at least a loose indicator of waning stability for our equilibria, we can begin to consider the implications of the solution plane that we have mapped. From our study of the lower equilibria we know that a turning point exists in the vicinity of $\hat{E}_0 \approx 0.52$, below which we cannot sustain meaningful emission when $B^{-1} \gg 1$. It is true that there is a region supporting emission as $B \to 1$ (marked on Fig. 8-30 as "high-B emission" and essentially the regime that was studied by Higuera [62]); however, this must practically disappear by the time $B^{-1} \sim 10$. As we jump beyond the turning point we begin to find highly-distorted (i.e., no longer "egg-shaped") solutions that are ostensibly stable. From the map we see that this family of upper equilibria extend out to $\hat{E}_0 > 1$ for intermediate B but are only tenable at smaller fields when the scale disparity is increased. Interestingly, all solution groups seem to terminate on the low-end near $\hat{E}_0 \approx 0.59$, which is still greater than the field of the lower turning point. This appears to leave a small gap in the field for which no stable solutions may be determined, and might signal a region of pulsating menisci analogous to those that are known in the cone-jet world. In any event, the fact that $\hat{E}_0 \approx 0.59$ is presumably a hard line, coupled with the decreasing field threshold at high B^{-1}, could suggest that there is a maximum feasible disparity B^{-1} (i.e., a maximum feasibly disparity between the characteristic emission scale r^* and the contact radius b_0). This is highlighted by the black line (which is somewhat notional, given that we have not densely mapped the solution space) in Fig. 8-30 separating the green and red areas.

Figure 8-31 delineates the meniscus shapes corresponding to the vertical solution group at $\hat{E}_0 = 0.70$ and highlights the transition from "egg-shaped" interfaces ($B \sim 1$) to highly-distorted ones that are typical of upper equilibria when $B \ll 1$. The most modestly curved solution corresponds to $B \approx 1/3$ while the black arrow indicates the

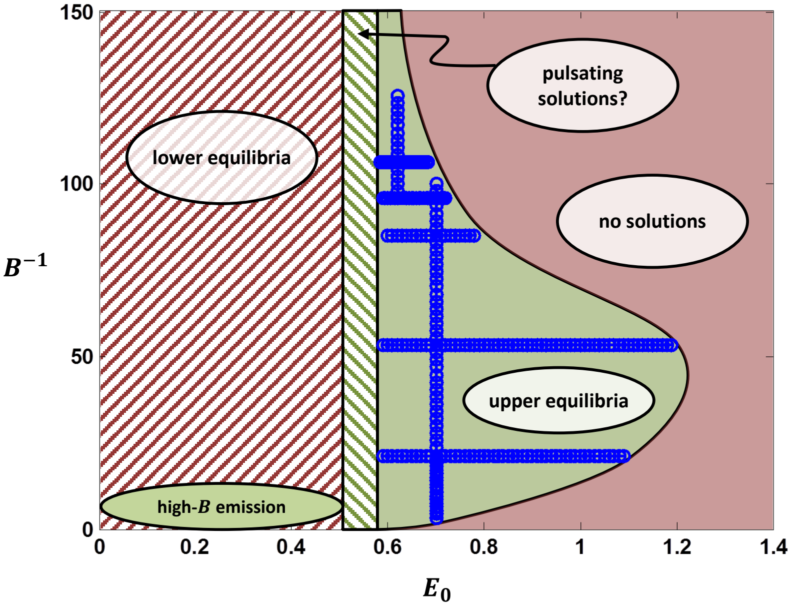

Figure 8-30: Map of the $\hat{E}_0$-B solution plane for $C_R = 10^3$. For $B \ll 1$ there exists a family of lower equilibria below a turning point at $\hat{E}_0 \approx 0.52$ that are "egg-shaped" and do not sustain meaningful emission. In contrast, above $\hat{E}_0 \approx 0.59$ we find a family of upper solutions that are highly-distorted and capable of sustaining strong evaporation. Feasible areas of the upper solution space are shown in green while areas in which we find no solutions are shown in red. The line of demarcation between these spaces is somewhat notional given that we have yet to densely map the plane (owing to computational cost).

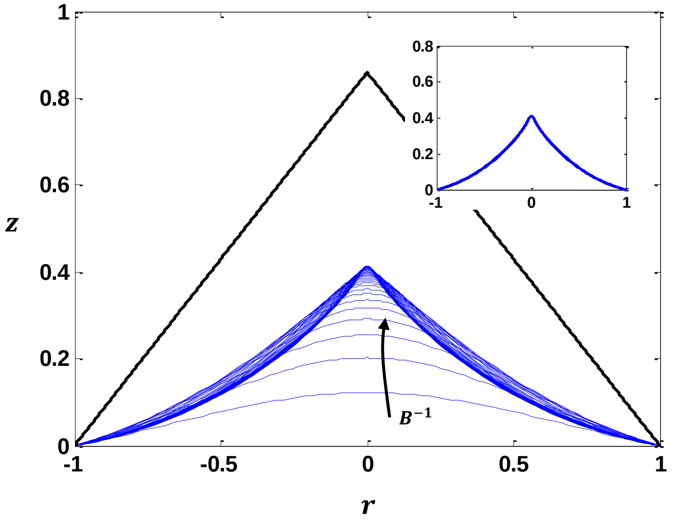

Figure 8-31: Meniscus shapes in dimensionless $\hat{r} - \hat{z}$ space for changing B along the line $\hat{E}_0 = 0.70$ with $C_R = 10^3$. The interface at the bottom with the smallest curvature corresponds to $B \approx 1/3$ while the arrow indicates the direction of increasing B^{-1}. The inset, also in $\hat{r} - \hat{z}$ coordinates, shows all solutions for which $B^{-1} > 50$ and suggests that a common shape is adopted when the scale disparity is sufficiently large. A classical Taylor structure is shown in black for comparison.

direction of increasing scale disparity. As we can see, the menisci for $B \ll 1$ begin to approach a common shape with an apparent point source at the tip. This shape is shown in the inset, where all solutions with $B^{-1} > 50$ are represented.

Figure 8-32 shows the computed length scale at the apices of the menisci along the same $\hat{E}_0 = 0.70$ solution group. By symmetry we know that the local surface tension is related to this scale r_t through

$$\frac{2\gamma}{r_t} = \gamma \nabla \cdot \vec{n} \tag{8.25}$$

and so the ratio of r_t to the characteristic r^* must be

$$\frac{b_0}{r_t} = \frac{1}{2}\hat{\nabla} \cdot \vec{n} = \hat{P}_{st}\left(\hat{r} = 0\right) \Rightarrow \frac{r^*}{r_t} = B \times \hat{P}_{st}\left(\hat{r} = 0\right) \tag{8.26}$$

This relationship is plotted in the figure as a function of B^{-1}. From the results we can see that the tip appears to asymptote to roughly $r_t \approx 2r^*$ for $B \ll 1$. With this in mind it also makes sense to investigate the associated evaporation properties. In Fig. 8-33 we show both the dimensionless current $\hat{I}$ and the approximately hydrostatic pressure in the meniscus ($\hat{P}_B = -\hat{I} \times C_R$) to which it is closely related. Like the tip size, the dimensionless evaporation appears to increase in the region of high-B before essentially leveling off for situations of large scale disparity. When $B \ll 1$ for the given parameter combination ($\hat{E}_0 = 0.70$ and $C_R = 10^3$) we see that changes in

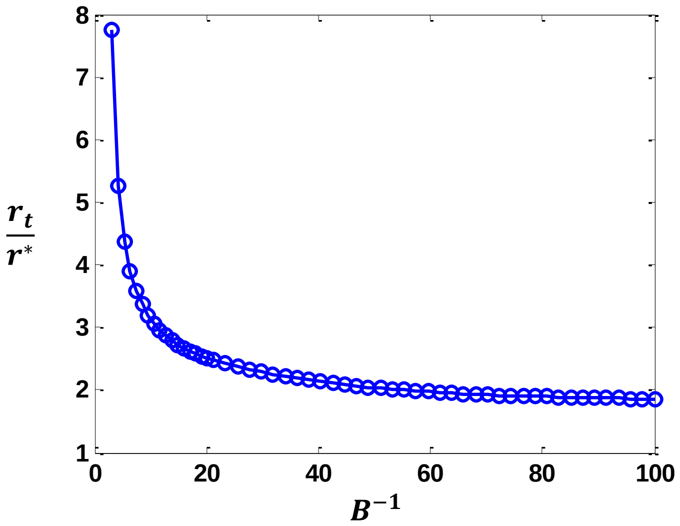

Figure 8-32: Dimensionless tip scale r_t/r^* for various B along the solution group $\hat{E}_0 = 0.70$ with $C_R = 10^3$. For large scale disparity $B \ll 1$ we see that the tip begins to asymptote to a common size in the neighborhood of $2r^*$.

the meniscus size have little effect on the liquid pressure. Apparently, the feeding system creates suction on the interface and maintains a negative pressure that is in the vicinity of half of the nominal capillary pressure $2\gamma/b_0$.

The preceding results (namely the curves from Figs. 8-32 and 8-33) are very interesting because they seem to suggest the possibility of a limiting solution as $B^{-1} \to \infty$ and $\hat{E}_0 \to 0.59$, roughly speaking. It is fair to wonder whether this solution could, after all, have certain characteristics in common with the classical Taylor structure in spite of the obvious macroscopic morphological differences highlighted by Fig. 8-31. For example, could regions outside of the activated apex but still very far from the contact location $\hat{r} = 1$ exhibit surface slopes and field distributions that are similar to those of Taylor? We will conclude this section on the $C_R = 10^3$ solution plane by briefly examining these possibilities.

In Fig. 8-34 we plot the scaled effective half-angle across the meniscus for solutions corresponding to $B^{-1} = [95.7, 106, 117, 125]$ (equivalent to approximately $b_0 = 4.5\ \mu$m, $5.0\ \mu$m, $5.5\ \mu$m, and $5.9\ \mu$m for the prototype fluid) along the vertical line $\hat{E}_0 = 0.62$. The effective half-angle at each point on the surface of the meniscus is defined here as

$$\theta_h = \tan^{-1}\left(-\frac{dr}{dz}\right) \tag{8.27}$$

where dz/dr is the local interface slope. This provides for easy comparison to the classical Taylor angle $\theta_T = 49.29° = 0.86$ radians, which is shown as a black line in the figure. Although the results suggest that the limiting solutions could have slopes in the basic vicinity of the Taylor angle for $\hat{r} \lesssim 0.1$, the comparison is clearly not perfect.

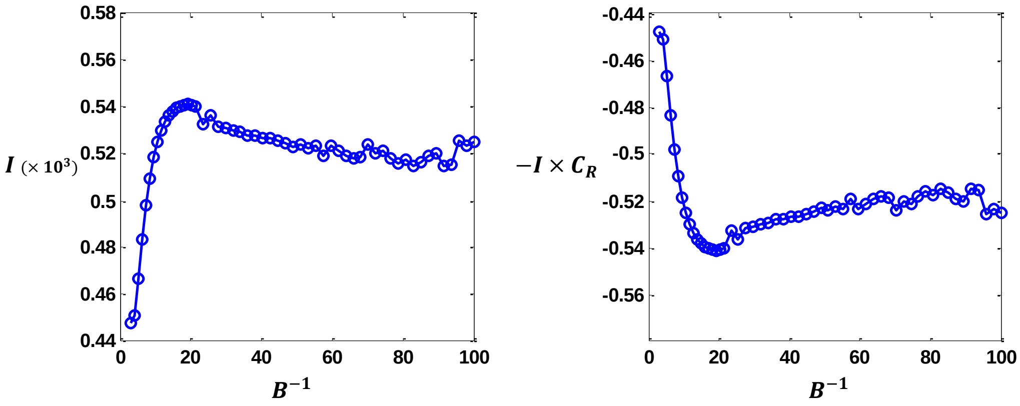

Figure 8-33: Dimensionless current and dimensionless hydrostatic pressure in the meniscus as functions of B along the line $\hat{E}_0 = 0.70$ with $C_R = 10^3$. **Left:** The dimensionless current $\hat{I}$ increases in the region of high-B and essentially levels off when $B \ll 1$. **Right:** The dimensionless pressure in the meniscus, $-\hat{I} \times C_R$, is directly related to the current and follows the same behavior. The feeding system apparently creates suction on the interface with a pressure modulus that is roughly half of the nominal capillary pressure $2\gamma/b_0$.

In Fig. 8-35 we now plot the distribution of dimensionless vacuum field $\hat{E}_n^v$ at the interface for the same menisci. For the classical Taylor structure we know that the vacuum field varies as [5]

$$E_T = \sqrt{\frac{2\gamma\cos\theta_T}{\epsilon_0 r}} \tag{8.28}$$

where r is the local cylindrical radius. After non-dimensionalizing through the use of our field scale $E_c = \sqrt{4\gamma/\epsilon_0 b_0}$ we find

$$\hat{E}_T = \sqrt{\frac{\cos\theta_T}{2\hat{r}}} \tag{8.29}$$

This distribution is shown as a solid black line in the figure while the simulated distributions are given in blue. The arrow indicates the direction of increasing B^{-1} for the latter. Unlike the comparison of the slopes, it is rather remarkable to note here the similarity between the basic Taylor theory and what we have identified numerically. The correspondence appears to extend across all parts of the meniscus (i.e., from $\hat{r}$ slightly greater than 0 all the way to $\hat{r} = 1$) and the arrow seems to suggest that for $B^{-1} \to \infty$ we could possibly recover an extremely large apex field similar to that of the perfectly sharp Taylor cone.

8.3.2 Variations in C_R ($B = 9.4 \times 10^{-3}$, $\hat{E}_0 = 0.62$)

In an effort to access different impedance values for mapping we have selected a point in the parameter space ($\hat{E}_0 = 0.62$ and $B = 9.4 \times 10^{-3}$, corresponding to $b_0 = 5$ μm

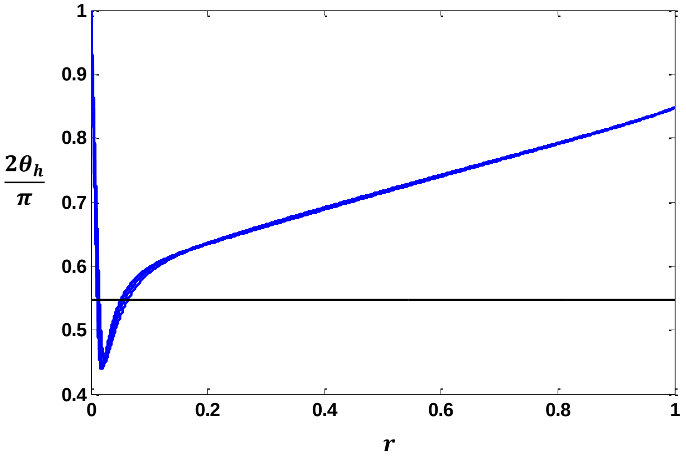

Figure 8-34: Effective internal half-angles for several simulated menisci along the line $\hat{E}_0 = 0.62$ with $C_R = 10^3$. The half-angle is defined as $\theta_h = \tan^{-1}(-dr/dz)$ and shown as a function of the dimensionless cylindrical radius $\hat{r}$ for menisci corresponding to $B^{-1} = 95.7$, 106, 117, and 125 (blue curves). The angle of the classical Taylor structure, $\theta_T = 0.86$ radians, is represented by the black line for comparison. The curves suggest that while a small region near the tip of high B^{-1} menisci could be in the neighborhood of the Taylor angle, the morphologies will likely always be somewhat disparate.

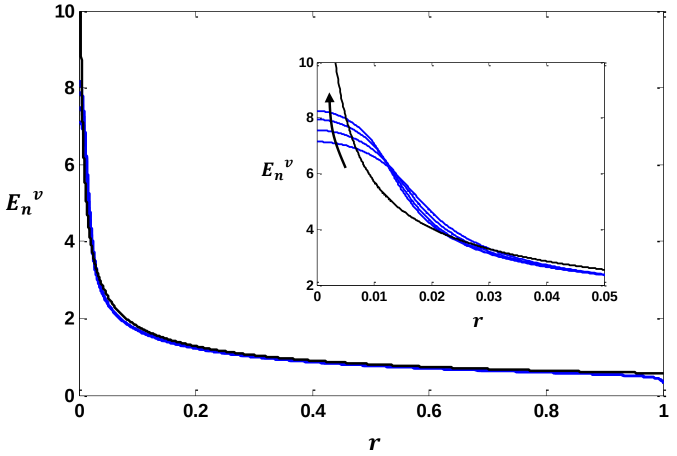

Figure 8-35: Distribution of dimensionless vacuum field $\hat{E}_n^v$ for several simulated menisci along the line $\hat{E}_0 = 0.62$ with $C_R = 10^3$. The vacuum field is shown as a function of the dimensionless cylindrical radius, $\hat{r}$. The blue curves correspond to the cases of $B^{-1} = 95.7$, 106, 117, and 125, where the arrow in the zoomed inset indicates the direction of increasing value. The black line represents the classical Taylor distribution (see, for example, Martinez-Sanchez [5]), which is provided for comparison. Unlike Fig. 8-34 for the slopes, these results exhibit remarkable correspondence between the conventional theory and the numerical calculations.

with the prototype fluid) and varied C_R over several orders of magnitude, starting at the known solution for $C_R = 1000$. In all cases we have done this while using $\beta = 0.05$ and $N = 10^4$ observation points equally spaced in r across the meniscus.

With the model we are able to slowly reduce the feeding impedance to a value of $C_R = 670$ on the low end before numerical oscillations begin to preclude further excursions. Insofar as we can attribute these oscillations to an actual physical instability (like we have already discussed), the fact that $C_R \to 0$ is not feasible would seem to suggest the upstream hydraulics do indeed play a very meaningful role in creating the upper equilibria. Similarly, it would seem to rule out the possibility of so-called frictionless feeding flows (at least for fluids that are not substantially affected by space charge effects, like the ILs we are capturing, since our model does not involve Poisson) that some authors talk about in connection with ion evaporation. At the opposite end of the spectrum, our simulations very easily reached $C_R = 3.31 \times 10^6$ before arbitrary termination. It is worth mentioning that we believe the impedance could have continued to stably increase almost indefinitely (excluding, of course, $C_R = \infty$ for previously stated reasons); however, by $C_R \sim 10^5$ or 10^6 the attendant current is already exceedingly small and no longer of great interest.

Figure 8-36 delineates shapes corresponding to the impedance values $C_R = 10^3$, 10^4, 10^5, and 10^6 and shows that macroscopic aspects of the meniscus do not change substantially in spite of the wide range of C_R. From the inset we can see that subtle morphological changes do occur in the vicinity of the tip, with larger impedance values corresponding to duller tips and lower impedance values corresponding to sharper tips. This relationship is further elucidated in Fig. 8-37, where we once again plot the dimensionless apex radius r_t/r^*. The results clearly indicate that an increasing impedance forces a related increase in r_t.

The fact that the tip sharpness varies with C_R is one indication that the evaporated current could be changing dramatically as we traverse the wide spectrum of impedance values. Figure 8-38 (left) shows the dimensionless $\hat{I}$ as a function of C_R and suggests that this is indeed the case. As we can see, a remarkably linear current-impedance relationship prevails with a slope that reduces the evaporation by nearly four orders of magnitude over the investigated range. Figure 8-38 (right) delineates the related quasi-hydrostatic pressure $\hat{I} \times C_R$ and shows that this is because the relationship is very nearly 1:1; i.e., $\hat{I} \times C_R \sim C_0$, where C_0 is some constant that is known to vary almost exclusively with $\hat{E}_0$ (recall our mapping of the $\hat{E}_0$-B plane for $C_R = 10^3$). There is, however, at least a small decrease in the hydrostatic pressure for increasing impedance, which must be the explanation for the noted changes in r_t.

8.3.3 Mapping of $\hat{E}_0$-B plane ($C_R = 10^4$)

In Figure 8-39 we depict our efforts to map the $\hat{E}_0$-B plane for the augmented impedance $C_R = 10^4$. The blue circles/lines again represent specific points within the parameter space for which we have obtained converged solutions. The reader will notice that, as before, we have left the very high end of B^{-1} relatively sparse due to meshing limitations in Comsol. The two points at which this limited further excursions are shown as red dots.

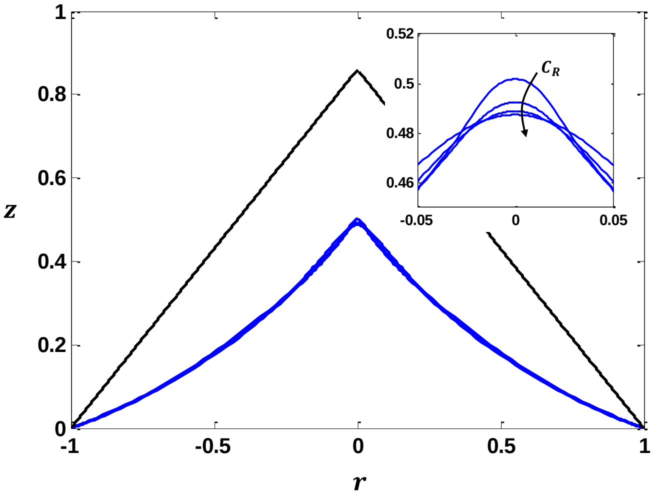

Figure 8-36: Meniscus shapes for various C_R in dimensionless $\hat{r}$-$\hat{z}$ space with $\hat{E}_0 = 0.62$ and $B = 9.4 \times 10^{-3}$. The four impedance values $C_R = [10^3, 10^4, 10^5, 10^6]$ are represented along with a classical Taylor structure (black) for comparison. While the macroscopic view does not reveal substantial changes in the menisci despite the large range of C_R, the inset (also in dimensionless $\hat{r}$-$\hat{z}$ space) shows that subtle morphological changes have occurred at the tip. The arrows indicates the direction of increasing impedance and suggests that higher C_R apparently lead to dulling.

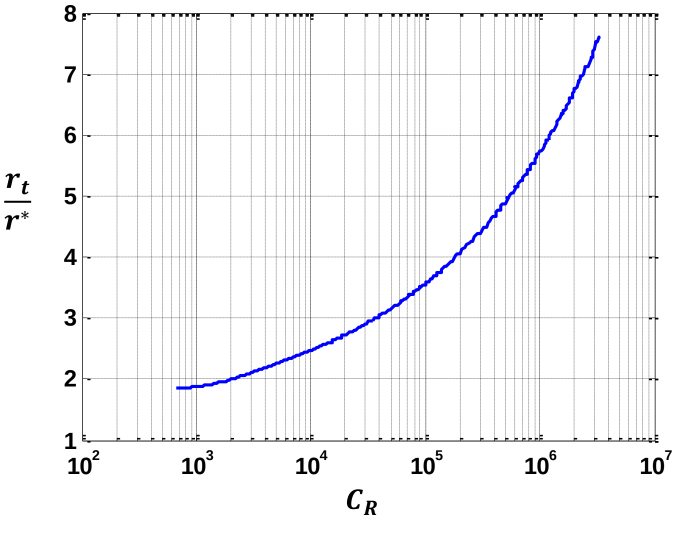

Figure 8-37: Dimensionless tip radii for various C_R with $\hat{E}_0 = 0.62$ and $B = 9.4 \times 10^{-3}$. The ratio of tip radius r_t to the characteristic r^* is plotted as a function of the impedance. The results confirm the notion that higher C_R reduce the sharpness of the meniscus apex.

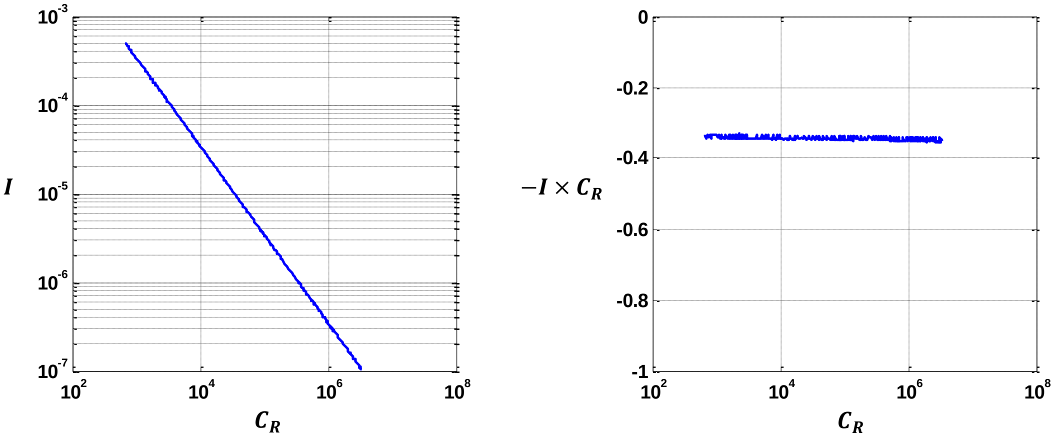

Figure 8-38: Dimensionless current and fluid pressure for various C_R with $\hat{E}_0 = 0.62$ and $B = 9.4 \times 10^{-3}$. **Left:** The dimensionless current $\hat{I}$ is shown as a function of C_R. **Right:** The corresponding quasi-hydrostatic pressure in the fluid, $\hat{I} \times C_R$, is also shown. The results suggest that fluid pressure is nearly constant but still slightly decreasing with C_R in a way that could explain the growing r_t. In turn, the increase in r_t clearly leads to dramatic reductions for the evaporated current.

Comparison of the map in Fig. 8-39 with its counterpart for $C_R = 10^3$ reveals that the boundary corresponding to the high-field side of the upper solution regime has been shifted to the right. In other words, for a given meniscus size B the increased impedance has apparently enabled access to a wider range of fields. It is likely, therefore, that the “limiting” solution associated with the $C_R = 10^4$ plane is situated at higher B^{-1} than the one that was suggested for the lower impedance $C_R = 10^3$.

8.3.4 Variations in ϵ_r ($C_R = 10^3$)

As a final numerical experiment we investigate here the tenability of several of our solutions with respect to the liquid permittivity ϵ_r. While it is known empirically that the IL EMI-BF4 ($k \sim 1$ S/m) is relatively amenable to ion evaporation under certain conditions, reaching the same emission regime with other fluids of similar conductivity (either doped solvents or other ionic liquids) can be decidedly more onerous. Although several factors could be to blame for this, in this section we explore the possibility of a connection to the permittivity.

All other things being essentially equal, when we move from one fluid in the laboratory to another of similar conductivity we are primarily modifying the prevailing ϵ_r (and, correspondingly, the charge relaxation time $\epsilon_r\epsilon_0/k$). In what follows we attempt to capture any attendant emission effects by selecting several points from the $\hat{E}_0$-B solution plane ($C_R = 10^3$) and slowly increasing the nominal $\epsilon_r = 10$ while observing changes in the menisci.

Figure 8-40 shows the three locations within the $\hat{E}_0$-B that we have selected for these investigations. These include

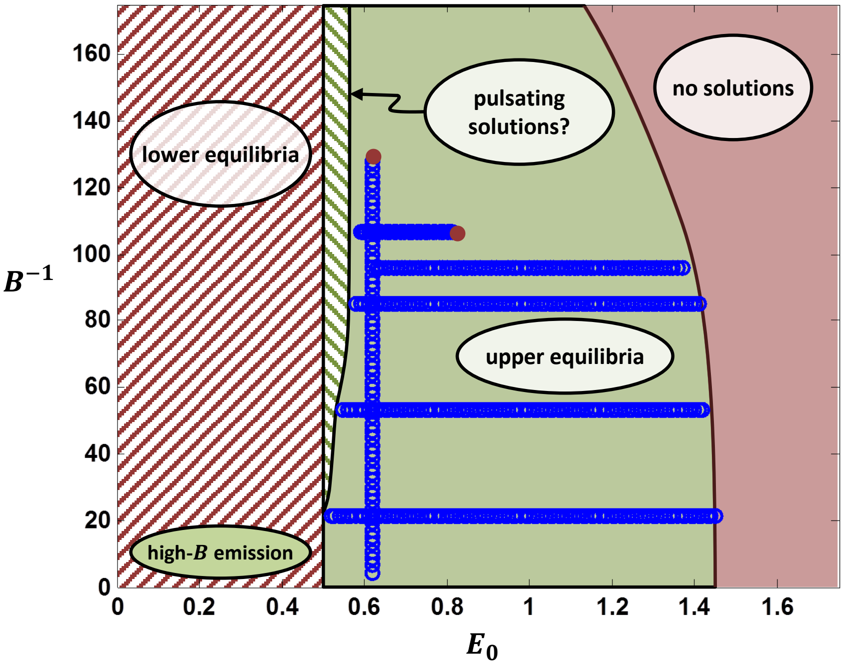

Figure 8-39: Map of the $\hat{E}_0$-B solution plane for $C_R = 10^4$. For $B \ll 1$ there exists a family of lower equilibria below a turning point at $\hat{E}_0 \approx 0.52$ that are "egg-shaped" and do not sustain meaningful emission. In contrast, above $\hat{E}_0 \approx 0.59$ we find a family of upper solutions that are highly-distorted and capable of sustaining strong evaporation. Feasible areas of the upper solution space are shown in green while areas in which we find no solutions are shown in red. The line of demarcation between these spaces is somewhat notional given that we have yet to densely map the plane (owing to computational cost); however, with respect to the map for $C_R = 10^3$ it has clearly been shifted to higher values of the field. This is apparently a symptom of the added stability conferred by the increased impedance.

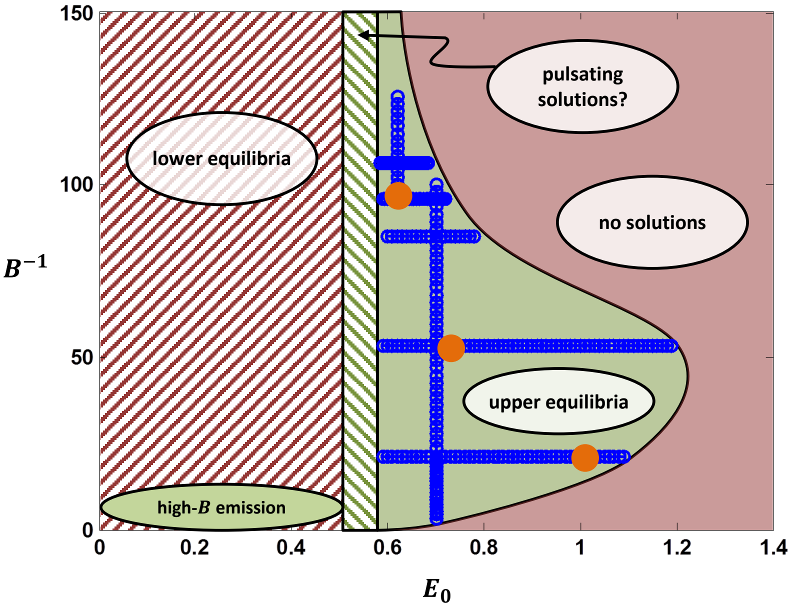

Figure 8-40: Points in the $\hat{E}_0$-B plane of $C_R = 10^3$ selected for permittivity studies. The three points examined are represented by the orange dots.

- **Point #1:** $\hat{E}_0 = 0.62$, $B^{-1} = 85.1$, $C_R = 10^3$
- **Point #2:** $\hat{E}_0 = 0.75$, $B^{-1} = 53.2$, $C_R = 10^3$
- **Point #3:** $\hat{E}_0 = 1.00$, $B^{-1} = 21.3$, $C_R = 10^3$

The maximum permittivities for which we were able to identify solutions corresponded to $\epsilon_r = 19$, $\epsilon_r = 25$, and $\epsilon_r = 36$ for Point #1, Point #2, and Point #3, respectively. In all cases the evaporated current was observed to remain constant in spite of the decreasing charge relaxation time, which ensured an invariant fluid pressure within the meniscus. This was apparently achieved by subtle elongations and sharpening of the menisci as the permittivity was slowly increased. Figure 8-41, for example, shows several shapes that were calculated for Point #1 in an effort to highlight this behavior.

Although the results presented here are not yet comprehensive, they do appear to suggest the possibly of a limiting permittivity (insofar as the other fluid parameters are fixed, at least) that decreases in the same direction as B; i.e., a limiting permittivity that decreases in some proportion to r^*/b_0. Given that EMI-BF4 is relatively apolar in comparison to many alternative fluids with $k \sim 1$ S/m, this is perhaps an additional clue as to its greater proclivity for evaporation. Further studies, however, will be needed to confirm this.

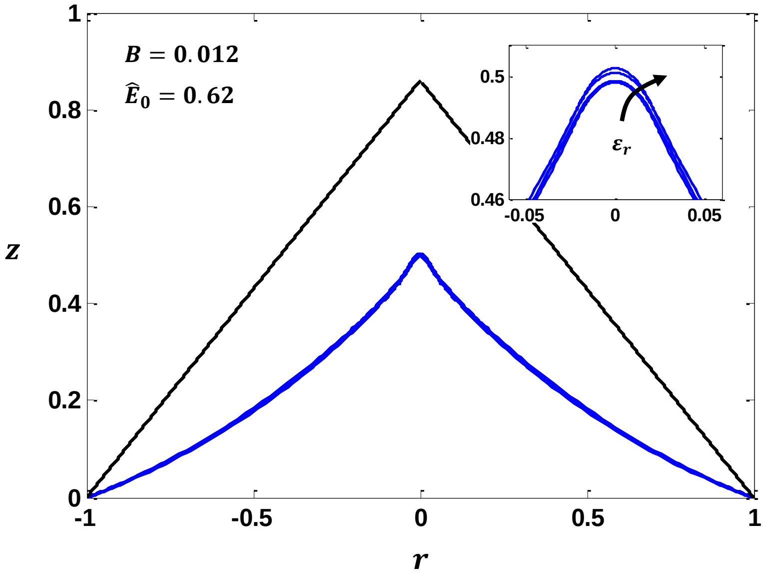

Figure 8-41: Meniscus shapes for several ϵ_r with $\hat{E}_0 = 0.62$, $B^{-1} = 85.1$, and $C_R = 10^3$ in dimensionless $\hat{r}$-$\hat{z}$ space. The blues curves correspond to ϵ_r = 10, 12, 14, 16, and 19 while a classical Taylor structure is given in black for comparison. Although the macroscopic structure of the meniscus apparently does not change as a function of the permittivity, the inset provides additional detail for the tips to highlight the localized sharpening and elongation.

8.4 Comparison of qualitative trends

The following is a list of qualitative similarities between the reported numerical results and known empirical phenomena. We believe that these represent additional measures of substantiation for the model.

- **Non-evaporative lower branch.** We have identified a family of solutions for $\hat{E}_0 \lesssim 0.52$ that are "egg-shaped" and do not appear to support meaningful levels of evaporation. This is congruent with empirical observations suggesting that interfaces with roughly uniform curvature are characteristic of low fields and gradually elongated with increasing $\hat{E}_0$ until a destabilization point, i.e., a turning point, is reached (see, for example, the account of Krpoun [4]).

- **Intermediate / pulsating regime.** We have identified a narrow range of intermediate fields within which we have been unable to compute stable solutions. This lies between the turning point of the lower solution family ($\hat{E}_0 \approx 0.52$ in all cases with $\hat{P}_r = 0$) and the smallest field belonging to its upper counterpart (roughly $\hat{E}_0 \approx 0.59$ in all cases with $\hat{P}_r = 0$), and suggests the existence of a dynamic regime that is analogous to the "pulsating" modes that are known throughout the cone-jet literature [95, 96].

- **Steady evaporation for large menisci.** The family of upper equilibria we have identified seem to admit the possibility of stead evaporation from menisci with large contact radii, i.e., situations involving $B \ll 1$. This is congruent with the findings of a large collection of empirical studies [29, 31, 36].

- ***I*-*V* linearity.** For fixed B we have found that the evaporated current is essentially linearly proportional to the downstream field $\hat{E}_0$. The same scaling relationship is reported by a large of number of empirical studies (in addition to the theoretical study of Higuera [62]) and believed to be a symptom of conduction-limited charge transport within ionic liquids [31, 25, 54].

- **I-B^{-1} proportionality.** In general our model suggests that the evaporated current is proportional to the size of the meniscus. For example, we have shown that as B^{-1} is increased for fixed $\hat{E}_0$ and C_R the dimensionless current $\hat{I}$ remains essentially constant. Because $I = \hat{I} \times kE_c b_0^2$, this requires that $I \propto b_0^{3/2}$. This is congruent with many empirical findings suggesting that large tubes or tips are capable of supporting higher throughputs (see, for example, the Castro [36] study on the relationship between tip curvature and current).

- **Relationship between stability and contact line.** Our results suggest that the range of stable $\hat{E}_0$ for the upper solution family is a decreasing function of the meniscus size. Although empirical field ranges are not often reported, this finding would seem to be congruent with aspects of the Castro [36] and Lozano [31] studies. Notwithstanding slight differences in the fluids that were used (Castro [36] used EMI-C(CN)$_3$ for which $k \approx 2.2$ S/m and $\gamma \approx 47.9$ dyn/cm, while Lozano [31] used EMI-BF4 for which $k \approx 1.36$ S/m and $\gamma \approx 43.2$ dyn/cm near room temperature), Castro [36] reports a stable range of $\sim$ 2225V - 2425V for a 50 μm emitter needle and Lozano [31] reports a range of at least $\sim$ 1600V - 2000V for a 20 μm needle. These suggest that the fields for the two tips were able to grow by roughly 10% and 25%, respectively, which is qualitatively similar to what our model would have predicted. Moreover, the Castro [36] report goes a step further to show that there apparently exists a maximum feasible meniscus size beyond which pure evaporation is no longer tenable. This is similar to what we have gleaned from the $\hat{E}_0$-B maps presented herein.

- **I-C_R inverse proportionality.** Through our C_R excursions we have shown that the evaporated current is apparently inversely proportional to the prevailing hydraulic impedance of the feeding system. This led to the finding that $\hat{I} \times C_R \approx C_0$, where C_0 is some constant. Lozano [31] has reported on evaporation from heated ionic liquids and determined that the effects of reduced viscosity are responsible for elevated currents in these fluids (this argument ignores possible conduction effects but remains essentially valid). Specifically, the author showed that reducing the viscosity by a factor of two led to a current that was increased in the same proportion. In terms of our notation, $C_R \propto \mu$ (since $R_h \propto \mu$) and so $\mu \to \mu/2 \Rightarrow I \to 2 \times I$, which is consistent with this empirical result.

8.5 Summary

We have investigated the properties of free-volume menisci by first considering their behavior at relatively low electric fields $\hat{E}_0$. Similar to what we found for their fixed-volume counterparts, the results suggest that a family of "egg-shaped" interfaces (where we might loosely define egg-shaped interfaces as those for which the Laplace pressure, $\gamma \nabla \cdot \vec{n}$, is not too disparate between the apex and the contact line) prevail over a finite domain. Beginning with the quiescent configuration $\hat{E}_0 = 0$, these menisci slowly elongate with increasing field until they abruptly expand in close proximity to a critical field, or "turning point". For a negligible reservoir pressure, $\hat{P}_r = 0$, this point roughly coincides with $\hat{E}_0 \approx 0.52$.

Consideration for the corresponding vacuum fields has shown that this family of "lower equilibria" are unable to sustain meaningful emission when large scale disparities ($B \ll 1$), similar to those that are often encountered in the laboratory, prevail. In view of the multitude of empirical studies suggesting that large menisci are indeed amenable to strong ion emission, this finding is somewhat troubling. The fact that the turning point typically signals the largest field for which steady equilibria will exist (like we saw with the fixed-volume problems, especially when $k \to \infty$ or the interface was in some way close to electrical relaxation) does not help.

In order to reconcile our findings with the body of empirical evidence we have looked to the widely-held belief that large menisci undergo a "snap over" transition from relatively smooth, egg-shaped morphologies to comparatively sharp ones. So long as this belief is physically founded, it has two implications for our efforts: (1) the notion of “snap over” seems to convey the kind of dynamic or unsteady transition that we could not hope to capture with the present model and offers an explanation for why we have not been able to reach emission by slowly increasing the field from zero; and (2) it could be that the “snap over” field is in the neighborhood of the turning point, in which case sharp but stable menisci might still reside at greater fields. Needless to say, the latter would be quite remarkable. While it is not strictly congruent with our knowledge of turning points for fixed-volume menisci, the free-volume counterpart represents a fundamentally unique problem in the sense that it incorporates a feeding system and the various additional physics with which it is associated. In view of that, it stands to reason that a new and previously uncharted family of stable equilibrium solutions could perhaps be enabled by the feeding mechanics and exist beyond the turning point of the lower branch.

With this in mind, we have investigated the possibility of a new family of “upper equilibria” by first making an educated guess as to a corresponding point in the parameter space (e.g. $\hat{E}_0 = 0.70$, $B \approx 1/20$, and $C_R = 10^3$ as inferred from Romero-Sanz [29]) and jumping directly to it without attempting to smoothly navigate the intervening territory between it and the turning point. The impetus for this is circumvention of any dynamic transition region that would presumably create issues for our model. With the help of a starting morphology that is sufficiently sharp, i.e., relatively conic, our iterative numerical routine has indeed identified an equilibrium geometry that is ostensibly stable but still very different from the egg-shapes we have seen. Rather than a relatively uniform curvature across the interface, this solution exhibits a high curvature at the tip, which supports strong evaporation on the order of what we might see in practice ($I \sim 100$ nA), that gradually decreases before switching signs near the contact line in order to compensate a negative hydraulic pressure (i.e., suction).

Beyond this prototype solution (corresponding to $\hat{E}_0 = 0.70$, $B \approx 1/20$, $C_R = 10^3$, and $\hat{P}_r = 0$ in our parameter space) we have slowly varied the field, contact line, and feeding impedance in an effort to populate select maps of the upper equilibria. Doing so has allowed us to glean several important characteristics of ion evaporation. These include:

- The upper solutions appear to be specifically enabled by the presence of a feeding impedance. We might rationalize the reason for this by considering the sharp tip of a steady activated meniscus. In the event of a small, sharpening perturbation the electrical traction and surface tension will both begin to grow. Owing to the increased field, it must also be true that the evaporated current will elevate and concurrently reduce the local fluid pressure through flow-impedance interactions. Even in situations where the growth in electrical traction outpaces the surface tension (which, of course, was the driving factor for instability in the fixed-volume problems, including those from the chapter on spheroids) it is possible that the reduced pressure could still suppress the perturbation. With this in mind, it makes sense that (1) we have been unable to identify low-B menisci when $C_R \to 0$, and (2) increasing C_R seems to improve stability characteristics, albeit at the expense of the current.

- In our model we have separated the upstream flow from that which occurs local to the liquid-vacuum interface. Our numerical calculations seem to validate this practice in the sense that they indicate that effects due to the latter are relatively insignificant. While the stress accumulated upstream ($\sim \hat{I} \times C_R$) is singularly important for the reasons that we have just argued, the additional stress accumulated within the meniscus itself is incremental at best and likely does very little to modify the overall mechanics of the problem. This finding is consistent with early hypotheses we derived based on the notion of a small capillary number, $Ca = \mu u^*/\gamma$.

- While the lower turning point occurs in the vicinity of $\hat{E}_0 \approx 0.52$, the low-field side of the upper solution family appears to universally terminate near $\hat{E}_0 \approx 0.59$. This would seem to suggest the existence of an intermediate regime of dynamic menisci that could be related to the pulsating modes that are known throughout the cone-jet literature.

- Our maps of the $\hat{E}_0$-B parameter plane indicate that the range of stable fields for the upper family decreases in some proportion to the meniscus size. While numerical issues have prevented us from rigorously exploring the region of low B, it is believed that this behavior could lead to a maximum feasible contact radius.

The collection of observations and findings arrived at throughout this thesis (particularly those reported in this chapter) could be very useful to future efforts aimed at designing pure ion sources. Specifically, we can now say that sizing of the working meniscus and its feeding system are critically important. While exact optimal values are difficult to discern for various reasons, large menisci are clearly ill-suited to evaporation and so $B^{-1} \lesssim$ 100-200 should likely be observed (at least for ILs similar to the prototype we have worked with), especially in situations where pure emission takes precedence over the current. C_R, on the other hand, is available for possibly modulating the corresponding current but should still be selected judiciously since a small impedance could similarly disrupt the emission mode. So-called frictionless flows, for which the viscous drop in the feeding line is very small in comparison to the capillary pressure, should therefore be actively avoided in spite of the common belief that they confer strong evaporative currents.

Chapter 9

Conclusions

In this chapter we review salient elements of the thesis and propose topics for future investigation.

9.1 Summary and discussion

Charge evaporation from electrified fluids is a very intriguing but still decidedly misunderstood phenomenon. While devices predicated upon it are believed to offer great promise (for example, FIB systems and microrockets), maturation and translational impact have been tempered by the attendant lack of *a priori* insight. This is acutely true in the context of so-called ionic liquids but also in relationship to liquid metals to some extent. In this thesis we have examined important aspects of the very multiphysical evaporation process and constructed a rigorous numerical model based on the meniscus of a prototypical ionic fluid. Our investigations of its behavior over a range of field and architectural conditions has uncovered (1)the existence of a high-field solution branch for the large meniscus regime; (2) the likelihood of a limiting meniscus size; and (3) critical stabilization properties enabled by the feeding system. Among other findings, we view these as a significant step toward a firm fundamental understanding of the electrically-assisted evaporation problem.

In order to inform the composition of the numerical model we have identified the various physics that could contribute to the evaporation process and analyzed their relative influences to order-of-magnitude accuracy. Notwithstanding potential atomistic effects, we believe that the corresponding list is essentially exhaustive for the continuum approach we have elected to take. Unlike many other studies (e.g. Taylor [3], Wohlhuter [71], Higuera [62]), the physics considered herein are inclusive of flow effects inside the meniscus and local heating due to Ohmic dissipation. In the case of the former, our basic analysis suggests that while upstream effects could play a significant role, owing to the possibility of an arbitrary impedance there, the flow in the immediate vicinity of the meniscus is likely rather meaningless as a result of the very low Capillary number, $Ca = \mu u^*/\gamma$, that typifies fluids of high specific charge. On the other hand, the conductivities of many ILs and some liquid metals exhibit strong thermal sensitivities that have given us to conclude that evaporation-induced heating could be important. We have also considered space charge influences due to the presence of evaporated species propagating outside of the liquid-dielectric interface. These are commonly dismissed out-of-hand for ILs but known to provide critical ballasting in the case of liquid metals (where high conductivities lead to extreme current densities). Although we also neglect them in the numerical formulation later on, in the interest of simplicity, the magnitude estimate hints that they could indeed affect the problem in a material way, especially in cases of high current.

In view of the fact that it is analytically tractable, after the order-of-magnitude estimates we treat the classical problem of a fixed-volume droplet stressed by a unidirectional electric field in free-space. Our analysis is very similar to that of Taylor [3] but extends it to include dielectric fluids of finite permittivity and the possibility of charge emission (albeit in a non-reactive, post-processing way that ignores, for example, the possibility of charge accumulation in the emitting droplet). We start by calculating equilibrium configurations using the corresponding two-point stress balance and find the well-known result that droplets stretching in the direction of the field are sometimes characterized by multi-valued elongation curves. For the case of an infinitely polar fluid (which is mathematically identical to a perfectly conducting fluid here), the elongation grows with increasing field until it reaches a value of roughly $Z \sim 2$ for dimensionless field $\hat{E}_0 \sim 0.2$. This coincides with a so-called "turning point". While no equilibrium solutions are found for fields greater than the one at the turning point, a second branch of highly elongated solutions co-exists below it. Stability analyses, however, suggest that it is not physical. Interestingly, as the permittivity of a dielectric fluid is decreased from $\epsilon_r \rightarrow \infty$ we see the turning point migrating toward higher fields and a gradual change in the multi-valued elongation behavior. Indeed, for permittivities below some special value $\epsilon_r \sim 20$ it disappears altogether and gives way to monotonic elongation curves. This would appear to underscore the important role that the liquid dipoles play in managing the stress at the interface and conferring stability. The possibility of emission is investigated by considering the electric fields acting on the perfectly conducting droplet. Given the noted stability properties, we examine these along the lower branch between $\hat{E}_0 = 0$ and the turning point and find that the tip is never comparable to the characteristic evaporation field E^* unless the quiescent waist of the droplet is itself comparable to the corresponding scale r^*, in spite of the elongation. We had hoped that spherical droplets with $r_0 \gg r^*$ could be stably stretched to the point of evaporation; however, it is clear now that such a scale disparity undoubtedly precludes that.

It is difficult to reconcile the results of the fixed-volume droplet with empirical observations of evaporation, where it is believed that menisci much larger than r^* can support strong emission. With that in mind, we have developed a rigorous model in which a meniscus of arbitrary intrinsic properties (e.g. surface tension γ and solvation energy ΔG) is anchored at the opening of a small hole in a plate. In general the plate could be composed of either a dielectric or a perfectly conducting material. The hole allows the meniscus to communicate with an upstream reservoir where a given back-pressure is enforced. The impedance of the intervening hydraulic line is arbitrary. A counter-electrode is also arranged far downstream of the meniscus and biased with respect the bottom of the anchoring plate such that a nearly uniform electric field prevails away from the liquid.

We have calculated steady axisymmetric solutions to the set of governing equations and identified two unique and ostensibly stable branches. The first of these is the "lower equilibrium branch" that exists for relatively small values of the dimensionless field $\hat{E}_0$. Investigation of the attendant elongation behavior for various reservoir pressure reveal that this family of solutions is reminiscent of known results for fixed-volume droplets in that they are somewhat "egg-shaped" and terminate at familiar turning points. Owing to their smooth morphologies, these solutions are unable to engender fields that are sufficiently strong for evaporation when there is a reasonable disparity in the important scales, i.e., when $B \ll 1$. As a result, the menisci for all $\{B : B \ll 1\}$ should collapse to the dimensionless curves reported herein.

Noting that the highest fields along the lower branch were observed for negligible back pressure (i.e., a reservoir pressure identical to the vacuum pressure), we have identified this case as a good candidate for further examination. The corresponding turning point is in the vicinity of $\hat{E}_0 \approx 0.52$. After carefully elevating the field to $\hat{E}_0 = 0.70$ and judiciously estimating a potential interface shape for $B \approx 1/20$ and $C_R = 10^3$ we have found a new solution which does support steady evaporation but no longer resembles the egg shapes from the lower branch; rather it is characterized by a sharp tip that gives way to a convex body. By slowly varying several parameters (namely $\hat{E}_0$ and B, but also C_R and ϵ_r to lesser extents) we have used this prototypical solution to uncover a new and extremely rich family of solutions belonging to an "upper equilibrium branch" that has never been seen before.

The turning point behavior along the lower branch suggests that no solutions should exist beyond the associated field so long as only electrical traction, surface tension, and the hydrostatic reservoir pressure prevail (since no emission occurs along the lower branch, these are the only non-trivial physics governing the problem). In view of this, we believe that the emission dynamics themselves are singularly responsible for enabling the new branch that is reported for higher stresses. Moreover, we speculate very specifically that the interaction of the evaporation-induced flow with the nonzero upstream impedance creates a suction effect which confers the necessary stability upon the interface. To conceptualize the manner in which this is possible we might consider the sharp apex of the meniscus where the electrical traction, surface tension, and pressure drop through the feeding line are all balanced when the interface is steady. If a perturbation arises such that the apex sharpens, the field will grow accordingly and begin to draw additional charge. Even in instances where the excursion in the corresponding electrical pressure has outpaced the augmented surface tension, the extra current could give rise to a perturbation in feeding pressure that restores the equilibrium configuration. Similarly, a dulling perturbation could reduce the feeding pressure and allow the newly unbalanced electrical traction to re-sharpen it.

As a result of the findings from the upper branch of solutions we can now postulate a notional collection of conditions that should typically be met if pure evaporation is to prevail. In instances where there is overlap between these basic conditions and the heuristics that were highlighted in the literature review we make use of tangible modeling efforts to offer new measures of quantitative guidance. Trade-offs between potentially desirable attributes (e.g. current and stability) are pointed out where appropriate. The conditions include:

- **Meniscus sizing.** From our maps it is clear that smaller menisci are more amenable to evaporation than very large ones, likely due to the enhanced effects of surface tension. For a typical ionic liquid it could be that a meniscus with $b_0 \lesssim 10\ \mu$m is wise, depending upon the impedance (which apparently influences the extent of the feasible regions in the B-$\hat{E}_0$ plane). Of course, very large γ have the capacity to augment this number as a result of the fact that they increase r^* and therefore the parameter B to which the problem is really linked. Also, in the event that the span of feasible $\hat{E}_0$ is somehow correlated to a measure of physical meniscus stability, as we have hypothesized in this thesis, smaller menisci will also be more immune to perturbations than their larger counterparts. This may, however, come at the penalty of a waning current that could necessitate the judicious election of a delicate compromise between b_0 and I.

- **Feeding architecture.** From our investigations it is clear that the feeding system plays a critical role in enabling evaporation from menisci when a scale disparity $B \ll 1$ exists (as it typically does in practical situations). Although we have shown that the impedance can be almost arbitrarily increased, the existence of a minimum feasible value appears likely. This, of course, would to preclude the possibility of so-called "frictionless" feeding flows that are sometimes believed to be desirable in connection with high currents. While we have observed an inverse I-C_R relationship that is congruent with this hypothesis, it is could be advisable to select a feeding architecture with $10^3 \lesssim C_R \lesssim 10^5$, where the high end of this range would be most appropriate for larger menisci. This owes to the fact that higher C_R were shown to activate additional regions of the B-$\hat{E}_0$ plane in our simulations.

- **Fluid permittivity.** While our permittivity analyses are less rigorous than other investigations in this thesis, the early results suggest the possibility of a maximum feasible value in the neighborhood of $\epsilon_r \approx 20$. It is interesting to speculate whether there is an analogy between this value and the critical one that is known for dielectric droplets in free-space (recall from Chapter 5 that $\epsilon_r \approx 20$ separates droplets with "turning points" from those that elongate monotonically). Although the reason for the observed threshold is somewhat unclear at present, it is likely related somehow to the arrangement of the fields and stresses near the tip of the meniscus and could explain to an extent why very polar fluids (e.g. organic solvents and certain exotic ILs) are notoriously fickle ion sources. An advisable condition, therefore, could be to strive for $\epsilon_r \lesssim 20$ where possible.

- **Fluid conductivity.** For Liquid Metal Ion Sources it is well known that space charge effects play an important role in governing the emission and making pure evaporation so readily accessible. In view of the similarities between the ballasting properties of heavy space charge (which tempers the growth of electrical stress in the event of a perturbation) and those of an impeding flow system (which counteracts the growth of electrical stress, in the event of a perturbation, by reducing the hydrostatic pressure in the meniscus) it is no surprise that the latter is an enabling facet of evaporation from liquids that are modestly conducting, e.g. ionic liquids. While our model and results do not encompass a space charge component, it is clear at this point that increasing the space charge around the meniscus could supplement the stabilizing influence of the feeding system or perhaps nullify it entirely as it does for liquid metals (where so-called "frictionless" feeding flows are in fact possible). With that in mind, it is likely advisable to make the fluid conductivity as high as possible in almost any situation since the evaporated current, and therefore the space charge, are essentially throttled by transport limitations in the liquid. Given that our results show $k \sim 1$ S/m likely puts us on the edge of a regime of space charge importance, aiming for $k \gg 1$ S/m, where possible, might make sense.

9.2 Thesis contributions

Through the course of this research we have identified and at least semi-quantified important aspects of IL evaporation in a way that could ultimately be of benefit to the full family of purely ionic electrospray ion technologies. Among other things, these have served to underscore the importance of sizing the meniscus and carefully engineering its feeding architecture. In what follows we briefly expound upon these and other important contributions.

- **Basic evaluation of influential physics**. We have identified a broad spectrum of potentially contributing physics and performed corresponding order-of-magnitude analyses. Unlike many other studies, these have revealed that both space charge and heating effects could play non-trivial roles in the process of IL ion evaporation, especially in the vicinity of high throughputs. Notwithstanding upstream hydraulics, which are perhaps critically important, we have also shown that the flow within the meniscus itself is a rather meaningless byproduct of the emission dynamics. This is directly evidenced through the small Capillary number that typifies fluids of high specific charge.

- **Analytical investigation of spheroidal menisci.** We have investigated the equilibrium and stability properties of both free- and fixed-volume spheroidal menisci through the use of several closed-form field solutions developed as part of the thesis. The results have demonstrated that such configurations are incapable of supporting meaningful emission unless the size of the meniscus is comparable to characteristic evaporation scale r^*. Given that evaporation from much larger menisci is believed to be feasible, our results have undoubtedly disqualified spheroids as possible interface candidates. Moreover, this has suggested that numerical recourse is likely unavoidable in the pursuit of evaporative modeling.

- **Development of a fundamental meniscus model.** We have constructed a rigorous mathematical framework for an evaporating IL meniscus attached to a feeding system of arbitrary impedance and reservoir pressure. Notwithstanding space charge effects, which were omitted in view of substantially greater simplicity, the framework is relevant to any liquid suspended at the end of a capillary tube, or possibly the opening of an individual pore, and has enabled the enforcement of several conditions (namely unconstrained volume but also $\epsilon_r \ll 100$) that have yet to receive theoretical treatment. A hybrid Matlab/Comsol numerical routine has also been developed for identifying steady, self-consistent solutions to the embodied equations.

- **Description of emission properties along the meniscus contact line.** When menisci are supported at the end of a sharp tube or a port in a dielectric plate it is likely that singular fields of the weak (i.e., integrable) variety prevail in the vicinity of the contact line. This owes to a corresponding geometric singularity (or, in reality, a near-singularity) that is well-known in wetting problems. Given that such fields could presumably engender evaporation themselves, we have developed corresponding closed-form Laplacian solutions and used these to identify conditions under which the "contact line emission" might be meaningful in comparison to its counterpart from the meniscus tip. The results suggest that emission is important beyond a specific contact angle, but that this angle is typically greater than what would be true of a Taylor cone.

- **Discovery of multiple solution branches for the free-volume problem.** In terms of the applied electric field, we have shown that two unique solution branches exist for the free-volume problem when a significant disparity in scales exists, i.e., $B \ll 1$. Of these, the lower branch is reminiscent of the stable but weakly distorted solutions from fixed-volume problems and terminates at a familiar "turning point". As the field is increased beyond the "turning point" we first intersect a small zone in which no solutions are evident (this is likely the realm of so-called pulsating emission modes described in the literature) and then a new and previously uncharted branch of ostensibly stable solutions, i.e., the upper branch. We believe that these are specifically enabled by the influence of the upstream impedance. Corresponding menisci are characterized by highly distorted morphologies that confer strong apex fields and result in currents that agree with empirical values.

- **Mapping of the B-$\hat{E}_0$ solution plane for several values of C_R.** We have mapped out important areas of the B-$\hat{E}_0$ solution plane, with a focus on the interesting situation of $B \ll 1$, for several values of impedance C_R. Each plane is typified by four distinct regions corresponding to the aforementioned solution branches. These include a region at low fields for which no meaningful emission is observed, a region of intermediate fields for which no solutions can be found, a region of higher fields for which we observe sharp and evaporating menisci (i.e., the "upper equilibria"), and a region of even higher fields for which we again can no longer identify stable equilibria. Among the upper solutions we have shown that the range of stable fields is apparently a decreasing function of the meniscus size and that this could suggest the existence of an interesting limiting structure. Variations in C_R have revealed that the landscape of the solution plane is sensitive to the feeding impedance and ostensibly confirmed the notion that augmented C_R could (1) confer additional stability on the menisci, and (2) enable easier access to larger contact lines.

- **Investigation of the dielectric influence.** We have selected several points within the $\hat{E}_0$-B plane for $C_R = 10^3$ and slowly varied the permittivity ϵ_r to identify any meaningful ramifications for evaporation. Our basic study has shown that increasing permittivity serves to augment the stress at the tip of the meniscus, much like it did for the fixed-volume dielectric droplets. Even when the relaxation time $\epsilon_r \epsilon_0 / k$ is decreasing (owing to fixed conductivity), this ensures an invariant current; however, at some threshold ϵ_r the elongation and sharpening of the meniscus is no longer tenable. Given this observation, we have argued that there could exist a maximum feasible permittivity for fluids with $k \sim 1$ S/m that may perhaps partially explain the difference in emission behavior between apolar ionic liquids such as EMI-BF4 and more polar alternatives.

- **Scrutiny of the Taylor archetype.** Throughout this thesis we have routinely juxtaposed our numerical structures with the classical Taylor archetype in a way that highlights important morphological differences. While we have uncovered but a small subset of the family of evaporating menisci, this effort has made it clear that the Taylor structure is not the thoroughly pervasive result that is so readily claimed in the body of contemporary literature. Notwithstanding these geometric disparities, our investigations of very sharp menisci (i.e., ones that may be pointing toward the limiting solution we have discussed) have revealed certain subtle similarities to the perfect cone solution (for example, in the distribution of vacuum field E_n^v) that could perhaps lead to more general theories in the future.

9.3 Suggestions for future work

Although the work presented in this thesis has begun to elucidate important theoretical aspects of ion evaporation, it is merely representative of a first step. High-value insights are still to be gleaned from future investigations that build upon what we have presented. In what follows we briefly outline what we believe to be several compelling areas of inquiry.

- **Space charge effects.** For simplicity we have neglected space charge in the present formulation of the model. In other words, we have solved Laplace instead of the more exact Poisson equation in the vacuum region. While this would appear to be a reasonable approximation for modestly conducting fluids producing gentle emission, our order-of-magnitude analysis suggests that the Poisson field in the vicinity of the activated portion of the meniscus could begin to approach a nontrivial fraction of its Laplacian counterpart (say 10^{-1}) as the current escalates. Given that the electrical stress goes like the square of fields, this would suggests that space charge effects could at some point affect a material change to shape of the interface. Similarly, the added ballasting might influence important stability characteristics and allow for situations of greater scale disparity to be identified.

Notwithstanding the space charge, we believe that the present model is nearly exhaustive from the perspective of a continuum approach. Substitution of Poisson for Laplace in the vacuum region might therefore represent the only missing link to a unified model capable of describing ionic liquids and liquid metals alike.

- **Influence of the electric field structure.** In the present formulation we have anchored the meniscus to a conducting plate for simplicity. In reality, however, it is possible that the fluid could exist on an insulating plate or at the end of a long, thin tube. Such configurations would necessarily modify the structure of the electric field in the vicinity of the interface. For example, we have shown that anchoring on a dielectric plate could lead to a singular field along the contact line. Future investigations might seek to explore related effects and determine the extent to which various anchoring media influence the evaporation behaviors we have uncovered.

- **Faster convergence properties.** Based on our experiences, dense computational meshes are needed to resolve the disparate scales that characterize large, activated menisci. In conjunction with our relatively slow interface relaxation method, these demand a relatively large numerical cost that has precluded us from exploring as much of the parameter space as we would have ideally liked. In other words, solution hunting was much too slow. Future investigations might address this issue by seeking to minimize the number of iterations required for convergence. One possible approach could be to formulate the interfacial propagation like a nonlinear root-finding problem, similar to what Wohlhuter [71] has done, and employ the framework we have outlined in the corresponding section of this thesis.

- **Detailed meniscus stability analysis.** We believe that the interfacial relaxation method employed herein is sufficient for identifying stable structures where they exist and avoiding anomalous results otherwise, i.e., avoiding convergence to physically unstable configurations. Indeed, the benchmarking experiments with known results would seem to corroborate this notion. In our experience, as we approach the bounds of physical stability with our method we begin to see greater numerical oscillations and a growing number iterations. Even if these represent qualitative measure of waning stability, they are far from quantitative. Future investigations might seek to quantify the relative stability of one solution with respect to another as a way of, for example, possibly establishing a feasible operating envelope with a safety factor.

- **Time-resolved modeling.** While the model presented herein is capable of identifying steady solutions for the evaporation problem, it is unable to resolve any related dynamic behaviors. Future investigations might borrow from the Higuera [62] formulation, for example, to create a time-resolved tool that can elucidate potentially interesting transients in the upper branch.

- **Atomistic issues.** For the present continuum formulation we have employed certain notions of a "leaky dielectric" as a result of their simplicity and heritage. As we noted in the literature review, however, it is possible that they may not capture the true microscopic physics. For example, we have assumed that the layer of charge at the liquid interface represents a vanishingly thin transition between bulk fluid and vacuum. Statistically speaking this would seem to make good sense if the free charges themselves were to occupy volumes that are small in comparison to the dipoles in the liquid. With ionic liquids this cannot be true though, since the charges themselves exist as parts of large molecules. The confusion is further intensified by Poisson, which suggests that the actual thickness of the surface charge layer is likely of sub-molecular scale. If that is the case, how can the charges truly be separated from the fluid? And what is really happening when the evaporating surface is "depleted" of charge?

  Among other things, we might also ask questions about the composition of the ionic liquid itself. Is it a two-fluid system of cations and anions? Or maybe a three-fluid systems of cations, anions, and a population of neutrals? In the event of the latter, it could be possible that carrier densities experience spatial fluctuations in the fluid even when quasineutrality is preserved. In other words, the bulk fluid properties might not be constant, in which case our formulation would not be strictly valid.

  Future investigations might seek to begin answering some of these questions by taking an atomistic approach to the evaporation problem, e.g., through the principles of so-called "molecular dynamics", or MD. While several pilot studies on electrosprayed beams are already underway (see, for example, Coles and Lozano [99]), new research could pay particular attention to the electrical structure of the liquid interface and charge distribution in the meniscus.

- **Meniscus spreading modes.** For the studies presented herein we have unconditionally "pinned" the contact line at a chosen radius. Given that the contact angle is unconstrained this would seem to model a perfectly non-wetting plate. As a matter of practicality, however, the surface of the plate may not always meet this condition, which could presumably allow the meniscus to spread out over the plate surface if the contact angle approaches the liquid-solid wetting angle. In this case, the contact radius would be free while the contact angle would be fixed to whatever the specific liquid-solid wetting angle is. Future investigations might endeavor to explore the possibility of steady menisci that satisfy these conditions.

- **Multi-cone emission modes.** Our attention in this research has been restricted to individual ion sources. It is apparent from the literature, however, that single sources might split into multiple sources under certain conditions. Future investigations might seek to uncover the mechanics of attendant reproduction processes and elucidate the manner in which they modify the meniscus behaviors reported herein.

- **Microscopy surveys.** The menisci reported in this thesis are almost entirely theoretical, corroborated only by laboratory measurements of indirect properties such as the current. In the future it would be very interesting to attempt to directly image steadily evaporating menisci such that important morphological properties can be firmly established. For example, in all instances of steady evaporation for the low-B regime we observe a stabilizing suction effect that creates convex interfaces. Can we see this in the laboratory? The size of the menisci represent an issue (the lower end of the visible spectrum is still a few hundred nanometers) for which electron microscopy is perhaps the only recourse, but this comes with its own challenges. Direct imaging would be very valuable but future researchers will need to be clever!

Appendix A

Analytical amplifier models

In this appendix we briefly review several analytical amplifier solutions that are widely referenced throughout the field-emitter literature and invoked in this thesis. These include the sphere-on-cone (SOC) model, the infinite hyperboloid, and the conducting plate with spheroidal protrusion.

A.1 Sphere-on-cone (SOC)

The so-called sphere-on-cone model involves a sphere and an infinite conical shaft that can be superimposed to create a structure loosely resembling many physical field emitters (Fig. A-1). It was very popular model in the early field-emission literature [85, 86, 87] but continues to be of utility today [74].

Structural properties of the electrical field formed between the sphere-on-cone and a counter electrode are analytically tractable in spherical space when the origin is identical to the vertex of the cone and coincident with the center of the sphere. In general, Laplace's equation in spherical coordinates is

$$\nabla^2\Phi = \frac{1}{r^2}\frac{\partial}{\partial r}\left(r^2\frac{\partial\Phi}{\partial r}\right) + \frac{1}{r^2\sin\theta}\frac{\partial}{\partial\theta}\left(\sin\theta\frac{\partial\Phi}{\partial\theta}\right) + \frac{1}{r^2\sin^2\theta}\frac{\partial^2\Phi}{\partial\phi^2} = 0 \tag{A.1}$$

where r is the spherical radius here, θ is the polar angle, and ϕ is its azimuthal counterpart. Where axial symmetry is appropriate, the third term in the expansion of the Laplacian operator is identically zero and this enables the possibility of a classical two-part product solution. Taking $\Phi = R\left(r\right)\Theta\left(\theta\right)$ and separating variables

$$\frac{1}{R}\frac{d}{dr}\left(r^2\frac{dR}{dr}\right) + \frac{1}{\Theta\sin\theta}\frac{d}{d\theta}\left(\sin\theta\frac{d\Theta}{d\theta}\right) = 0 \tag{A.2}$$

which can only be true when the modulus of either term on the LHS is equal to the so-called separation constant (essentially an eigenvalue of the differential operator). Insofar as this constant evaluates to $\pm n\left(n+1\right)$, where n is an arbitrary integer such that $n \in \mathbb{Z}^+$, we have, for example

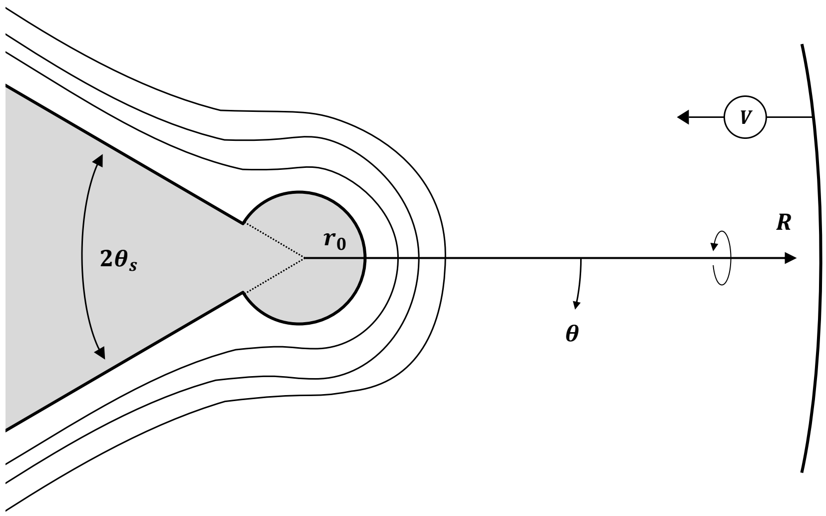

Figure A-1: Sphere-on-cone (SOC) model. A sphere (radius r_0) and an infinite conical shaft (half-angle θ_s) are superimposed to create a field-amplifier structure that has a closed-form analytical solution to the Laplace equation. Several equipotential surfaces are shown between the solid assembly and a distant counter-electrode (radius R along the zenith line).

$$\underbrace{\frac{1}{R}\frac{d}{dr}\left(r^2\frac{dR}{dr}\right)}_{n(n+1)}+\underbrace{\frac{1}{\Theta\sin\theta}\frac{d}{d\theta}\left(\sin\theta\frac{d\Theta}{d\theta}\right)}_{-n(n+1)}=0 \tag{A.3}$$

The R-term in this relationship then gives

$$\frac{d}{dr}\left(r^2\frac{dR}{dr}\right)-n\left(n+1\right)R=0 \tag{A.4}$$

for which we can try $R=C\cdot r^p$. The solution is

$$p\left(p+1\right)=n\left(n+1\right)\Rightarrow p=n,-\left(n+1\right) \tag{A.5}$$

and this yields

$$R\left(r\right)=Ar^n+Br^{-(n+1)} \tag{A.6}$$

Similarly, for the Θ-term we find

$$\frac{d}{d\theta}\left(\sin\theta\frac{d\Theta}{d\theta}\right)+\left[n\left(n+1\right)\sin\theta\right]\Theta=0 \tag{A.7}$$

which, of course, is the form that Legendre's equation takes when

$$\Theta\left(\theta\right)=C\cdot P_n\left(\cos\theta\right)+D\cdot Q_n\left(\cos\theta\right) \tag{A.8}$$

where P_n and Q_n are the Legendre functions of the first and second kind, respectively. Of these, the latter can be discarded because it is divergent along the polar axis ($\theta = 0 \Rightarrow \cos\theta = 1$ and $Q_n(1) \to \infty$).

Generally speaking, the total solution for the electric potential Φ is now found by summing over all possible separation constants, i.e.

$$\Phi(r,\theta) = A + \sum_{n=1}^{\infty} \left[B r^{n} + C r^{-(n+1)} \right] P_n(\cos\theta) \tag{A.9}$$

though this involves an infinite series that is oftentimes inconvenient. Rather than rigorously pursuing this sum, for the SOC model we instead truncate the series to a single term

$$\Phi(r,\theta) = \left[B r^{m} + C r^{-(m+1)} \right] P_m(\cos\theta) \tag{A.10}$$

and invoke the Legendre function of fractional order

$$P_m(\cos\theta) = {}_2F_1\left(-m, m+1; 1; \frac{1-\cos\theta}{2} \right) \tag{A.11}$$

where ${}_2F_1$ is the hypergeometric function and m is no longer restricted to the set of integers. This reduces the problem to three unknown constants (B, C, and m) which are easily identified through the boundary conditions

$$\begin{aligned} &\Phi(r = r_0, \theta) = 0 \\ &\Phi(r = R, \theta = 0) = V \\ &\Phi(r, \theta = \pi - \theta_s) = 0 \end{aligned}$$

The reference potential on the sphere and its conical shaft is set to zero here for mathematical convenience. Also notice that the downstream electrode, biased to the relative potential V, is specified only at the zenith location ($r = R, \theta = 0$). Incidentally, this provides the electrode with interesting topographical characteristics that are sometimes useful to study later on. After applying these conditions

$$\Phi(r,\theta) = V \left(\frac{r}{R} \right)^{m} \frac{\left[1 - \left(\frac{r_0}{r} \right)^{2*m+1} \right]}{\left[1 - \left(\frac{r_0}{R} \right)^{2*m+1} \right]} P_m(\cos\theta) \tag{A.12}$$

or, when $r_0 \ll R$

$$\Phi(r,\theta) \approx V \left(\frac{r}{R} \right)^{m} \left[1 - \left(\frac{r_0}{r} \right)^{2*m+1} \right] P_m(\cos\theta) \tag{A.13}$$

with the Legendre function subject to

$${}_2F_1\left(-m, m+1; 1; \frac{1+\cos\theta_s}{2} \right) = 0 \tag{A.14}$$

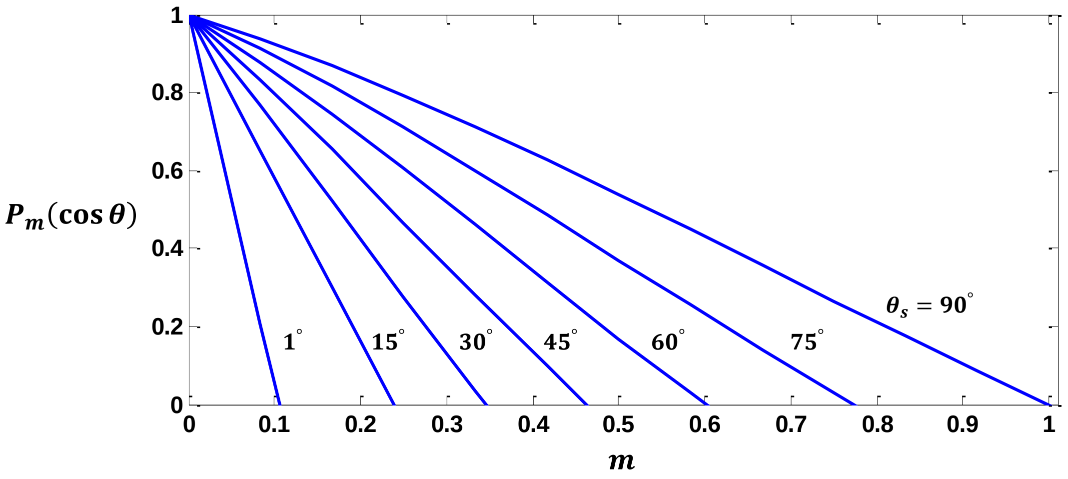

Figure A-2: Plot of $P_m(\cos\theta)$ as a function of the Legendre order m with θ_s a parameter. The value of the appropriate m is determined by locating the root for a desired cone half-angle. For example, $m = 1$ corresponds to $\theta_s = \pi/2$ which is the case of a spherical protrusion on a semi-infinite slab. The case of $\theta_s = 0$ is degenerate but it is believed that $m \to 0.088$ in the limit.

Unfortunately this relationship must be solved numerically. In Fig. A-2 we plot $P_m(\cos\theta)$ as a function of the fractional order m with θ_s a parameter. The appropriate value of m is determined by identifying the location of the root.

A.2 Infinite hyperboloid

Like the sphere-on-cone, it is not uncommon for physical field-emitter diodes to resemble hyperboloidal structures, especially near their apices where the important physics take place. This is very useful in that it facilitates modeling activities in prolate spheroidal space, among other systems, where analytical solutions to atypical Laplacian problems are sometimes tractable. The prolate spheroidal system is the cylindrical analog to planar elliptical coordinates and results from the rotation of that system about its confocal axis. This produces a collection of spheroids that are complemented by an orthogonal set of hyperboloids of revolution.

From Abramowitz and Stegun [82], prolate spheroidal coordinates are commonly defined by the cylindrical transformation

$$r = \alpha \sinh\mu \sin\nu \tag{A.15}$$

$$z = \alpha \cosh\mu \cos\nu \tag{A.16}$$

where $\mu \in [0, \infty)$, $\nu \in [0, \pi]$, and azimuthal symmetry has been imposed (see Fig. A-3). The proportionality constant α offers spatial modulation of the transformation while μ and ν paramterize the ellipsoidal and hyperboloidal surfaces, respectively. The general form of the corresponding Laplacian is

$$\nabla^2\Phi = \frac{1}{\alpha^2\left(\sinh^2\mu + \sin^2\nu\right)}\left[\frac{\partial^2\Phi}{\partial\mu^2} + \frac{\partial^2\Phi}{\partial\nu^2} + \coth\mu\frac{\partial\Phi}{\partial\mu} + \cot\nu\frac{\partial\Phi}{\partial\nu}\right] \tag{A.17}$$

If we choose a curve ν_0 that is geometrically similar to an emitter of interest (this is typically done with the apex curvature in mind) and adopt a second hyperboloid as our counter-electrode, the problem conveniently reduces to one of a single variable, ν. For the specific boundary conditions

$$\begin{aligned}\Phi\left(\nu = \nu_0\right) &= V\\ \Phi\left(\nu = \pi/2\right) &= 0\end{aligned}$$

the homogeneous solution to Eq. A.17 becomes

$$\Phi\left(\nu\right) = V\frac{\ln\left[\frac{1-\cos\nu}{1+\cos\nu}\right]}{\ln\left[\frac{1-\cos\nu_0}{1+\cos\nu_0}\right]} \tag{A.18}$$

The distribution of electrical fields in the inter-electrode region ($\mu \in [0,\infty)$ and $\nu \in [\nu_0, \pi/2]$) is then

$$\vec{E} = -\nabla\Phi = -\frac{\partial\Phi}{\partial\nu}\frac{\partial\nu}{\partial n} \tag{A.19}$$

where ∂n is the differential in the direction normal to the local ν surface and equivalent to $\partial n = \left(\partial r^2 + \partial z^2\right)^{1/2}$. This can be related to ν with the help of the transformations (Eqs. A.15 and A.16)

$$\begin{aligned}\partial r|_\mu &= \alpha\sinh\mu\cos\nu\partial\nu\\ \partial z|_\mu &= -\alpha\cosh\mu\sin\nu\partial\nu\\ \Rightarrow \partial n &= \partial\nu\cdot\alpha\cosh\mu\cos\nu\sqrt{\tanh^2\mu + \tan^2\nu}\end{aligned}$$

so that we can arrive at the electric vector field

$$\vec{E} = \frac{2V}{a\cosh\mu\sin\nu\cos\nu\sqrt{\tanh^2\mu + \tan^2\nu}}\ln^{-1}\left[\frac{1+\cos\nu_0}{1-\cos\nu_0}\right]\vec{i}_\nu \tag{A.20}$$

where we have written in μ-ν variables for convenience.

A.2.1 Hyperboloid selection and tip field

It is conventional to select an hyperboloid ν_0 based upon its tip sharpness. The radius of curvature of the apex in cylindrical space is exactly $R_c = \left(z''\right)^{-1}$ since the first derivative of $z(r)$ vanishes due to symmetry on the axis. Imposing an arbitrary

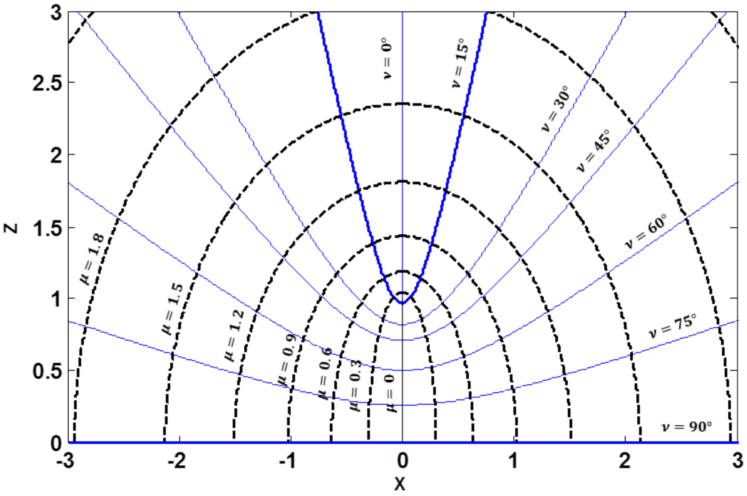

Figure A-3: Prolate spheroidal coordinates. Inscribed ellipses (μ) intersect hyperboloids of revolution (ν) to form an orthogonal system that is often convenient in the solution of certain Laplacian problems.

tip-to-plate distance d (note that $\alpha = d/\cos\nu_0$ in this case) yields

$$\left(\frac{d^2 z}{dr^2}\right)_{\nu_0,\mu=0} = \frac{\cot^2\nu_0}{d} \tag{A.21}$$

and this defines a non-trivial ν_0 such that

$$\tan\nu_0 = \sqrt{R_c/d} \tag{A.22}$$

It is straightforward at this point to choose the correct amplifier surrogate for a given geometric sharpness R_c/d. The corresponding field at the tip follows after noting the trigonometric relationships

$$\sin\nu_0 = (1 + d/R_c)^{-1/2}$$
$$\cos\nu_0 = (1 + R_c/d)^{-1/2}$$

In the sharp tip limit, $R_c \ll d$, we find the field modulus

$$E \sim \frac{2V}{R_c \ln\left(\frac{4d}{R_c}\right)} \tag{A.23}$$

which is the foundation for several analytical field-emission treatments seen throughout the literature [5, 4, 25].

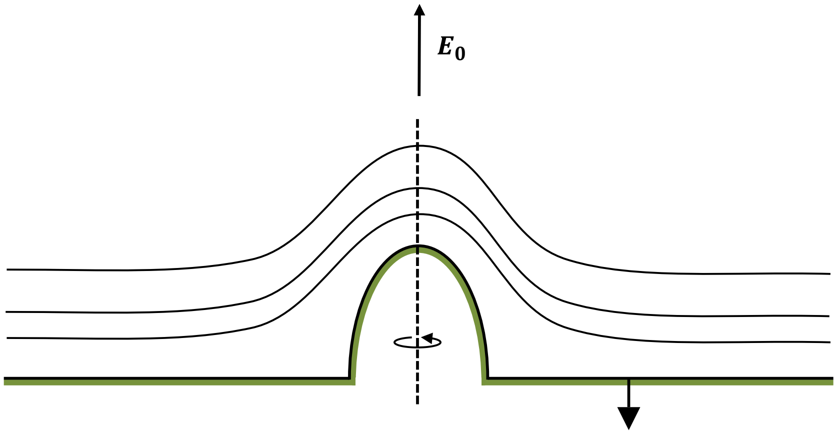

Figure A-4: Diagram of prolate spheroidal structure protruding from a flat semi-infinte slab. A prescribed field is uniform at infinity and produces equipotential surfaces that asymptotically approach flat planes. The associated Laplacian problem for the potential field is mathematically equivalent to a prolate spheroid suspended in a uniform background field directed along the line connecting the focii.

A.3 Conducting spheroid on a conducting, semi-infinite plate

A third analytical field model involves a conducting spheroidal structure that is either protruding from a conducting, semi-infinite plate or suspended in a uniform external field, both of which are mathematically equivalent. It is similar to the SOC model for $\theta_s \to \pi$, in fact it should be nearly identical when the protrusion is exactly hemispherical, but otherwise generalizes the problem to both oblate and prolate structures (Fig. A-4).

We will focus here on those of the prolate variety and work in the coordinate systems described by the cylindrical transformation from Eqs. A.15 and A.16. Starting from the general form for the Laplacian in the corresponding space, Eq. A.17, we are to solve the problem defined by the boundary conditions

$$\begin{aligned} \Phi\left(\mu_0, \nu\right) &= 0 \\ \Phi\left(\mu, \nu = \pi/2\right) &= 0 \\ \vec{E}\left(\mu \to \infty, \nu = 0\right) &= E_0 \cdot \vec{i}_z \end{aligned}$$

in which the spheroid and the plate (or mid-plane) are set to a reference potential while a uniform field is prescribed far downstream. Note that the problem is now more involved than the single-variable case for infinite hyperboloids and that it necessarily entail variations in both μ and ν (two spatial dimensions). In view of this we can adopt a product solution of the form $\Phi\left(\mu, \nu\right) = F(\mu) \cdot G(\nu)$ and immediately try $G(\nu) = \cos\nu$ by inspection to satisfy the reference potential on the plate. Plugging this into the Laplacian gives

$$\frac{d^2F}{d\mu^2} + \coth\mu \frac{dF}{d\mu} - 2F = 0 \tag{A.24}$$

for which the general solution is

$$\Phi\left(\mu,\nu\right) = C_1 \cos\nu \cosh\mu \left[1 + C_2\left(\frac{1}{\cosh\mu} + \ln\{\frac{\sinh\mu}{1+\cosh\mu}\}\right)\right] \tag{A.25}$$

The second constant of integration, C_2, is readily identified from the first boundary condition, $\Phi\left(\mu_0,\nu\right) = 0$, with the result that

$$\Phi\left(\mu,\nu\right) = C_1 \cos\nu \cosh\mu \left[1 - \frac{\frac{1}{\cosh\mu} + \ln\{\frac{\sinh\mu}{1+\cosh\mu}\}}{\frac{1}{\cosh\mu_0} + \ln\{\frac{\sinh\mu_0}{1+\cosh\mu_0}\}}\right] \tag{A.26}$$

For the first constant we can examine the axial part of the potential, $\Phi\left(\mu,\nu=0\right)$. The electric field on this line is $E_{ax} = -(d\Phi/d\mu)\cdot(d\mu/dz)$ where $d\mu/dz = (\alpha\sinh\mu)^{-1}$ from the coordinate transformations

$$E_{ax} = \frac{-C_1}{\alpha}\left[1 - \frac{\ln\{\frac{\sinh\mu}{1+\cosh\mu}\} + \frac{\cosh\mu}{\sinh^2\mu}}{\frac{1}{\cosh\mu_0} + \ln\{\frac{\sinh\mu_0}{1+\cosh\mu_0}\}}\right] \tag{A.27}$$

Assuming now that the downstream field is imposed very far from the tip of the spheroid, we have that

$$\lim_{\mu\to\infty} E_{ax} = -\frac{C_1}{\alpha} \tag{A.28}$$

and this gives $-C_1/\alpha = E_0$ for satisfaction of the final boundary condition. After substituting this back into the relationship for the full potential distribution we find

$$\Phi\left(\mu,\nu\right) = -\alpha E_0 \cos\nu \left[\cosh\mu - \frac{1 + \cosh\mu\cdot\ln\{\frac{\sinh\mu}{1+\cosh\mu}\}}{\frac{1}{\cosh\mu_0} + \ln\{\frac{\sinh\mu_0}{1+\cosh\mu_0}\}}\right] \tag{A.29}$$

which is now a complete and unique solution for the semi-infinite region above the conducting plate (or mid-plane) and external to the spheroid.

A.3.1 Spheroid surface field and amplification

For reference it will also be helpful to explicitly derive the field acting on the surface of the spheroid, $E_n = -d\Phi/dn|_{\mu_0}$ where n denotes the direction of the outward surface normal. From the chain rule we have that $E_n = -(d\Phi/d\mu)\cdot(d\mu/dn)$ with

$$\frac{d\mu}{dn} = \left[\alpha\cos\nu\cosh\mu\sqrt{\tanh^2\mu + \tan^2\nu}\right]^{-1} \tag{A.30}$$

again a result of the cylindrical transformations. This leads to

$$E_n = \frac{E_0}{\cosh\mu\sqrt{\tanh^2\mu + \tan^2\nu}}\left[\sinh\mu - \frac{\coth\mu + \sinh\mu\cdot\ln\{\frac{\sinh\mu}{1+\cosh\mu}\}}{\frac{1}{\cosh\mu_0} + \ln\{\frac{\sinh\mu_0}{1+\cosh\mu_0}\}}\right] \tag{A.31}$$

which we can evaluate at $\mu = \mu_0$ to find

$$\left(\frac{E_n}{E_0}\right)_{\mu_0} = \frac{1}{\sqrt{\tanh^2\mu_0 + \tan^2\nu}}\left[\frac{\tanh\mu_0 - \coth\mu_0}{1 + \cosh\mu_0\cdot\ln\{\frac{\sinh\mu_0}{1+\cosh\mu_0}\}}\right] \tag{A.32}$$

which is an expression for the result that we seek, albeit one in cumbersome variables. It is sometimes useful to make the extra step of writing it in terms of the aspect ratio, z_0/r_0, where z_0 is the height of the spheroid at the zenith and r_0 is the radial width at the mid-plane. Letting $Z = z_0/r_0$ gives

$$\left(\frac{E_n}{E_0}\right)_{\mu_0} = \frac{1}{\sqrt{1 + (Z\cdot\tan\nu)^2}}\left[\frac{Z^2 - 1}{\frac{Z}{\sqrt{Z^2-1}}\ln\left(Z + \sqrt{Z^2-1}\right) - 1}\right] \tag{A.33}$$

At the mid-plane ($\nu \to \pi/2$) we can easily see that the $\tan\nu$ in the denominator becomes unbounded and drives the modulus of the local field to zero. Conversely, the same $\tan\nu$ disappears at the zenith and we are left with an amplification factor that varies in a highly nonlinear way with Z. For reference purposes, a plot of the global amplification properties is shown in Fig. A-5 with the spheroidal aspect ratio as a parameter. Note that the result $(E_n/E_0)_{\mu_0,\nu=0} = 3$ is well-known for $Z \to 1$.

A.4 Dielectric spheroid on a conducting, semi-infinite plate

A related spheroidal model involves the case of a dielectric structure, rather than a conducting one, protruding from a conducting semi-infinite plate (or, equivalently, suspended in a uniform background field; see Fig. A-6). As in the previous section we will focus here on prolate geometries and work in the coordinate system defined by the cylindrical transformations of Eqs. A.15 and A.16. We wish to solve the problem governed by the boundary conditions

$$\Phi\left(\mu, \nu = \pi/2\right) = 0$$
$$\vec{E}\left(\mu \to \infty, \nu = 0\right) = E_0\cdot\vec{i}_z$$

as well as the interfacial conditions

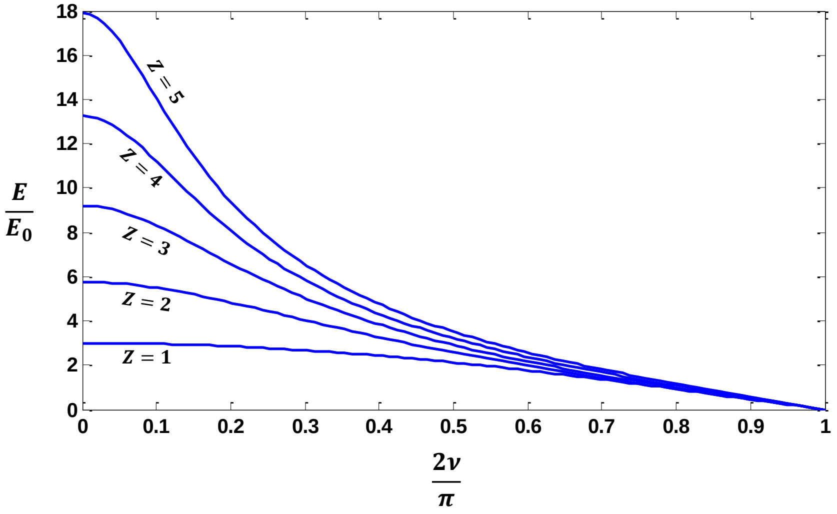

Figure A-5: Plot of the surface amplification for a spheroidal protrusion of prolate form factor. The amplification, E/E_0, is shown as a function of the angle ν with the aspect ration Z as a parameter. Note that $E/E_0 = 3$ at the zenith ($\nu = 0$) for $Z = 1$ and that it is possible to corroborate this result with other models, e.g. the SOC model with $\theta_s = \pi/2$.

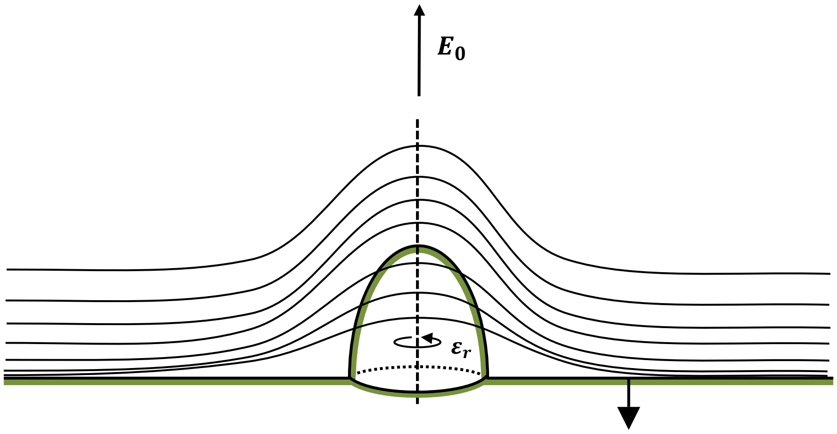

Figure A-6: Diagram of a dielectric prolate spheroidal structure protruding from a flat semi-infinte slab. A prescribed field is uniform at infinity and produces equipotential surfaces that asymptotically approach flat planes. The associated Laplacian problem for the potential field is mathematically equivalent to a prolate spheroid suspended in a uniform background field directed along the line connecting the focii. This problem is similar to the one for the conducting protrusion but now allows for the equipotential lines to permeate the structure.

$$\Phi^v\left(\mu_0,\nu\right) = \Phi^d\left(\mu_0,\nu\right)$$
$$\vec{E}^v\left(\mu_0,\nu\right)\cdot\vec{n} = \epsilon_r\left[\vec{E}^d\left(\mu_0,\nu\right)\cdot\vec{n}\right]$$

where the superscripts v and d signify properties in the vacuum and dielectric regions, respectively; where ϵ_r is the relative permittivity of the dielectric; and where $\vec{n}$ is the unit normal vector on its surface. This is a problem in which an electric field that is uniform far downstream creates potential gradients near the plate (or mid-plane) that may or may not leak into the protrusion.

We can start by invoking the general solution to Laplace's equation in axisymmetric prolate speroidal space (Eq. A.25) and writing expressions for the potential fields both internal and external to the dielectric

$$\Phi^d\left(\mu,\nu\right) = C_1\cos\nu\cosh\mu\left[1 + C_2\left(\frac{1}{\cosh\mu} + \ln\{\frac{\sinh\mu}{1+\cosh\mu}\}\right)\right]$$
$$\Phi^v\left(\mu,\nu\right) = C_3\cos\nu\cosh\mu\left[1 + C_4\left(\frac{1}{\cosh\mu} + \ln\{\frac{\sinh\mu}{1+\cosh\mu}\}\right)\right]$$

For Φ^d we can immediately take $C_2 \rightarrow 0$ by inspection because the potential must be bounded in the dielectric as $\mu \rightarrow 0$. The surviving constant in the expression for the dielectric field, C_1, is then determined by recognizing that the potential must be uniform across the dielectric-vacuum interface. From $\Phi^v(\mu_0) = \Phi^d(\mu_0)$ we have that

$$\Phi^d\left(\mu,\nu\right) = C_3\cos\nu\cosh\mu\left[1 + C_4\left(\frac{1}{\cosh\mu_0} + \ln\left\{\frac{\sinh\mu_0}{1+\cosh\mu_0}\right\}\right)\right] \tag{A.34}$$

To determine the first of the vacuum constants, C_3, we can again consider the axial part of the potential, $\Phi^v(\mu,\nu = 0)$. The electric field on this line is $E_{ax} = -(d\Phi/d\mu)\cdot(d\mu/dz)$ by the chain rule with $d\mu/dz = (\alpha\sinh\mu)^{-1}$ following from the coordinate transformations

$$E_{ax} = -\left.\frac{d\Phi^v}{d\mu}\frac{d\mu}{dz}\right|_{\nu=0} = -\frac{C_3}{\alpha}\left[1 + C_4\left(\frac{1}{\cosh\mu} + \ln\left\{\frac{\sinh\mu}{1+\cosh\mu}\right\}\right)\right] - \frac{C_3C_4\left(\coth\mu - \tanh\mu\right)}{\alpha\sinh\mu} \tag{A.35}$$

If the downstream field is imposed very far from the tip of the spheroid

$$\lim_{\mu\rightarrow\infty} E_{ax} = -\frac{C_3}{\alpha} \tag{A.36}$$

which gives $C_3 = -\alpha E_0$. The final constant, C_4, is identified by invoking the jump condition for the interfacial electric field, $E_n^v(\mu_0) = \epsilon_r \cdot E_n^d(\mu_0)$ or

Table A.1: Field results for a dielectric spheroid on a conducting plate (dielectric part)

Field	Dielectric
	$\mu \in [0, \mu_0]$ $\nu \in [0, \pi/2]$
Φ	$\frac{-\alpha E_0 \cos\nu \cosh\mu}{1-(\epsilon_r-1)\sinh^2\mu_0\left[1+\cosh\mu_0\cdot\ln\left\{\frac{\sinh\mu_0}{1+\cosh\mu_0}\right\}\right]}$
$E_n^d\left(\mu_0\right) = -\left.\frac{d\Phi^d}{d\mu}\frac{d\mu}{dn}\right\vert_{\mu_0}$	$\frac{E_0 \tanh\mu_0\left(\tanh^2\mu_0+\tan^2\nu\right)^{-1/2}}{1-(\epsilon_r-1)\sinh^2\mu_0\left[1+\cosh\mu_0\cdot\ln\left\{\frac{\sinh\mu_0}{1+\cosh\mu_0}\right\}\right]}$
$E_t^d\left(\mu_0\right) = -\left.\frac{d\Phi^d}{d\nu}\frac{d\nu}{dt}\right\vert_{\mu_0}$	$\frac{E_0 \tan\nu\left(\tanh^2\mu_0+\tan^2\nu\right)^{-1/2}}{1-(\epsilon_r-1)\sinh^2\mu_0\left[1+\cosh\mu_0\cdot\ln\left\{\frac{\sinh\mu_0}{1+\cosh\mu_0}\right\}\right]}$

$$\left.\frac{d\Phi^v}{d\mu}\frac{d\mu}{dn}\right|_{\mu_0} = \epsilon_r \left.\frac{d\Phi^d}{d\mu}\frac{d\mu}{dn}\right|_{\mu_0} \Rightarrow \left.\frac{d\Phi^v}{d\mu}\right|_{\mu_0} = \epsilon_r \left.\frac{d\Phi^d}{d\mu}\right|_{\mu_0} \tag{A.37}$$

The derivatives of the potential fields with respect to μ are

$$\begin{aligned}
\frac{d\Phi^d}{d\mu} &= -\alpha E_0 \cos\nu \sinh\mu \left[1 + C_4\left(\frac{1}{\cosh\mu_0} + \ln\left\{\frac{\sinh\mu_0}{1+\cosh\mu_0}\right\}\right)\right] \\
\frac{d\Phi^v}{d\mu} &= -\alpha E_0 \cos\nu \sinh\mu \left[1 + C_4\left(\frac{1}{\cosh\mu} + \ln\left\{\frac{\sinh\mu}{1+\cosh\mu}\right\}\right)\right] - C_4 \alpha E_0 \cos\nu\left(\coth\mu - \tanh\mu\right)
\end{aligned}$$

and allow us to find after a measure of algebraic manipulation

$$C_4 = \frac{-1}{\frac{1}{\cosh\mu_0} + \ln\left\{\frac{\sinh\mu_0}{1+\cosh\mu_0}\right\} + \frac{\tanh\mu_0 - \coth\mu_0}{(\epsilon_r-1)\sinh\mu_0}} \tag{A.38}$$

Substituting this back into the field expressions leads to the results that are summarized in the tables.

The tangential electric fields in the tables are equivalent at the interface, as they should be, and following from taking

$$\frac{d\nu}{dt} = \frac{-1}{\alpha\cos\nu\cosh\mu\sqrt{\tanh^2\mu + \tan^2\nu}} \tag{A.39}$$

with the help of the cylindrical transformations. We can now take a look at two interesting limits: one in which $\epsilon_r \to 1$ and the other in which $\epsilon_r \to \infty$. The first is the limit in which the dielectric essentially becomes part of the vacuum and vanishes.

Table A.2: Field results for a dielectric spheroid on a conducting plate (vacuum part)

Field	Vacuum
	$\mu \in [\mu_0, \infty)$ $\nu \in [0, \pi/2]$
Φ	$-\alpha E_0 \cos\nu \cosh\mu \left[1 - \frac{\frac{1}{\cosh\mu} + \ln\left\{\frac{\sinh\mu}{1+\cosh\mu}\right\}}{\frac{1}{\cosh\mu_0} + \ln\left\{\frac{\sinh\mu_0}{1+\cosh\mu_0}\right\} + \frac{\tanh\mu_0 - \coth\mu_0}{(\epsilon_r - 1)\sinh\mu_0}}\right]$
$E_n^v(\mu_0) = -\left.\frac{d\Phi^v}{d\mu}\frac{d\mu}{dn}\right\|_{\mu_0}$	$\frac{\epsilon_r E_0 \tanh\mu_0 \left(\tanh^2\mu_0 + \tan^2\nu\right)^{-1/2}}{1 - (\epsilon_r - 1)\sinh^2\mu_0 \left[1 + \cosh\mu_0 \cdot \ln\left\{\frac{\sinh\mu_0}{1+\cosh\mu_0}\right\}\right]}$
$E_t^v(\mu_0) = -\left.\frac{d\Phi^v}{d\nu}\frac{d\nu}{dt}\right\|_{\mu_0}$	$\frac{E_0 \tan\nu \left(\tanh^2\mu_0 + \tan^2\nu\right)^{-1/2}}{1 - (\epsilon_r - 1)\sinh^2\mu_0 \left[1 + \cosh\mu_0 \cdot \ln\left\{\frac{\sinh\mu_0}{1+\cosh\mu_0}\right\}\right]}$

If we consider the normal components of the fields at the interface we find

$$\lim_{\epsilon_r \to 1} E_n^v(\mu_0) = \lim_{\epsilon_r \to 1} E_n^d(\mu_0) = \frac{E_0 \tanh\mu_0}{\sqrt{\tanh^2\mu_0 + \tan^2\nu}} \tag{A.40}$$

On the axis, $\tan\nu \to 0$ to give $E_n^v = E_n^d = E_0$ as expected. This is the solution for a flat plate subjected to a uniform field. The limit at the opposite end of the spectrum involves the dielectric becoming extremely polar. Again considering the normal fields

$$\lim_{\epsilon_r \to \infty} E_n^d(\mu_0) = 0$$

$$\lim_{\epsilon_r \to \infty} E_n^v(\mu_0) = \frac{E_0}{\sqrt{\tanh^2\mu_0 + \tan^2\nu}} \frac{\tanh\mu_0 - \coth\mu_0}{\left[1 + \cosh\mu_0 \cdot \ln\left\{\frac{\sinh\mu_0}{1+\cosh\mu_0}\right\}\right]}$$

Unsurprisingly, from E_n^v we recover the solution for a fully conducting, equipotential protrusion (see previous section).

Appendix B

Additional mathematical notes

This appendix contains notes on the evaluation of viscous stress tensors and the divergence for surface normal vectors, both of which are referenced in this thesis, using several common coordinate systems.

B.1 Divergence of a surface normal

Evaluating the divergence of the normal vector for a liquid-gas interface (and sometimes a liquid-liquid interface, though not in the present case) is important for identifying the associated surface tension properties. Though several related methods exist for computing this tension, the one involving $\nabla \cdot \vec{n}$ is seemingly the most general.

In the subsections that follow we calculate normal vectors for arbitrary surfaces parameterized in several common coordinate spaces. While these are sometimes available by inspection we take the more general approach of introducing a function that vanishes along the interface, say $F(\boldsymbol{x}) = 0$ where $\boldsymbol{x}$ is a vector of appropriate coordinate parameters, and finding the normalized gradient $\vec{n} = \nabla F / |\nabla F|$. We then compute the divergence of this vector before simplifying the result for typical topographical configurations, e.g. axisymmetry.

B.1.1 Cartesian space

Consider a surface that projects onto the $x - y$ plane defined by $z = h(x, y)$ (Fig. B-1). We can write a function F that vanishes on the surface

$$F\left(x, y, z\right) = 0 = h\left(x, y\right) - z \tag{B.1}$$

The gradient and its magnitude for this functional are $\nabla F = h_x \vec{i}_x + h_y \vec{i}_y - \vec{i}_z$ and $|\nabla F| = \sqrt{1 + h_x^2 + h_y^2}$, respectively, where the x and y subscripts denote partial derivatives on those parameters. These provide for the surface normal vector

$$\vec{n} = \frac{\nabla F}{|\nabla F|} = \frac{h_x \vec{i}_x + h_y \vec{i}_y - \vec{i}_z}{\sqrt{1 + h_x^2 + h_y^2}} \tag{B.2}$$

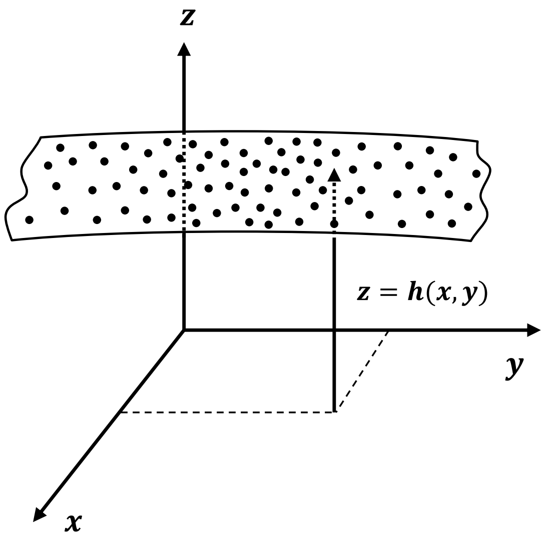

Figure B-1: Surface parameterized in cartesian space with $z = h(x, y)$.

After taking the divergence of this normal we find the general result

$$\nabla \cdot \vec{n} = \frac{h_{xx}\left(1 + h_y^2\right) + h_{yy}\left(1 + h_x^2\right) - 2h_x h_y h_{xy}}{\left(1 + h_x^2 + h_y^2\right)^{3/2}} \tag{B.3}$$

which we might verify by investigating a perfectly spherical surface of radius R centered about the origin. Recognizing that $R^2 = x^2 + y^2 + z^2$ we solve for interface expression $z = \sqrt{R^2 - x^2 - y^2}$ and its derivatives

$$\begin{aligned}
h_x &= -\frac{x}{\sqrt{R^2 - x^2 - y^2}} \\
h_y &= -\frac{-y}{\sqrt{R^2 - x^2 - y^2}} \\
h_{xx} &= -\frac{R^2 - y^2}{\left(R^2 - x^2 - y^2\right)^{3/2}} \\
h_{yy} &= -\frac{R^2 - x^2}{\left(R^2 - x^2 - y^2\right)^{3/2}} \\
h_{xy} &= -\frac{xy}{\left(R^2 - x^2 - y^2\right)^{3/2}}
\end{aligned}$$

After substituting these we see that $\nabla \cdot \vec{n} = -2/R$ and find the tension $P_{st} = -\gamma \nabla \cdot \vec{n} = 2\gamma/R$ we would expect.

The general result can be somewhat cumbersome and circumnavigating it is often facilitated by working in spatial regions with fewer degrees of freedom. For example, for a surface that is two-dimensional with $z = h(x)$ the general result reduces to just

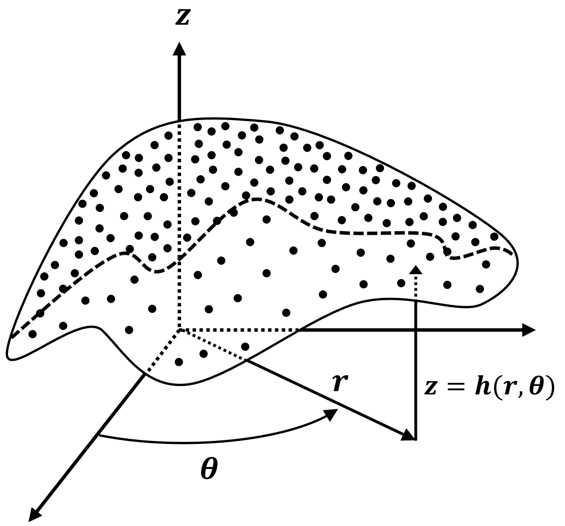

Figure B-2: Surface parameterized in cylindrical space with $z = h(r, \theta)$.

$$\nabla \cdot \vec{n} = \frac{h_{xx}}{\left(1 + h_x^2\right)^{3/2}} \tag{B.4}$$

The corresponding radius of curvature in this case, simply $R_c = |\nabla \cdot \vec{n}|^{-1}$, is well-known and can be verified through many external mathematical references.

B.1.2 Cylindrical space

Surface with z dependent

Consider a surface that projects onto the $r - \theta$ plane defined by $z = h(r, \theta)$, where r and θ are respectively the radial and azimuthal coordinates (Fig. B-2). This parameterization can be useful for interfaces that may have some periodicity in r, such as a wave. We can write the function F on this surface

$$F\left(r, \theta, z\right) = 0 = h\left(r, \theta\right) - z \tag{B.5}$$

The normalized gradient of this functional evaluates to

$$\vec{n} = \frac{\nabla F}{|\nabla F|} = \frac{h_r \vec{i}_r + \frac{h_\theta}{r} \vec{i}_\theta - \vec{i}_z}{\sqrt{1 + h_r^2 + \left(\frac{h_\theta}{r}\right)^2}} \tag{B.6}$$

and has a divergence

$$\nabla \cdot \vec{n} = \frac{\left(1 + h_r^2\right) h_r + r \cdot h_{rr} + h_\theta^2 \left(\frac{h_{rr}}{r} + \frac{2h_r}{r^2}\right) - \frac{h_r h_\theta h_{r\theta}}{r} + \frac{\left(1 + h_r^2\right) h_{\theta\theta}}{r}}{r \left[1 + h_r^2 + \left(\frac{h_\theta}{r}\right)^2\right]^{3/2}} \tag{B.7}$$

which we arrive at after a considerable amount of algebraic manipulation. In the event that the surface is axisymmetric, as we often assume in this thesis, then $z = h(r)$ only and we can observe the reduced result

$$\nabla \cdot \vec{n} = \frac{\left(1 + h_r^2\right) h_r + r \cdot h_{rr}}{r \left(1 + h_r^2\right)^{3/2}} \tag{B.8}$$

To verify this we can consider a perfectly spherical surface of radius R. In this case the expression for the interface becomes $z = \sqrt{R^2 - r^2} = h(r)$ and the derivatives are

$$\begin{aligned} h_r &= -\frac{r}{\sqrt{R^2 - r^2}} \\ h_{rr} &= -\frac{-R^2}{\left[R^2 - r^2\right]^{3/2}} \end{aligned}$$

After substituting these we find

$$\nabla \cdot \vec{n} = -\frac{2}{R} \tag{B.9}$$

along with the associated tension, $P_{st} = -\gamma \nabla \cdot \vec{n} = 2\gamma/R$, as expected. Similarly, we might check the case of a perfect cone with $z = -r \cdot \cot\theta_c$ where θ_c is its half-angle. Using $h_r = -\cot\theta_c$ and $h_{rr} = 0$ we see that $\nabla \cdot \vec{n} = -\cos\theta_c/r$. The spherical form of this result, where the spherical radius is $r_s = r/\sin\theta_c$, is known

$$\nabla \cdot \vec{n} = -\frac{\cot\theta_c}{r_s} \tag{B.10}$$

and may be verified elsewhere [5].

Surface with r dependent

Consider a surface that projects onto the $z - \theta$ plane defined by $r = h(\theta, z)$ (Fig. B-3). This parameterization could be useful for interfaces that may have some periodicity in z, such as a fluid tube or jet. The function F on the surface is

$$F(r, \theta, z) = 0 = h(\theta, z) - r \tag{B.11}$$

The normalized gradient of this functional evaluates to

$$\vec{n} = \frac{\nabla F}{|\nabla F|} = \frac{-r\vec{i}_r + h_\theta \vec{i}_\theta + r \cdot h_z \vec{i}_z}{\sqrt{r^2\left(1 + h_z^2\right) + h_\theta^2}} \tag{B.12}$$

and has a divergence

$$\nabla \cdot \vec{n} = \frac{r\left(1 + h_z^2\right)\left(h_{\theta\theta} - r\right) - 2h_\theta\left(h_\theta + r \cdot h_z \cdot h_{\theta z}\right) + r \cdot h_{zz}\left(r^2 + h_\theta^2\right)}{\left[r^2\left(1 + h_z^2\right) + h_\theta^2\right]^{3/2}} \tag{B.13}$$

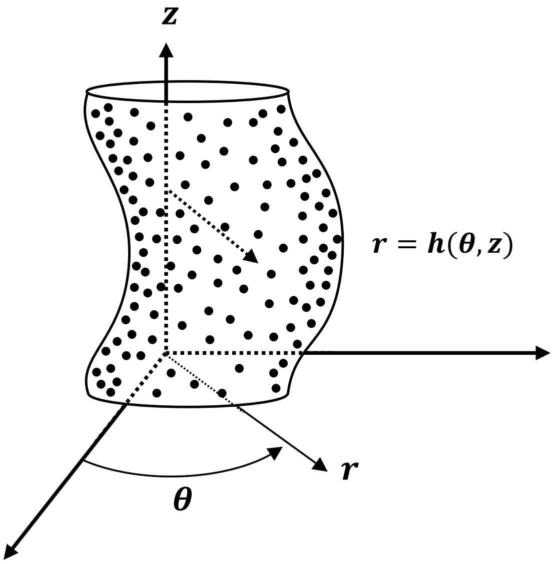

Figure B-3: Surface parameterized in cylindrical space with $r = h(\theta, z)$.

In the event that the surface is axisymmetric, so that $r = h(z)$ only, we can take $h_\theta = h_{\theta\theta} = h_{\theta z} = 0$ and reduce the result to

$$\nabla \cdot \vec{n} = \frac{-\left(1 + h_z^2\right) + r \cdot h_{zz}}{r\left(1 + h_z^2\right)^{3/2}} \tag{B.14}$$

To verify this we might check the case in which the surface is perfectly cylindrical with $r(z) = R$. This necessitates that $h_z = h_{zz} = 0$ and we find that

$$\nabla \cdot \vec{n} = -\frac{1}{R} \tag{B.15}$$

on the surface along with the tension $P_{st} = -\gamma \nabla \cdot \vec{n} = \gamma / R$. This is the result that we would expect. Similary, we might again check the perfect cone that is now given by $r = -z \cdot \tan\theta_c$. Using $h_z = -\tan\theta_c$, $h_{zz} = 0$, and converting to the spherical radius $r_s = r / \sin\theta_c$ gives

$$\nabla \cdot \vec{n} = -\frac{\cot\theta_c}{r_s} \tag{B.16}$$

which is the same as before.

B.1.3 Spherical space

Surface with r dependent

Consider a surface defined by $r = h(\theta, \phi)$ where r is the spherical radius, θ is the polar angle, and ϕ is its azimuthal counterpart (Fig. B-4). This parameterization could be useful for interfaces that have some periodicity in θ, such as a bubble. The function F on the surface is

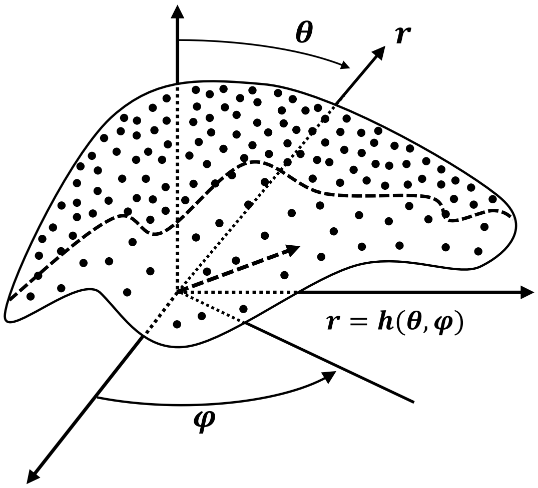

Figure B-4: Surface parameterized in spherical space with $r = h(\theta, \phi)$.

$$F\left(r, \theta, \phi\right) = 0 = h\left(\theta, \phi\right) - r \tag{B.17}$$

The normalized gradient of this function evaluates to

$$\vec{n} = \frac{-r \cdot \vec{i}_r + h_\theta \vec{i}_\theta + \frac{h_\phi}{\sin\theta}\vec{i}_\phi}{\sqrt{r^2 + h_\theta^2 + \left(\frac{h_\phi}{\sin\theta}\right)^2}} \tag{B.18}$$

and has a divergence

$$\nabla \cdot \vec{n} = \frac{1}{r^2}\frac{\partial}{\partial r}\left(r^2 n_r\right) + \frac{1}{r\sin\theta}\frac{\partial}{\partial\theta}\left(n_\theta \sin\theta\right) + \frac{1}{r\sin\theta}\frac{\partial n_\phi}{\partial\phi} \tag{B.19}$$

where n_r, n_θ, and n_ϕ are the mutually orthogonal components of $\vec{n}$. The expanded version of this expression after taking derivatives is quite involved and so we provide the results here in segmented form

$$\frac{1}{r^2}\frac{\partial}{\partial r}\left(r^2 n_r\right) = \frac{r^2 - 3\left[r^2 + h_\theta^2 + \left(\frac{h_\phi}{\sin\theta}\right)^2\right]}{\left[r^2 + h_\theta^2 + \left(\frac{h_\phi}{\sin\theta}\right)^2\right]^{3/2}}$$

$$\frac{1}{r\sin\theta}\frac{\partial}{\partial\theta}\left(n_\theta \cdot \sin\theta\right) = \frac{\sin\theta \cdot h_{\theta\theta}\left[r^2 + \left(\frac{h_\phi}{\sin\theta}\right)^2\right] + \cos\theta \cdot h_\theta\left[r^2 + h_\theta^2 + 2\left(\frac{h_\phi}{\sin\theta}\right)^2\right] - \frac{h_\theta \cdot h_\phi \cdot h_{\theta\phi}}{\sin\theta}}{r\sin\theta\left[r^2 + h_\theta^2 + \left(\frac{h_\phi}{\sin\theta}\right)^2\right]^{3/2}}$$

$$\frac{1}{r\sin\theta}\frac{\partial n_\phi}{\partial\phi} = \frac{h_{\phi\phi}\left(r^2 + h_\theta^2\right) - h_\theta \cdot h_\phi \cdot h_{\theta\phi}}{r\sin^2\theta\left[r^2 + h_\theta^2 + \left(\frac{h_\phi}{\sin\theta}\right)^2\right]^{3/2}}$$

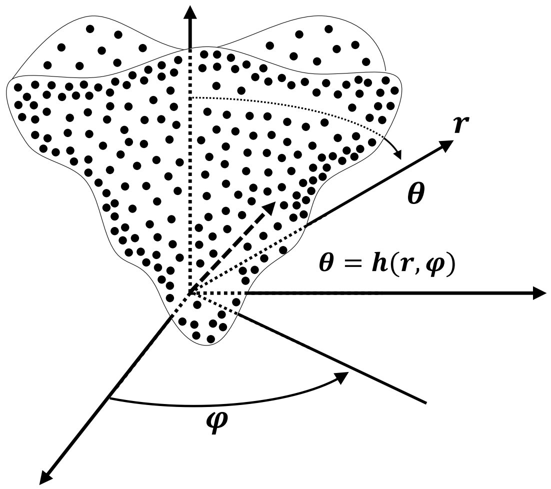

Figure B-5: Surface parameterized in spherical space with $\theta = h(r, \phi)$.

It is likely that there are many algebraic simplifications we have not invoked. When the surface is symmetric about the azimuthal axis we have that $h_\phi = h_{\phi\phi} = h_{\theta\phi} = 0$ and the solution reduces to

$$\nabla \cdot \vec{n} = \frac{-2r^2 - 3h_\theta^2 + r \cdot h_{\theta\theta} + \cot\theta \left(r \cdot h_\theta + \frac{1}{r} h_\theta^3\right)}{\left(r^2 + h_\theta^2\right)^{3/2}} \tag{B.20}$$

A very crude check of this is possible by considering the simple case of a perfectly spherical surface, with $r(\theta) = r_0$, so that $h_\theta = h_{\theta\theta} = 0$ also. When this is true,

$$\nabla \cdot \vec{n} = -\frac{2}{r_0} \tag{B.21}$$

on the surface and the associated tension becomes

$$P_{st} = -\gamma \nabla \cdot \vec{n} = \frac{2\gamma}{r_0} \tag{B.22}$$

as would be expected.

Surface with θ dependent

Now consider a surface defined by $\theta = h(r, \phi)$ so that θ is the dependent parameter (Fig. B-5). This parameterization could be useful for interfaces that have some periodicity in r, such as a wave again or a conical structure. The function F on the surface is

$$F(r, \theta, \phi) = 0 = h(r, \phi) - \theta \tag{B.23}$$

The normalized gradient of this function evaluates to

$$\vec{n} = \frac{\nabla F}{|\nabla F|} = \frac{r \cdot h_r \vec{i}_r - \vec{i}_\theta + \frac{h_\phi}{\sin\theta}\vec{i}_\phi}{\sqrt{1 + (r \cdot h_r)^2 + \left(\frac{h_\phi}{\sin\theta}\right)^2}} \tag{B.24}$$

and has a divergence that is still equal to Eq. B.19. Piecewise, the terms in this expression are

$$\frac{1}{r^2}\frac{\partial}{\partial r}\left(r^2 n_r\right) = \frac{r \cdot h_{rr} + 3h_r + 2r^2 h_r^3 - \frac{r \cdot h_r \cdot h_\phi \cdot h_{r\phi}}{\sin^2\theta}}{\left[1 + (r \cdot h_r)^2 + \left(\frac{h_\phi}{\sin\theta}\right)^2\right]^{3/2}}$$

$$\frac{1}{r\sin\theta}\frac{\partial}{\partial\theta}\left(n_\theta \cdot \sin\theta\right) = -\frac{\cot\theta}{r} \cdot \frac{1 + (r \cdot h_r)^2 + 2\left(\frac{h_\phi}{\sin\theta}\right)^2}{\left[1 + (r \cdot h_r)^2 + \left(\frac{h_\phi}{\sin\theta}\right)^2\right]^{3/2}}$$

$$\frac{1}{r\sin\theta}\frac{\partial n_\phi}{\partial\phi} = \frac{h_{\phi\phi}\left[1 + (r \cdot h_r)^2\right] - r^2 \cdot h_r \cdot h_\phi \cdot h_{r\phi}}{r\sin^2\theta\left[1 + (r \cdot h_r)^2 + \left(\frac{h_\phi}{\sin\theta}\right)^2\right]^{3/2}}$$

For the axisymmetric case we have that $h_\phi = h_{\phi\phi} = h_{r\phi} = 0$ and the solution reduces to

$$\nabla \cdot \vec{n} = \frac{r \cdot h_{rr} + 3h_r + 2r^2 h_r^3}{\left[1 + (r \cdot h_r)^2\right]^{3/2}} - \frac{\cot\theta}{r}\left[1 + (r \cdot h_r)^2\right]^{-1/2} \tag{B.25}$$

As a crude check we can again investigate a very simple case. Consider the conical surface given by $\theta(r) = \theta_0$ and further observe that this necessarily implies $h_r = h_{rr} = 0$. The reduced result now becomes

$$\nabla \cdot \vec{n} = -\frac{\cot\theta_0}{r} \tag{B.26}$$

on the surface. The associated tension is

$$P_{st} = -\gamma\nabla \cdot \vec{n} = \frac{\gamma\cot\theta_0}{r} \tag{B.27}$$

which is well-known and can be verified by, for example, Meusnier's theorem [5].

B.1.4 Summary

A distillation of the important normal vector and divergence results is provided in the table.

Table B.1: Normal vectors and their divergence values for surfaces parameterized in several common coordinate systems

Coordinate system	$\boldsymbol{\vec{n}}$	$\boldsymbol{\nabla\cdot\vec{n}}$	
		General	2D
Cartesian $z=h(x,y)$	$\frac{h_x\vec{i}_x+h_y\vec{i}_y-\vec{i}_z}{\sqrt{1+h_x^2+h_y^2}}$	$\frac{h_{xx}\left(1+h_y^2\right)+h_{yy}\left(1+h_x^2\right)-2h_xh_yh_{xy}}{\left(1+h_x^2+h_y^2\right)^{3/2}}$	$\frac{h_{xx}}{(1+h_x^2)^{3/2}}$
Cylindrical $z=h(r,\theta)$	$\frac{h_r\vec{i}_r+\frac{h_\theta}{r}\vec{i}_\theta-\vec{i}_z}{\sqrt{1+h_r^2+\left(\frac{h_\theta}{r}\right)^2}}$	$\frac{\left(1+h_r^2\right)h_r+r\cdot h_{rr}+h_\theta^2\left(\frac{h_{rr}}{r}+\frac{2h_r}{r^2}\right)}{r\left[1+h_r^2+\left(\frac{h_\theta}{r}\right)^2\right]^{3/2}}+\frac{-\frac{h_rh_\theta h_{r\theta}}{r}+\frac{\left(1+h_r^2\right)h_{\theta\theta}}{r}}{r\left[1+h_r^2+\left(\frac{h_\theta}{r}\right)^2\right]^{3/2}}$	$\frac{\left(1+h_r^2\right)h_r+r\cdot h_{rr}}{r(1+h_r^2)^{3/2}}$
Cylindrical $r=h(\theta,z)$	$\frac{-r\vec{i}_r+h_\theta\vec{i}_\theta+r\cdot h_z\vec{i}_z}{\sqrt{r^2(1+h_z^2)+h_\theta^2}}$	$\frac{r\left(1+h_z^2\right)(h_{\theta\theta}-r)-2h_\theta(h_\theta+r\cdot h_z\cdot h_{\theta z})}{\left[r^2(1+h_z^2)+h_\theta^2\right]^{3/2}}+\frac{r\cdot h_{zz}\left(r^2+h_\theta^2\right)}{\left[r^2(1+h_z^2)+h_\theta^2\right]^{3/2}}$	$\frac{-\left(1+h_z^2\right)+r\cdot h_{zz}}{r(1+h_z^2)^{3/2}}$
Spherical $r=h(\theta,\phi)$	$\frac{-r\cdot\vec{i}_r+h_\theta\vec{i}_\theta+\frac{h_\phi}{\sin\theta}\vec{i}_\phi}{\sqrt{r^2+h_\theta^2+\left(\frac{h_\phi}{\sin\theta}\right)^2}}$	$\frac{\cos\theta\cdot h_\theta\left[r^2+h_\theta^2+2\left(\frac{h_\phi}{\sin\theta}\right)^2\right]-\frac{h_\theta\cdot h_\phi\cdot h_{\theta\phi}}{\sin\theta}}{r\sin\theta\left[r^2+h_\theta^2+\left(\frac{h_\phi}{\sin\theta}\right)^2\right]^{3/2}}+\frac{\sin\theta\cdot h_{\theta\theta}\left[r^2+\left(\frac{h_\phi}{\sin\theta}\right)^2\right]}{r\sin\theta\left[r^2+h_\theta^2+\left(\frac{h_\phi}{\sin\theta}\right)^2\right]^{3/2}}+\frac{r^2-3\left[r^2+h_\theta^2+\left(\frac{h_\phi}{\sin\theta}\right)^2\right]}{\left[r^2+h_\theta^2+\left(\frac{h_\phi}{\sin\theta}\right)^2\right]^{3/2}}+\frac{h_{\phi\phi}\left(r^2+h_\theta^2\right)-h_\theta\cdot h_\phi\cdot h_{\theta\phi}}{r\sin^2\theta\left[r^2+h_\theta^2+\left(\frac{h_\phi}{\sin\theta}\right)^2\right]^{3/2}}$	$\frac{-2r^2-3h_\theta^2+r\cdot h_{\theta\theta}}{\left(r^2+h_\theta^2\right)^{3/2}}+\frac{\cot\theta\left(r\cdot h_\theta+\frac{1}{r}h_\theta^3\right)}{\left(r^2+h_\theta^2\right)^{3/2}}$
Spherical $\theta=h(r,\phi)$	$\frac{r\cdot h_r\vec{i}_r-\vec{i}_\theta+\frac{h_\phi}{\sin\theta}\vec{i}_\phi}{\sqrt{1+(r\cdot h_r)^2+\left(\frac{h_\phi}{\sin\theta}\right)^2}}$	$\frac{r\cdot h_{rr}+3h_r+2r^2h_r^3-\frac{r\cdot h_r\cdot h_\phi\cdot h_{r\phi}}{\sin^2\theta}}{\left[1+(r\cdot h_r)^2+\left(\frac{h_\phi}{\sin\theta}\right)^2\right]^{3/2}}-\frac{\cot\theta}{r}\cdot\frac{1+(r\cdot h_r)^2+2\left(\frac{h_\phi}{\sin\theta}\right)^2}{\left[1+(r\cdot h_r)^2+\left(\frac{h_\phi}{\sin\theta}\right)^2\right]^{3/2}}+\frac{h_{\phi\phi}\left[1+(r\cdot h_r)^2\right]-r^2\cdot h_r\cdot h_\phi\cdot h_{r\phi}}{r\sin^2\theta\left[1+(r\cdot h_r)^2+\left(\frac{h_\phi}{\sin\theta}\right)^2\right]^{3/2}}$	$\frac{r\cdot h_{rr}+3h_r+2r^2h_r^3}{\left[1+(r\cdot h_r)^2\right]^{3/2}}-\frac{\cot\theta}{r}\left[1+(r\cdot h_r)^2\right]^{-1/2}$

B.2 Evaluation of the viscous (deviatoric) tensor

For single-phase laminar flows we can, in general, write the Navier-Stokes momentum equation

$$\rho\frac{\partial\vec{u}}{\partial t}+\rho\left(\vec{u}\cdot\nabla\right)\vec{u}=\nabla\cdot\left[-p\boldsymbol{I}+\boldsymbol{\tau}\right]+\vec{F} \tag{B.28}$$

where ρ is the fluid density (kg/m^3), $\vec{u}$ is the velocity vector (m/s), p is the hydrostatic pressure (Pa), $\boldsymbol{I}$ is the identity matrix, $\boldsymbol{\tau}$ is the viscous or so-called deviatoric stress tensor, and $\vec{F}$ is a vector representing any net body force (N/m^3). In order to evaluate this equation it is necessary to expand the tensor $\boldsymbol{\tau}$ and relate it to the flow variables. In the case of Newtonian fluids, for example, it is known that there is a linear relationship between this tensor and its strain rate counterpart. When the fluid is also incompressible Stokes showed that

$$\boldsymbol{\tau}=\mu\left[\nabla\vec{u}+\left(\nabla\vec{u}\right)^T\right] \tag{B.29}$$

Here, $\nabla\vec{u}$ is a quantity describing spatial changes in the given velocity field. It is a 2nd rank tensor which, while similar to the speed gradient vector $\nabla\left(\sqrt{\vec{u}\cdot\vec{u}}\right)$, is sometimes the source of confusion. For a vector quantity $\vec{a}$ that exists in $\mathbb{R}^3$ with basis vectors $(\boldsymbol{e}_i,\boldsymbol{e}_j,\boldsymbol{e}_k)$ the gradient is defined as, in general

$$\nabla\vec{a}=\frac{\partial\vec{a}}{\partial x_j}\otimes\boldsymbol{e}_j=\frac{\partial a_i}{\partial x_j}\boldsymbol{e}_i\otimes\boldsymbol{e}_j \tag{B.30}$$

where $\boldsymbol{e}_i\otimes\boldsymbol{e}_j$ is the so-called dyadic or outer product of those two basis vectors. This operation is performed over all indices i, j, and k. When working in systems for which the basis vectors are fully uncoupled, e.g. cartesian space, the result is very simple. For example, consider the vector $\vec{a}=X\cdot\boldsymbol{e}_x+Y\cdot\boldsymbol{e}_y$ and observe that

$$\frac{\partial a_x}{\partial x_j}\otimes\boldsymbol{e}_j=\frac{\partial X}{\partial x}\boldsymbol{e}_x\otimes\boldsymbol{e}_x+\frac{\partial X}{\partial y}\boldsymbol{e}_x\otimes\boldsymbol{e}_y \tag{B.31}$$

which involves the outer products

$$\boldsymbol{e}_x\otimes\boldsymbol{e}_x=\begin{pmatrix}1&0\\0&0\end{pmatrix}\qquad\qquad\boldsymbol{e}_x\otimes\boldsymbol{e}_y=\begin{pmatrix}0&1\\0&0\end{pmatrix}$$

This allows us to very easily generalize the result in such a system to simply

$$\left(\nabla\vec{a}\right)_{i,j}=\frac{\partial a_i}{\partial x_j} \tag{B.32}$$

exactly as we would do for the Jacobian of a scalar quantity. Where the vector gradient becomes a bit trickier, however, is when the basis vectors couple (as in cylindrical and spherical systems). Now consider the cylindrical vector $\vec{a}=R\cdot\boldsymbol{e}_r+\Theta\cdot\boldsymbol{e}_\theta$ and observe that the first azimuthal derivative of the radial component is

$$\frac{1}{r}\frac{\partial R\cdot \boldsymbol{e}_r}{\partial\theta}\otimes\boldsymbol{e}_\theta = \frac{1}{r}\frac{\partial R}{\partial\theta}\boldsymbol{e}_r\otimes\boldsymbol{e}_\theta + \frac{R}{r}\frac{\partial\boldsymbol{e}_r}{\partial\theta}\otimes\boldsymbol{e}_\theta = \frac{1}{r}\frac{\partial R}{\partial\theta}\boldsymbol{e}_r\otimes\boldsymbol{e}_\theta + \frac{R}{r}\boldsymbol{e}_\theta\otimes\boldsymbol{e}_\theta \tag{B.33}$$

and involves the outer products

$$\boldsymbol{e}_r\otimes\boldsymbol{e}_\theta = \begin{pmatrix}0 & 1\\ 0 & 0\end{pmatrix} \qquad\qquad \boldsymbol{e}_\theta\otimes\boldsymbol{e}_\theta = \begin{pmatrix}0 & 0\\ 0 & 1\end{pmatrix}$$

Owing to the confusion associated with the tensor quantity $\nabla\vec{u}+(\nabla\vec{u})^T$ we examine it briefly in what follows. In order to facilitate ease of use throughout this thesis we expand it in several common coordinate systems and offer simplifications for geometries with reduced dimensionality, e.g. axisymmetric ones.

B.2.1 Cartesian space

In cartesian space we take the velocity vector

$$\vec{u} = u\cdot\vec{i}_x + v\cdot\vec{i}_y + w\cdot\vec{i}_z \tag{B.34}$$

and note that the gradient operator is

$$\nabla \rightarrow \frac{\partial}{\partial x}\otimes\vec{i}_x + \frac{\partial}{\partial y}\otimes\vec{i}_y + \frac{\partial}{\partial z}\otimes\vec{i}_z \tag{B.35}$$

Under these conditions the vector gradient $\nabla\vec{u}$ becomes

$$\nabla\vec{u} = \begin{pmatrix}\frac{\partial u}{\partial x} & \frac{\partial u}{\partial y} & \frac{\partial u}{\partial z}\\ \frac{\partial v}{\partial x} & \frac{\partial v}{\partial y} & \frac{\partial v}{\partial z}\\ \frac{\partial w}{\partial x} & \frac{\partial w}{\partial y} & \frac{\partial w}{\partial z}\end{pmatrix} \tag{B.36}$$

and yields the full tensor

$$\nabla\vec{u}+(\nabla\vec{u})^T = \begin{pmatrix} 2\frac{\partial u}{\partial x} & \left(\frac{\partial u}{\partial y}+\frac{\partial v}{\partial x}\right) & \left(\frac{\partial u}{\partial z}+\frac{\partial w}{\partial x}\right)\\ \left(\frac{\partial u}{\partial y}+\frac{\partial v}{\partial x}\right) & 2\frac{\partial v}{\partial y} & \left(\frac{\partial v}{\partial z}+\frac{\partial w}{\partial y}\right)\\ \left(\frac{\partial u}{\partial z}+\frac{\partial w}{\partial x}\right) & \left(\frac{\partial v}{\partial z}+\frac{\partial w}{\partial y}\right) & 2\frac{\partial w}{\partial z}\end{pmatrix} \tag{B.37}$$

When the problem is two-dimensional and $\vec{u} = u\cdot\vec{i}_x + v\cdot\vec{i}_y$ the tensor reduces to the 2x2 section in the upper left-hand quadrant.

B.2.2 Cylindrical space

In cylindrical space we take the velocity vector

$$\vec{u} = u\cdot\vec{i}_r + v\cdot\vec{i}_\theta + w\cdot\vec{i}_z \tag{B.38}$$

where r is the cylindrical radius, θ the azimuthal angle, and z the vertical height. Note that the cylindrical gradient operator is now

$$\nabla \to \frac{\partial}{\partial r} \otimes \vec{i}_r + \frac{1}{r}\frac{\partial}{\partial \theta} \otimes \vec{i}_\theta + \frac{\partial}{\partial z} \otimes \vec{i}_z \tag{B.39}$$

Under these conditions the vector gradient $\nabla\vec{u}$ becomes

$$\nabla\vec{u} = \begin{pmatrix} \frac{\partial u}{\partial r} & \left(\frac{1}{r}\frac{\partial u}{\partial \theta} - \frac{v}{r}\right) & \frac{\partial u}{\partial z} \\ \frac{\partial v}{\partial r} & \left(\frac{u}{r} + \frac{1}{r}\frac{\partial v}{\partial \theta}\right) & \frac{\partial v}{\partial z} \\ \frac{\partial w}{\partial r} & \frac{1}{r}\frac{\partial w}{\partial \theta} & \frac{\partial w}{\partial z} \end{pmatrix} \tag{B.40}$$

and yields the full tensor

$$\nabla\vec{u} + (\nabla\vec{u})^T = \begin{pmatrix} 2\frac{\partial u}{\partial r} & \left[\frac{1}{r}\frac{\partial u}{\partial \theta} + r\frac{\partial}{\partial r}\left(\frac{v}{r}\right)\right] & \left(\frac{\partial u}{\partial z} + \frac{\partial w}{\partial r}\right) \\ \left[\frac{1}{r}\frac{\partial u}{\partial \theta} + r\frac{\partial}{\partial r}\left(\frac{v}{r}\right)\right] & \left[\frac{u}{r} + \frac{1}{r}\frac{\partial v}{\partial \theta}\right] & \left(\frac{\partial v}{\partial z} + \frac{1}{r}\frac{\partial w}{\partial \theta}\right) \\ \left(\frac{\partial u}{\partial z} + \frac{\partial w}{\partial r}\right) & \left(\frac{\partial v}{\partial z} + \frac{1}{r}\frac{\partial w}{\partial \theta}\right) & 2\frac{\partial w}{\partial z} \end{pmatrix} \tag{B.41}$$

When the problem is two-dimensional and $\vec{u} = u \cdot \vec{i}_r + w \cdot \vec{i}_z$ the tensor reduces to the 2x2 section defined by

$$\nabla\vec{u} + (\nabla\vec{u})^T = \begin{pmatrix} 2\frac{\partial u}{\partial r} & \left(\frac{\partial u}{\partial z} + \frac{\partial w}{\partial r}\right) \\ \left(\frac{\partial u}{\partial z} + \frac{\partial w}{\partial r}\right) & 2\frac{\partial w}{\partial z} \end{pmatrix} \tag{B.42}$$

B.2.3 Spherical space

In spherical space we take the velocity vector

$$\vec{u} = u \cdot \vec{i}_r + v \cdot \vec{i}_\theta + w \cdot \vec{i}_\phi \tag{B.43}$$

where r is the spherical radius, θ is the polar angle, and ϕ is its azimuthal counterpart. Note that the spherical gradient operator is now

$$\nabla \to \frac{\partial}{\partial r} \otimes \vec{i}_r + \frac{1}{r}\frac{\partial}{\partial \theta} \otimes \vec{i}_\theta + \frac{1}{r\sin\theta}\frac{\partial}{\partial \phi} \otimes \vec{i}_\phi \tag{B.44}$$

Under these conditions the vector gradient $\nabla\vec{u}$ becomes

$$\nabla\vec{u} = \begin{pmatrix} \frac{\partial u}{\partial r} & \left[\frac{1}{r}\frac{\partial u}{\partial \theta} - \frac{v}{r}\right] & \left[\frac{1}{r\sin\theta}\frac{\partial u}{\partial \phi} - \frac{w}{r}\right] \\ \frac{\partial v}{\partial r} & \left[\frac{u}{r} + \frac{1}{r}\frac{\partial v}{\partial \theta}\right] & \left[\frac{1}{r\sin\theta}\frac{\partial v}{\partial \phi} - \cot\theta\left(\frac{w}{r}\right)\right] \\ \frac{\partial w}{\partial r} & \frac{1}{r}\frac{\partial w}{\partial \theta} & \left[\frac{u}{r} + \cot\theta\left(\frac{v}{r}\right) + \frac{1}{r\sin\theta}\frac{\partial w}{\partial \phi}\right] \end{pmatrix} \tag{B.45}$$

and yields the full tensor

$$\nabla\vec{u}+(\nabla\vec{u})^T = \begin{pmatrix} 2\frac{\partial u}{\partial r} & \left[\frac{1}{r}\frac{\partial u}{\partial \theta} + \left(\frac{\partial v}{\partial r} - \frac{v}{r}\right)\right] & \left[\frac{1}{r\sin\theta}\frac{\partial u}{\partial \phi} + \left(\frac{\partial w}{\partial r} - \frac{w}{r}\right)\right] \\ \left[\frac{1}{r}\frac{\partial u}{\partial \theta} + \left(\frac{\partial v}{\partial r} - \frac{v}{r}\right)\right] & 2\left[\frac{u}{r} + \frac{1}{r}\frac{\partial v}{\partial \theta}\right] & \left[\frac{1}{r\sin\theta}\frac{\partial v}{\partial \phi} + \left(\frac{1}{r}\frac{\partial w}{\partial \theta} - \cot\theta\cdot\frac{w}{r}\right)\right] \\ \left[\frac{1}{r\sin\theta}\frac{\partial u}{\partial \phi} + \left(\frac{\partial w}{\partial r} - \frac{w}{r}\right)\right] & \left[\frac{1}{r\sin\theta}\frac{\partial v}{\partial \phi} + \left(\frac{1}{r}\frac{\partial w}{\partial \theta} - \cot\theta\cdot\frac{w}{r}\right)\right] & 2\left[\frac{u}{r} + \cot\theta\left(\frac{v}{r}\right) + \frac{1}{r\sin\theta}\frac{\partial w}{\partial \phi}\right] \end{pmatrix} \tag{B.46}$$

When the problem is two-dimensional and $\vec{u} = u\cdot\vec{i}_r + v\cdot\vec{i}_\theta$ the tensor reduces to the 2x2 section defined by

$$\nabla\vec{u}+(\nabla\vec{u})^T = \begin{pmatrix} 2\frac{\partial u}{\partial r} & \left[\frac{1}{r}\frac{\partial u}{\partial \theta} + \left(\frac{\partial v}{\partial r} - \frac{v}{r}\right)\right] \\ \left[\frac{1}{r}\frac{\partial u}{\partial \theta} + \left(\frac{\partial v}{\partial r} - \frac{v}{r}\right)\right] & 2\left[\frac{u}{r} + \frac{1}{r}\frac{\partial v}{\partial \theta}\right] \end{pmatrix} \tag{B.47}$$

B.2.4 Summary

Table B.2.4 contains a distillation of the important results for evaluating the viscous stress tensor in several common coordinate spaces.

Table B.2: The tensor $\nabla\vec{u} + (\nabla\vec{u})^T$ calculated in several common coordinate systems and dimensionalities

Coordinate system	$\nabla\vec{u} + (\nabla\vec{u})^T$	
	General	2D
Cartesian $\vec{u} = u\vec{i}_x + v\vec{i}_y + w\vec{i}_z$	$\begin{pmatrix} 2\frac{\partial u}{\partial x} & \left(\frac{\partial u}{\partial y} + \frac{\partial v}{\partial x}\right) & \left(\frac{\partial u}{\partial z} + \frac{\partial w}{\partial x}\right) \\ \left(\frac{\partial u}{\partial y} + \frac{\partial v}{\partial x}\right) & 2\frac{\partial v}{\partial y} & \left(\frac{\partial v}{\partial z} + \frac{\partial w}{\partial y}\right) \\ \left(\frac{\partial u}{\partial z} + \frac{\partial w}{\partial x}\right) & \left(\frac{\partial v}{\partial z} + \frac{\partial w}{\partial y}\right) & 2\frac{\partial w}{\partial z} \end{pmatrix}$	$\begin{pmatrix} 2\frac{\partial u}{\partial x} & \left(\frac{\partial u}{\partial y} + \frac{\partial v}{\partial x}\right) \\ \left(\frac{\partial u}{\partial y} + \frac{\partial v}{\partial x}\right) & 2\frac{\partial v}{\partial y} \end{pmatrix}$
Cylindrical $\vec{u} = u\vec{i}_r + v\vec{i}_\theta + w\vec{i}_z$	$\begin{pmatrix} 2\frac{\partial u}{\partial r} & \left[\frac{1}{r}\frac{\partial u}{\partial \theta} + r\frac{\partial}{\partial r}\left(\frac{v}{r}\right)\right] & 0 \\ \left[\frac{1}{r}\frac{\partial u}{\partial \theta} + r\frac{\partial}{\partial r}\left(\frac{v}{r}\right)\right] & \left[\frac{u}{r} + \frac{1}{r}\frac{\partial v}{\partial \theta}\right] & 0 \\ \left(\frac{\partial u}{\partial z} + \frac{\partial w}{\partial r}\right) & \left(\frac{\partial v}{\partial z} + \frac{1}{r}\frac{\partial w}{\partial \theta}\right) & 0 \end{pmatrix} + \begin{pmatrix} 0 & 0 & \left(\frac{\partial u}{\partial z} + \frac{\partial w}{\partial r}\right) \\ 0 & 0 & \left(\frac{\partial v}{\partial z} + \frac{1}{r}\frac{\partial w}{\partial \theta}\right) \\ 0 & 0 & 2\frac{\partial w}{\partial z} \end{pmatrix}$	$\begin{pmatrix} 2\frac{\partial u}{\partial r} & \left(\frac{\partial u}{\partial z} + \frac{\partial w}{\partial r}\right) \\ \left(\frac{\partial u}{\partial z} + \frac{\partial w}{\partial r}\right) & 2\frac{\partial w}{\partial z} \end{pmatrix}$
Spherical $\vec{u} = u\vec{i}_r + v\vec{i}_\theta + w\vec{i}_\phi$	$\begin{pmatrix} 2\frac{\partial u}{\partial r} & 0 & 0 \\ \left[\frac{1}{r}\frac{\partial u}{\partial \theta} + \left(\frac{\partial v}{\partial r} - \frac{v}{r}\right)\right] & 0 & 0 \\ \left[\frac{1}{r\sin\theta}\frac{\partial u}{\partial \phi} + \left(\frac{\partial w}{\partial r} - \frac{w}{r}\right)\right] & 0 & 0 \end{pmatrix} + \begin{pmatrix} 0 & \left[\frac{1}{r}\frac{\partial u}{\partial \theta} + \left(\frac{\partial v}{\partial r} - \frac{v}{r}\right)\right] & 0 \\ 0 & 2\left[\frac{u}{r} + \frac{1}{r}\frac{\partial v}{\partial \theta}\right] & 0 \\ 0 & \left[\frac{1}{r\sin\theta}\frac{\partial v}{\partial \phi} + \left(\frac{1}{r}\frac{\partial w}{\partial \theta} - \cot\theta \cdot \frac{w}{r}\right)\right] & 0 \end{pmatrix} + \begin{pmatrix} 0 & 0 & \left[\frac{1}{r\sin\theta}\frac{\partial u}{\partial \phi} + \left(\frac{\partial w}{\partial r} - \frac{w}{r}\right)\right] \\ 0 & 0 & \left[\frac{1}{r\sin\theta}\frac{\partial v}{\partial \phi} + \left(\frac{1}{r}\frac{\partial w}{\partial \theta} - \cot\theta \cdot \frac{w}{r}\right)\right] \\ 0 & 0 & 2\left[\frac{u}{r} + \cot\theta\left(\frac{v}{r}\right) + \frac{1}{r\sin\theta}\frac{\partial w}{\partial \phi}\right] \end{pmatrix}$	$\begin{pmatrix} 2\frac{\partial u}{\partial r} & 0 \\ \left[\frac{1}{r}\frac{\partial u}{\partial \theta} + \left(\frac{\partial v}{\partial r} - \frac{v}{r}\right)\right] & 0 \end{pmatrix} + \begin{pmatrix} 0 & \left[\frac{1}{r}\frac{\partial u}{\partial \theta} + \left(\frac{\partial v}{\partial r} - \frac{v}{r}\right)\right] \\ 0 & 2\left[\frac{u}{r} + \frac{1}{r}\frac{\partial v}{\partial \theta}\right] \end{pmatrix}$

Appendix C

1D space charge limitations for field emitters

While individual IL electrospray emitters typically operate far from space-charge restrictions (see Lenguito [20] for basic arguments based on a spherical diode model) it is believed that densely populated arrays may be limited by the same Child-Langmuir threshold that governs the performance of other electrostatic engines (e.g the ion engine). As Lozano points out, the associated effects could become important when the emitter pitch dips below 10^{-4} to 10^{-5} m, depending upon specific emission conditions [21].

Derivation of the classical Child-Langmuir law for one-dimensional space-charge limited current begins by invoking Poisson's equation

$$\frac{d^2\Phi}{dz^2} = -\frac{\rho}{\epsilon_0} \tag{C.1}$$

and applying it to the inter-electrode gap, i.e. the space between the dense emission plane and the extractor, with boundary conditions $\Phi\left(z=0\right) = 0$ and $\Phi\left(z=-d\right) = -V$. The current density in this region, $j = en_iv_i$, varies with the axial velocity of the emitted charges. Through a simple balance between kinetic and electrostatic potential energies we can write $v_i = \sqrt{2q/m\left(-\Phi\right)}$, where $\Phi = \Phi\left(z\right)$, and substitute this in Poisson to find

$$\frac{d^2\Phi}{dz^2} = -\frac{j}{\epsilon_0}\left[2\frac{q}{m}\left(\Phi\right)\right]^{-1/2} \tag{C.2}$$

If we now recognize that

$$\frac{d^2\Phi}{dz^2} = \frac{1}{2}\frac{d}{d\Phi}\left(\frac{d\Phi}{dz}\right)^2 \tag{C.3}$$

we can perform a first integration that yields the result

$$\left(\frac{d\Phi}{dz}\right)^2 = \frac{4j}{\epsilon_0}\sqrt{\frac{-\Phi}{2q/m}} + C \tag{C.4}$$

where the constant of integration, C, may be used to prescribe a standing field magnitude at either boundary. In the classical Child-Langmuir analysis, $C \to 0$ and indicates a vanishing field at the emission plane. A subsequent integration leads to the well-known results

$$j_{CL} = \frac{4}{9}\epsilon_0\sqrt{2\frac{q}{m}}\frac{V^{3/2}}{d^2} \tag{C.5}$$

$$\left(\frac{F}{A}\right)_{CL} = \frac{8}{9}\epsilon_0\left(\frac{V}{d}\right)^2 \tag{C.6}$$

for limiting current and thrust densities, respectively. Ion engines and other electrostatic plasma accelerators typically produce charges upstream of the non-neutral grid spaces and do not require large fields to stream particles. The Child-Langmuir results are valid in these situations but begin to break down for field emission devices where strong entry gradients are an unavoidable facet of the ionization process, as several authors have detailed [22, 23, 24]. In the case of electrosprays, for example, we can see direct evidence of this by formulating a simple pressure balance. For steady emission to occur, hydraulic and electrostatic forces must approach a nominal equilibrium such that

$$\frac{1}{2}\epsilon_0 E^2 + P_f \sim P_c + \Delta P \tag{C.7}$$

where the first term on the LHS describes the driving electrical traction (nominally, E ∼ V/d in the 1D case) while the second term corresponds to an imposed hydrostatic pressure that may originate, for example, in a liquid reservoir supplying the emission zone. On the RHS, P_c is some characteristic surface tension force acting on the electrified liquid interface and ΔP is the pressure drop carrying liquid between a reservoir (where P_f is the reference pressure) and the emission region.

For situations in which a substantive feed pressure is employed, it is possible that the sustaining electrical traction need not be very large (lending validity to Eqs. C.5 and C.6) but this manner of operation is not always the most favorable. At the opposite end of the spectrum, where $P_f \to 0$, we sometimes find architectural simplicities that follow from passive hydraulics. There, the emission physics likely preclude a vanishing surface traction as suggested by Eq. C.7. Ignoring the hydrodynamic pressure drop for a moment (as others have shown, $\Delta P \ll P_c$ in many situations of practical interest [25]), we see that $\epsilon_0 E^2/2 \sim P_c$ for steady spraying when P_f is insignificant. More formally, we can write

$$\left(\frac{d\Phi}{dz}\right)^2_{z=0} \sim \frac{4\gamma}{\epsilon_0 r_P} \tag{C.8}$$

for steady emission to prevail, where γ is a characteristic fluid surface energy (J/m^2) and r_P is a principal length scale dictating the surface tension pressure. In closed-flow and hybrid emitters, r_P is closely related to either the capillary radius or pore dimension. After substituting this condition for the constant in Eq. C.4 and

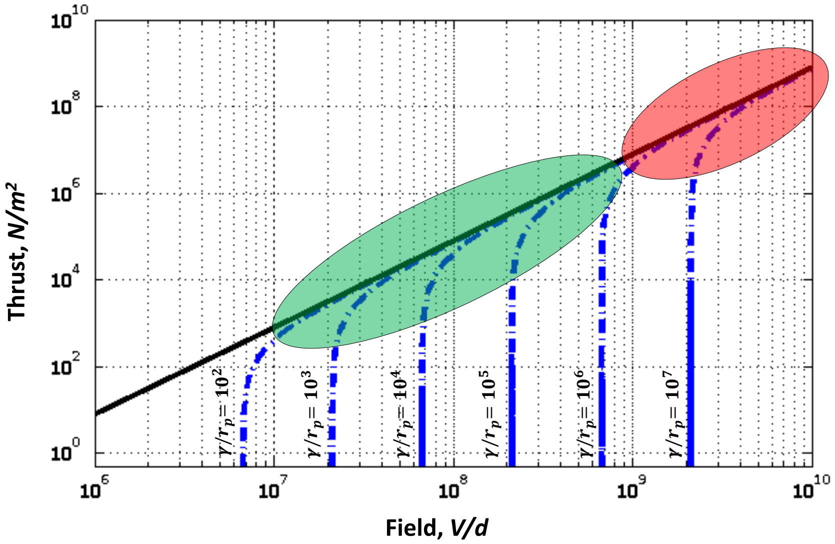

Figure C-1: 1D space charge thresholds. The classical Child-Langmuir limit is shown in black alongside cases of nonzero surface fields in blue. The green highlight indicates upper bounds in the feasible V/d region while the red highlight reflects a regime that is likely precluded by manufacturing and insulation issues with electrosprays.

performing a second integration we find an expression of the form

$$\zeta^2 + \sqrt{\zeta_0}\left[(2-\zeta)\sqrt{1+\zeta}\right] = 0 \tag{C.9}$$

which is general and encompasses the subset of Child-Langmuir results. Here we have defined the dimensionless pressures

$$\zeta = \frac{F/A}{P_c} \tag{C.10}$$

$$\zeta_0 = \frac{(F/A)_{CL}}{P_c} \tag{C.11}$$

Solutions to this expression have been computed for several values of P_c and plotted alongside the classical Child-Langmuir limit in Figure C-1. Due to manufacturing and insulation challenges, small electrospray systems generally operate in the voltage band from 10^3 - 10^4 V with electrode gaps between 10^{-4} and 10^{-5} m. These values indicate a feasible V/d range spanning 10^7 - 10^9 V/m. From the figure we see that this range coincides with limiting thrust densities (greater than 10^3 Pa) that are still well-beyond the laboratory performance of state-of-the-art electrosprays.

Bibliography

[1] Zeleny, J., "The Electrical Discharge From Liquid Points, and a Hydrostatic Method of Measuring the Electric Intensity at Their Surfaces," *The Physical Review*, vol. III, no. 2, February 1914.

[2] Zeleny, J., "Instability of Electrified Liquid Surfaces," *The Physical Review*, vol. X, no. 1, July 1917.

[3] Taylor, G., "Disintegration of Water Drops in an Electric Field," *Proceedings of the Royal Society A*, vol. 280, no. 1382, 28 July 1964.

[4] Krpoun, R. and Shea, H., "A method to determine the onset voltage of single and arrays of electrospray emitters," *Journal of Applied Physics*, vol. 104, 064511 (2008).

[5] Martinez-Sanchez, M., "Colloidal Engines," MIT 16.522 Space Propulsion course notes, lectures 23-25.

[6] Fernandez de La Mora, J., "The Fluid Dynamics of Taylor Cones," *Annual Review of Fluid Mechanics*, 39:217-43, 2007.

[7] Iribarne, J., and Thomson, B., "On the evaporation of small ions from charged droplets," *Journal of Chemical Physics*, 64, 2287 (1976).

[8] Guerrero, I., Bocanegra, R., Higuera, F., and Fernandez de la Mora, J., "Ion evaporation from Taylor cones of propylene carbonate mixed with ionic liquids," *Journal of Fluid Mechanics*, vol. 591, pp. 437-459, 2007.

[9] Loscertales, I. and Fernandez de la Mora, J. "Experiments on the kinetics of field evaporation of small ions from droplets," *The Journal of Chemical Physics*, 103, 5041 (1995).

[10] Fedkiw, T. and Lozano, P., "Development and characterization of an iodine field emission ion source for focused ion beam applications," *Journal of Vacuum Science & Technology B*, 27, 2648 (2009).

[11] Fedkiw, T. P., "Characterization of an Iodine-Based Ionic Liquid Ion Source and Studies on Ion Fragmentation," *SM Thesis*, Massachusetts Institute of Technology, Department of Aeronautics and Astronautics, 2010.

[12] Lozano, P. and Martinez-Sanchez, M., "Efficiency Estimation of EMI-BF4 Ionic Liquid Electrospray Thrusters," *41st AIAA/ASME/SAE/ASEE Joint Propulsion Conference & Exhibit*, 10-13 July 2005, Tucson, AZ, AIAA 2005-4388.

[13] Sutton, G. and Oscar, B., *Rocket Propulsion Elements*. Hoboken, NJ: Wiley 2010. 8th Ed.

[14] Jahn, R. G., *Physics of electric propulsion*. New York: McGraw-Hill, 1968.

[15] Goebel, D. and Katz, I., *Fundamentals of Electric Propulsion: Ion and Hall Thrusters*. Hoboken, NJ: John Wiley & Sons, 2008.

[16] Turner, M. J. L., *Rocket and Spacecraft Propulsion: Principles, Practice and New Developments*. Chichester, UK: Praxis Publishing, 2009. 3rd Ed.

[17] Lozano, P., "Analytical Approximations for Low Thrust Maneuvers," MIT 16.522 Space Propulsion course notes, Lecture 5 (2011).

[18] Maral, G. and Bousquet, M., *Satellite Communications Systems: Systems, Techniques and Technology*. Chichester, UK: John Wiley & Sons Ltd, 2009. 5th Ed.

[19] Helvajian, H. and Janson, S., Ed., *Small Satellites: Past, Present, and Future*. Norwood, MA: Books24x7.com, 2008.

[20] Lenguito, G., Fernandez de la Mora, J., and Gomez, A., "Design and Testing of Multiplexed Electrospray with Post-Acceleration for Space Propulsion Applications," *47th AIAA/ASME/SAE/ASEE Joint Propulsion Conference & Exhibit*, 31 July - 03 August 2011, San Diego, CA, AIAA 2011-5590.

[21] Lozano, P., "Studies on the Ion-Droplet Mixed Regime in Colloid Thrusters," *Doctoral Thesis*, Massachusetts Institute of Technology, Department of Aeronautics and Astronautics, 2003.

[22] Stern, T. E., Gossling, B. S., and Fowler, R. H., "Further Studies in the Emission of Electrons from Cold Metals," *Proc. R. Soc. Lond. A*, 124 (1929), pp. 699-723.

[23] Barbour, J., Dolan, W., Trolan, J., Martin, E., and Dyke, W., "Space-Charge Effects in Field Emission," *Physical Review*, vol. 92, no. 1, 1953.

[24] Anderson, W., "Role of space charge in field emission cathodes," *Journal of Vacuum Science & Technology B*, 11 (1993), pp. 383-386.

[25] Courtney, D., "Ionic Liquid Ion Source Emitter Arrays Fabricated on Bulk Porous Substrates for Spacecraft Propulsion," *Doctoral Thesis*, Massachusetts Institute of Technology, Department of Aeronautics and Astronautics, June 2011.

[26] Perel, J., "Alkali Metal Ion Sources," *Journal of the Electrochemical Society*, vol. 115, issue 12, 343C-350C, 1968.

[27] Mahoney, J., Yahiku, A., Daley, H., Moore, R., and Perel, J., "Electrohydrodynamic Ion Source," *Journal of Applied Physics*, vol. 40, no. 13, December 1969.

[28] Perel, J., Mahoney, J., Moore, R., and Yahiku, A., "Research and Development of a Charged-Particle Bipolar Thruster," *AIAA Electric-Propulsion and Plasmadynamics Conference*, Colorado Springs, CO, 11-13 September 1967, AIAA 67-728.

[29] Romero-Sanz, I., Bocanegra, R., Fernandez de la Mora, J., and Gamero-Castano, M., "Source of heavy molecular ions based on Taylor cones of ionic liquids operating in the pure ion evaporation regime," *Journal of Applied Physics*, vol. 94, no. 5, 1 September 2003.

[30] Garoz, D., Bueno, C., Larriba, C., Castro, S., Romero-Sanz, I., Fernandez de la Mora, J., Yoshida, Y., and Saito, G., "Taylor cones of ionic liquids from capillary tubes as sources of pure ions: The role of surface tension and electrical conductivity," *Journal of Applied Physics*, 102, 064913 (2007).

[31] Lozano, P. and Martinez-Sanchez, M., "Ionic liquid ion sources: characterization of externally wetted emitters," *Journal of Colloid and Interface Science*, 282 (2005), 415-421.

[32] Lozano, P. and Martinez-Sanchez, M., "Ionic liquid ion sources: suppression of electrochemical reactions using voltage alternation," *Journal of Colloid and Interface Science*, 280 (2004), 149-154.

[33] Lozano, P., "Energy properties of an EMI-Im ionic liquid ion source," *Journal of Physics D: Applied Physics*, 39 (2006), pp. 126-134.

[34] Larriba, C., Castro, S., Fernandez de la Mora, J., and Lozano, P., "Monoenergetic source of kilodalton ions from Taylor cones of ionic liquids," *Journal of Applied Physics*, 101, 084303 (2007).

[35] Castro, S., Larriba, C., Fernandez de la Mora, J., Lozano, P., Sumer, S., Yoshida, Y., and Saito, G., "Effect of liquid properties on electrosprays from externally wetted ionic liquid ion sources," *Journal of Applied Physics*, 102, 094310 (2007).

[36] Castro, S. and Fernandez de la Mora, J., "Effect of tip curvature on ionic emissions from Taylor cones of ionic liquids from externally wetted tungsten tips," *Journal of Applied Physics*, 105, 034903 (2009).

[37] Perez-Martinez, C., and Lozano, P., "Visualization of beams from ionic liquid ion sources for focused ion beam applications," *Journal of Vacuum Science & Technology B*, 06F601 (2012).

[38] Perez-Martinez, C., Rojas-Herrera, J., and Lozano, P., "Alternative emitter substrates for Ionic Liquid Ion Source implementation in focused ion beams," *Microelectronic Engineering*, 123 (2014), pp. 13-17.

[39] Gassend, B., "A Fully Microfabricated Two-Dimensional Electrospray Array with Applications to Space Propulsion," *Doctoral Thesis*, Department of Aeronautics and Astronautics, Massachusetts Institute of Technology, June 2007.

[40] Velasquez, L. F., Carretero, J., Ankinwande, A., and Martinez-Sanchez, M., "The Concept and Development of a Micro-Fabricated Colloid Thruster Array," *39th AIAA/ASME/SAE/ASEE Joint Propulsion Conference and Exhibit*, 20-23 July 2003, Huntsville, AL, AIAA 2003-4850.

[41] Velasquez-Garcia, L. F., Martinez-Sanchez, M., and Akinwande, A., "Two-dimensional Micro-fabricated Colloid Thruster Arrays," *40th AIAA/ASME/SAE/ASEE Joint Propulsion Conference and Exhibit*, 11-14 July 2004, Fort Lauderdale, FL, AIAA 2004-3595.

[42] Gassend, B., Velasquez-Garcia, L., Akinwande, A., and Martinez-Sanchez, M., "A Microfabricated Planar Electrospray Array Ionic Liquid Ion Source With Integrated Extractor," *Journal of Microelectromechanical Systems*, vol. 18, no. 3, June 2009.

[43] Garza, T., Lozano, P., Velasquez-Garcia, L., and Martinez-Sanchez, M., "The Characterization of Silicon Wettability and Properties of Externally Wetted Microfabricated Electrospray Thruster Arrays," *29th International Electric Propulsion Conference*, Princeton University, 31 October - 4 November 2005, IEPC-2005-195.

[44] Garza, T., Lozano, P., Velasquez-Garcia, L., and Martinez-Sanchez, M., "Propellant Spread over Silicon Electrospray Surfaces," *42nd AIAA/ASME/SAE/ASEE Joint Propulsion Conference & Exhibit*, 9-12 July 2006, Sacramento, CA, AIAA 2006-4640.

[45] Krpoun, R. and Shea, H., "Integrated out-of-plane nanoelectrospray thruster arrays for spacecraft propulsion," *Journal of Micromechanics and Microengineering*, 19 (2009), 045019 (10pp).

[46] Krpoun, R., Smith, K., Stark, J., and Shea, H., "Tailoring the hydraulic impedance of out-of-plane micromachined electrospray sources with integrated electrodes," *Applied Physics Letters*, 94, 163502 (2009).

[47] Lenguito, G. and Gomez, A., "Pressure-Driven Operation of Microfabricated Multiplexed Electrospray of Ionic Liquid Solutions for Space Propulsion Applications," *Journal of Microelectromechanical Systems*, accepted.

[48] Smith, K., Stark, J., Krpoun, R., and Shea, H., "Performance of a microfabricated Colloid thruster system," *31st International Propulsion Conference*, Ann Arbor, MI, 20-24 September 2009, IEPC-2009-189.

[49] Dandavino, S., Ataman, C., Chakraborty, S., Shea, H., Ryan, C., and Stark, J., "Progress Towards a Miniaturized Electrspray Thruster for Propulsion of Small Spacecraft," *48th AIAA/ASME/SAE/ASEE Joint Propulsion Conference & Exhibit*, 30 July - 01 August 2012, Atlanta, GA, AIAA 2012-4024.

[50] Ryan, C., Daykin-Iliopolous, A., Stark, J., Salaverri, A., Vargas, E., Rangsten, P., Dandavino, S., Ataman, C., Chakraborty, S., Courtney, D., and Shea, H., "Experimental progress towards the MicroThrust MEMS electrospray electric propulsion system," *33rd International Electric Propulsion Conference*, Washington, DC, 6-10 October 2013, IEPC-2013-146.

[51] Dandavino, S., Ataman, C., Chakraborty, S., Shea, H., Ryan, C., and Stark, J., "Design and Fabrication of the thruster heads for the MicroThrust MEMS electrospray propulsion system," *33rd International Electric Propulsion Conference*, Washington, DC, 6-10 October 2013, IEPC-2013-127.

[52] Legge, R., Lozano, P., and Martinez-Sanchez, M., "Fabrication and Characterization of Porous Metal Emitters for Electrospray Thrusters," *30th International Electric Propulsion Conference*, Florence, Italy, 17-20 September, 2007, IEPC-2007-145.

[53] Legge, R., "Fabrication and Characterization of Porous Metal Emitters fo Electrospray Applications," *SM Thesis*, Department of Aeronautics and Astronautics, Massachusetts Institute of Technology, June 2008.

[54] Legge, R. and Lozano, P., "Electrospray Propulsoin Based on Emitters Microfabricated in Porous Metals," *Journal of Propulsion and Power*, vol. 27, no. 2, March-April 2011.

[55] Courtney, D., Li, H., Gomez Maqueo, P. D., Fedkiw, T., and Lozano, P., "On the Validation of Porous Nickel as Substrate Material for Electrospray Ion Propulsion," *46th AIAA/ASME/SAE/ASEE Joint Propulsion Conference & Exhibit*, 25-28 July 2010, Nashville, TN, AIAA 2010-7020.

[56] Courtney, D, Li, H., and Lozano, P., "Emission measurements from planar arrays of ionic liquid ion sources," *Journal of Applied Physics D: Applied Physics*, 45 (2012), 485203.

[57] Courtney, D., Li, H., and Lozano, P., "Electrochemical Micromachining on Porous Nickel for Arrays of Electrospray Ion Emitters," *Journal of Microelectromechanical Systems*, vol. 22, no. 2, April 2013.

[58] Coffman, C. and Lozano, P., "On the Manufacturing and Emission Characteristics of a Novel Borosilicate Electrospray Source," *49th AIAA/ASME/SAE/ASEE Joint Propulsion Conference & Exhibit*, 14-17 July 2013, San Jose, CA, AIAA 2013-4035.

[59] Saville, D. A., "ELECTROHYDRODYNAMICS: The Taylor-Melcher Leaky Dielectric Model," *Annu. Rev. Fluid Mech.*, 1997, 29:27-64.

[60] Taylor, G. I., "Studies in electrohydrodynamics I - The circulation produced in a drop by an electric field" *Proc. R. Soc. A*, 291:159-66, 1966.

[61] Melcher, J. R. and Taylor, G. I., "Electrohydrodynamics: a review of the role of interfacial sheer stresses," *Annu. Rev. Fluid Mech.*, 1:111-46, 1969.

[62] Higuera, F. "Model of the meniscus of an ionic-liquid ion source," *Physical Review E*, 77, 026308 (2008).

[63] Probstein, R. F., *Physicochemical Hydrodynamics: An Introduction.* London: Butterworth, 1989.

[64] Wakai, C., Oleinikova, A., Ott, M., and Weingartner, H., "How Polar are Ionic Liquids? Determination of the Static Dielectric Constant of an Imidazolium-based Ionic Liquid by Microwave Dielectric Spectroscopy," *The Journal of Physical Chemistry B: Letters*, 109, 17028-17030, 2005.

[65] Huang, M., Jiang, Y., Sasisanker, P., Driver, G., and Weingartner, H., "Static Relative Dielectric Permittivities of Ionic Liquids at 25°C," *Journal of Chemical & Engineering Data*, 56, 1494-1499, 2011.

[66] Rosenkilde, C. E., "A dielectric fluid drop in an electric field," *Proc. Roy. Soc. A.*, 312, pp. 473 - 494 (1969).

[67] Brazier-Smith, P. R., "Stability and Shape of Isolated and Pairs of Water Drops in an Electric Field," *Physics of Fluids*, 14, 1 (1971).

[68] Miksis, M. J., "Shape of a drop in an electric field," *Phys. Fluids*, 24 (11), 1981.

[69] Sherwood, J. D., "Breakup of fluid droplets in electric and magnetic fields," *J. Fluid Mech.*, vol. 188, pp. 133-146 (1988).

[70] Basaran, O. A. and Scriven, L. E., "Axisymmetric Shapes and Stability of Pendant and Sessile Drops in an Electric Field," *Journal of Colloid and Interface Science*, vol. 140, no. 1, 1990.

[71] Wohlhuter, F. K. and Basaran, O. A., "Shapes and stability of pendant and sessile dielectric drops in an electric field," *J. Fluid Mech.*, vol. 235, pp. 481 - 510, 1992.

[72] Boudouvis, A., Puchalla, J., and Scriven, L., "Magnetohydrostatic equilibria of ferrofluid drops in external magnetic fields," *Chem. Eng. Comm.*, vol. 67, pp. 129 - 144, 1988.

[73] Xie, J., Canonica, M., and Lozano, P., "Fabrication of Electrospray Thrusters by Sintering Glass Microspheres," *49th AIAA/ASME/SAE/ASEE Joint Propulsion Conference & Exhibit*, 14-17 July 2013, San Jose, CA, AIAA 2013-3824.

[74] Lozano, P., Martinez-Sanchez, M., and Lopez-Urdiales, J., "Electrospray emission from nonwetting flat dielectric surfaces," *Journal of Colloid and Interface Science*, 276 (2004), pp. 392-399.

[75] Solymar, L. and Walsh, D., *Electrical properties of materials.* New York: Oxford University Press (8th Ed., 2010).

[76] Hummel, R., *Electronic Properties of Materials.* New York: Springer (4th Ed., 2012).

[77] Landau, L. D. and Lifshitz, E. M., *Electrodynamics of Continuous Media.* Pergamon Press, 1960.

[78] Melcher, J. R., *Continuum Electromechanics.* Cambridge, MA: MIT Press, 1981.

[79] Zahn, M., *Electromagnetic Field Theory: A Problem Solving Approach.* Massachusetts Institute of Technology: MIT OpenCourseWare.

[80] Coffman, C. and Lozano, P., "On the electrospray emission from porous media and implications for emitter optimization," *Propulsion and Energy Forum: 50th AIAA/ASME/SAE/ASEE Joint Propulsion Conference*, 28-30 July 2014, Cleveland, OH, AIAA 2014-3695.

[81] Batchelor, G. K., *An introduction to fluid dynamics.* Cambridge, UK; New York, NY: Cambridge University Press, 2000 (1st Cambridge Mathematical Library ed.).

[82] Abramowitz, M. and Stegun, I., eds., *Handbook of Mathematical Functions with Formulas, Graphs, and Mathematical Tables.* New York: Dover (1964).

[83] *CRC Standard Mathematical Tables.* Boca Raton, FL: CRC Press, 1987.

[84] Suvorov, V. G. and Litvinov, E. A., "Dynamic Taylor cone formation on liquid metal surface: numerical modelling," *J. Phys. D: Appl. Phys.*, 33 (2000), pp. 1245-1251.

[85] Dyke, W. and Dolan, W., *Advances in Electronics and Electron Physics.* Vol. VIII (Academic, New York, 1956).

[86] Wiesner, J. C. and Everhart, T. E., "Point-cathode electron sources-electron optics of the initial diode region," *J. Appl. Phys.*, 44, 2140 (1973).

[87] Ward, J. W. and Seliger R. L., "Trajectory calculations of the extraction region of a liquid-metal ion source," *J. Vac. Sci. Technol.*, 19(4), Nov./Dec. 1981.

[88] Deyko, A., et al., "Measuring and predicting $\Delta_{vap}H_{298}$ values of ionic liquids," *Phys. Chem. Chem. Phys.*, 2009, 11, 8544-8555.

[89] Zaitsau, D. H., et al., "Structure-Property Relationships in Ionic Liquids: A Study of the Anion Dependence in Vaporization Enthalpies of Imidazolium-Based Ionic Liquids," *ChemPhysChem* 2012, 13, 1868-1876.

[90] Stoppa, A., Zech, O., Kunz, W., and Buchner, R., "The Conductivity of Imidazolium-Based Ionic Liquids from (-35 to 195) °C. A. Variation of Cation's Alkyl Chain," *J. Chem. Eng. Data* 2010, 55, 1768-1773.

[91] Vila, J., et al., "Liquid-solid-liquid phase transition hysteresis loops in the ionic conductivity of ten imidazolium-based ionic liquids," *Fluid Phase Equilibria*, 320 (2012), 1-10.

[92] Pantano, C., Ganan-Calvo, A. M., and Barrero, A., "Zeroth-order, electrohydrostatic solution for electrospraying in cone-jet mode," *J. Aerosol Sci.*, Vol. 25, No. 6, pp. 1065-1077, 1994.

[93] Fernandez De La Mora, J. and Loscertales, I. G., "The current emitted by highly conducting Taylor cones," *J. Fluid Mech.* (1994), vol. 260, pp. 155-184.

[94] Eustathopoulos, N., Nicholas, M. G., and Drevet, B., *Wettability at High Temperatures*. Oxford, England, UK: Pergamon Materials Series, 1999 (Volume 3).

[95] Cloupeau, M. and Prunet-Foch, B., "Electrostatic spraying of liquids: Main functioning modes," *Journal of Electrostatics*, 25 (1990), pp. 165-184.

[96] Cloupeau, M. and Prunet-Foch, B., "ELECTROHYDRODYNAMIC SPRAYING FUNCTIONING MODES: A CRITICAL REVIEW," *J. Aerosol Sci.*, Vol. 25, No. 6, pp. 1021-1036, 1994.

[97] Ganan-Calvo, A. M. and Montanero, J. M., "Revision of capillary cone-jet physics: Electrospray and flow focusing," *PHYSICAL REVIEW E*, 79, 066305 (2009).

[98] Herrada, M. A., Lopez-Herrera, J. M., Ganan-Calvo, A. M., Vega, E. J., Montanero, J. M., and Popinet, S., "Numerical simulation of electrospray in the cone-jet mode," *PHYSICAL REVIEW E*, 86, 026305 (2012).

[99] Coles, T. M. and Lozano, P. C., "Investigating Efficiency Losses from Solvated Ion Fragmentation in Electrospray Thruster Beams," *49th AIAA/ASME/SAE/ASEE Joint Propulsion Conference*, 14-17 July 2013, San Jose, CA, AIAA 2013-4033.

[100] Hardy, S. C., "THE SURFACE TENSION OF LIQUID GALLIUM," *Journal of Crystal Growth*, 71 (1985), 602-606.